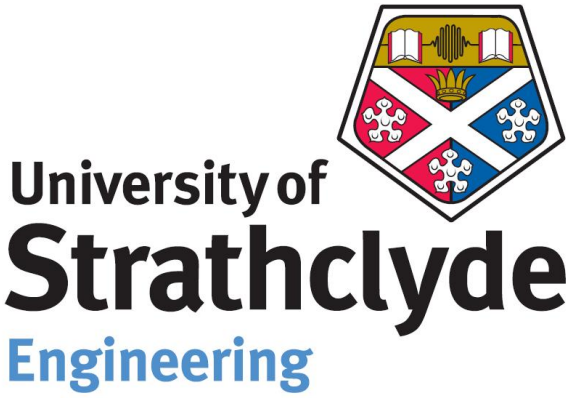

Department of Chemical and Process Engineering

COMPUTATIONAL MODELLING AND DESIGN OF BIOINSPIRED SILICA MATERIALS

ALESSIA CENTI

This dissertation is submitted for the degree of

Doctor of Philosophy

May 2017

Alessia Centi: *Computational modelling and design of bioinspired silica materials*

SUPERVISORS:
Miguel Jorge (University of Strathclyde, UK)
Jan Sefcik (University of Strathclyde, UK)

LOCATION:
Glasgow

To my granddad who once asked me if he could move to Scotland with me so he could take care of me. You would be really proud of me now but still not convinced it was really necessary to go so far away.

DECLARATION

This thesis is the result of the author's original research. It has been composed by the author and has not been previously submitted for examination which has led to the award of a degree.

Alessia Centi
Glasgow, May 2017

ABSTRACT

The use of bio-inspired methods for production of mesoporous silicas could lead to significant improvements in the synthetic conditions at which these materials are traditionally produced, removing the need for strong pH as well as high temperatures and pressures, and opening the way for milder treatments for template removal. However, due to the complexity of these systems, with many processes occurring simultaneously and high dependence on the specific synthetic conditions, obtaining a detailed description of their mechanism of formation based only on experimental methods is often very difficult. To overcome this difficulty, simulations methods, particularly molecular dynamics, have been developed and used to shed some light into this complex but fascinating problem.

In the present thesis, the processes underlying the synthesis of bio-inspired silica materials are investigated at computational level by means of a multi-scale approach. This methodology has two major advantages: it enables to explore longer time and length scales, beyond the current limit of atomistic simulations, while allowing to maintain realism at the lower resolution levels, which are calibrated to match properties obtained at higher levels of theory.

The work can be divided into two main parts. The first part aims to provide more insight into the synthesis of two early examples of bio-inspired materials (HMS and MSU-V), by means of a combination of atomistic and coarse-grained simulations. HMS and MSU-V materials share some common characteristics: they are both synthesised using amine surfactants as templates and a neutral templating route has been proposed to explain their formation. By simulating their synthesis at different pH values, it was possible to show that charged species are necessary to promote mesophase formation (disordered packing of rod-like micelles for HMS materials and lamellar structures for HMS). In both systems, in fact, neutral species produced phase separation of the templating materials into an unstructured and non-porous phase, and the lack of interactions with silicates indicates that these conditions cannot lead to structural organisation. Hence, molecular dynamics simulations reveal that, similarly to other mesoporous silicas and contrary to what has been previously hypothesised, charge matching interactions rather than hydrogen bonds are responsible for the self-assemble this class of materials. This knowledge

is fundamental to provide further control over the properties of these solids and target their design for specific applications.

In the second part, atomistic simulations are used to help elucidate the mechanism of template removal from a bio-inspired silica material by solvent extraction. This revealed that mild post-synthetic acid treatments allow to remove the templating additive by reducing, and eventually switching off, its interaction with the silica material. In agreement with experimental findings, which show that the majority of the additive is removed between pH 5 and 4, simulations indicate that at pH below 4.2 thermal fluctuations are sufficient to cause widespread release of the template. This result suggests that molecular simulations can be used as a simple and inexpensive tool for choosing appropriate solvents and experimental conditions in the material purification processes.

PUBLICATIONS

Parts of the following chapters have been published in:

Chapter 4 Currently in preparation

Chapter 5 Centi, A. and Jorge, M. 'Molecular Simulation Study of the Early Stages of Formation of Bioinspired Mesoporous Silica Materials'. *Langmuir* 32.28 (2016), pp. 7228–7240. DOI: 10.1021/acs.langmuir.6b01731

Chapter 6 Manning, J. R. H., Yip, T., Centi, A., Jorge, M. and Patwardhan, S. V. 'An eco-friendly, tunable and scalable method for producing porous functional nanomaterials designed using molecular interactions'. *ChemSusChem* (2017). DOI: 10.1002/cssc.201700027

Above all, don't fear the difficult moments. The best comes from them.

— Rita Levi Montalcini

ACKNOWLEDGMENTS

These years in Scotland were a great adventure for me, the new things I learnt, the places I saw and the people I met along the way all contributed to make this journey truly memorable.

The person I would like to thanks the most is my supervisor Dr. Miguel Jorge. His support, guidance and patience throughout my PhD were invaluable. Miguel, I really admire your enthusiasm and passion and I am grateful for all the research or just life related chats that encouraged me to keep going. A big thanks also goes to the rest of the group: Carlos, Chris, Andrew and Nile as well as to Siddharth and Joe. Thanks for your support, encouragement and for making our meetings always so interesting and enjoyable.

Javier, David, Scott, Craig, Paul, Carlota, Evan, Dorin, Maryam and Hrvojka thanks for the banter, the chats and all the good memories. Ross, thanks for teaching me the basic of "surviving" in Glasgow and for all the amazing evenings in Mount Florida, I couldn't have hoped for a better flatmate. Patrick, thanks for being the rational one in our duo, but most importantly for providing me with unlimited hugs, laughs and food (including the best carbonara ever) over the last crazy months.

Amici, grazie per tutte le chat, i messaggi e le discussioni su whatsapp che, nonostante la lontananza, mi fanno sentire come se fossi lì con voi. Nicoletta, Vittorio, Davide e Luigia non so come farei senza di voi, grazie per esserci sempre, per parlare di cose serie o di cose stupide.

E soprattuto un grazie enorme alla mia mamma e al mio papà che mi hanno sempre incoraggiata a fare ciò che mi rende felice, so quanto siete orgoglisi di me ma io lo sono ugualmente di voi.

CONTENTS

LIST OF FIGURES

LIST OF TABLES

NOMENCLATURE

LATIN LETTERS

$[M_n]$	Concentration of clusters with n molecules
ΔH_{imm}	Heat of immersion
$\hat{H}$	Hamiltonian
$[\equiv SiO^-]$	Number of siloxide ions per area of surface
[Additive]	Number of additive molecules per area of surface
$\langle E_{int} \rangle$	Average energy of interaction
$\mathbf{a}$	Acceleration
$\mathbf{b}$	Box vector
$\mathbf{F}$	Force
$\mathbf{p}$	Momentum
$\mathbf{r}$	Position vector
$\mathbf{v}$	Velocity
$\mathbf{W}$	Coupling parameter for the Parrinello-Rahman barostat
$\tilde{p}$	Momentum of the real system for the Nosé-Hoover thermostat
$\tilde{p}_{\tilde{s}}$	Momentum of the heat bath for the Nosé-Hoover thermostat
$\tilde{Q}$	Mass parameter for the Nosé-Hoover thermostat
$\tilde{s}$	Time scaling parameter for the Nosé-Hoover thermostat
A	General dynamical variable
A	Surface area
a	Steepness of the well of the Morse potential
a_0	Area per head group of surfactant molecule

b	Bond length
C_n	Constants for Ryckaert-Bellemans torsional potential
C_{pp}	Packing parameter
d	Pore diameter
$d\tilde{t}$	Time step of the extended system for the thermostat
D_e	Depth of the well of the Morse potential
E	Energy
E_{LRC}	Long-range energy correction
$E_{surface-in-vacuum}$	Energy of a surface in vacuum
$E_{surface-in-water}$	Energy of a surface immersed in water
E_{water}	Energy of a water box
E_1	Heat of adsorption
$E_{Additive\text{-}SiO^-}$	Energy of interaction between additive and siloxide ions
E_L	Heat of condensation
f	Angle force constant
g	Size of surfactant aggregate
$g(r)$	Radial distribution function
$g^A(r)$	Atomistic RDF
$g^{CG}(r)$	Coarse-grained RDF
h	Planck constant
K	Kinetic energy
k	Number of iterations
K_{angle}	MARTINI angle force constant
K_{bond}	MARTINI bond force constant
k_θ	Angle constant
k_B	Boltzmann constant

k_b	Spring constant for bond stretching
K_d^i	Equilibrium constant for the silica dimer deprotonation
K_m^i	Equilibrium constant for the silica monomer deprotonation
l_c	Length of the hydrophobic chain of a surfactant molecule
m	Mass
MW_{SURF}	Molecular weight of DDACl surfactants
MW_{WAT}	Molecular weight of water
N	Number of molecules
n	Size of the cluster
N_{df}	Number of degrees of freedom for the Nosé-Hoover thermostat
N_{SURF}	Number of surfactant molecules
N_{WAT}	Number of water molecules
P	Pressure
P_0	Pressure of the bath for the Berendsen and Parrinello-Rahman barostat
P_{LRC}	Long-range pressure correction
P_0	Saturation pressure
Q	Partition function
q	Point charge
Q_{NPT}	Isothermal-isobaric partition function
Q_{NVT}	Canonical partition function
R	Distance between CG beads
R_{bond}	MARTINI equilibrium bond distance
r_0	Equilibrium bond length
r_{ij}	Position of molecule i relative to molecule j, $(\mathbf{r_i} - \mathbf{r_j})$
T	Temperature

t	Time
T_0	Temperature of the heat bath for the Berendsen and Nosé-Hoover thermostat
$T_{current}$	Instantaneous temperature for the v-rescaling thermostat
$T_{required}$	Desired temperature for the v-rescaling thermostat
U	Potential energy
U^{CG}	Coarse-grained potential
U_{angle}	Angle bending potential
$U_{bond-harmonic}$	Harmonic potential
$U_{bond-morse}$	Morse potential
U_{bonded}	Potential energy associated to bonded interactions
U_{bond}	Bond stretching potential
$U_{dihedral}$	Dihedral angle torsion potential
U_{LJ}	Lennard-Jones potential
$U_{non-bonded}$	Potential energy associated to non-bonded interactions
$U_{rb-OPLS}$	OPLS torsional potential
U_{rb}	Ryckaert-Bellemans torsional potential
$U_{van\,der\,Waals}$	van der Waals potential
$U_{Coulomb}$	Coulomb's law
$U_{electrostatic}$	Electrostatic potential
V	Volume
v	Volume of the hydrophobic chain of a surfactant molecule
V_0	Constant with the units of volume
V_1, V_2, V_3, V_4	Coefficients of the Fourier series for OPLS torsional potential
V_a	Volume of gas adsorbed
V_b	Volume of the box

V_m	Monolayer coverage
X_1	Mole fraction of amphiphile monomers
X_{CMC}	Mole fraction at CMC
X_g	Mole fraction of surfactant aggregates of size g
D	Lamellar liquid crystal
E	Hexagonal liquid crystal
H_1	Hexagonal phase
L	Liquid phase, isotropic micellar solution
L_α	Lamellar phase
L_1	Isotropic phase
N_{agg}	Aggregation number
X.nW	Crystal hydrate having n water molecules
X_α, X_β	Dry crystal

GREEK LETTERS

β	Isothermal compressibility
$\left(\frac{\Delta\mu_g^0}{k_B T}\right)_{\text{deformation}}$	Free energy of deformation of the surfactant tail
$\left(\frac{\Delta\mu_g^0}{k_B T}\right)_{\text{head}}$	Free energy due to repulsive interactions between head groups
$\left(\frac{\Delta\mu_g^0}{k_B T}\right)_{\text{interface}}$	Free energy of formation of the aggregate core-water interface
$\left(\frac{\Delta\mu_g^0}{k_B T}\right)_{\text{transfer}}$	Free energy of transfer of the surfactant tail
$\Delta\mu_g^0$	Difference between the standard chemical potentials of a surfactant molecule in an aggregate of size g and a of single surfactant molecule dispersed in solution
η	Scaling factor for the Berendsen barostat

λ	Scaling factor for the v-rescaling thermostat
μ_1^0	Standard chemical potential of amphiphile monomers
μ_g^0	Standard chemical potential of surfactant aggregates of size g
$\phi_1, \phi_2, \phi_3, \phi_4$	Phase angles of the Fourier series for OPLS torsional potential
ϕ_{ijkl}	Dihedral angle (zero-cis convention)
Ψ	Dihedral angle (zero-trans convention)
σ_{ij}	Equilibrium distance at which the Lennard-Jones potential is equal to zero
τ	Coupling parameter for the Berendsen thermostat
τ_p	Coupling parameter for the Berendsen barostat
Θ	CG bond angle
Θ_0	CG equilibrium bond angle
θ_0	Equilibrium angle
θ_{ijk}	Angle between two bonds
ε_0	Permittivity of free space
ε_{ij}	Depth of the Lennard-Jones potential well
ε_r	Relative permittivity of the material
ρ	Probability density function

ABBREVIATIONS

NPT	Number of molecules, Pressure, Temperature
NVE	Number of molecules, Volume, Energy
NVT	Number of molecules, Volume, Temperature
A	Acid treated sample
A+C	Acid treated and the Calcinated sample
AA	Atomistic

AF	MARTINI Antifreeze particle
BET	Brunauer, Emmett and Teller
BJH	Barrett, Joyner and Halenda
C	Calcinated sample
CG	Coarse-Graining
Cl	Chloride
CMC	Critical Micelle Concentration
COM	Centre of Mass
CT	Cooperative Templating
CTAB	Cetyltrimetylammonium Bromide
cub	Cubic
DADD	1,12-diaminododecane
$DADD_d$	Doubly charged diaminododecane
$DADD_n$	Neutral diaminododecane
$DADD_s$	Singly charged diaminododecane
DCM	Dichloromethane
DDA	Dodecylamine
DDA^+	Dodecylammonium
DDACl	Dodecylammonium chloride
DETA	Diethylenetriamine
DLS	Dynamic Light Scattering
DMSO	Dimrthyl sulfoxide
EPR	Electron Paramagnetic Resonance
FM	Force Matching
hex	Hexagonal
HMS	Hexagonal Mesoporous Silica

I	Inorganic species
IBI	Iterative Boltzmann Inversion
IEP	Isoelectric Point
IMC	Inverse Monte Carlo
lam	Lamellar
LC	Liquid crystalline
LCT	Liquid Crystal Templating
LJ	Lennard-Jones
M	Counter-ion
MCM	Mobil Composite Matter
MCM-41	Mobil Composition Matter No. 41
MD	Molecular Dynamics
MSU-V	Michigan State University V
N	Non-ionic surfactants
NMR	Nuclear Magnetic Resonance
OPLS	Optimized Potential for Liquid Simulations
pbc	Periodic Boundary Conditions
PEHA	Pentaethylenehexamine
PMS	Periodic Mesoporous Silica
QM	Quantum Mechanics
RDF	Radial Distribution Function
S	Surfactant
SAXS	Small-Angle X-Ray scattering
SBA-15	Santa Barbara Amorphous No. 15
SDV	Silica Deposition Vesicle
SI	Anionic silica monomer

SISI	Doubly charged silica dimers
SISN	Singly charged silica dimers
SN	Neutral silica monomer
SNSN	Neutral silica dimers
SPC/E	Extended Simple Point Charge
TEM	Transmission Electron Microscopy
TEOS	Tetraethoxysilane
TMA	Tetramethylammonium
TRFQ	Time-Resolved Fluorescence Quenching
U	Untreated sample
WR	Sample treated with Water reflux
X	Counter-ion
XRD	X-Ray Diffraction

1

INTRODUCTION

Templating is a well known technique which makes use of pre-existing structures to direct material synthesis. Because of its versatility, templated synthesis is employed to produce a large variety of silica based materials, from the ordered crystalline structures of synthetic zeolites, to solids with a hierarchical arrangement of pores called periodic mesoporous silicas (PMS). Amongst the second class of materials, MCM-41 is probably the most studied representative. Its name stands for Mobil Composition Matter No. 41, from the Mobil laboratories where it was first synthesised [3]. MCM-41 has hexagonally ordered pores which, contrary to zeolites, are made of amorphous silica, and forms around self-assembled surfactant aggregates, rather than single molecules or metal ions [4].

As well as being used at industrial level to produce materials with high morphological control, templating is also employed by many biological organisms to produce their intricate siliceous structures. This process, known as biosilicification, takes place at mild conditions and is meditated by polypeptides and long-chain polyamines, which have been found to both catalyse silica deposition and direct structure formation [5]. Because of these characteristics, biosilicification has been seen as an inspiring process to mimic during the production of mesoporous silicas under more favourable conditions through bio-inspired synthesis. This greener alternative for porous silicas production allows to obtain materials with even better morphological control than those obtained with traditional methods, as well as easier removal of the template by means of solvent extraction.

Since their discovery, many studies have focussed on understanding the templating mechanism underlying the synthesis of PMS. Their scope was to gain direct control over synthetic conditions and formation mechanisms to further apply this knowledge to the design of tailored materials. The approach adopted at the time was mainly indirect: possible routes of formation were postulated comparing different synthetic conditions and relating them to the final structure of the material. In this context, molecular dynamics (MD) simulations were able to shed some light, clarifying many aspects of their formation mechanisms [6, 7]. Conversely, mechanistic understanding of bio-inspired synthesis is still limited and essentially

relying on experimental observations. Achieving more detailed knowledge about the synthesis mechanism of this class of material is likely to lead the production of novel porous solids with superior properties to use as supports for catalysis, in separation and purifications processes, as well as carriers for drug delivery.

The objective of this thesis is to use multi-scale MD simulations (atomistic and coarse-grained) for the investigation of the mechanism of formation of bio-inspired silica materials. This approach means that results obtained at the higher levels of theory were used to develop models at lower resolution, allowing to maintain realism across all the simulations performed. Two examples of bio-inspired materials with similar characteristics (i.e. synthesis at ambient temperature and directed by self-assembly of amines) were considered: HMS [8] and MSU-V materials [9]. By modelling bio-inspired synthesis using different levels of simulation detail, information about molecular processes and interactions involved in the different stages of the synthesis were obtained. Furthermore, in the context of greener methods for mesoporous materials production, another objective of this thesis is to study, by means of atomistic MD simulations, the feasibility of a novel solvent extraction process for template removal from bio-inspired silica.

1.1 DISSERTATION OUTLINE

The remainder of the thesis is organised as follows. An overview of silica and surfactant chemistry, as well as of the most relevant experimental and simulation studies on mesoporous silica materials is provided in Chapter 2. Particular emphasis is given to those works focussed on providing mechanistic insight into the synthetic process of these materials. The fundamental principles of MD simulations are introduced in Chapter 3, where atomistic as well as coarse-grained methods are described. Particular attention is given to the MARTINI model for coarse-grained simulations [10], which is then further developed and validated in Chapter 4. Here the synthesis of the first example of bio-inspired materials considered (i.e. HMS) is investigated, while the formation of the second type of bio-inspired silica (i.e. MSU-V), under different pH conditions, is studied in Chapter 5 by means of a combination of atomistic and coarse-grained simulations. In Chapter 6, atomistic simulations are used to identify the molecular interactions behind template removal from bio-inspired silica using a mild solvent extraction procedure. Finally, in Chapter 7 conclusions and future work are presented.

2

MESOPOROUS SILICA MATERIALS: EXPERIMENTAL AND SIMULATION STUDIES

Porous solid materials are classified according to the size of their pore diameters (d) into microporous ($d < 2\,\text{nm}$), mesoporous ($2 < d < 50\,\text{nm}$) and macroporous materials ($d > 50\,\text{nm}$). Naturally occurring and synthetic zeolites (e.g. ZSM-5, zeolite Y), aluminophosphate (e.g. $AlPO_4$-n) and silicoaluminophosphate (e.g. SAPO-n) molecular sieves are typical examples of crystalline microporous materials. Zeolites are widely used in catalysis because of their ion-exchange character as well as for adsorption and separation processes; however, due to their small pore size, zeolites' applicability is limited to molecules with small diameters. Already in 1990 a synthetic procedure, based on the intercalation of alkyltrimethylammonium surfactants into a layered silicate (Kanemite), which afforded materials having larger pores, was reported by Yanagisawa et al. [11]. Unfortunately, due to the lack of detailed characterisation, these materials were mostly disregarded. It was only two years later, in 1992, when the MCM (also called M41S) family of ordered mesoporous silicas was discovered in the Mobil laboratories [12], that the demand for porous solids suited to treat large molecules (for example from water streams) was satisfied. Using quaternary ammonium surfactants as templates, Mobil researchers were able to produce materials having much larger pores (up to 10 nm) in comparison to zeolites, amorphous pore walls, but crystal-like order of the porous network. Such regular arrangement of channels is the direct consequence of the self-assembly of surfactants into highly ordered mesophases so that a variety of structures can be formed by tuning their synthetic conditions. After their synthesis, the final porous structure is created by removing the template, either by calcination or by solvent extraction.

As well as experimenting new routes for the production of templated mesoporous silicas, research has also focussed on other issues related to these materials. These include their chemical and physical characterisation, directed to understanding their mechanism of formation, but also the investigation of greener alternative methods for both material synthesis and template removal. With regard to the first point, already Beck et al. in the original paper describing the synthesis of MCM-41

[12] proposed two possible synthetic routes that could lead to the formation of this material (see section 2.2), suggesting the difficulties in obtaining a conclusive answer based only on experimental information due to the complexity of the characterization process. Furthermore, there is no single experimental technique that can be used to study the many phenomena simultaneously taking place during the synthesis of these materials. It follows that in more recent years, simulation techniques have been employed to complement experiments shedding light on the molecular processes that lead to the formation of such materials, and have often provided the link between microscopic phenomena and macroscopic observation [13–17]. For the development of greener templated synthesis methods, on the other hand, researchers have looked at biosilicification (i.e. the incorporation of inorganic silicon into living organisms) as an inspiring process to mimic for the production of porous silicas in a more efficient way. This has promoted the creation of a new class of materials called bio-inspired silica, which makes use of polyamines as templating agents and has the advantage of allowing mild methods for template removal.

In this thesis, molecular simulations have been applied to study the synthesis of bio-inspired silica materials (Chapter 5 and 4), as well as to investigate alternative methods for template removal based on solvent extraction (Chapter 6). The present chapter provides an overview on the topic, both from an experimental and from a computational point of view. In section 2.1 some basic concepts regarding surfactant and silica chemistry are discussed and in section 2.2 the efforts made to understand the synthesis of mesoporous silica materials are reviewed. Studies on the process of biosilification and on bio-inspired silicas are presented in section 2.3. Lastly, in section 2.4 theoretical studies applying molecular simulations for the investigation of material synthesis are presented.

2.1 OVERVIEW OF SURFACTANT AND SILICA CHEMISTRY

As mentioned in the introduction, the synthesis of mesoporous silica materials is based on templating processes. The large variety of templates that can be used to guide material synthesis makes this method not only very versatile but also quite intriguing. In a first instance, templates can be classified into hard and soft templates. Belonging to the first class are colloidal particles, both individually and as assemblies, solid surfaces, membranes, nanowires and nanotubes as well as some

naturally occurring minerals. Soft templates include macro and microemulsions, vesicles, micelles with different shapes and arrangements, polymer networks, hydrogels and some biomolecules such as assemblies of peptides and proteins [18].

With such a great number of different mesostructures that can be used to direct material synthesis, it is evident why a detailed understanding of the molecular mechanism is such a crucial point towards achieving tailored material design. Before discussing the efforts made to understand the mechanism of formation of mesoporous and bio-inspired silica materials in more detail, fundamental concepts of surfactant and silica chemistry will be introduced.

2.1.1 *Chemistry of Surfactants*

As will be further illustrated in section 2.2, quaternary ammonium surfactants are used to direct the synthesis of MCM-type materials. Surfactants (also called "surface active agents") are molecules which combine a polar hydrophilic moiety (the surfactant head) and a non-polar hydrophobic part (the surfactant tail) [19]. They are used as detergents as well as in pharmaceutical, agriculture and microelectronic industries [20]. Because of their amphiphilic character, surfactants display two striking features: at low concentration they adsorb on surfaces (or at interfaces) displaying so called surface activity, whereas above a certain threshold concentration they aggregate to form micelles or liquid crystalline (LC) phases [19, 21]. The concentration at which self-assembly begins is referred as the critical micelle concentration (CMC) and, for a certain type of surfactant molecule, depends on temperature and pH [22].

Surface activity is the tendency of surfactants to reduce the surface (in case of gas/liquid phase) or interfacial (in case of two immiscible phases, i.e. liquid-liquid or liquid-solid) tension. Surface and interfacial tension originates from unbalanced intermolecular forces at the system boundary [21, 23]. Because of this imbalance, a liquid in contact with a gas tends to minimise its surface area (e.g. formation of water droplets) or, similarly, two liquid phases can become immiscible. When surfactants are present, they accumulate at the boundary of the system and orient so that their hydrophobic tails face the less polar phase while their hydrophilic heads are in contact with the more polar phase. By doing this, the cohesive forces at the system boundary, responsible for the creation of the tension, are destroyed and the energy (or work) necessary to alter the surface area reduced.

As surfactant concentration is increased, the surface area available for adsorption decreases and molecules start to accumulate in the bulk. However, the presence of a hydrophobic tail means that surfactant molecules prefer to aggregate so that contact with water is minimised. This process is referred as self-assembly and consists in the spontaneous aggregation of molecules that, in a disordered system, come together to form ordered patterns or structures. The key fact about molecular self-assembly is that it is not influenced by any external force, only weak interactions such as hydrogen bonds, electrostatic and hydrophobic/hydrophilic interactions guide the process. As more surfactants continue to be added, the system evolves from a micellar solution (i.e. an isotropic phase comprising micelles and monomers in equilibrium, L_1) to a system dominated by long-ranged order and referred as lyotropic liquid crystalline phase. Examples of lyotropic liquid crystals are hexagonal (H_1), lamellar (L_α) and bicontinous phases. Because of its very fast dynamics (nanosecond scale) and very short length scales (nanometre), investigation of the initial steps of the process of surfactant self-assembly is very difficult by means of experimental techniques [24].

Tanford [25], Israelachvili, Mitchell and Ninham [26] as well as Nagarajan and Ruckenstein [27] were among the first to provide a description of the thermodynamics governing amphiphile self-assembly. The system of interest can be seen as a multicomponent solution containing amphiphile monomers in equilibrium with surfactant aggregates of different sizes and shapes. Hence, the chemical potential of the two phases can be written as:

$$\frac{1}{g}\left[\mu_g^0 + k_B T \ln(X_g)\right] = \mu_1^0 + k_B T \ln(X_1), \tag{2.1}$$

where μ_g^0 is the standard chemical potential of surfactant aggregates of size g and mole fraction X_g, μ_1^0 the standard chemical potential of amphiphile monomers with a mole fraction X_1, T is temperature and k_B is the Boltzmann constant. Equation (2.1) can be rearranged to obtain an aggregate size distribution equation:

$$X_g = (X_1)^g \exp\left(-\frac{\mu_g^0 - g\,\mu_1^0}{k_B T}\right) = (X_1)^g \exp\left(-\frac{g\Delta\mu_g^0}{k_B T}\right), \tag{2.2}$$

where $\Delta\mu_g^0$ represents the difference between the standard chemical potentials of a surfactant molecule in an aggregate of size g and of a single surfactant molecule dispersed in solution. Equation (2.1) can be simplified considering that X_g and X_1

are of the same order of magnitude and that g is normally a large number, giving the result in Equation (2.3)

$$\frac{\mu_g^0}{g} = \mu_1^0 + k_B T \ln(X_1). \tag{2.3}$$

Then, considering that the CMC, X_{CMC}, is defined as the value of X_1 at which the concentration of surfactants in solution equals the concentration of surfactants in aggregate form (i.e. $X_1 = \sum g X_g = X_{CMC}$), the following relation is obtained by combining Equation (2.2) and Equation (2.3):

$$\ln(X_{CMC}) = \frac{\Delta\mu_g^0}{k_B T}. \tag{2.4}$$

The term on the right hand side of Equation (2.4) can be obtained considering that the difference in standard free energy between an amphiphile in an aggregate of size g and an amphiphile in solution is the sum of different contributions, as expressed in Equation (2.5):

$$\left(\frac{\Delta\mu_g^0}{k_B T}\right) = \left(\frac{\Delta\mu_g^0}{k_B T}\right)_{transfer} + \left(\frac{\Delta\mu_g^0}{k_B T}\right)_{deformation} + \left(\frac{\Delta\mu_g^0}{k_B T}\right)_{interface} + \left(\frac{\Delta\mu_g^0}{k_B T}\right)_{head}. \tag{2.5}$$

The first term, $\left(\frac{\Delta\mu_g^0}{k_B T}\right)_{transfer}$, describes the free energy associated to the transfer of the hydrocarbon tail of the surfactant from an unfavourable water environment to the hydrophobic micelle core. This contribution is negative and depends on the tail groups but not on the aggregate size or shape [28]. The term $\left(\frac{\Delta\mu_g^0}{k_B T}\right)_{deformation}$ is referred as the deformation free energy. This contribution is positive and it is due to the conformation constraints to which surfactant tails inside the micelle core are subject to (i.e. the part of the tail closer to the head is located at the interface with water while the hydrocarbon groups in the aggregate core have to maintain a uniform density) [22]. The third term, $\left(\frac{\Delta\mu_g^0}{k_B T}\right)_{interface}$, is also positive and accounts for the free energy contribution associated with the formation of an interface in the region where the hydrophobic core is in contact with water. The last term, $\left(\frac{\Delta\mu_g^0}{k_B T}\right)_{head}$, arises from the repulsion interactions between the surfactant polar heads and is made up of three contributions: i) the repulsion due to steric interactions, ii) due to dipole-dipole interactions, in the case of zwitterionic molecules and iii) due to ionic interactions when charged head groups are present

[22]. It follows from this description that the free energy of transfer is responsible for the aggregation process, then the deformation and interface terms promote the growth of the aggregates while their finite size is the consequence of the repulsive interactions between polar head groups.

The type of aggregates that a certain surfactant molecule can produce is related to its nature (if it is charged or uncharged) as well as to the relative size of its hydrophobic and hydrophilic parts. As described by Israelachvili [21], self-assembly is the result of two competing forces: attractive hydrophobic interactions between hydrocarbon chains, which tend to minimise the interfacial area per molecule in contact with water, and repulsion interactions between hydrophilic heads (steric but also double-layer contributions, if the molecule is charged), which favour an increase of the interfacial area and, hence, solvation of the head groups. The relative balance between these two forces influences the type and size of the aggregate formed and it can be expressed as a function of the geometrical characteristics of the surfactant molecule: area per head group (a_0), volume (v) and length (l_c) of the hydrophobic chain. By calculating or estimating these three terms, the type of aggregate formed can be determined through the calculation of the critical packing parameter $C_{pp} = v/l_c a_0$ (see Figure 2.1). It follows that spherical micelles are formed when single chained surfactants or lipids having large head groups, such as anionic surfactants, are used ($C_{pp} < 1/3$), whereas single-chained surfactants or lipids with small head groups, such as non-ionic surfactants or anionic surfactants at high salt concentration, form cylindrical micelles ($1/3 < C_{pp} < 1/2$). On the other hand, when bulky molecules (such as branched or double-chain surfactants or lipids) are used, these cannot pack as closely and prefer to form lamellae instead. Lamellar structures can be curved, i.e. vesicles when the head group is large ($1/2 < C_{pp} < 1$), or flat, i.e. bilayer when the head group is small ($C_{pp} = 1$). Finally, inverted or reverse micelles are formed when surfactants with small head groups or large tails are used ($C_{pp} > 1$) [20, 21]. It is important to notice that the presence of other dissolved species in the solution (e.g. ions or inorganic molecules) is likely to affect the packing parameter and hence influence the type of mesophase that is formed. The interaction of surfactants with inorganic silicates is thus crucial step in the formation of mesoporous materials. In the following section, an overview of the the reactions involving silica species will be provided.

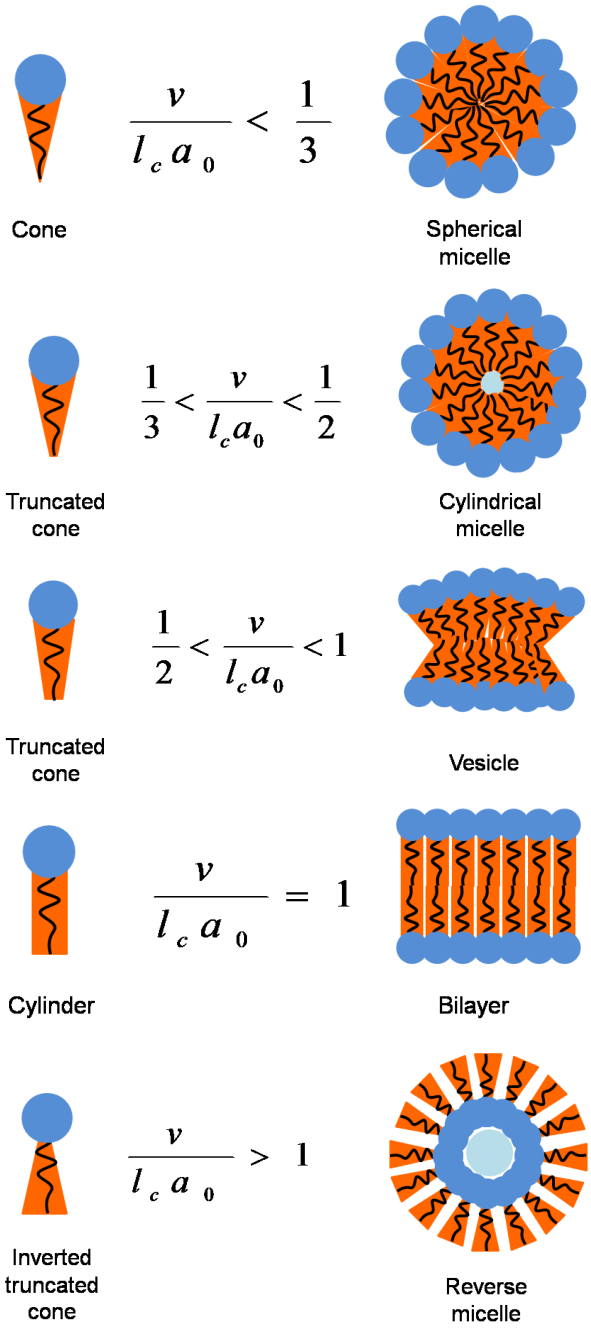

Figure 2.1: Surfactant structures that can be predicted from the calculation of the packing parameter.

2.1.2 *Chemistry of silica*

Sol-gel chemistry is a flexible method used to produce ceramic materials with great morphology control. As the name suggests, sol-gel synthesis consists in the transformation of a suspension of colloidal particles in a liquid (the sol) into a three-dimensional rigid phase consisting of a continuous network in a continuous liquid (the gel) [4, 29]. In the case of silica sol, the colloidal particles, also called precursors, are metal alkoxides, specifically alkoxysilanes, among which the most studied and used compound is TEOS (tetraethoxysilane) [29]. During the sol-gel process, TEOS molecules undergo hydrolysis and condensation reactions, which eventually lead to the formation of the gel network. In the hydrolysis step, Equation (2.6), one alkoxysilane group ($Si(OR)_4$) is converted into a silanol ($OH\text{-}Si(OR)_3$) plus an alcohol (ROH). In the second step, condensation takes place and the silanol reacts with another silanol group, Equation (2.7), or with an alkoxysilane group, Equation (2.8), to produce a siloxane group and, respectively, a water or an alcohol molecule (i.e. water or alcohol condensation).

$$Si(OR)_4 + H_2O \underset{\text{Esterification}}{\overset{\text{Hydrolysis}}{\rightleftharpoons}} HO{-}Si(OR)_3 + ROH, \tag{2.6}$$

$$(OR)_3Si{-}OH + HO{-}Si(OR)_3 \underset{\text{Hydrolysis}}{\overset{\text{Water condensation}}{\rightleftharpoons}} (OR)_3Si{-}O{-}Si(OR)_3 + H_2O, \tag{2.7}$$

$$(OR)_3Si{-}OH + Si(OR)_4 \underset{\text{Alcoholysis}}{\overset{\text{Alcohol condensation}}{\rightleftharpoons}} (OR)_3Si{-}O{-}Si(OR)_3 + ROH. \tag{2.8}$$

The development of condensation and reverse reactions, hydrolysis and alcoholysis, leads to the creation of the gel network in a process referred as silica polymerisation. As Iler pointed out, it was believed until 1940 that polymerisation took place through the progressive branching and cross-linking of siloxane chains (Si-O-Si), in a process similar to that affecting many organic polymers [30]. It was Carman who recognised for the first time that silica polymerisation proceeds through the formation of discrete particles, resulting from silicic acid polymerisation, which then aggregate and connect to form polymer networks [31].

Monosilicic acid $Si(OH)_4$ is the simplest soluble form of silica [5]. Its structure consists of a silicon atom tetracoordinated with four oxygen atoms. Monosilicic acid, also called orthosilicic acid, exists in its monomeric form in solution with water at 25 °C for concentrations lower than 2×10^{-3} M [30]. However, when the concentration is increased it tends to polymerise very quickly, first forming oligomers (polymers with molecular weight up to 100,000 Da) and then colloidal particles [30]. The isoelectric point (IEP) of monosilicic acid, i.e. the pH at which its net charge is zero, is reported to be between 2 and 3 [30, 32]. Below the IEP silicates are positively charged while above this point they exist as anions. At these conditions, deprotonation equilibria can be written in the following form:

$$SiO_{i-1}(OH)^{(i-1)-}_{5-i} \overset{Km^i}{\rightleftharpoons} SiO_i(OH)^{i-}_{4-i} + H^+, \tag{2.9}$$

$$Si_2O_i(OH)^{(i-1)^-}_{7-i} \overset{Kd^i}{\rightleftharpoons} Si_2O_{i+1}(OH)^{i-}_{6-i} + H^+, \tag{2.10}$$

where K^i_m and K^i_d are the equilibrium constants for the monomer and the dimer reaction, respectively. It should be noted that silicates speciation depends not only on pH, but also on other factors such as type of cosolvent or ions in solution [33].

Polymerisation of silica has been described by Iler to occur in three distinct stages:

1. polymerisation of silicic acid monomers to form particles;
2. particle growth;
3. gel formation

Figure 2.2 schematically depicts the stages and aggregates formed during silica polymerisation as a function of pH. As already mentioned, in the first step monomeric silicic acid polymerises so that the formation of siloxane bonds (Si-O-Si) is maximised and the number of uncondensed $Si(OH)_4$ is reduced, favouring the formation of polysilicic acids (e.g. dimers, trimers and cyclic oligomers):

$$-SiOH + -SiOH = -SiOSi- + H_2O. \tag{2.11}$$

The reaction in Equation (2.11) proceeds with a silicon atom, as intermediate, coordinated with five or six oxygen atoms [30] and it is accompanied by water formation. This initial step is rapidly followed by the addition of monomers and linkage

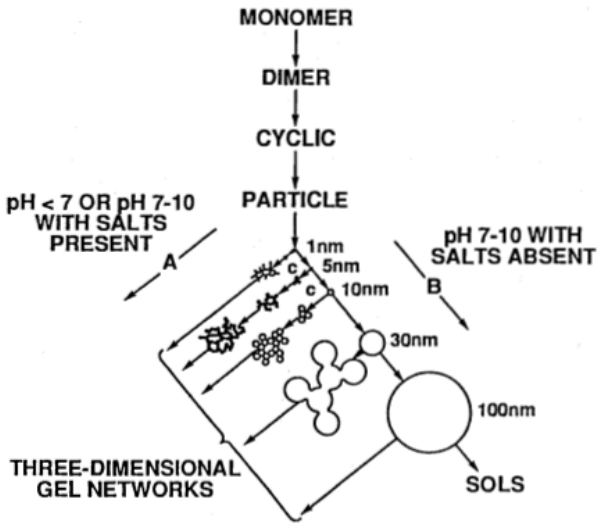

Figure 2.2: pH dependence of silica polymerisation: below pH = 7 silicates bear very little charge and formation of networks is favoured (route A); at pH between 7 and 10 repulsion between negatively charged particles prevents aggregation so that polymerisation continues through particle growth (route B). [30].

of polymers, leading to the formation of spherical units. These spherical particles increase in size in the next step, until they reach dimensions of approximately 5 to 10 nm at pH above 7 when the particle growth is reduced (route B in Figure 2.2). However, for reactions at lower pH, particles already stop increasing in size when they reach dimensions of $2-4$ nm (route A in Figure 2.2) [30]. The process of particle growth is due to the continuous polymerization of monomeric silicic acid as well as to silica deposition on large aggregates, caused by the fact that small particles are more soluble than larger ones (Ostwald ripening). Finally, for pH below 7, when the particles in suspension carry very little charge, three-dimensional networks are formed as a result of the arrangement in chains and branches. On the other hand, at high pH repulsion between negatively charged silica particles prevents aggregation and the process continues through particle growth. As these processes occur, silica is converted into a gel causing an increase of both the molecular mass and viscosity of this phase.

In the following, the concepts herein introduced will be further expanded to provide a short overview on PMS and bio-inspired synthesis.

2.2 MESOPOROUS MATERIALS: SYNTHESIS AND CHALLENGES

The three major representatives of the MCM-class of materials are displayed in Figure 2.3; they show hexagonal (MCM-41), cubic (MCM-48) or lamellar (MCM-50) phases. The innovative synthetic approach used to fabricate them opened the way

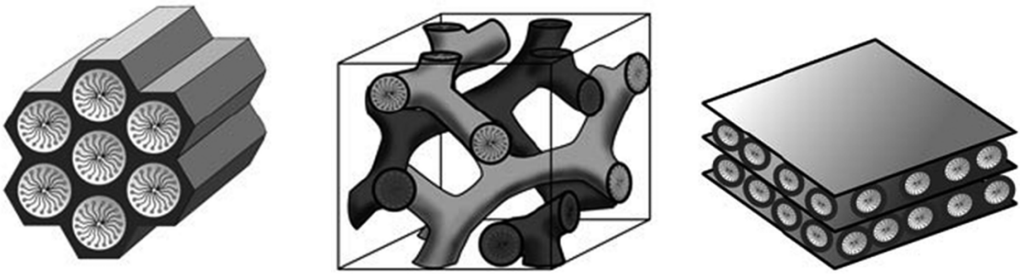

(a) MCM-41 (b) MCM-48 (c) MCM-50

Figure 2.3: Different types of MCM structures. (a), hexagonal MCM-41 formed at Sur/Si < 1; (b), cubic MCM-48 formed at Sur/Si ≈ 1 and (c), lamellar MCM-50 at Sur/Si > 1. Figure adapted from Reference [34]

for an increasing number of mesoporous materials obtained using alternative templating molecules and pH conditions. An example of this is the discovery in 1998 of a new type of silica-based ordered material, synthesised in acidic conditions by Zhao et al. [35] and designated as SBA-15 (Santa Barbara Amorphous No. 15). Like MCM-41, SBA-15 possesses a hexagonal structure with even larger pores, up to 30 nm, as the result of the use of amphiphilic triblock copolymers, namely Pluronics, as templating agents. SBA-15 was shown to have higher hydrothermal stability than MCM-41 due to the presence of thicker silica walls. Moreover, in the same years, the family of so called bio-inspired materials also appeared [8, 9, 36–38]. This type of mesoporous silicas, which will be described in more detail in section 2.3, makes use of long chain polyamines to direct structure formation, through a process similar to that used by some biological organisms to create their siliceous structures, and has the advantage of taking place at milder conditions.

With regard to the efforts made to understand the mechanism of formation of mesoporous silica materials, MCM-41 is probably the most studied member of this class. In its typical preparation, solutions of cetyltrimethylammonium bromide (CTAB) and TEOS are mixed together and then heated to 100 °C. CTAB surfactants are positively charged, and when their concentration is above the CMC they self-

assemble forming spherical micelles. Under conditions of high pH, anionic silicates polymerise around the template to produce ordered hexagonal mesophases. To explain this mechanism, Beck et al. have proposed two possible pathways, as illustrated in Figure 2.4 [12]. The first route referred as "liquid crystal initiated"

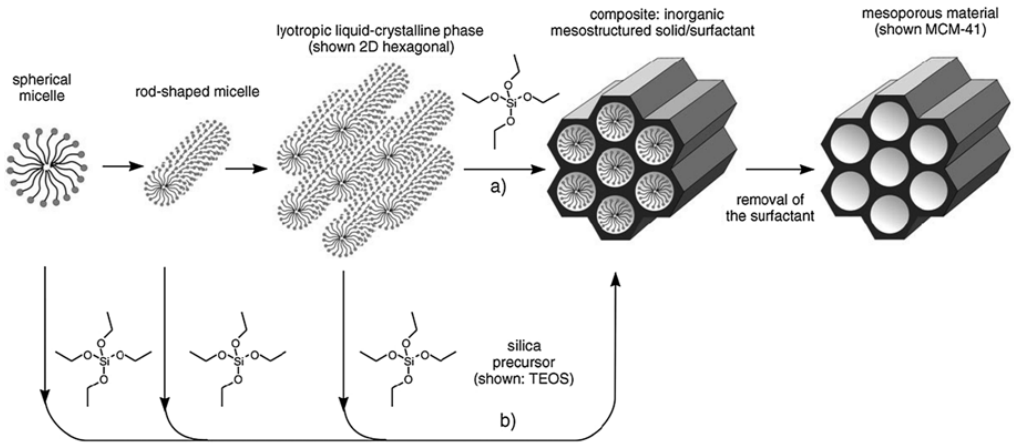

Figure 2.4: Possible routes for the formation of MCM-41 as postulated by Beck et al.: a) liquid crystal templating (LCT) mechanism, b) cooperative liquid crystal templating (CT) mechanism [12]. Figure adapted from [34].

or "liquid crystal templating (LCT)" proposes that the hexagonal arrangement of CTAB surfactants is only driven by surfactant concentration and conditions of the synthesis, suggesting that the silica precursors are only "spectators" until precipitation begins (route a in Figure 2.4). In the second model, referred as "silicon anion initiated" or "cooperative templating (CT)", it is the presence of silica that promotes micelle ordering and/or their transformation into ordered mesophases (route b in Figure 2.4).

Following Beck's initial attempt to understand MCM-41 synthesis, alternative pathways were proposed by other groups. Chen et al. hypothesised, on the basis of nuclear magnetic resonance (NMR)studies, that before the spontaneous assembly into the final hexagonal mesostructure takes place, multiple silica layers surround the rod-like micelles [39]. The formation mechanism proposed by Monnier et al., instead, suggests that the process is initiated by the surfactant assembly into lamellar layers which are then converted into the final hexagonal mesophase as the condensation of the silica networks progresses [40]. According to Steel et al., horizontal layers of silicates grow between the cylindrical surfactant phase in the first

step of the synthesis; subsequent condensation and wrinkling of such layers cause them to create ordered hexagonal channels around the template [41].

One key feature of the templating mechanism identified by Monnier et al. [40] and then further explored by Firouzi et al. [42], is its cooperative nature, which is the direct consequence of the interactions between oppositely charged organic and inorganic species. The authors point out that solutions of CTAB surfactants in water form hexagonal or lamellar phases at concentrations much larger (between 25 and 70 % by weight) than those used for the synthesis of mesoporous materials (as low as 1 %). Hence, the formation of phases with such long-range order must be the consequence of the addition of silicates to the solution. They identified three main processes that take place after CTAB micelles are formed: i) multidentate binding of silica oligomers to the micelles, ii) silica polymerisation at the interface and iii) charge matching between organic and inorganic species [40, 42]. As already said, at the high pH of the synthesis, CTAB surfactants are positively charged and produce isotropic micellar solutions; silicates, on the other hand, are prevalently negatively charged at high pH. When the the two precursor solutions are mixed together silicates can replace bromide counter-ions at the interface and strongly bind to it. This promotes silica polymerisation at the interface, since the negative charge carried by the silicates is partially screened by the presence of cationic surfactants. By doing this, the electrostatic repulsion between aggregates is diminished and long-range order favoured.

The general methodology illustrated here, based on ion-pair interactions, has been also extended to prepare materials using different metal oxides as well as different pH conditions. Depending on the charge of surfactants (S), inorganic species (I) and possible counter-ions (X or M), a total of seven alternative pathways were proposed [43]. The simplest option is to use direct routes, involving only silicates and surfactants: S^+I^- or S^-I^+. Also possible are two indirect routes, involving organic and inorganic species with the same charge and a counter-ion with opposite charge: $S^+X^-I^+$ at acidic pH (where X^- can be a chloride or bromide ion) and $S^-X^+I^-$ at basic pH (where X^+ can be a sodium or potassium ion). Finally, neutral templating routes based on hydrogen bond interactions between uncharged organic and inorganic species have also been proposed (S^oI^o, N^oI^o and $N^oX^-I^+$, where N^o represents a non-ionic surfactant) [8, 36]. Some examples of materials produced according to these different synthetic paths can be found in Table 2.1.

Despite advances in this field, still many open questions remain about PMS synthesis, particularly regarding the role of templates and organic species during

Table 2.1: Examples of mesoporous materials produced with different interactions between organic and inorganic species; hex, hexagonal; lam, lamellar and cub, cubic [43].

Interaction type	Example materials (structure)	Reference
S^+I^-	MCM-41 (hex)	[12]
	MCM-48 (cub)	[12]
	MCM-50 (lam)	[12]
$S^+X^-I^+$	SBA-3 (hex)	[44]
S^-I^+	Mg, Al, Ga, Mn, Fe, Co, Ni, Zn oxides (lam)	[44]
$S^-M^+I^-$	zinc oxide (lam)	[44]
	alumina (lam)	[44]
S^oI^o	HMS (hex)	[36]
N^oI^o	MSU-X (hex)	[45]
$N^oX^-I^+$	SBA-15 (hex)	[35]

the different stages of the process. This includes, for example, understanding how synthesis is initiated and proceeds at different pH conditions, the degree of silica polymerisation during the mesophase formation and whether the nature of the template materials affects polymerisation and/or condensation [46]. As will be discussed in the next section, this situation is even less clear for bio-inspired silica materials.

2.3 FROM BIOSILICIFICATION TO BIOMIMETIC APPROACH

So far the focus has been on examples of templating approaches employed for the production of ordered mesoporous materials that are used in industrial processes (e.g. for catalysis, separation, drug delivery, etc.). However, it is known that templating synthesis is also used by many biological organisms. Diatoms, sponges and radiolarians, for example, form their sophisticated skeletons and shells transferring silicic acid from marine environments and incorporating it intra or extra-cellularly to produce ornate amorphous silica structures [47]. This very common but complex process is known as biosilicification and has the advantage, in comparison to industrial processes, of taking place at mild conditions (aqueous media, ambient temperature, neutral pH). Furthermore, the hierarchically ordered structures found in nature display a morphological control (from tens of nanometres up to

hundreds of micrometers [48]) that can be hardly reached in industrially produced silica and never at these conditions. For these reasons, biosilicification has attracted increasing interest in recent years, directed to capture the mechanism of synthesis of silica in such mild conditions and possibly mimic it for the production of bio-inspired silica-based materials [49]. Several phenomenological models have been proposed in order to explain experimental observations, but a complete understanding of the synthesis mechanisms taking place at the molecular level during biosilicification is still lacking. Like in the case of traditional mesoporous materials, such detailed knowledge is essential to provide further control over the properties of the solids and enable targeted design of bio-inspired silicas.

2.3.1 *Biosilicification in Nature and attempts to understand its mechanism*

In previous studies, specific biomolecules denoted as silaffins and silicateins have been extracted from diatoms and sponges respectively [50]. Furthermore, long-chain polyamines have been discovered in both species but, more interestingly, polyamines appear to be the only type of biomolecules found in a particular order of diatoms called *Coscinodiscus* [51]. The first class of biomolecules, silaffins, consists of polypeptides with molecular weight ranging between 4 to 17 kDa [52] with several post-translation modifications such as long-chain polyamines linked to lysine residues and a high degree of phosphorylation of serine groups. On the other hand, long-chain polyamines contain N-methyl-propylamine repeating units (around 20) attached to putrescine groups [53], but their exact chemical structure differs from species to species.

Silaffins and long-chain polyamines both possess two important functions essential for the synthesis of the cell walls, i.e. the ability to accelerate silica precipitation and to self-assemble into larger aggregates which can then direct the formation of patterns and structures [5]. The catalytic activity of amines and polyamines was demonstrated by Mizutani et al. by testing the effect that different organic molecules have on the rate of polymerization and gelation of silicic acid [54]. It was found that the rate of polymerization increases, and the same effect is shown for the rate of gelation, when these species are added to the system. However, polyamines show a higher effect on both monitored rates, whereas only a moderate effect is observed for simple amines (linear diamines, triamines, tetramines, etc.). This result proves that the catalytic activity of amino components is in strict relation to

the number of amino groups in the molecules, but also to their relative arrangement. Further characterisation analyses on silica gels revealed that amino groups, in addition to catalysing silica precipitation, directly react with silicic acid and coprecipitate with it as they are found in the gel in different amounts (e.g. small amounts of simple amines and larger amounts of polyamines), which reflects their different catalytic activities. The second important property of silaffins and long-chain polyamines is their ability to form large aggregates, promoted by weak interactions such as hydrogen bonds, electrostatic and hydrophobic/hydrophilic interactions, through self-assembly [50]. However, the detailed mechanism by which these supra-molecular aggregates are formed has not yet been elucidated.

One of the first attempts to explain the formation of diatoms siliceous cell walls was in 2002 when, on the basis of electron microscopy studies, Sumper proposed a model which was able to predict the honeycomb-like structure observed in diatoms belonging to the genus of *Coscinodiscus* [51]. This particular species possesses hexagonal arrays that are reminiscent of the pore structures observed in periodic mesoporous silicas (PMS) [12]. According to the mechanistic model proposed, pattern formation in marine organisms is mediated by repeating phase separation processes in which emulsions of microdroplets are gradually reduced into aggregates of lower size, i.e. nanodroplets and micelles [51]. These droplets contain polyamine molecules which are speculated to arrange in a hexagonal fashion allowing silica to precipitate at the interface where the droplets are in contact with the aqueous environment rich in silicic acid (see Figure 2.5). When silica starts precipitating, the

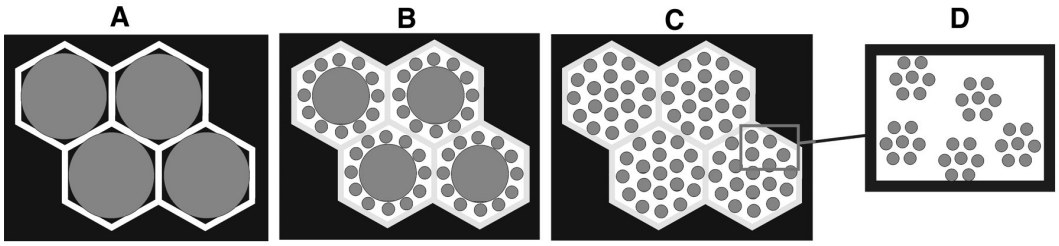

Figure 2.5: Schematic representation of the templating mechanism of *Coscinodiscus* diatoms as proposed by Sumper. Figure adapted from [51].

fraction of polyamines is reduced by coprecipitation, hence causing the droplets to break up into smaller units. This process keeps repeating until the complete depletion of amine sources, causing phase separation to stop.

Even though this model is able to qualitatively explain patterns and structures observed in nature, other models have been proposed in this context as well. The

description of biosilicification given by Vrieling et al. [55], for example, goes in the opposite direction. In fact, if the "separation model" proposed by Sumper predicts the largest structures to be formed at the beginning of the process [51], Vrieling's model predicts the largest aggregates towards the end [55]. The mechanism postulated is based on the fact that the presence of silaffins and polyamines causes silica to form aggregates of increasing size. Such silica structures can then interact with peptide clusters which in turn become larger. Both structures, silica and peptide aggregates, continue to grow in size and to densify so that the silica deposition vesicle (SDV) expands, first on a plane and then in height, until it reaches its final size.

2.3.2 *Examples of bio-inspired material synthesis*

The short overview provided above indicates that still many uncertainties need to be clarified to fully understand biosilicification, particularly concerning the role played by polyamine surfactants, ions, silicic acid and the other species in solution. In this regard, it is interesting to note that when scientists first looked at biosilicification as an inspiring process to mimic the production of porous materials in a more efficient way, it turned out that practical attempts to produce bio-inspired silica-based materials also helped to elucidate some aspects of this complex process. Belton et al. conducted a systematic study on several types of amines and polyamines, including two examples of naturally occurring ones (spermine and spermidine), in order to elucidate the effect exerted on silica condensation rate by some distinctive conformational features [56]. Particularly, the characteristics examined were: degree of polymerization, level of methylation and length of the amine chain spacers. All these modifications are believed to have a precise impact on the ability of amine systems to produce microemulsions and to catalyse silica polymerization. Results show that a higher degree of polymerization and methylation positively influence these functions by reducing the number of charged species in solution and enhancing the hydrophobic character. It is also found that when the chain spacer contains more than 3 carbon atoms, the ability to form droplets is decreased because more amino groups become positively charged. For this reason, the authors conclude that there is no distinct effect on the synthesis using spermine and spermidine.

One of the first examples of a biomimetic templating approach applied to the design of porous silica materials was reported by Tanev and Pinnavaia. Diamines with variable length of the alkyl chain (from 8 to 12 carbons) were used as templating agents for silica precipitation from TEOS [37]. The synthesis occurs at ambient temperature and the product obtained, denoted as MSU-V, shows a hierarchical lamellar structure. Tanev and Pinnavaia postulated a possible mechanism of formation of MSU-V materials based on hydrogen bonding interactions between neutral diamines and neutral alkoxysilane species (see Figure 2.6). According to this

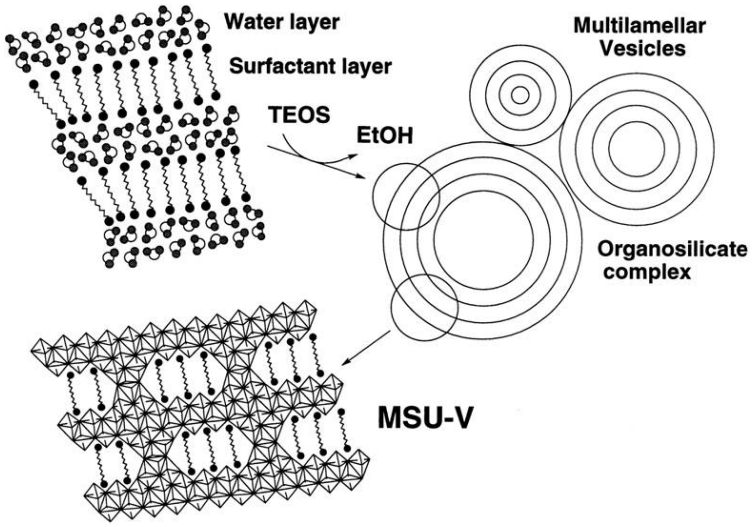

Figure 2.6: Assembly mechanism for the formation of MSU-V materials proposed by Tanev and Pinnavaia. Figure adapted from [38].

mechanism, neutral diamines form large aggregates which eventually evolve into multilamellar vesicles, i.e. layers of surfactant intercalated with water layers. Silica species derived from TEOS hydrolysis are supposed to penetrate such vesicles establishing hydrogen bonds with the amino groups of the surfactant. Therefore, silica oligomers will grow in both vertical and horizontal direction and the final material will present a significant amount of framework cross-linking. The complexity of the synthesis makes it hard to decouple all the processes taking place simultaneously (phase equilibrium, self-assembly, silica hydrolysis and condensation) which explains the difficulty to establish an unambiguous mechanistic description sorely based on experimental information.

It was observed that all porous materials prepared according to this method showed relatively small micropores; therefore the same group investigated the

possibility of building materials with larger pores simply by using diamines with longer alkyl chains, up to 22 carbon atoms [8]. The results show that in order to obtain ordered materials, higher temperatures and higher surfactant to silica ratios are required when long-chain diamines are used as surfactants, due to the low solubility of these molecules at ambient temperature (diamine solubility decreases with increasing number of carbon spacers). The new samples of MSU-V materials produced in this way exhibit gallery-confined mesopores with dimensions ranging between 2.0 and 2.7 nm as a result of the larger distance between lamellar layers.

In the same years, the group of Tanev and Pinnavaia has proposed a similar neutral templating route (S^0I^0) for the synthesis of a class of hexagonal mesoporous molecular sieves which took the name of HMS materials [9, 36]. The typical preparation involved TEOS hydrolysis in the presence of primary amines (C_nH_{2n+1}) with variable chain lengths (up to 18 carbons), water and ethanol as co-solvent at temperatures ranging from ambient to 80 °C. Comparison of HMS and MCM-41 (the latter synthesised with both S^+I^- and $S^+X^-I^+$ templating) reveal significantly different chemical and physical properties between the two types of hexagonal molecular sieves. X-ray diffraction (XRD) and transmission electron microscopy (TEM) characterisation show that HMS materials possess less long-range order (see Figure 2.7) and thicker pore walls when compared to the MCM-41 analogues, as well as higher degree of framework cross-linking which results in a higher thermal stability when the material is subject to calcination. Furthermore, HMS materials exhibit smaller particle sizes and possess defects caused by non-ideal channel packing, features that can facilitate access to framework confined mesopores in catalysis and separation applications [9, 36].

According to the authors, the lower degree of order and regularity observed for HMS materials is the direct consequence of the weak hydrogen bond interactions which dominate the synthesis of this class of molecular sieves [9, 36]. They postulate, in fact, a mechanism of formation based on non-ionic interactions between amine surfactant head groups and neutral silicates, which enable the organisation of the rodlike micelles into short-range hexagonal mesophases. The S^0I^0 templating route was further supported by the apparent absence of features characteristic of protonated species in the ^{14}N NMR spectra and by the relatively simple solvent extraction method used to remove the template [9, 36].

The efficient synthesis methods employed to produce bio-inspired silica materials make them quite interesting from an environmental point of view. However, like it was observed for other examples of templating synthesis, the possibility of

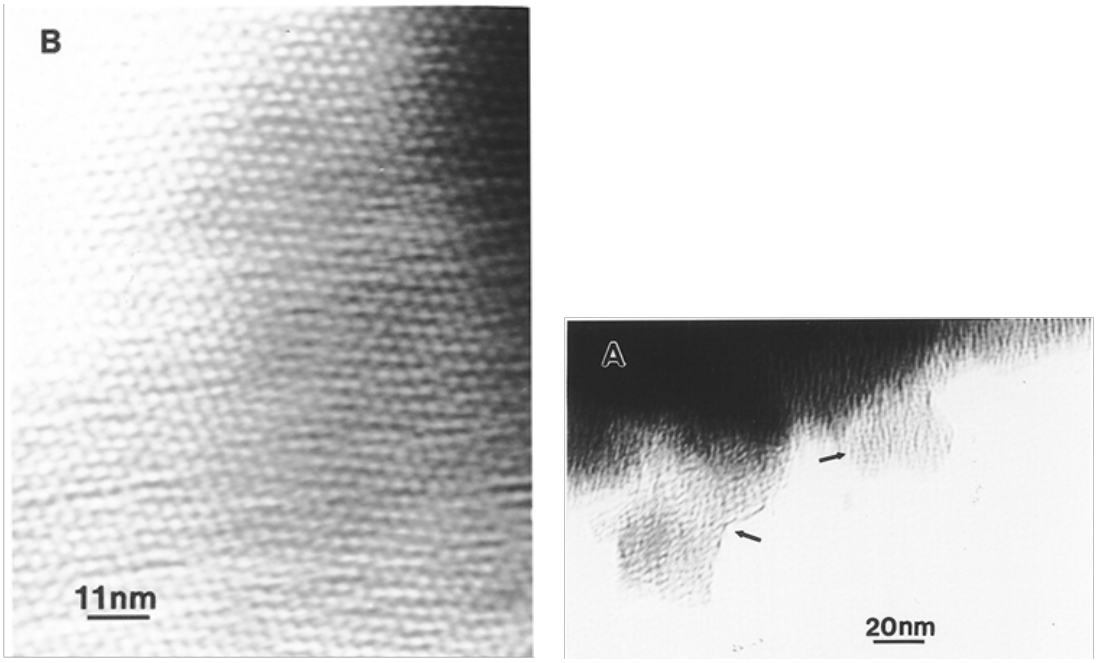

(a) (b)

Figure 2.7: TEM micrographs for HMS (a) and MCM-41 (b) materials. Figure adapted from [9].

further developing and improving these methods strictly depends on obtaining a more detailed knowledge of the processes occurring at molecular level. In addition to the techniques mentioned in this and in the previous section (NMR, TEM, XRD), a wide range of *in situ* characterisation methods have been used to investigate mesophase formation during the self-assembly process that leads to material synthesis [57]. These include i) electron paramagnetic resonance (EPR), which allows to look inside the micelle structures and obtain information regarding the interactions between surfactants and silicates [58, 59], ii) fluorescence techniques, such as spectrofluorometry and time-resolved fluorescence quenching (TRFQ), which can be used to monitor changes in the micelle properties induced by the addition of silicate species [60], iii) dynamic light scattering (DLS) and iv) small-angle X-ray scattering (SAXS), which are used to determine particle size distribution and other structural properties of the evolving mesophases [61]. In the case of bio-inspired materials, however, current understanding of the synthesis mechanism is even more incomplete than for conventional PMS materials (e.g. MCM-41). In this thesis, molecular simulations will be applied to shed some light on these mechanisms at molecular level.

2.4 MOLECULAR SIMULATIONS AS A TOOL TO UNDERSTAND MATERIAL SYNTHESIS

To complement experimental studies in the investigation of formation mechanisms of mesoporous silica materials, several simulation techniques have been developed and employed [46] over the past years. One of the first examples of this approach is the work of Bhattacharya and Mahanti where the aggregation of ionic surfactants in the presence of host particles and for different densities was studied using 2D off-lattice Monte Carlo simulations [13]. This simplified model, consisting of surfactants interacting by a Lennard-Jones and bond-bending potential with a screened coulombic term, was able to show an increased ordering in the micellar aggregation when the host particles are present in the system, in agreement with experimental evidence.

Another attempt to understand the synthesis of surfactant templated materials with lattice Monte Carlo simulations was done by Siperstein and Gubbins [14]. Using a simple chain-like surfactant model developed by Larson et al. [62], they built a three-dimensional system consisting of strong interactions between surfactants

and inorganic species, while water molecules were treated in a simplified way that does not account for hydrogen bonding. Without taking into account silica condensation, they were able to produce hexagonal and lamellar phases in qualitative agreement with experimental conditions (i.e. the hexagonal phase formed at low surfactant to silica ratios while the lamellar structure formed at high concentrations of surfactants) [14]. This same approach was later extended by Patti et al. to simulations of hybrid organic-inorganic ordered materials [15] using both inorganic and hybrid precursors. Furthermore, the lattice model for surfactant-water interactions developed by Siperstein and Gubbins [14] was later adapted and combined with a lattice model for silica polymerization developed by Jin, Auerbach and Monson [63]. In order to clarify the synthetic mechanism of MCM-41, the authors tested two different simulation procedures: a "two-step synthesis" approach and a "one-step synthesis" approach [63]. In the first case, high pH and low temperatures are used at the beginning to obtain ordered structures (lamellar and hexagonal, which are observed to reversibly transform into one another by changing the temperature, in agreement with experiments [64]), followed by a step at low pH and high temperature that promotes silica condensation around these structures. In the one-step approach, on the other hand, silica condensation is allowed to take place at the beginning of the synthesis. It is found that mesoscale ordering is obtained only when the two-step route is followed, whereas only little order is observed if silica polymerization is allowed to occur simultaneously to surfactant aggregation, in agreement with experimental results [3] and supporting the cooperative templating mechanism [42]. Despite the simplifications employed, these studies showed that it is possible to reproduce structural characteristics arising from silica/surfactant self-assembly using computer simulations; nevertheless, given the complexity of the system, a more accurate and realistic description can only be obtained using off-lattice models.

In more recent years, the increase in computer capabilities has allowed for more detailed atomistic simulations, in which all the species taking part in the synthetic process are modelled explicitly. Jorge performed large molecular dynamics simulations of n-decyltrimethylammonium bromide (DeTAB) surfactants and compared the performance of all-atom and united-atom approaches [16]. This study provided not only structural properties of these aggregates but also an insight into the mechanism of micellar formation, by identifying specific steps of the process. Following these results, silica monomers as well as oligomers were added to the system of DeTAB surfactants, to study the self-assembly process that leads to the formation

of PMS. It was found that the strong interactions between surfactant head-groups and silicates are responsible for the adsorption of the latter at the interface and the subsequent micellar growth, while promoting reciprocal interactions among these aggregates [6, 65]. Once again computer resources are the bottleneck in molecular modelling, therefore to be able to obtain a representative picture of this system at later stages of synthesis, the same group developed a coarse-grained (CG) approach based on the MARTINI model [10, 66]. By matching atomistic and coarse-grained micelle density profiles, they were able to develop a model for neutral and anionic silica monomers. These models were then used to carry out long CG simulations of the precursor solution (i.e. the system containing silica monomers, CTAB surfactants and water) for PMS materials, and results compared with simulations containing only surfactants and water (i.e. reference solution). It was found that in the absence of silicates, CTAB surfactants aggregate to form spherical micelles and that the driving force for the sphere-to-rod transition in PMS materials synthesis is the presence of anionic silicates which, by adsorbing on the micelle surface, screen the repulsion between aggregates while favouring micelle fusion [17]. Pérez-Sánchez et al. have then extended their model to include silica oligomers, demonstrating that subsequent micellar aggregation and co-operative formation of hexagonally ordered silica materials is caused by the presence of dimers or higher oligomeric silicates. These multiply charged species act as bridges between neighbouring rods allowing for the formation of ordered hexagonal liquid crystal phases [7].

Although there are still some open questions, the modelling work described above has significantly contributed to further our understanding of MCM-41 synthesis. By comparison, no molecular modelling studies have yet been carried out on bio-inspired silica materials. The work described in Chapters 4 and 5 attempts to provide a better understanding of the synthesis mechanism of two classes of bio-inspired silica materials (MSU-V and HMS materials) using the same approach employed by Jorge and co-workers to look into the synthesis of PMS [6, 7, 17, 65].

3

MOLECULAR DYNAMICS SIMULATIONS

Computer simulations, especially molecular dynamics (MD), have become in recent years a very popular tool to design new materials as well as to study biological systems. Today, simulations represent a flexible, relatively cheap and quick instrument to complement experimental studies, particularly when experiments would be too expensive or dangerous. In addition to that, simulations allow to compute quantities that are just impossible to measure otherwise (e.g. velocities of atoms and molecules) and to get direct insight into several different phenomena like protein folding [67, 68], micelle formation [69, 70], partitioning between solvents [71], etc.. The progress made in the field of computational chemistry and molecular modelling has been possible because of the tremendous growth of computational power: the increasing number of supercomputers accessible to academia and industry has promoted the development of novel algorithms specifically designed for parallel computing and therefore able to exploit these resources. To have an idea of the progress made in this field one can consider the first MD simulation of liquid argon performed by Rahman [72] in 1964: Rahman's argon system was composed of 864 particles and the interactions modelled only through a Lennard-Jones potential. Nowadays, systems with millions of atoms can be simulated for hundreds, even thousands of nanoseconds, and MD techniques are applied to look into a wide range of problems.

In the first part of this chapter, the fundamental principles of molecular dynamics simulations are introduced, focussing specifically on classical atomistic simulations. In the second part, coarse-grained methods (CG) are described with particular attention to the MARTINI approach [10] for coarse-graining.

3.1 MD PRINCIPLE AND THE IDEA OF COMPUTER EXPERIMENTS

In molecular dynamics simulations, trajectories of atoms interacting in the system, which are then used to derive all the properties of interest, are calculated by numerically solving Newton's equations of motion. The forces acting in the system

are defined through empirical force fields (see section 3.2.2) and the connection between microscopic states and macroscopic observable properties is given by statistical mechanics [73]. In statistical mechanics, averages are defined as ensemble averages, based on the fundamental assumption that every microscopic state of a many-body system with a certain N (number of molecules), V (volume) and E (energy) has the same probability to be occupied [73]. On the other hand, molecular dynamics simulations, by definition, follow the evolution of a system over time by computing positions $\mathbf{r}^N(t)$ and momenta $\mathbf{p}^N(t)$ at each step until the equilibrium state is reached. Hence, for a given observable A, its instantaneous value will fluctuate over time but, if that quantity is measured for a period of time long enough to allow the system to reach its equilibrium state, the computed value will approach the true average value:

$$\overline{A} = \lim_{t\to\infty} \frac{1}{t} \int_{t=0}^{t} A\left(\mathbf{p}^N(t), \mathbf{r}^N(t)\right) dt. \tag{3.1}$$

Unfortunately, for systems of interest in computer simulations (of the order of 10^{23} particles) it is not possible to integrate this equation. The goal of statistical mechanics is to take averages over all the possible configurations of the system (i.e. the ensemble), meaning across the 6N dimensional phase space (3 positions and 3 momenta for each atom) providing the correct weighting function so that Equation 3.1 becomes:

$$\langle A \rangle = \int\int d\mathbf{p}^N \, d\mathbf{r}^N \, A\left(\mathbf{p}^N, \mathbf{r}^N\right) \rho\left(\mathbf{p}^N, \mathbf{r}^N\right), \tag{3.2}$$

where ρ is the probability density, which represents the probability of finding in the ensemble a configuration which has positions $\mathbf{r}^N$ and momenta $\mathbf{p}^N$. This simplification is made possible by the "ergodicity hypothesis" which ensures that, for the type of systems studied in computer simulations, time averages are equivalent to ensemble averages. In the canonical ensemble, N, V and T are kept constant and the probability density function can be expressed by the Boltzmann distribution:

$$\rho(\mathbf{p}^N, \mathbf{r}^N) = \frac{\exp\left(\frac{-E(\mathbf{p}^N, \mathbf{r}^N)}{k_B T}\right)}{Q}, \tag{3.3}$$

where k_B is the Boltzmann constant and Q the partition function, i.e. a function describing the statistical properties of a system at the thermodynamic equilibrium.

The partition function of system consisting of N identical classical particles in the canonical ensemble is:

$$Q_{NVT} = \frac{1}{N!}\frac{1}{h^{3N}}\int\int d\mathbf{p}^N\, d\mathbf{r}^N\, \exp\left[\frac{-\hat{H}(\mathbf{p}^N, \mathbf{r}^N)}{k_B T}\right], \tag{3.4}$$

where h is the Planck constant, while the Hamiltonian $\hat{H}$ is given by the total energy:

$$\hat{H}(\mathbf{p}^N, \mathbf{r}^N) = K(\mathbf{p})^N + U(\mathbf{r})^N, \tag{3.5}$$

with K representing the kinetic energy of the system and U its potential energy.

Real experiments, however, do not usually occur at constant volume, therefore, rather than the canonical ensemble, the isothermal-isobaric ensemble is more commonly used in MD simulations. In this case, number of particles (N), pressure (P) and temperature (T) are kept constant and the partition function is given by:

$$Q_{NPT} = \frac{1}{N!}\frac{1}{h^{3N}}\frac{1}{V_0}\int dV \int d\mathbf{p}^N\, d\mathbf{r}^N\, \exp\left[\frac{-(\hat{H}(\mathbf{p}^N, \mathbf{r}^N) + PV)}{k_B T}\right], \tag{3.6}$$

where V_0 is a constant and has the units of volume. It should be noted that switching between different ensembles is achieved, in practice, in MD simulations through the implementation of barostats and thermostats, which will be discussed later (see section 3.2.4).

Molecular dynamics simulations are often referred as "computer experiments" [73, 74] because, just like in a real experiment, to run an MD simulation the system must first be "prepared" by fixing the number of molecules and choosing an appropriate force field. Then, Newton's equations of motion are solved until the system reaches the equilibrium state and only at this point "measurements" can be performed by averaging over computed trajectories. This will be the focus of the following section.

3.2 MODELLING THE SYSTEM

As already mentioned, there are at least three minimum inputs that must be specified prior to starting a molecular dynamics simulation:

1. the initial configuration of the system;

2. a force field describing the force acting on each atom of each molecule (i.e. describing the interaction between particles);
3. the sampling algorithm.

Each of these inputs is described in more detail below.

3.2.1 *Initial configuration*

In molecular dynamics, atoms forming a given molecule are represented by beads connected through springs. Topologies are necessary to express the internal connectivity of every type of molecule which, along with Cartesian coordinates of all the particles, are the starting point of MD calculations. In practice, it is necessary to have a representative molecule of all the species present in the system, for which specific topologies and an initial set of coordinates can be defined. At this point, the starting configuration is created by adding to the simulation box as many molecules as needed. Topologies can be created by hand for relatively simple molecules, however, this can be significantly more complex for very large molecules, like for example proteins, for which the specific 3D structure is very important. In the last case, molecular structures, including atomic connectivity and coordinates, can be downloaded from the RCSB Protein Data Bank [75], a collection of all the available protein structures derived from X-ray diffraction or NMR studies. On the other hand, coordinates of simple molecules can be generated using commercial software packages, such as Molden [76] or Avogadro [77].

The simulation box created in this way is considerably smaller than the real system for which one wants to compute properties. To overcome this limitation, periodic boundary conditions (pbc) are applied. This means that replicas of the simulation box are created in all directions, so that if a molecule leaves the box from one end of the box, the same molecule will reappear at the opposite end. The simplest and most common type of periodic cell is the cubic box, however other types of periodic cells exist. The truncated octahedron and the rhombic dodecahedron, for example, more closely resemble a sphere and are often preferred to simulate liquids [78]. Another important thing to consider when choosing the simulation box is that it has to be large enough to reproduce the main features of the system of interest, avoiding so called finite size effects which could cause artefacts in the results. The importance of choosing a box having the appropriate size and shape will be further discussed in Chapter 6, where two parallelepiped

cells, respectively high 7 and 14 nm, have been used to simulate amine molecules interacting with amorphous silica surfaces.

3.2.2 *Force Fields*

Choosing an appropriate force field for the system is probably one of the most important aspects of an MD simulation since the correct representation of the scientific problem one aims to model will depend on this choice. A force field is a semi-empirical set of parameters used to represent the potential energy of a particular set of atoms and molecules according to a specific mathematical function. Many force fields have been developed (TraPPE [79], OPLS [80], GAFF [81], etc.) on the basis of both experiments and quantum mechanical calculations. However, different force fields are able to reproduce more or less accurately different experimental properties. Quantum mechanical methods deal with electrons which provide a very accurate representation of the system but, at the same time, increase substantially the computational cost. Most of the problems of interest in molecular modelling are too large to be described with quantum mechanical methods. However, it is feasible to use a classical description by means of force field methods, which ignore the motions of electrons and describe the evolution of the system over time as a function of the nuclei position only. Moreover, there is yet another approximation that is necessary to make when using the force field method and it is related to the fact that potentials are "pair effective". This means that electrostatic and van der Waals interactions (which will be described in a while) are calculated only between pairs of interacting particles, but potential functions are specifically parametrised in order to account for many-body effects in this effective pairwise model [82]. Clearly, the interaction between two molecules is affected by the presence of all the other molecules; however, the computational complexity increases considerably just by including a term that represents the interaction between three molecules. Such complexity justifies the use of an approximated model which does not represent the real interaction between a pair of isolated particles but provides, in practice, a good representation for molecular dynamics applications.

Considering that the force, $\mathbf{F}$, is the negative gradient of a scalar potential energy function:

$$\mathbf{F}(\mathbf{r}) = -\nabla U(\mathbf{r}), \tag{3.7}$$

and that for a system of interacting particles, the potential energy is described as the sum of bonded and non-bonded interactions, it follows:

$$U(\mathbf{r}) = \sum U_{\text{bonded}}(\mathbf{r}) + \sum U_{\text{non-bonded}}(\mathbf{r}), \tag{3.8}$$

where:

$$U_{\text{bonded}} = U_{\text{bond}} + U_{\text{angle}} + U_{\text{dihedral}}, \tag{3.9}$$

and

$$U_{\text{non-bonded}} = U_{\text{electrostatic}} + U_{\text{van der Waals}}. \tag{3.10}$$

In the following discussion, a brief description of the main components of these two terms will be given.

BONDED INTERACTIONS Bonded potentials include bond stretching, angle bending and dihedral torsion which, respectively, describe 2-, 3-, and 4-body interactions of covalently bonded atoms. The two most common functions used to describe bond length potentials between two atoms i and j are the harmonic potential and the Morse potential (see Figure 3.1). The first one (Equation (3.11)) approxim-

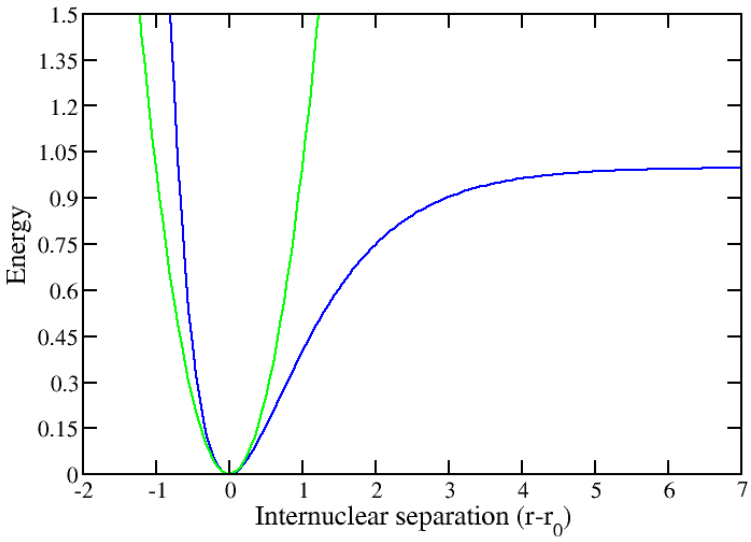

Figure 3.1: Bond length potential; harmonic in green and Morse in blue for $k = 2$, $De = 1$ and $a = 1$.

ates the covalent bonds to harmonic oscillators:

$$U_{\text{bond}-\text{harmonic}}(r_{ij}) = k_b (r_{ij} - r_0)^2, \tag{3.11}$$

where $r_{ij} = \|\mathbf{r_i} - \mathbf{r_j}\|$ represents the distance between atoms, r_0 the equilibrium distance and k_b the spring constant. Bonds modelled as harmonic potentials cannot be broken and therefore they are suitable only to represent distances close to the equilibrium point. On the other hand, the Morse potential (see Figure 3.1) explicitly includes the effect of bond breaking (force tends to zero for infinite distance) and makes use of an an-harmonic function:

$$U_{\text{bond}-\text{morse}}(r_{ij}) = D_e \left[1 - \exp\left(-a\left(r_{ij} - r_0\right)\right)\right]^2, \tag{3.12}$$

where D_e is the depth of the well and a defines the steepness of the well, which can be rewritten in terms of the harmonic force constant k_b:

$$a = \sqrt{\frac{k_b}{2 D_e}}. \tag{3.13}$$

It is worth noting that when performing MD simulations, it is common to keep bond distances fixed to a precise value in order to use a larger time step in the integration algorithm and speed up the calculations. To achieve this, constraint algorithms like LINCS [83], SHAKE [84] or SETTLE [85] are applied.

The bond angle potential describes the angular vibration between three atoms i, j, k and is commonly described using a harmonic function similar to the bond stretching:

$$U_{\text{angle}}(\theta_{ijk}) = k_\theta \left(\theta_{ijk} - \theta_0\right)^2, \tag{3.14}$$

where θ_{ijk} is the angle between vectors $\mathbf{r_{ij}} = \mathbf{r_i} - \mathbf{r_j}$ and $\mathbf{r_{kj}} = \mathbf{r_k} - \mathbf{r_j}$, θ_0 is the equilibrium angle, and k_θ is the angle constant.

In order to adequately predict the torsional energy of even simple molecules, it is necessary to add another interaction term to take into account the angular spring between the planes formed by the first three and last three of four i, j, k, l consecutively bonded atoms [86]. This term is the torsional angle potential, also

known as dihedral angle potential, and the function most often used to describe it is the Ryckaert-Bellemans function:

$$U_{rb}(\phi_{ijkl}) = \sum_{n=0}^{5} C_n \left(\cos\left(\Psi\right)\right)^n, \tag{3.15}$$

where C_n are the constants specific for the force field selected, ϕ_{ijkl} is the dihedral angle and $\Psi = \phi_{ijkl} - 180°$. In the case of the OPLS force field [80], which has been used for most of the present work, the Ryckaert-Bellemans dihedral function is defined with a Fourier series so that:

$$U_{rb-OPLS}(\phi_{ijkl}) = \frac{1}{2}\Big[V_1\left(1+\cos\left(\phi-\phi_1\right)\right) + V_2\left(1+\cos\left(2\phi-\phi_2\right)\right) + V_3\left(1+\cos\left(3\phi-\phi_3\right)\right) + V_4\left(1+\cos\left(4\phi-\phi_4\right)\right)\Big], \tag{3.16}$$

where V_1, V_2, V_3, V_4 are coefficients of the Fourier series and ϕ_1, ϕ_2, ϕ_3, ϕ_4 are phase angles. By applying trigonometric relations, Equation (3.16) can be converted to the form of Equation (3.15), and an equivalence between parameters can be established.

It is important to note at this point that most of the conformational changes are not caused by bond stretching or angle bending (which are referred to as "hard degrees of freedom") but depend on the complex interplay between torsional potential and non-bonded interactions [82]. In the following paragraph the latter are discussed.

NON-BONDED INTERACTIONS Non-bonded potentials describe interactions between all atom pairs that are not linked by covalent bonds either within the same molecule, for atoms separated by a minimum of three bonds, or between two different molecules. This term takes into account repulsion and dispersion interactions as well as Coulomb interactions. The computation of non-bonded interactions at every time step of an MD simulation is the most demanding term, even when fast evaluation methods are used.

Dispersion and repulsion terms are usually expressed with the Lennard-Jones (LJ) potential:

$$U_{LJ}(r_{ij}) = 4\,\varepsilon_{ij}\left[\left(\frac{\sigma_{ij}}{r_{ij}}\right)^{12} - \left(\frac{\sigma_{ij}}{r_{ij}}\right)^{6}\right], \tag{3.17}$$

where r_{ij} gives the distance between two atoms i and j, ε_{ij} is the minimum of the potential energy, also called the depth of the well, and σ_{ij} is the equilibrium distance between two molecules at which the potential energy is equal to zero. Repulsive forces due to overlapping of electron orbitals are short range forces represented by the term r^{-12}, whereas long-range attraction forces (for example caused by interactions between instantaneous dipoles) are represented by the term r^{-6}.

The Lennard-Jones potential approaches 0 as r_{ij} increases, so it is usually truncated to 0 past a cut-off radius (r_c in Figure 3.2). To calculate the LJ parameters of

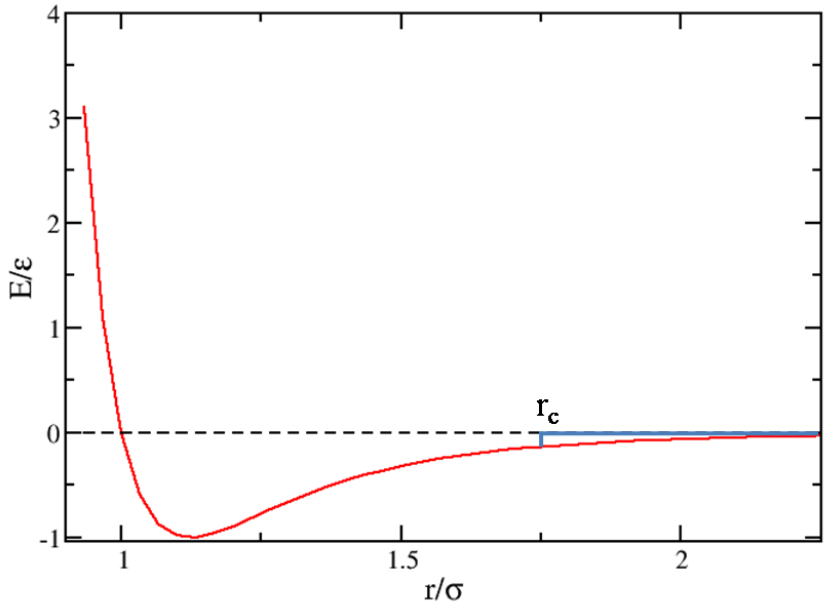

Figure 3.2: The Lennard-Jones potential function for $\varepsilon = 0.1$ eV and $\sigma = 0.3$ nm.

a pair of non-identical interacting atoms, Lorentz-Berthelot combination rules are normally used:

$$\sigma_{ij} = \frac{1}{2}\left(\sigma_{ii} + \sigma_{jj}\right), \tag{3.18}$$

and

$$\varepsilon_{ij} = \left(\varepsilon_{ii} \cdot \varepsilon_{jj}\right)^{\frac{1}{2}}. \tag{3.19}$$

To represent the electrostatic potential the classical Coulomb law is used:

$$U_{\text{Coulomb}}(r_{ij}) = \frac{1}{4\pi\varepsilon_0}\frac{q_i q_j}{\varepsilon_r r_{ij}}, \tag{3.20}$$

where $\varepsilon_0 = 8.85418782 \cdot 10^{-12}\ \text{C}^2\,\text{m}^{-2}\,\text{N}^{-1}$ is the permittivity of free space, $\varepsilon_r = 1$ is the relative permittivity of the material, q_i and q_j are the charges and $r_{ij} = \|\mathbf{r_i} - \mathbf{r_j}\|$ gives the distance between a pair of atoms. It follows that when two atoms have charges with the same sign the potential energy is repulsive, while it is attractive when they have opposite signs.

It is worth noting at this point that the interactions for third neighbours, also referred to as 1-4 interactions, receive a special treatment depending on the specific force field. In some cases, like for example in OPLS [80], such interactions are included but scaled by a constant factor to prevent the van der Waals term assuming too large values, compared to the torsional one, when the two atoms occasionally become very close. In the particular case of OPLS the same scaling factor is also applied to Coulomb contributions.

LONG-RANGE INTERACTIONS Long-range corrections arise from the fact that both Lennard-Jones and Coulomb interactions are reduced to zero after a certain cutoff distance. Since using a very large simulation cell is usually not a practical solution and simply neglecting these interactions beyond the cutoff leads to an incorrect representation of the system, specific correction methods have been developed to treat long-range forces [82, 87].

Concerning LJ interactions, dispersion corrections are necessary to consider the effect of cutoffs on energy and pressure, whereas it is safe to assume that such cutoffs are long enough to neglect the correction for repulsion interactions [88]. These long-range correction terms for energy and pressure (E_{LRC} and P_{LRC}) are usually calculated assuming that the radial distribution function $g(r)$ (i.e. the probability of finding a pair of atoms at a certain distance r over the probability of having a completely random distribution of atoms of the same density) equals 1 past the cutoff distance. From this assumption, analytical expressions for E_{LRC} and P_{LRC} can be derived using the relations that link energy and pressure to radial distribution. It should be noted that depending on the type of simulation ensemble, such corrections should be applied to the instantaneous values of energy and pressure (*NPT* for instance) or to the final values (*NVT* or *NVE*) [78].

The Ewald summation method was originally introduced to compute electrostatics energies of ionic crystals [89] but it is now widely used to deal with long-range electrostatics interactions. The basic idea is to replace the slowly-converging summation of the total electrostatic energy for N particles and their periodic images with two rapidly-converging series: one in the direct space and one in the reciprocal space [88]. Nevertheless, the computational cost for the reciprocal part is still extremely high because it scales with N^2(or $N^{\frac{3}{2}}$ when a better algorithm is used) and therefore other methods have been proposed in this context as well. One of these is the Particle Mesh Ewald (PME) method [90, 91] which improves the performance of the summation in the reciprocal space.

3.2.3 *Sampling algorithms*

Time integration algorithms are numerical methods used to solve equations of motions: the time is discretised into time steps Δt, and using positions and other derivatives (depending on the specific algorithm used) at time t, the same quantities at $t + \Delta t$ can be computed. It follows that ideally such algorithms should be computationally fast but accurate at the same time. The three most popular algorithms used in MD are:

- the leap-frog algorithm,
- the Verlet algorithm,
- the velocity Verlet algorithm.

The so called leap-frog algorithm [92] makes use of positions $\mathbf{r}$ at time t and velocities $\mathbf{v}$ at $t - \frac{\Delta t}{2}$ to solve Newton's equations:

$$\mathbf{r}(t + \Delta t) = \mathbf{r}(t) + \mathbf{v}\left(t + \frac{\Delta t}{2}\right)\Delta t, \tag{3.21}$$

$$\mathbf{v}\left(t + \frac{\Delta t}{2}\right) = \mathbf{v}\left(t - \frac{\Delta t}{2}\right) + \mathbf{a}(t)\,\Delta t, \tag{3.22}$$

where $\mathbf{a}(t)$ is the acceleration:

$$\mathbf{a}(t) = \frac{\mathbf{F}(t)}{m} = -\left(\frac{1}{m}\nabla U\left(\mathbf{r}(t)\right)\right), \tag{3.23}$$

with $\mathbf{F}(t)$ being the force acting at time t on a particle having mass m.

The Verlet algorithm [93] calculates the same trajectories as the leap-frog but positions are updated in the following manner:

$$\mathbf{r}(t+\Delta t) = 2\,\mathbf{r}(t) - \mathbf{r}(t-\Delta t) + \mathbf{a}(t)\,\Delta t^2 + \mathcal{O}(\Delta t^4), \tag{3.24}$$

where $\mathcal{O}(\Delta t^4)$ is the truncation error.

The velocity Verlet algorithm is similar to the leap-frog algorithm but is faster and more accurate: the positions of the atoms are updated every Δt steps while the velocities are updated every $\Delta t + \frac{\Delta t}{2}$ steps:

$$\mathbf{r}(t+\Delta t) = \mathbf{r}(t) + \mathbf{v}(t)\,\Delta t + \frac{1}{2}\,\mathbf{a}(t)\,\Delta t^2, \tag{3.25}$$

$$\mathbf{v}\left(t+\frac{\Delta t}{2}\right) = \mathbf{v}(t) + \frac{1}{2}\,\mathbf{a}(t)\,\Delta t, \tag{3.26}$$

$$\mathbf{a}\left(t+\Delta t\right) = -\left(\frac{1}{m}\nabla U\big(\mathbf{r}(t+\Delta t)\big)\right), \tag{3.27}$$

$$\mathbf{v}\left(t+\Delta t\right) = \mathbf{v}\left(t+\frac{\Delta t}{2}\right) + \frac{1}{2}\,\mathbf{a}(t+\Delta t)\,\Delta t. \tag{3.28}$$

It should be noted that in this case accelerations only depend on the positions and do not depend on the velocities.

3.2.4 *Thermostats and barostats*

The microcanonical (constant *NVE*) is the default ensemble for MD simulations. However, in the majority of applications, temperature and/or pressure need to be controlled. This is achieved through the implementation of thermostats and barostats as described in the following paragraphs.

THERMOSTATS Several methods have been developed to control the temperature in MD simulations, with different intents (i.e. preserving the correct dynamics or the correct thermodynamics of the system). Here the most common ones will

be discussed, with particular emphasis towards the types of thermostat that have been employed and tested in this work.

The equipartition theorem relates the temperature of a system to its kinetic energy (K), and hence to the atomic velocities, according to the relation [82]:

$$K = \left\langle \sum_{i=1}^{N} \frac{1}{2} m_i v_i^2 \right\rangle = \frac{3}{2} N k_B T. \tag{3.29}$$

It follows that the simplest way to keep the temperature constant is by multiplying the velocities of each particle in the system by a factor λ at each time step:

$$\lambda = \sqrt{T_{\text{required}}/T_{\text{current}}}, \tag{3.30}$$

where T_{required} is the desired temperature and T_{current} is the instantaneous temperature as obtained from the kinetic energy. This type of thermostat (referred as v-scaling) does not correctly reproduce the canonical ensemble (i.e. thermal fluctuations are not possible) and it is, therefore, not recommended for production runs but can be used for equilibration.

Similarly to the v-scaling thermostat, the Berendsen temperature coupling [94] also scales the velocity at each step. This is achieved by coupling the system with an imaginary heat bath at constant temperature T_0 and introducing a coupling parameter τ:

$$\frac{dT(t)}{dt} = \frac{1}{\tau}\big(T_0 - T(t)\big). \tag{3.31}$$

This additional parameter determines the strength of the coupling between bath and system (a large τ means weak coupling, i.e. it will take longer for the system to reach the desired temperature). The Berendsen thermostat suffers from the same limitations of the v-scaling thermostat since it does not produce thermodynamically correct energy fluctuations. It must be noted that the error introduced by the thermostat scales with $1/N$ [88]. This means that for very large systems, ensemble averages will not be dramatically affected but fluctuation properties (e.g. heat capacities) will.

In this work, the Berendsen thermostat was used during the relaxation steps while for production runs the Nosé-Hoover thermostat was employed. This thermostat, first introduced by Nosé [95] and then further developed by Hoover [96], is based on an extended-ensemble approach, which considers the bath as part of

the (extended) system. For this purpose, a time-scaling parameter, $\tilde{s}$, is added so that the time step of the extended system, $d\tilde{t}$, equals:

$$d\tilde{t} = \tilde{s}dt, \tag{3.32}$$

An artificial mass $\tilde{Q}$ is also defined. This has the function of adjusting the strength of the coupling with the heat bath, so that high values of $\tilde{Q}$ produce loose coupling while low values cause tight coupling. The formulation of the Hamiltonian for this extended system can be expressed as:

$$\hat{H} = \sum_{i=1}^{N} \frac{\tilde{\mathbf{p}}_i^2}{2m_i\tilde{s}^2} + U(\tilde{\mathbf{r}}^N) + \frac{\tilde{\mathbf{p}}_{\tilde{s}}^2}{2\tilde{Q}} + N_{df}k_B T_0 \ln s, \tag{3.33}$$

where $\tilde{p}$ and $\tilde{p}_{\tilde{s}}$ are the momenta for the real system and for the heat bath, respectively, N_{df} is the number of degrees of freedom and T_0 the desired temperature. Using this formulation the extended system effectively represents a microcanonical ensemble, however the real system does not since the total energy is not conserved and thermal fluctuations are allowed (i.e., the real system is in the canonical ensemble).

BAROSTATS When performing MD simulations it is often required to maintain both temperature and pressure constant. From a thermodynamic point of view, for a system to maintain its pressure fixed a certain change in volume is required. Such change can happen in all directions, producing isotropic pressure coupling, or only in one, leading to semi-isotropic pressure coupling. For this purpose several different barostats have been developed and implemented in the simulation codes. Here only the Berendsen [94] and Parrinello-Rahman [97] barostats will be discussed. It must be noted that, due to its dependence on the virial, pressure fluctuations are usually very large (i.e. the virial changes more quickly with positions than, for instance, the internal energy does). When using the Berendsen algorithm [94], pressure control is obtained by coupling the system with a pressure bath so that:

$$\frac{dP(t)}{dt} = \frac{1}{\tau_p}\big(P_0 - P(t)\big), \tag{3.34}$$

where τ_p is the coupling constant, P_0 is the pressure of the bath and $P(t)$ the instantaneous pressure. In the case of isotropic pressure coupling, the volume is

changed by altering positions and box vectors at each time step by means of a scaling factor η defined as follows:

$$\eta = 1 - \frac{\Delta t}{\tau_p}\beta(P - P_0), \tag{3.35}$$

where β is the isothermal compressibility of the system. This approach provides the correct average pressure, however just like in the analogous thermostat it does not simulate the correct *NPT* ensemble [88].

A more correct representation is achieved when using the Parrinello-Rahman algorithm [97]. In this case, the equation of motion is applied to the box vectors ($\mathbf{b}$) so that:

$$\frac{d\mathbf{b}^2}{dt^2} = V_b \mathbf{W}^{-1} \mathbf{b}'^{-1}(P(t) - P_0), \tag{3.36}$$

where V_b is the volume of the box and W a parameter providing the magnitude of the coupling. From Equation (3.36) the equations of motion for the particles in the system can be obtained.

3.2.5 *Limitations*

When performing molecular dynamics simulations, one thing to keep in mind is that this powerful tool has some intrinsic limitations. First of all, as mentioned before when describing the force field method, MD simulations make use of a classical description of the interatomic interactions. This means that electrons are not present in the system, they are treated by means of a potential energy surface which is a function of the position of the nuclei only (the Born-Oppenheimer approximation [98]). However, this reduced level of detail is sufficient for most MD applications. Furthermore, it allows to explore larger systems compared to quantum mechanics (QM) methods. The further development and expansion of MD methods is however strictly related to the availability of accurate potential functions.

Another limitation arises from the fact that the atomic motion is also classical, meaning that the classical Newton's law is used to describe collisions of atoms and particles. This is, in most of the cases, a reasonable approximation, however for very light atoms, like hydrogen or helium, quantum effects become important and this approximation is not valid any more (as well as for simulations at low temperature).

As discussed in the previous sections, because of the finite size of the simulation box and because, in reality, only a very small portion of the system will be in contact with the boundaries (e.g. walls of the container or surfaces), periodic boundary conditions must be applied. These, however, do not represent a natural situation in most cases and therefore fluids simulated will differ from the real ones because of this periodicity. In this respect, the choice of the box size and shape is very important. To eliminate the possibility of artefacts in the simulation results caused by the finite size of the computational cell does, results obtained with systems of different sizes should be compared.

Another very important aspect are the limitations due to time and length scales. A typical time step in an MD simulation is on the order of a femtosecond. Given the current computer power, only processes that occur within $100 - 1000$ ns can be simulated, and this is a severe limitation for the study of several systems. Length scale is also an important limitation because any structural feature of interest and any spatial correlation length one aims to reproduce with simulations should be smaller than the size of the computational cell (around $10 - 20$ nm maximum). With regard to this last aspect, time and length scale limitations can be overcome by replacing atomistic models with coarse-grained ones which, by reducing the degrees of freedom (i.e. the level of detail of molecular interactions), allow significantly longer and larger simulations without losing computational efficiency. In the following section, coarse-grained methods will be discussed in more detail, mostly focussing on the MARTINI approach to coarse-graining [66] which was used in this work.

3.3 COARSE-GRAINING AND MULTI-SCALE MODELLING

The term multi-scale modelling refers to the combination of different simulation techniques used to investigate complex phenomena that have inherently different time and length scales. The field of application ranges from biology and biomedicine where multi-scale modelling is used, for example, to model tumour growth [99, 100], to pharmacology where it is used as a tool to guide drug design and delivery [101]. In engineering, applications include fluid dynamics [102, 103] and material science [104] which is the relevant context for this work. Figure 3.3 shows a typical multi-scale diagram: models with a high level of detail, such as quantum methods, are limited to very small time and length scales, thus to access larger

spatial and temporal scales simplified models are needed. The aim of multi-scale

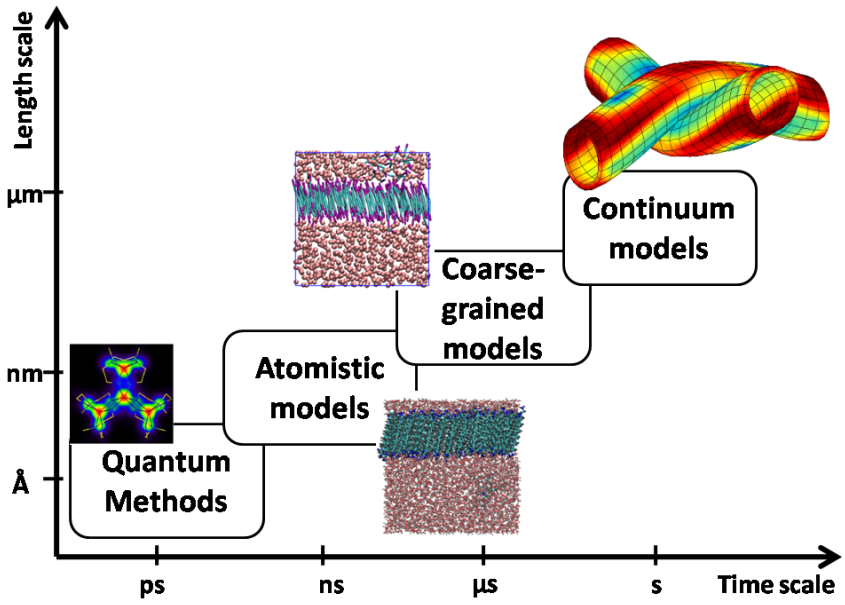

Figure 3.3: Schematic diagram showing the time and length scales accessible with different computational methods. Figure for quantum methods adapted from [105] and Figure for continuum models adapted from [106].

modelling is to link the different characteristic scales of resolution by producing unified or integrated models that comprise all the information acquired at each level of simulation. Two approaches are possible: the "bottom-up" approach, when information obtained from a higher level of theory is used to develop large scale models; and the "top-down" approach, when macroscale observations are used to build models at the more detailed scales. In the following discussion CG methods will be addressed, with a particular focus on the MARTINI approach to coarse-graining [10] which has been employed in this work and will be further described in Chapters 4 and 5.

3.3.1 *Different approaches to coarse-graining*

The aim of every coarse-grained model is to simplify and speed up the calculations while being able to correctly reproduce the physical behaviour captured with atomistic simulations. This simplification is achieved by grouping together a certain number of atoms, and sometimes also molecules, into beads or CG sites

which interact trough effective potentials, leading to a significant computational improvement [107].

The first question to ask when approaching a coarse-graining problem is *"how much to coarse-grain?"*. This translates, in practice, to choosing the most appropriate mapping scheme, or in other words the degree of coarse-graining, for the problem one aims to study. In this regard, united-atom models, where hydrogen atoms are lumped together with the heavier atom they are attracted to [80], could be considered as the lowest possible level of coarse-graining. In coarse-grained models usually from four to six heavy atoms (i.e. non-hydrogen atoms), representing specific functional groups, are mapped into a single CG bead. However, some systems might require a more detailed description in order to correctly capture specific functions (e.g. side-chain interactions in proteins [108]), in this case finer models are used for this purpose. On the opposite end, higher-level models which group together clusters of compounds, for instance amino acids [109], into a single bead have also been employed.

The next problem to solve is *"how to treat the solvent?"*. When performing full atomistic simulations most of the computational time is spent in calculating interactions between solvent molecules. The solvent, in the majority of cases water, plays an important role in MD simulations since it screens electrostatic interactions. When it comes to finding more efficient ways to represent water, one possibility is to use implicit solvent methods. In this case, instead of representing each water molecule as a discrete entity, the solvent is treated as a continuous medium having the average properties of the real fluid and an effective dielectric constant [110]. Implicit solvent models are simple and fast but not adequate to describe all kind of systems (e.g. high concentration of ions in solution [111]). For this reason, it is more common to adopt explicit CG models. The simplest approach consists in mapping one water molecule to one CG water bead, this however only marginally reduces the computational cost due to the presence of the solvent [112]. A more efficient strategy consist in mapping bundles of water molecules into a single CG bead. In this case, however, depending on the method used to obtain the CG potential, an algorithm able to dynamically assign molecules to clusters might be necessary [113, 114]. One limitation of this type of models is their lack of charges, which requires the addition of an implicit dielectric constant for the screening of electrostatics [67]. To solve this issue several models have been developed to account for water polarizability [115–117]. Among these models it is worth mentioning the polarizable MARTINI water model [115] which introduces two additional beads carrying

charges connected to the LJ site. The improved representation of the dielectric behaviour of water comes at the cost of a higher computational cost (simulations are about three times slower than with the standard MARTINI water model [115]) which might not justify the use in all applications.

At this point, the following step is to obtain a CG force field. Two main strategies are possible: the fitting can be based on information extracted directly from atomistic simulations (also referred as systematic CG methods) or based on properties measured experimentally (such as the MARTINI force field). Belonging to the first class are structure-based and force matching methods, which parametrise the CG force field so that specific target distributions obtained from atomistic simulations are matched (i.e. bottom-up approach) [118]. As the name suggests, structure-based methods aim to use effective CG potentials to reproduce structural properties, such as bond, angle, dihedral or radial distributions, calculated for a reference atomistic system [119]. Among these methods it is worth mentioning the iterative Boltzmann inversion (IBI) [120] and the inverse Monte Carlo (IMC) techniques [121]. The theoretical principle on which both methods are based is the Henderson theorem [122] which states that, for a pairwise additive system, there is only one effective pair potential that is able to reproduce a given radial distribution function (RDF). Starting from an initial guessed potential, IBI iteratively refines it using a correction term that is proportional to the difference between atomistic ($g^{A}(r)$) and coarse-grained ($g^{CG}(r)$) RDFs so that:

$$U^{CG}_{k+1}(r) = U^{CG}_{k} + k_B T \ln\left[\frac{g^{CG}_{k}(r)}{g^{A}(r)}\right], \tag{3.37}$$

where U^{CG}_{k+1} and U^{CG}_{k} are the potentials at the iteration $k+1$ and k, respectively.

Similarly to the IBI method, the IMC is also based on iterations to match target RDFs but in this case the correction term takes into account that a change of the potential function at a certain distance can produce a change in the RDFs at all distances, leading to a faster convergence of the algorithm. With regard to force matching methods (FM), these were originally developed by Ercolessi and Adams [123] and then further improved by Izvekov and Voth [124]. In this case instead of matching atomistic and coarse-grained RDFs, the average force acting on CG sites is matched with forces acting at the atomistic level.

Bottom-up approaches for CG produce effective potentials that are optimised for a specific system. This limits the transferability across different systems, when

for example one component is changed, but also across the same system when the temperature or the concentration of one species is significantly altered. Practically, these methods require to run new atomistic simulations for each new system one wants to reproduce, hence restricting their general applicability. As an alternative to systematic CG methods, the MARTINI force field, based on a building block principle, will be presented in the next section.

3.3.2 *The MARTINI force field*

Differently from the methods described so far, the MARTINI force field [10, 66] has been developed with an another philosophy in mind: rather than aiming at accurately reproducing structural characteristics of specific systems, the emphasis is on flexibility and transferability between different systems [125]. This is achieved by means of an empirical (or top-down approach) in which non-bonded interactions between the building blocks of the force field, the different CG bead types, are extensively parametrised against thermodynamic data such as free energies of vaporisation, free energies of hydration and, in particular, water/oil partition coefficients.

THE MAPPING PROCEDURE The MARTINI protocol for mapping recommends to represent, on average, four heavy atoms with one CG interaction site. It follows that, for example, a butane molecule is represented with one bead whereas an octane molecule consists of two beads. Consistently with this mapping procedure, four water molecules are equivalent to a single CG water bead. An exception to this philosophy are monoatomic ions, which are modelled to represent the ion and the first solvation shell (i.e. six water molecules) in a single bead. Furthermore, the four-to-one approach becomes inadequate for representing molecules containing ring structures, and a finer mapping (usually two or three molecules to one CG bead) is necessary to produce the correct geometry. For this purpose a smaller type of bead, called "S-bead", is introduced. More details about the specific interactions will be provided below.

One of the main features of the MARTINI force field is its simplicity and adaptability to use in a wide range of applications. This characteristic can be seen in the limited number of particle types and levels of interactions that are defined in the force field. To account for the different chemical nature of the CG beads, four

main types of beads are specified: polar (P), non-polar (N), apolar (C), and charged (Q). Non-polar and charged beads are then further distinguished based on their hydrogen donor/acceptor character into: donor (d), acceptor (a), donor-acceptor (da) and none (O). Polar and apolar beads, instead, are differentiated according to their level of polarity with numbers going from 1 to 5, where 1 represents low polarity and 5 high polarity. This leads to a total of 18 levels of interactions. Some examples of molecule definitions can be found in Table 3.1 (for more topology examples see Reference [10]). There is one last particle type that needs to be discussed: the antifreeze particle (AF). An undesirable effect of the MARTINI model for water is that freezing occurs at higher temperature than expected (between 280 and 300 K). To solve this issue, it is sufficient to replace approximately 10 % of the standard water beads (P_4) with AF particles, labelled BP_4. This special type of AF bead, which interacts through a larger σ and a higher ε with standard water beads, prevents water from freezing by disrupting the formation of the crystalline lattice. More details about AF particles and their interactions are provided below.

Table 3.1: Examples of MARTINI mapping for selected molecules and ions.

Molecule	Topology
butane	C_1
octane	C_1-C_1
propane	C_2
benzene	SC_5-SC_5-SC_5
butanol	N_{da}
propanol	P_1
ethanol	P_2
water	P_4
sodium ion	Q_d
chloride ion	Q_a

NON-BONDED INTERACTIONS Non-bonded interactions are modelled through a standard Lennard-Jones potential (see Equation (3.17)). The value of σ is set to 0.47 nm for all particle types with few exceptions that will be discussed below: i) S-type beads, ii) antifreeze particles (AF) and iii) interactions between charged beads and apolar beads C_1 or C_2. Moreover, there are a total of ten levels, ranging from

"*supra attractive*" (O) to "*supra repulsive*" (IX). The full list of interactions together with the corresponding ε and σ values is provided in Table 3.2.

Table 3.2: Levels of interactions and corresponding ε and σ values in the MARTINI force field. It must be noted that for ring-ring interactions (i.e. interactions between S-type beads) the value of ε is reduced to 75 % of the standard values while σ is set to 0.43 nm.

Level	ε (kJ mol^{-1})	σ (nm)
O - *supra attractive*	5.6	0.47
I - *attractive*	5.0	0.47
II - *almost attractive*	4.5	0.47
III - *semi attractive*	4.0	0.47
IV - *intermediate*	3.5	0.47
V - *almost intermediate*	3.1	0.47
VI - *semi repulsive*	2.7	0.47
VII - *almost repulsive*	2.3	0.47
VIII - *repulsive*	2.0	0.47
IX - *supra repulsive*	2.0	0.62

As already discussed in the previous section, smaller beads are necessary to reproduce the geometry of molecules containing rings. For this purpose, only for the interactions between S-type beads, the value of ε is reduced to 75 % of the standard values while σ is set to 0.43 nm. It was also discussed the need to add AF to avoid unwanted freezing. These AF particles are effectively standard water beads for all interactions, with the sole exception of the P_4-BP_4 interaction (interaction between standard CG water and antifreeze) for which a larger σ (0.57 instead of 0.47 nm) and a higher ε (5.6 kJ mol^{-1} instead of 5.0 kJ mol^{-1}) are used. Finally, as shown in Table 3.2, a larger σ (0.62 nm) is also required for the level IX of interaction. This is done so that charged particles keep their hydration shell when interacting with hydrophobic beads.

BONDED INTERACTIONS Bonded interactions are parametrised by matching structural distributions, such as bond or angle distributions, obtained from atom-

istic simulations. Similarly to atomistic force fields, harmonic functions are used to represent both bond (Equation (3.38)) and angle (Equation (3.39)) potentials:

$$U_{bond}(R) = \frac{1}{2} K_{bond}(R - R_{bond})^2, \tag{3.38}$$

with the equilibrium distance R_{bond} equal to 0.47 nm and the force constant K_{bond} equal to 1250 kJ mol^{-1} nm^{-2}. And:

$$U_{angle}(\Theta) = \frac{1}{2} K_{angle}\Big[\cos(\Theta) - \cos(\Theta_0)\Big]^2, \tag{3.39}$$

with the angle force constant K_{angle} equal to 25 kJ mol^{-1} and the equilibrium bond angle Θ_0 equal to 180°.

LIMITATIONS OF THE MARTINI FORCE FIELD Despite the wide applicability of the MARTINI force field, there are some intrinsic limitations of the model that should be considered. The first one is given by limited resolution imposed by the four-to-one mapping procedure, which could result in difficulties in reproducing some structural features. Furthermore, CG mapping in the MARTINI spirit is not always unambiguous. This means that a specific molecule can be represented using different types of beads but also, in some cases, a different number of beads, leading to a certain degree of uncertainty. Another important limitation is related to the difficulty in interpreting the time scale of CG simulations. The kinetics of CG systems are a lot faster in comparison to atomistic simulations, however it is difficult to estimate a general speed-up factor that can be used to calculate the realistic time. It is suggested that an average scaling factor of four should be used, however it is also noted that the effective speed-up is strictly dependent on the type of molecules [125], possibly implying that a specific calibration is necessary for each system investigated. Finally, one last thing to consider is that, because the parametrisation is based on free energies and the degrees of freedom are reduced in comparison to atomistic simulations, there is an entropy loss, compensated by an enthalpy loss, which implies that the temperature dependence of thermodynamic properties may not be not accurate.

The MARTINI force field has been employed in this work to study the synthesis of HMS [9] materials (Chapter 4) and to complement atomistic simulations in the investigation of the mechanism of formation of MSU-V materials (Chapter 5).

4

UNDERSTANDING THE SYNTHESIS OF HMS MATERIALS

As discussed in section 2.3.2, despite belonging to the same family of MCM-41, HMS materials possess less long-range order and thicker pore walls when compared to their more well studied hexagonal analogues [9]. Tanev and Pinnavaia, who synthesised these materials for the first time, have suggested that the absence of charged interactions between silicates and primary aliphatic amines, which are used to direct their synthesis, is responsible for the lower degree of order and regularity [9]. The templating mechanism proposed is, in fact, based on hydrogen bond interactions between uncharged organic and inorganic species (S^oI^o assembly), which are speculated to arrange into hexagonal mesophases when mixed in solution with water and ethanol. The mild conditions of the synthesis (temperatures ranging between ambient and 80 °C and atmospheric pressure) together with the inexpensive and easily removable templating materials (i.e. through solvent extraction rather than calcination), are key advantages offered by amine-directed synthesis of mesoporous silicas. Furthermore, HMS materials present enhanced catalytic properties as a result of their non-perfect channel packing and textural mesoporosity, which are shown to facilitate access to framework mesopores [126, 127].

Despite the interest generated by HMS materials, only few experimental studies have attempted to elucidate their formation. Among these, Caldararu et al. [128] and Galarneau et al. [129] have used electron paramagnetic resonance (EPR) to investigate the molecular interactions occurring during the different stages of synthesis. They have shown that silicates strongly bind on surfactant micellar aggregates, promoting micelle elongation and formation of "worm-like" frameworks [128, 129]. These results have provided more insight into the formation mechanism of HMS materials but still many questions regarding the nature of the interactions between organic and inorganic species and their effect on the long-range order remain unsolved.

In section 2.4 some examples of computational studies applied to the investigation of material synthesis have been introduced, however, so far, none of them has focussed on HMS materials. Here, results from molecular dynamics (MD) simula-

tions of the precursor solutions for HMS materials are presented. The starting point for these simulations is the work of Tanev and Pinnavaia, which have synthesised HMS by adding TEOS (1.0 mol) to a solution of dodecylamine (DDA; 0.27 mol) in water (29.6 mol) and ethanol (9.09 mol) [9]. As said above, DDA surfactants are expected to form rod like micelles upon addition of TEOS and then evolve into hexagonal mesophases. Unfortunately, the currently accessible computational resources do not allow to access these phases with atomistic (AA) simulations [17]. This limitation can be overcome with coarse-grained (CG) models which, by reducing the computational detail, allow to simulate larger systems on longer time scales. The approach used herein is based on the work of Pérez-Sánchez et al., who developed a CG model for silicates within the MARTINI force field [10, 66] and employed it to successfully demonstrate the cooperative mechanism behind the formation of MCM-41 [7, 17]. In the following, this model is further parametrised to describe the considered HMS system.

4.1 DEVELOPMENT AND VALIDATION OF THE COARSE-GRAINED MODEL

The procedure used by Pérez-Sánchez et al. to establish interaction levels for their CG model consists in comparing density profiles of preformed aggregates of the same size from AA and CG simulations [7]. By tuning interactions at the CG level, the best set of parameters that reproduces AA results can be found. Here, the same methodology is applied to obtain parameters for the precursor solution of HMS materials. This contains DDA surfactants (charged or neutral), counter-ions, as well as silica monomers and oligomers (charged or neutral) in solution with water. Given the high complexity of the system, a trial-and-error approach to parametrise the individual interactions between all considered species simultaneously would be too laborious. Instead, the final set of parameters was obtained in a progressive manner: first, parameters for the systems containing only surfactants and water (reference systems) were obtained. Subsequently, more species were added (monomers, followed by dimers) in such a way that interactions already parametrised could be used at the more complex levels. Therefore, at each stage only a limited number of unknown interactions had to be determined. Another advantage of this procedure is that each step of the model development allows to validate the previously obtained interactions.

A summary of all the simulations performed at atomistic and coarse-grained level can be found in Table 4.1 and Table 4.2, respectively. It should be noted that

Table 4.1: Number of molecules in each atomistic MD simulation of preformed aggregates used to develop parameters of the coarse-grained model. DDA^+, charged surfactant; DDA, neutral surfactant; Cl, chloride ion; SI, anionic silica monomer; SN, neutral silica monomer; SISI, silica dimer with two charges; SISN, silica dimer with one charge and SNSN, neutral silica dimer. The final box size is approximately 8.1 nm in all directions.

System	DDA^+	DDA	Cl	SI	SN	TMA	SISI	SISN	SNSN	water
AA-DDA^+	70		70							16420
AA-DDA^+ + SI	70			70						16420
AA-DDA^+ + SN	70		70		70					16420
AA-DDA^+ + SI + SN	70			70	70					16420
AA-DDA^+ + SISI	70						35			16420
AA-DDA^+ + SISN	70		35					35		16420
AA-DDA^+ + SNSN	70		70						35	16420
AA-DDA		70								16420
AA-DDA + SN		70			70					16420
AA-DDA + SI + TMA		70		70		70				16420
AA-DDA + SN + SI + TMA		70		70	70	70				16420

counter-ions are necessary in order to obtain overall neutrality in the reference system when DDA^+ are used and in the system with anionic silica and DDA surfactants. Chloride (Cl) and tetramethylammonium (TMA) ions are chosen for this purpose. The former are chosen because of the availability of experimental data (e.g. phase diagrams, aggregation numbers, CMC, etc.) for the system dodecylammonium chloride-water, that will be later used to validate the performance of the CG model for charged surfactants (see section 4.1.2). TMA ions, instead, are used because they are not expected to play an important role during the aggregation process [16].

All simulations were performed using the package GROMACS 4.6 [88] and all the images presented were produced using the software VMD [130]. In the following paragraphs, computational details for AA and CG simulations are provided.

COMPUTATIONAL DETAILS FOR AA SIMULATIONS Initial configurations for AA simulations were created by placing in the center of the simulation box a preformed micelle consisting of 70 surfactants (charged or neutral) made using the software Packmol [131]. This number was chosen because it corresponds approx-

Table 4.2: Number of beads in each coarse-grained MD simulations of preformed aggregates used to develop parameters of the coarse-grained model. DDA^+, charged surfactant; DDA, neutral surfactant; Cl, chloride ion; SI, anionic silica monomer; SN, neutral silica monomer; SISI, silica dimer with two charges; SISN, silica dimer with one charge and SNSN, neutral silica dimer.

System	DDA^+	DDA	Cl	SI	SN	TMA	SISI	SISN	SNSN	water
CG-DDA^+	70		70							4000
CG-DDA^+ + SI	70			70						4105
CG-DDA^+ + SN	70		70		70					4000
CG-DDA^+ + SI + SN	70			70	70					4105
CG-DDA^+ + SISI	70						35			4105
CG-DDA^+ + SISN	70		35					35		4053
CG-DDA^+ + SNSN	70		70						35	4000
CG-DDA		70								4105
CG-DDA + SN		70			70					4105
CG-DDA + SI + TMA		70		70		70				4105
CG-DDA + SN + SI + TMA		70		70	70	70				4105

imately to the measured aggregation number for this system at 50 °C (see section 4.1.2). It should be noted that these conditions were selected because the same temperature can also be used to simulate the precursor solution of HMS materials (see section 4.2), i.e. HMS synthesis is reported between ambient temperature to 80 °C, as discussed in section 2.3.2. In the next step, all the other species (silica monomers, dimers and counter-ions) were randomly added to the box and the system solvated with a fixed number of water molecules (see Table 4.1). The original reacting mixture for HMS materials contains also ethanol, however, to reduce the complexity of the simulations this was neglected and replaced by water, as done previously in modelling the synthesis of MCM-41 [6, 16, 65].

For each AA system studied, an energy minimisation step followed by two short equilibration steps (first *NVT* and then *NPT*) were performed. Then, the system was run for production at 323 K in the *NPT* ensemble for at least 10 ns. The temperature was kept constant using the Nosé-Hoover thermostat [95] and the pressure fixed at 1 bar employing the Parrinello-Rahman barostat [97]. The equations of motion were integrated using the leap-frog algorithm [92] with a time step of 2 fs. The simulation boxes were always cubic with periodic boundary conditions applied in x, y and z directions.

Water molecules were modelled using the SPC/E (Extended Simple Point Charge) potential [132], a rigid three-site model widely used in MD simulations. Point

charges are located on both the oxygen (Ow) and the two hydrogens (Hw), whereas only the oxygen atom has Lennard-Jones parameters. The SPC/E model is a re-parametrisation of the classic SPC model to include a polarisation correction term which results in improvement of both density and diffusion constant. DDA surfactants are amphiphilic molecules, which means they contain a hydrophilic head (the amino group) connected to a hydrophobic chain (the tail) made of twelve carbon atoms. As shown in Figure 4.1, DDA molecules exist in the neutral form at high pH (> 12) and become progressively ionised (DDA^+) when the pH is decreased, so that at pH lower than 8 only charged species are found. A representation of the two types of surfactants is provided in Figure 4.2. Label Hn represents hydrogen

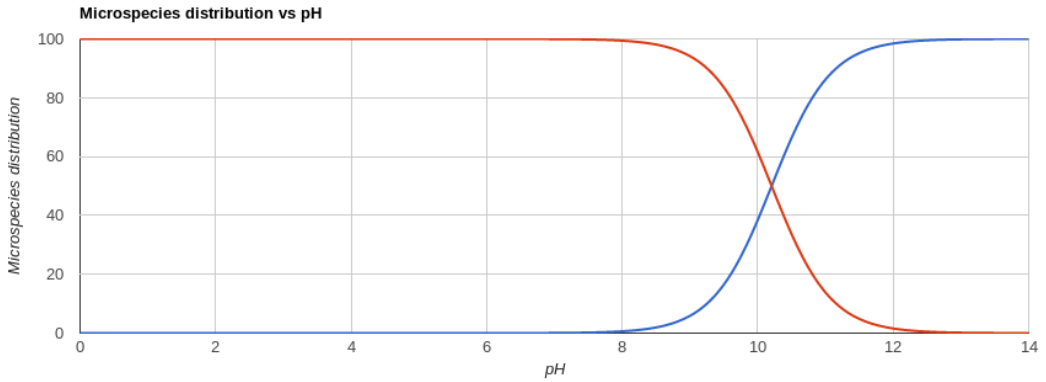

Figure 4.1: pH curve for the system dodecylamine-water produced using chemicalize.org by ChemAxon Ltd [133]. Charged DDA, red and uncharged DDA, blue. pKa = 10.21.

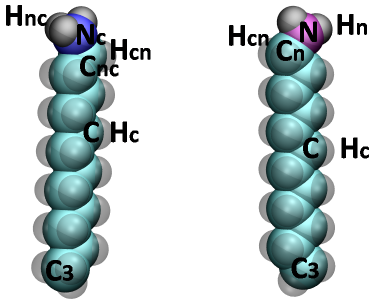

(a) DDA (b) DDA^+

Figure 4.2: All-atom representations of the DDA surfactant in different charge states. Neutral nitogens, purple; charged nitrogens, blue; carbons, cyan and hydrogens, gray.

atoms belonging to amino groups, with N indicating a nitrogen and Cn a carbon bonded to it. The hydrogens on Cn atoms are referred as Hcn while those on carbons C and C3 in the hydrocarbon chain are called Hc. When the amine heads are charged the hydrogen atoms in the amino groups take the name Hnc while the nitrogens are indicated with Nc and the carbons bonded to them Cnc. To describe surfactants and counter-ions, such as bromide and TMA, the OPLS (Optimized Potentials for Liquid Simulations) all-atom force field [80, 81] was used. This was validated against experimental properties, such as liquid density and enthalpy of vaporization, by Caleman et al. [134] for several compounds, among which simple amines. Parameters used for silica monomers and dimers are taken from the work of Jorge et al. [6]. Figure 4.3 shows all the inorganic species considered. The no-

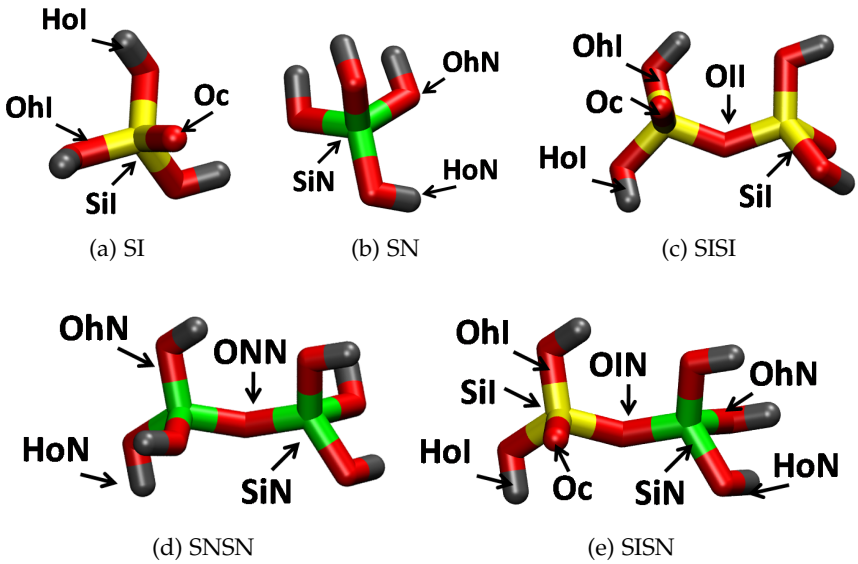

(a) SI (b) SN (c) SISI

(d) SNSN (e) SISN

Figure 4.3: All-atom representations of the different silicate species: SI, anionic monomer; SN, neutral monomer; SISI, dimer with two charges; SNSN, neutral dimer and SISN, dimer with one charge. Neutral silicons, green; charged silicons, yellow; oxygens, red and hydrogens, gray.

menclature for silicates is as follows: SiN and SiI are used for neutral and anionic silicons respectively, OhN and HoN for oxygen and hydrogen atoms belonging to hydroxyl groups in neutral species, while OhI and HoI are used for the corresponding atoms of hydroxyl groups when these are part of anionic species, Oc is a charged oxygen and finally OII, ONN, and OIN represent oxygen atoms linking, respectively, two anionic silicons, two neutral silicons, or one anionic and one neutral silicon. The potential energy function is represented as the sum of angle

bending, dihedral torsion, Lennard-Jones interactions and Coulomb electrostatic terms. Non-bonded interactions are calculated only for atoms that are separated by three or more bonds, while the 1-4 interactions are scaled down by a factor of 0.5. Bond lengths were constrained by applying the LINCS algorithm [135], a cutoff of 1.2 nm was applied to short-range dispersion interactions and the same distance for the particle-mesh Ewald method (PME) [90, 136] to take into account the long-range Coulomb electrostatics. Finally, a long-range dispersion correction term was added to both energy and pressure. Details of the entire set of parameters used can be found in Tables A.1- A.4 of Appendix A.

COMPUTATIONAL DETAILS FOR CG SIMULATIONS The CG systems were created similarly to the atomistic ones by placing a preformed micelle of CG surfactants in the center of a simulation box of approximately 8 nm. In the next step, all other species were added and the system solvated with a pre-equilibrated box of CG water. As discussed in section 3.3.2, a CG Cl ion bead in the MARTINI model includes also its solvation shell (6 water molecules), while one CG water bead corresponds to 4 atomistic water molecules. Therefore the number of CG water beads, in each system was adjusted to match the concentration of the corresponding AA simulation, as shown in Table 4.2. Another thing to consider is that the MARTINI model for water tends to undergo freezing at temperatures higher than expected (around ambient temperature). To avoid this issue it is normally recommended to replace 10 % of the water with antifreeze (AF) particles (BP_4 type beads), as explained in section 3.3.2. With regard to this work, it was decided not to add any antifreeze particles since the temperature used in the simulations (50 °C) is considerably above the freezing temperature of the MARTINI model for water.

Prior to the production runs, the CG systems were energy minimised, followed by a short relaxation step. Production simulations were then performed in the *NPT* ensemble for up to 40 ns by keeping the temperature constant at 323 K using the velocity-rescaling thermostat [137] and the pressure fixed at 1 bar using the Parrinello-Rahman barostat [97]. The equations of motion were integrated using the the leap-frog algorithm [92] with a time step of 40 fs, and cubic periodic boundary conditions were applied in all directions. The CG models tested will be discussed in detail in section 4.1.2.

Trajectories were analysed using an adaptation of the Hoshen-Kopelman cluster-counting algorithm [138]. For this purpose, two surfactant molecules were considered part of the same cluster if at the atomistic level the distance between the

last four atoms (one carbon and three hydrogens), or at coarse-grained level the distance between the last tail beads, was less than 0.75 nm. This value was chosen since it is close to the position of the first minimum in the respective RDFs. The equation used to compute the number-average cluster size for clusters larger than 4 molecules is:

$$< CN_N >_4 = \frac{\sum_{n=4}^{\infty} n[M_n]}{\sum_{n=4}^{\infty} [M_n]}, \tag{4.1}$$

where n indicates the size of the clusters and $[M_n]$ the concentration of clusters with n molecules. The cluster-counting algorithm allowed to calculate AA and CG average density profiles, measured from the micelle centre of mass (COM), which will be presented and discussed in section 4.1.1 and section 4.1.2.

4.1.1 *Atomistic simulations*

In the following, results from AA simulations of preformed micelles in the reference, monomeric and dimer systems are discussed. For each system considered, the final snapshot obtained and the average micelle density profile are presented. It must be noted that the density profiles are calculated considering that the surfactant head consists only of the ammonium group (i.e. one nitrogen and three hydrogens) in the case of charged surfactants, or of the amine group (i.e. one nitrogen and two hydrogens) in the case of neutral surfactants, while the tail contains the entire hydrophobic part of the surfactant (i.e. 12 carbons and 25 hydrogens).

THE REFERENCE SYSTEM Based on the speciation of dodecylamine surfactants (see Figure 4.1), two cases are considered for the reference system:

- high pH (> 12), containing only neutral DDA and water;
- pH < 8, containing charged DDA^+ and chloride counter-ions in water.

Figure 4.4 shows the final configurations ((a) and (c)) and the average micelle density profiles ((b) and (d)) obtained. Comparison of the density profiles obtained for the two systems shows that the neutral heads are more shifted towards the core of the micelle than the charged heads. Furthermore, water molecules are present inside the core of the micelle when neutral surfactants are used. This is not a surprising result since DDA surfactants are not supposed to form micelles at these

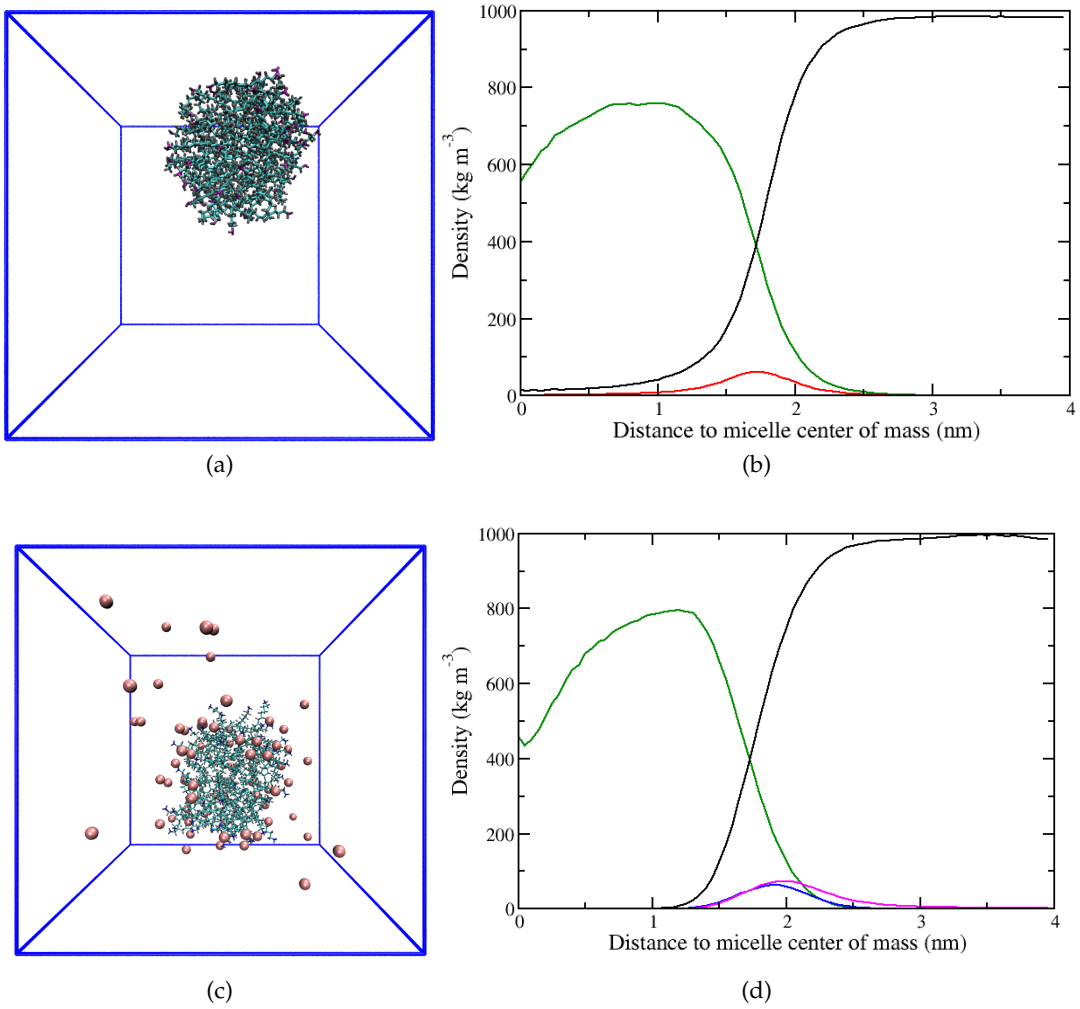

Figure 4.4: Snapshots of the final configurations obtained for a preformed micelle of DDA (a) and DDA^+ with chloride counter-ions in water (c). Corresponding average micelle density profiles ((b) and (d)). Colour code for the snapshots is: neutral nitrogens, purple; charged nitrogens, blue; oxygens, red; hydrogens gray; carbon, cyan and chloride, pink; water has been removed for clarity. Colour code for the density profile is: neutral surfactant heads, red; charged surfactant heads, blue; surfactant tails, dark green; chloride ions, pink and water, black.

high pH conditions. It is important to consider, in fact, that the neutral form of DDA is not soluble in water [139] and cosolvents like ethanol are normally used to improve dissolution. Therefore, the shape and size of the micellar aggregate observed here are likely to change if the system is simulated for longer. Nevertheless, the density profiles obtained can be used to develop CG models, according to the procedure described earlier, as long as the comparison with CG results is done over a period during which the aggregate remains stable.

With regard to the charged system, another thing to notice is that chloride ions adsorb very close to the surfactant head (Figure 4.4-(d)). This close arrangement of counter-ions around the micelle surface has been reported also for the system CTAB-water [17]. Bromide and chloride ions have different sizes in solution [140] as well as a different number of bounded water molecules (more for bromide than for chloride) [141]. For these reasons, bromide ions are expected to bind more closely to the micelle surface in comparison to chloride ions. Interestingly, this behaviour was not observed when comparing the present system with the system containing CTAB surfactants, suggesting that the nature of the surfactant head plays a major role in these systems and, particularly, that the small head of DDA surfactants allows counter-ions to arrange close to the micelle head, even when large ions are used.

SYSTEM WITH MONOMERS Results obtained by adding silica monomers (both anionic and neutral) to preformed micelles of surfactants in water are presented here. Six systems have been considered in total, three with neutral surfactants:

- DDA and neutral silica in water;
- DDA, anionic silica and TMA in water;
- DDA with anionic and neutral silica, TMA and water;

and three with charged surfactants:

- DDA^+ and anionic silica in water;
- DDA^+, neutral silica and chloride ions in water;
- DDA^+ with anionic and neutral silica in water.

Figure 4.5 shows the final configurations ((a) and (c)) and the density profiles ((b) and (d)) when neutral silica monomers (SN) are added to preformed micelles of

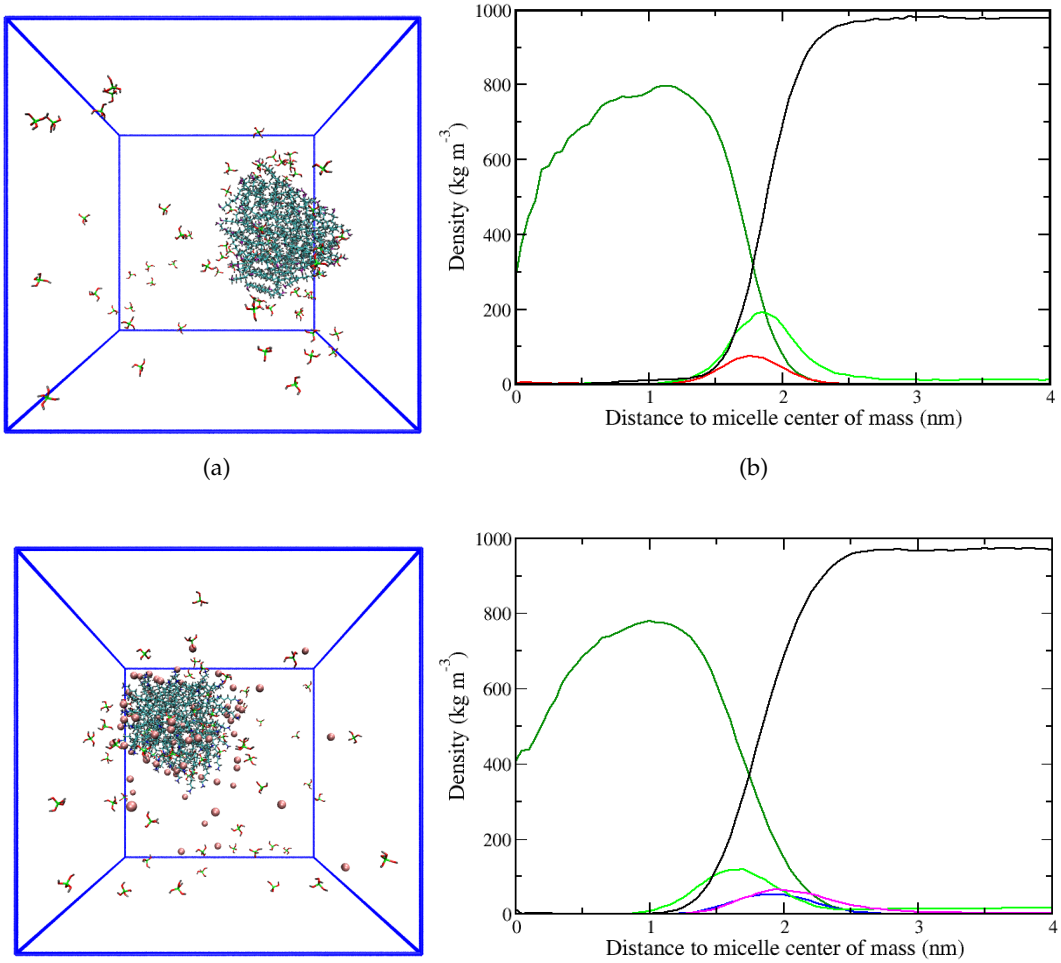

Figure 4.5: Snapshots of the final configurations obtained for a preformed micelle of DDA with SN (a) and for DDA^+ with SN and chloride ions in water (c). Corresponding average micelle density profiles ((b) and (d)). Colour code for the snapshots is: neutral nitrogens, purple; charged nitrogens blue; oxygen, red; hydrogens, gray; carbons, cyan; chloride ions, pink and neutral silicons, green; water has been removed for clarity. Colour code for the density profile is: neutral surfactant heads, red; charged surfactant heads, blue; surfactant tails, dark green; chloride ions, pink; neutral silica monomers, green and water black.

DDA and DDA^+ respectively. Comparing the density profiles shows quite different behaviour for the two systems. The SN monomer seems to adsorb quite close to the surfactant head when this is neutral, while for charged surfactants it tends to adsorb inside the micelle. To better understand the interactions occurring in the neutral system, formation of hydrogen bonds was assessed using the utility *g_hbond*. Indeed, hydrogen bonds are formed between neutral silica monomers and the neutral surfactant heads. However, calculation of the donor-acceptor distribution distances indicates that this interaction is quite weak compared to the other hydrogen bond interactions taking place in the system (see Figure 4.6). As described by

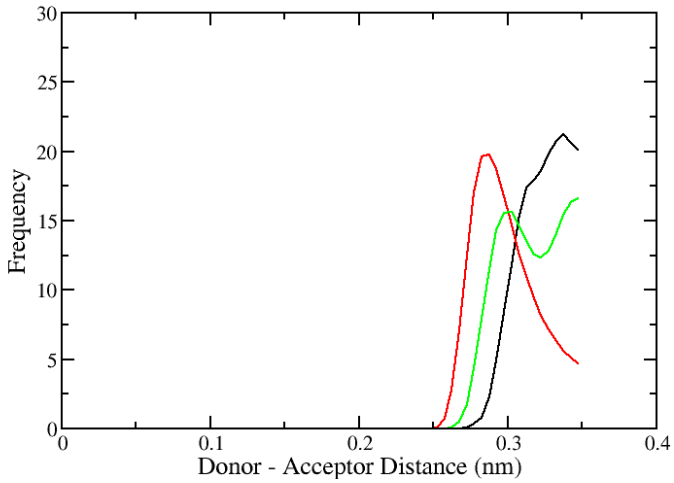

Figure 4.6: Distributions of donor-acceptor distances for the system containing a preformed micelle of DDA with SN monomer. Black, between surfactant heads and SN monomers; red, between surfactant heads and water; green, between SN monomers and water.

Jeffrey, hydrogen bonds can be classified according to their donor-acceptor distance into "strong, mostly covalent" (between 0.22 and 0.25 nm), "moderate, mostly electrostatic" (between 0.25 and 0.32 nm) and "weak, electrostatic" (between 0.32 and 0.4 nm) [142]. Figure 4.6 shows that the donor-acceptor distance for the hydrogen bonds formed between surfactant heads and SN monomers (black line) is in the range of weak electrostatic interactions, whereas the hydrogen bonds formed by water with surfactant heads and SN monomers (red and green lines, respectively) correspond to moderate electrostatic interactions. As such, the affinity observed between SN and surfactants micelles is most likely due to hydrophobic interactions than to hydrogen bond formation in these systems.

The results obtained when anionic silica (SI) monomers are added are shown in Figure 4.7. Also in this case the two systems produce quite different results: in the neutral system most of the monomers are in the bulk together with TMA counterions; conversely, in the charged system, due to charge-matching interactions, SI monomers adsorb at the micelle interface and only few monomers remain in the bulk, as can be seen from the final snapshot in Figure 4.7-(c).

When an equal number of SN and SI monomers is added to a preformed micelle of neutral surfactants, similarly to the previously discussed systems, neutral silica monomers adsorb at the micelle interface while anionic ones remain in the bulk, as shown in Figure 4.8-(b). Interestingly when charged surfactants are considered, it seems that the presence of anionic monomers adsorbed on the surfactant heads causes more neutral monomers to move from the bulk to the micelle interface, in comparison to the first discussed case (cf. panels (c) and (d) for Figure 4.5 and Figure 4.8).

SYSTEM WITH DIMERS Lastly, the results obtained adding silica dimers are discussed. Three systems are considered:

- doubly charged dimers (SISI) and DDA^+ in water;
- singly charged dimers (SISN) and DDA^+ in water;
- neutral dimers (SNSN) and DDA^+ in water.

Figure 4.9 shows the final configurations and the average micelle density profile obtained. It can be noticed that SISI dimers, like SI monomers, adsorb at the micelle interface whereas SISN and SNSN dimers tend to adsorb closer to the micelle core.

In the following, the AA density profiles described so far are used for the development of the CG models.

4.1.2 *Coarse-grained simulations*

Herein, the development of the CG model, which will be used then for production runs of large systems in section 4.2, is discussed. The systems investigated are presented in the same order that was used to develop the interaction parameter matrix (Table 4.2), i.e. minimising the number of unknown interactions at each stage of the parametrisation. It should be noted that the standard mass of a MARTINI bead is 72 a.u.; however, for the purpose of the density profile calculation, real

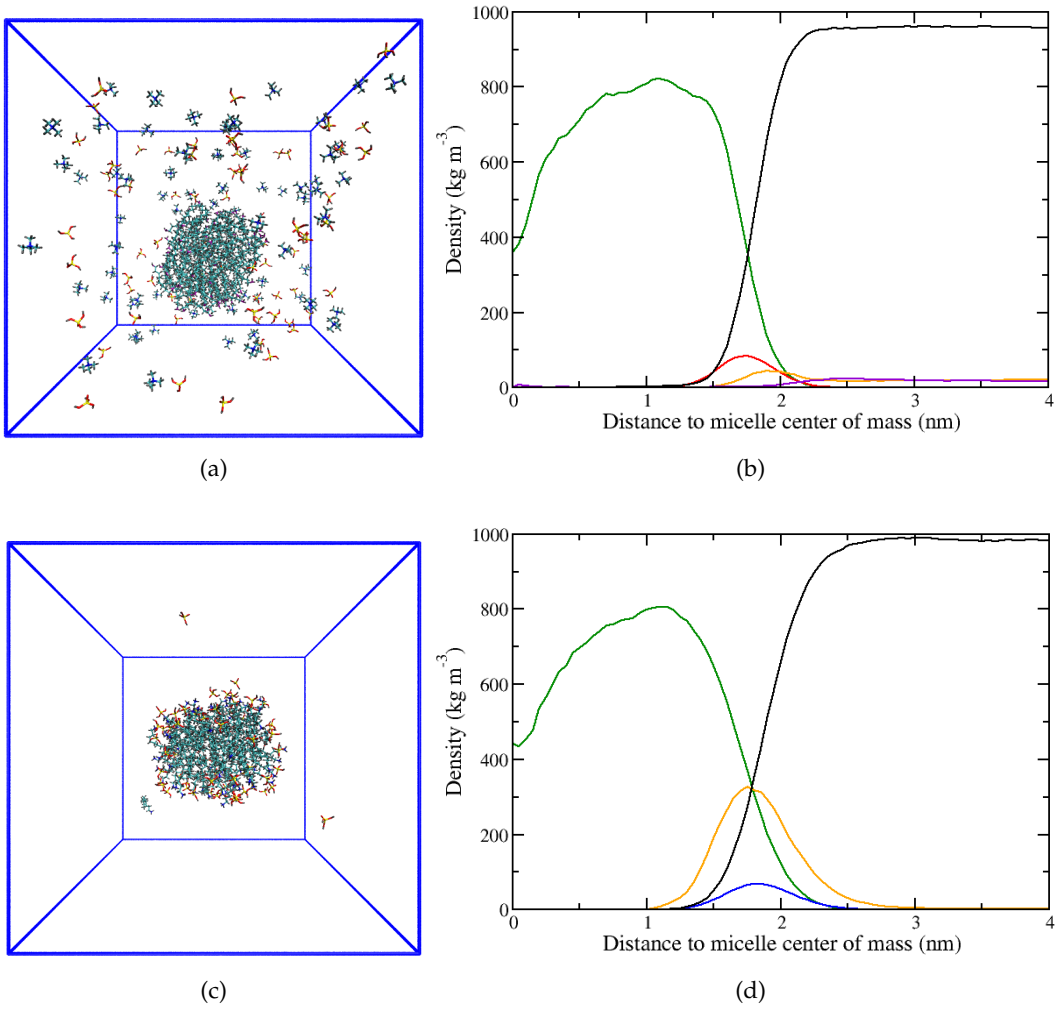

Figure 4.7: Snapshots of the final configurations obtained for a preformed micelle of DDA with SI and TMA (a) and for DDA^+ with SI in water (c). Corresponding average micelle density profiles ((b) and (d)). Colour code for the snapshots is: neutral nitrogens, purple; charged nitrogens, blue; oxygens, red; hydrogens, gray; carbons, cyan and anionic silicons, yellow; water has been removed for clarity. Colour code for the density profile is: neutral surfactant heads, red; charged surfactant heads, blue; surfactant tails, dark green; TMA ions, purple; anionic silica monomers, yellow and water, black.

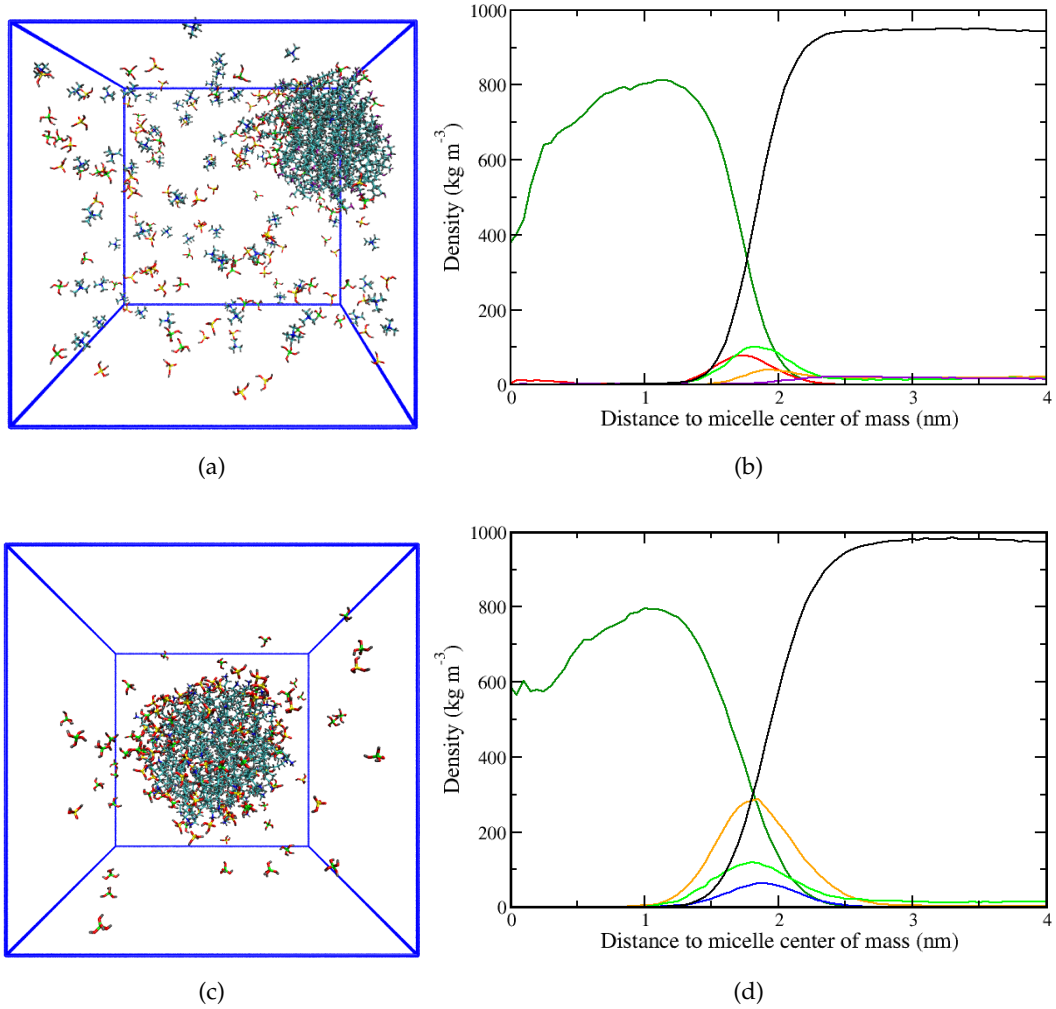

Figure 4.8: Snapshots of the final configurations obtained for a preformed micelle of DDA with SN, SI and TMA (a) and for DDA^+ with SN and SI in water (c). Corresponding average micelle density profiles ((b) and (d)). Colour code for the snapshots is: neutral nitrogens, purple; charged nitrogens blue; oxygens red; hydrogens, gray; carbons, cyan; neutral silicons, green and anionic silicons, yellow; water has been removed for clarity. Colour code for the density profile is: neutral surfactant heads, red; charged surfactant heads, blue; surfactant tails, dark green; TMA ions, purple; neutral silica monomers, green; anionic silica monomers, yellow and water, black.

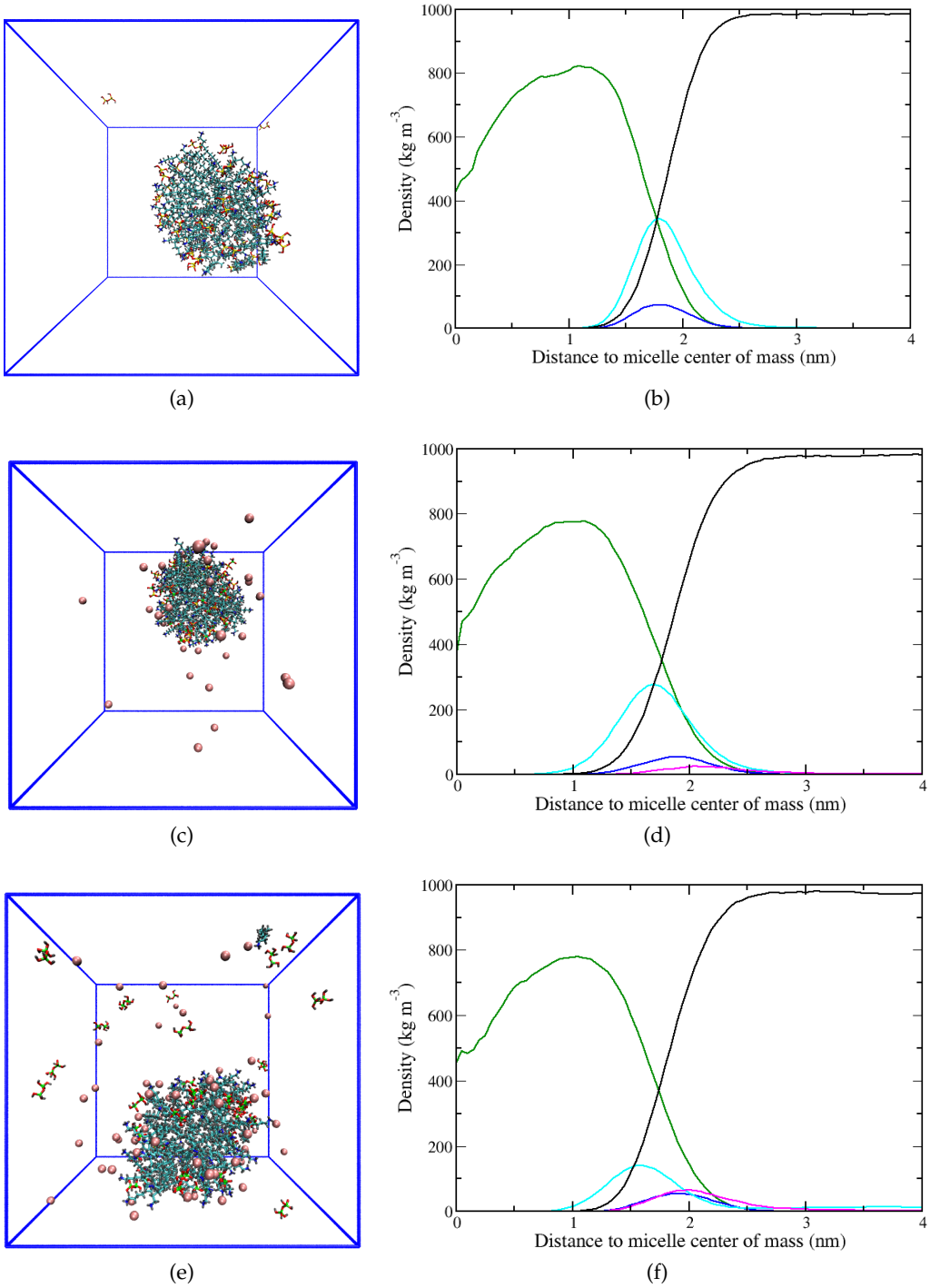

Figure 4.9: Snapshots of the final configurations obtained for a preformed micelle of DDA^+ with SISI (a), SISN (c) and SNSN dimers (e). Corresponding average micelle density profiles ((b), (d) and (f)). Colour code for the snapshot is: charged nitrogens blue; oxygens, red; hydrogens, gray; carbons, cyan; chloride ions, pink; neutral silicons, green and anionic silicons, yellow; water has been removed for clarity. Colour code for the density profile is: charged surfactant heads, blue; surfactant tails, dark green; chloride ions, pink; dimers, cyan and water, black.

masses were attributed to each bead to match the corresponding atomistic group (i.e. head, tail, monomer, dimers, etc.). For example the mass of the bead representing the charged head is approximately 17 a.u. (i.e. the mass of one nitrogen and three hydrogens), while the mass of the SN bead is approximately 96 a.u. (i.e. the mass of one silicon atom, four oxygens and four hydrogens), etc.

INFLUENCE OF DIFFERENT HEAD BEADS FOR CHARGED SURFACTANTS One of the first things to decide when developing a CG model is the mapping scheme, i.e. fixing how many atoms are represented by each CG bead. According to the MARTINI protocol, on average four heavy atoms should be represented with one CG site [10]. This approach means that for some molecules the mapping is not univocal and other factors (like for example molecule symmetry) have to be taken into account in order to find the most appropriate representation. Figure 4.10 displays a schematic representation of the mapping scheme adopted for each species considered. With regards to the charged surfactants, the conventional mapping strategy suggests to use a Q_d bead for the head (the positively charged NH_3 group plus three adjacent CH_2 groups) and three C_2 beads for the tail, with each C_2 representing three carbon atoms and the associated hydrogens (Figure 4.10-(a)). Here the effect of using different bead types for the head group (Q_d, Q_o or Q_{da}) will be explored, by comparing how well atomistic micelle density profiles are reproduced by each of the mapping schemes adopted. The other species present are solvated chloride counter-ions, which are mapped with one Q_a bead (Figure 4.10-(c)), and P_4 water beads (Figure 4.10-(e)). The full list of interactions considered is displayed in Table 4.3. It should be noted that for this test standard MARTINI values are used for bonds and angles parameters.

Figure 4.11 shows the micelle density profiles obtained using the different mapping schemes described above. The agreement with AA simulations seems to be slightly improved when Q_d or Q_{da} beads are used (see Figure 4.11-(a), (b), (e) and (f)), however none of the head types considered produced a perfect match. The lower magnitude of the CG peaks and larger spread in the distribution of head groups suggests that coarse-grained micelles are more disordered than atomistic micelles. This behaviour is confirmed by looking at the snapshot in Figure 4.12. Here, the final configuration obtained when using the chosen bead type for the surfactant head, Q_d, is displayed; final configurations obtained with other head types produced qualitatively similar results.

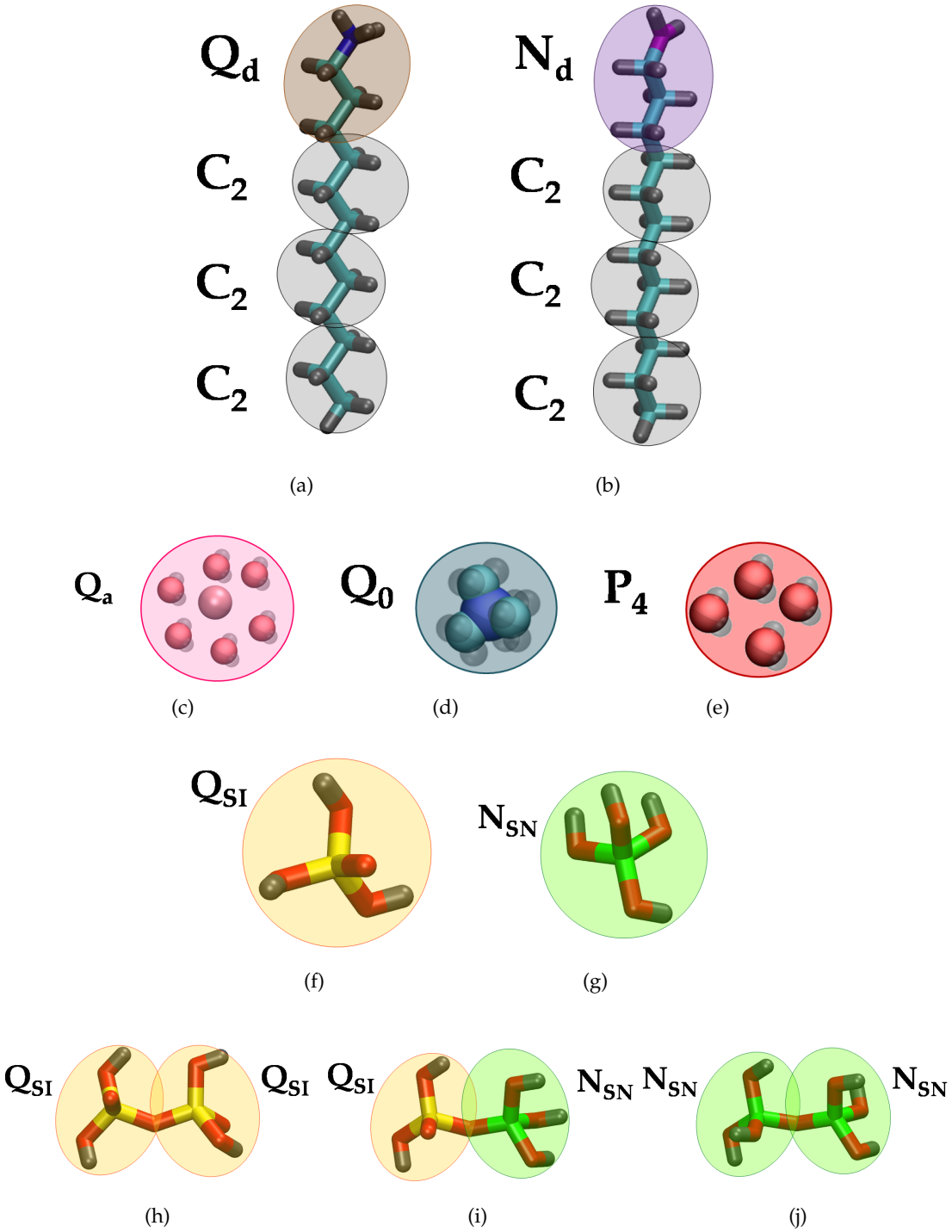

Figure 4.10: Schematic representation of the CG mapping schemes adopted in this work. DDA surfactant, (a); DDA^+ surfactant, (b); solvated chloride counter-ions, (c); TMA counter-ions, (d); water, (e); anionic silica monomer, (f); neutral silica monomer, (g); doubly deprotonated dimer, (h); singly deprotonated dimer, (i) and neutral dimer, (j).

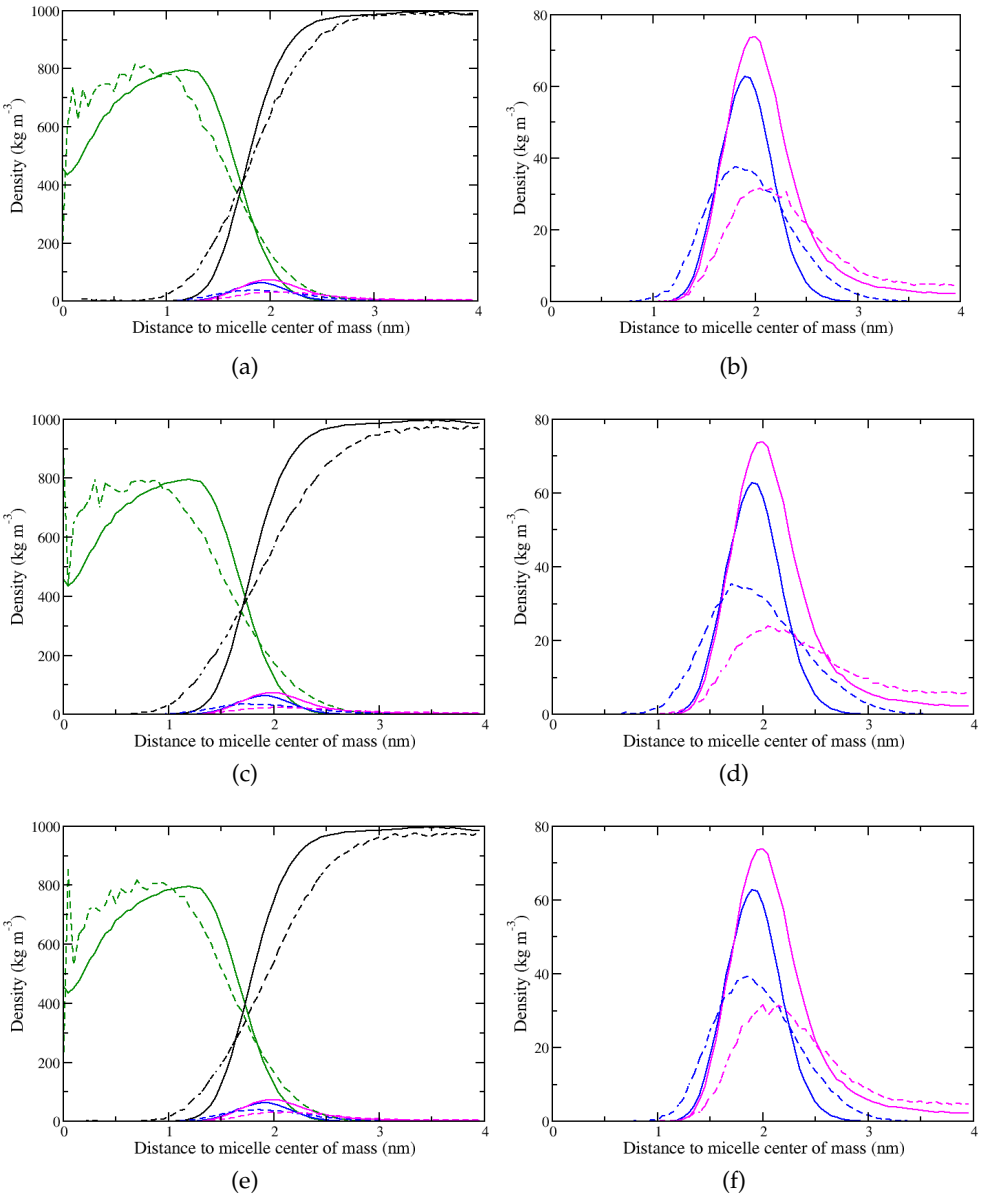

Figure 4.11: Comparison between atomistic (solid lines) and coarse-grained (dashed lines) average micelle density profiles obtained for the reference system with DDA^+ surfactants. Different standard MARTINI beads types are used for the head group: (a)-(b), Q_d; (c)-(d), Q_o and (e)-(f), Q_{da}. Tails, dark green; charged heads, blue; chloride ions, pink and water, black.

Table 4.3: Matrix of interaction for standard MARTINI beads considered to test the influence of the head type for charged surfactants [10, 66]. For more details about bead types and description of interaction levels see section 3.3.2.

	Q_{da}	Q_d	Q_a	Q_o	P_4	C_2
Q_{da}	O	O	O	II	O	IX
Q_d	O	I	O	II	O	IX
Q_a	O	O	I	II	O	IX
Q_o	II	II	II	IV	O	IX
P_4	O	O	O	O	I	VII
C_2	IX	IX	IX	IX	VII	IV

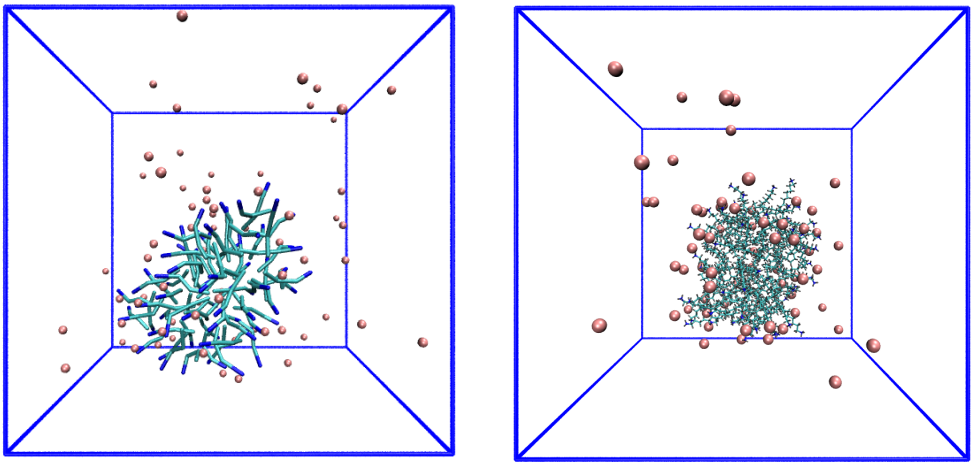

(a) (b)

Figure 4.12: Snapshots comparing the final configurations obtained with coarse-grained (a) and atomistic (b) simulations for the reference system with DDA^+ surfactants. Standard MARTINI parameters ($f = 25\ kJ\,mol^{-1}$ and $b = 0.47$ nm) and Q_d bead type are employed. Colour code for the CG snapshot is: DDA^+ heads, blue; DDA^+ tails, cyan and chloride counter-ions, pink. Colour code for the AA snapshot is the same as in Figure 4.4-(c).

To try to improve agreement with AA simulations, force field parameters, such as bond length or angle force constants, can be modified. Reducing the bond length, for example, should improve the position of the chloride peak, shifting it to the left, while increasing the angle force constant should make CG surfactants more rigid. The effect of altering these two parameters is discussed below.

INFLUENCE OF ANGLE FORCE CONSTANT FOR CHARGED SURFACTANTS The standard values for bond length (b) and angle force constant (f) in the MARTINI force field are 0.47 nm and 25 kJ mol^{-1} respectively. Figure 4.13-(c) and (d) show the average density profiles obtained when a higher angle force constant (50 kJ mol^{-1}) is used. Increasing the angle force constants improves agreement with AA results,

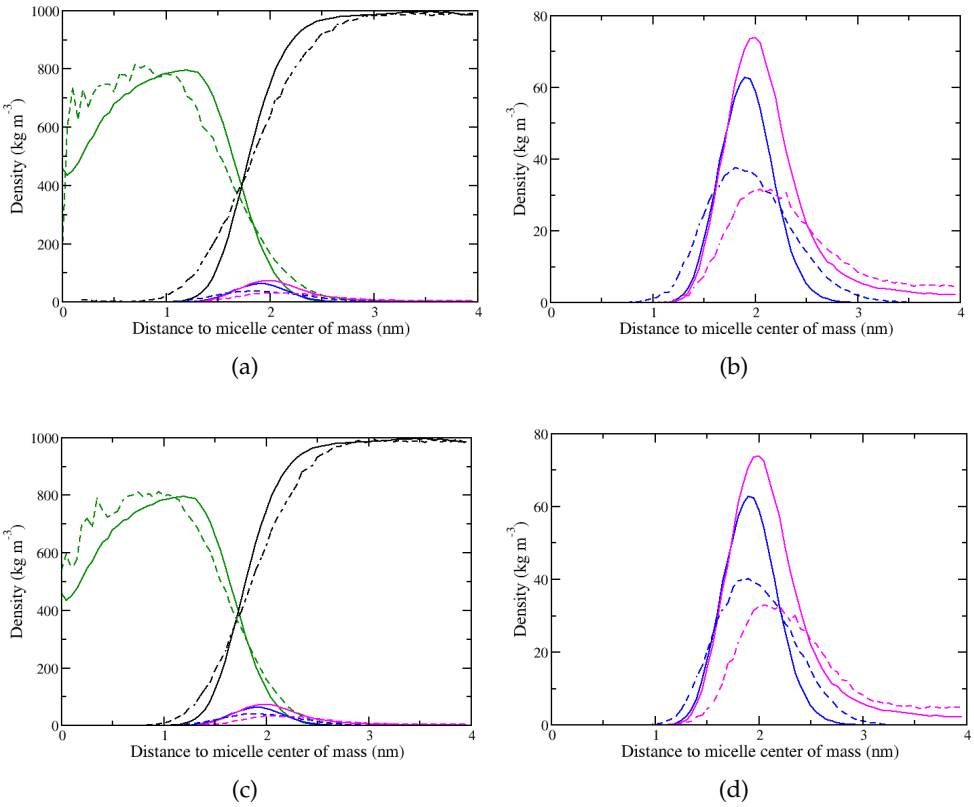

Figure 4.13: Comparison between atomistic (solid lines) and coarse-grained (dashed lines) average micelle density profiles obtained for the reference system with DDA^+ surfactants. Standard MARTINI bond length (b = 0.47 nm) and different angle force constants are used: (a)-(b), f = 25 kJ mol^{-1} and (c)-(d), f = 50 kJ mol^{-1}. Colour code is the same as in Figure 4.11.

producing narrower surfactant head profile as well as steeper tail and water distributions. Higher values of the angle force constant (up to $f = 500$ kJ mol^{-1}) were also tested producing even better agreement with AA results. However, when these very high angle force constant values were employed to model large systems, unphysical results were obtained, showing freezing at high surfactant concentration due to the extreme rigidity of the model. Therefore, use of angle force constant values above 50 kJ mol^{-1} are not recommended. With regard to the chloride profile, this appears to be identical in the two cases considered (cf. Figure 4.13-(b) and (d)). This poor agreement between AA and CG profiles for chloride counter-ions could be explained by the larger size of the ion at CG level. In fact, by including also a solvation shell, CG chloride ions are not allowed to adsorb as close to the surfactant heads as they do atomistically.

INFLUENCE OF BOND LENGTH FOR CHARGED SURFACTANTS The effect of reducing the bond length from the default value to $b = 0.45$ nm is shown in Figure 4.14, where average density profiles obtained from simulations performed using different angle force constants ((a)-(b), $f = 25$ kJ mol^{-1} and (c)-(d), $f = 50$ kJ mol^{-1}) are compared. Reducing the bond length does not improve the position of the chloride peak. On the contrary, the agreement with the AA head profile seems to be worse, independent of the force constant used: the head distributions appear broader and the position of the peaks are shifted.

This analysis indicates that, for the models considered here, the best agreement between AA and CG micelle density profiles is obtained by mapping the head group of DDA^+ with a Q_d bead. Furthermore, increasing the force constant from 25 to 50 kJ mol^{-1} improves model agreement, whereas no improvement is obtained when the bond length is decreased.

NEUTRAL SURFACTANTS Consistently with the parametrisation chosen for the charged system, DDA surfactants are modelled using the recommended N_d bead for the head group, three C_2 beads for the tail, standard bond length $b = 0.47$ nm and angle force constant $f = 50$ kJ mol^{-1} (Figure 4.10-(b)). The final snapshot obtained is displayed in Figure 4.15-(a) while in Figure 4.16 the average micelle density profile is shown. Both the snapshot and the profile densities show that the neutral micelles are more disordered than charged ones. Some of the head groups are located inside the micelle core (Figure 4.16-(b)) but also some water penetrates inside. As discussed earlier when presenting the AA profiles for this system, neut-

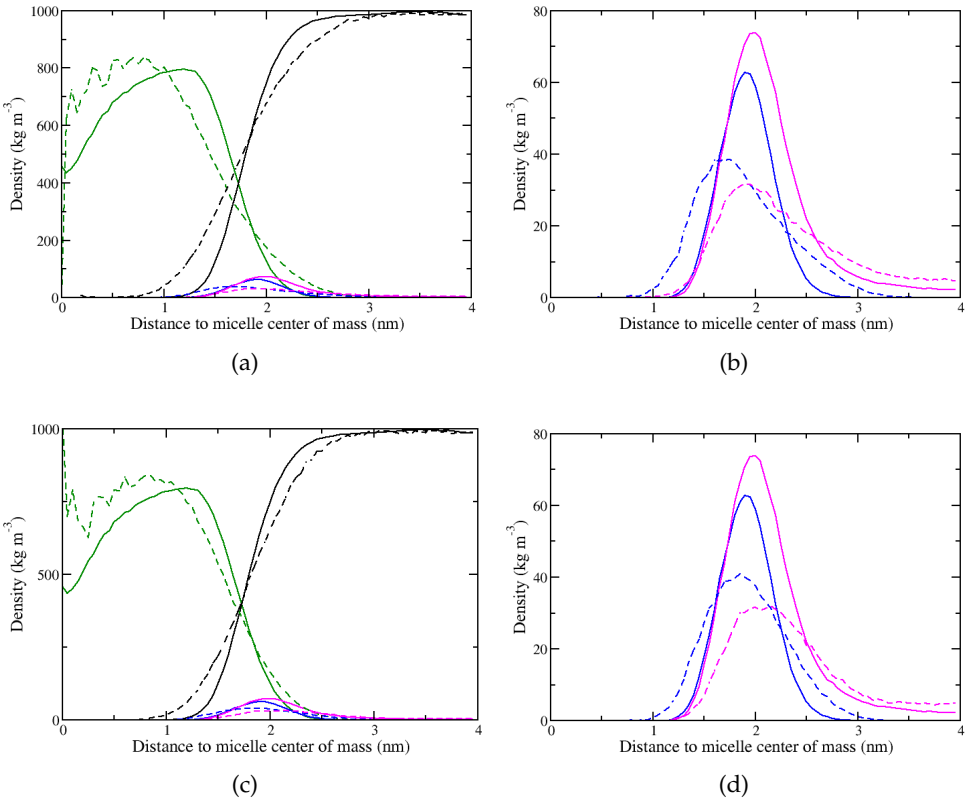

Figure 4.14: Comparison between atomistic (solid lines) and coarse-grained (dashed lines) average micelle density profiles obtained for the reference system with DDA^+ surfactants. A reduced bond length (b = 0.45 nm) and different angle force constants are used: (a)-(b), f = 25 kJ mol^{-1} and (c)-(d), f = 50 kJ mol^{-1}. Colour code is the same as in Figure 4.11.

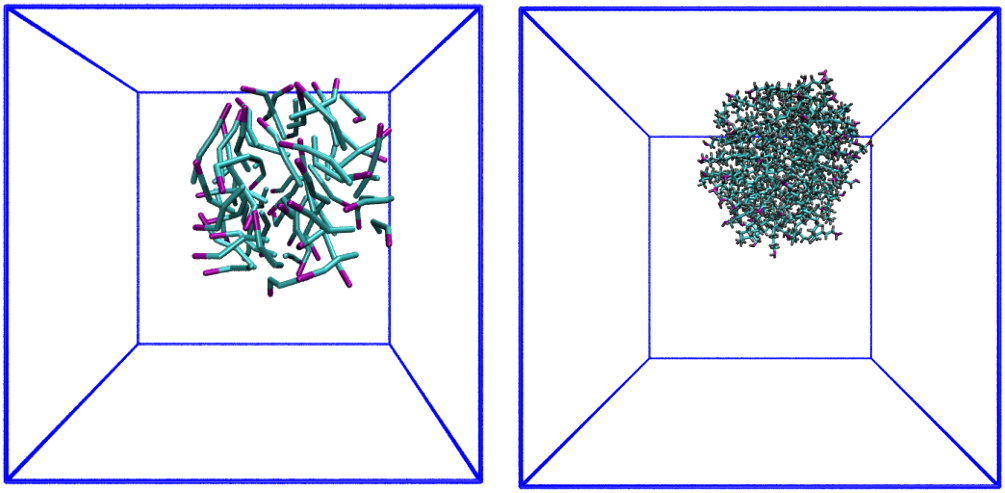

(a) (b)

Figure 4.15: Snapshots comparing the final configurations obtained with coarse-grained (a) and atomistic (b) simulations for the reference system with DDA surfactants. Parameters for the CG model are: $f = 50\ kJ\,mol^{-1}$ and $b = 0.47$ nm. Colour code for the CG snapshot is: DDA heads, purple and DDA tails cyan. Colour code for the AA snapshot is the same as in Figure 4.4-(a).

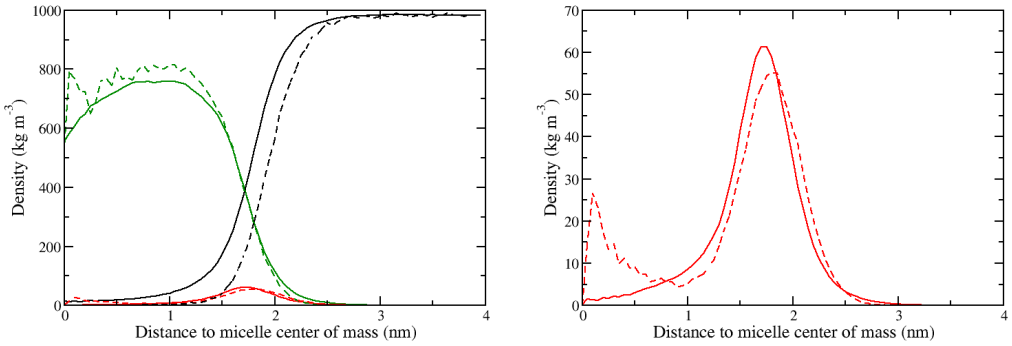

(a) (b)

Figure 4.16: Comparison between atomistic (solid lines) and coarse-grained (dashed lines) average micelle density profiles obtained for the reference system with DDA surfactants, using $b = 0.47$ nm and $f = 50\ kJ\,mol^{-1}$. Tails, dark green; neutral heads, red and water, black.

ral DDA surfactants do not dissolve in pure water [139]. The presence of head groups in the core of the neutral micelle is an indication that, at these conditions, micelles are not the stable aggregation state. Both AA and CG simulations were run for 40 ns and averages were obtained over the entire length of the production run, however, because of the four-to-one mapping used in the MARTINI force field, CG dynamics are expected to be accelerated by a factor of approximately four [10]. Because of these fast dynamics, identifying the exact trajectory length for which AA and CG systems display the same structural behaviour is not trivial. Since the objective here is to find the best CG model to represent this system, focus was placed on matching the peak positions and their relative width. Nevertheless, it can be assumed that for long enough simulation times the two systems (AA and CG) will behave in the same way.

With all the parameters necessary to describe the reference systems established, the next step was to look at systems containing silica monomers and counter-ions. Figure 4.10-(f) and (g) shows the CG mapping procedure adopted for these species as well as for TMA counter-ions Figure 4.10-(d).

DDA$^+$ WITH ANIONIC SILICA The first system investigated was the monomeric solution of charged surfactant and anionic silica monomers (referred as Q_{SI}) in equal ratio. Four interactions in this system were not present in the MARTINI force field:

- Q_{SI}-Q_{SI};
- Q_{SI}-Q_d;
- Q_{SI}-C_2;
- Q_{SI}-P_4;

however the Q_{SI}-Q_{SI} and the Q_{SI}-P_4 interaction levels have been already parametrised by Pérez-Sánchez et al. and shown to produce good results when used to investigate formation of periodic mesoporous silicas (PMS) [7, 17], so they have also been adopted in this work. Furthermore, the interaction Q_{SI}-C_2 was assumed, in agreement with the MARTINI philosophy, to be equal to the Q_{SI}-C_1, which was also established by Pérez-Sánchez et al. [7, 17]. Hence, the only interaction left to parametrise for the considered system is between anionic silica beads and surfactant heads (Q_{SI}-Q_d). Three different levels were tested: i) O (*supra attractive*),

ii) I (*attractive*) and iii) II (*almost attractive*), defined according to Table 3.2 in section 3.3.2. A representative snapshot of the final configuration obtained for the system with Q_{SI}-Q_d = II is show in Figure 4.17-(a). It should be noted that no significant difference was observed in the final configurations obtained for the three parametrisation schemes considered. More information about this system can be

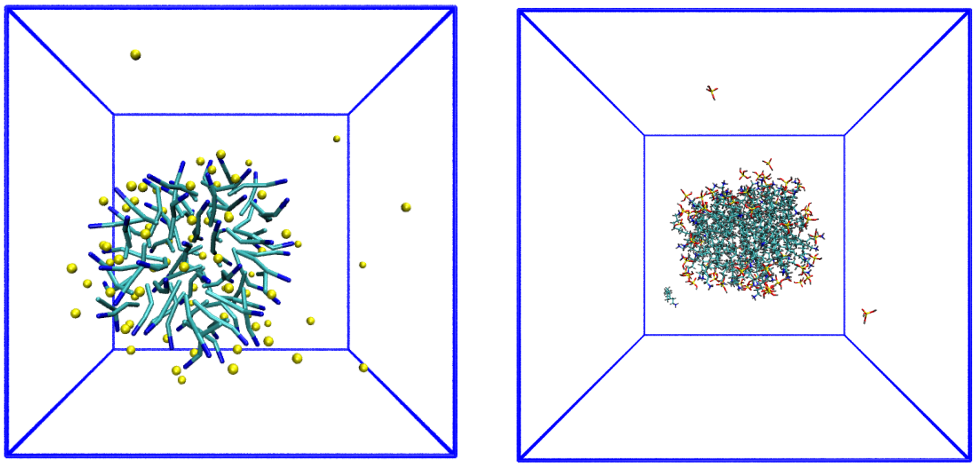

(a) (b)

Figure 4.17: Snapshot comparing the final configurations obtained with coarse-grained (a) and atomistic simulations (b) for the system with anionic silica monomers and DDA^+ surfactants, using Q_{SI}-Q_d = II for the CG model. Colour code for the CG snapshot is the same as in Figure 4.12 with SI in yellow. Colour code for the AA snapshot is the same as in Figure 4.7-(c).

obtained by looking at the average micelle density profiles displayed in Figure 4.18. The behaviour of the three models considered is overall quite similar and the main difference observed is for the SI profile at short distances from the micelle core. Here, for the two most attractive levels of interactions considered, SI peaks are present near the micelle core at CG level, however the AA results show no sign of these peaks (see Figure 4.18-(b) and (d)). For this reason the lower level of interaction (Q_{SI}-Q_d = II) was chosen for the present system. Even lower interaction values were not considered since these are expected to produce broader SI profiles, by reducing too much the attraction between Q_{SI} and Q_d beads and bringing it to close to the strength of the interaction between Q_{SI} and C_2 beads (i.e. IV, *intermediate*).

DDA WITH NEUTRAL SILICA The monomeric solution with DDA surfactants and an equal ratio of neutral silica monomer (referred as N_{SN}) was considered.

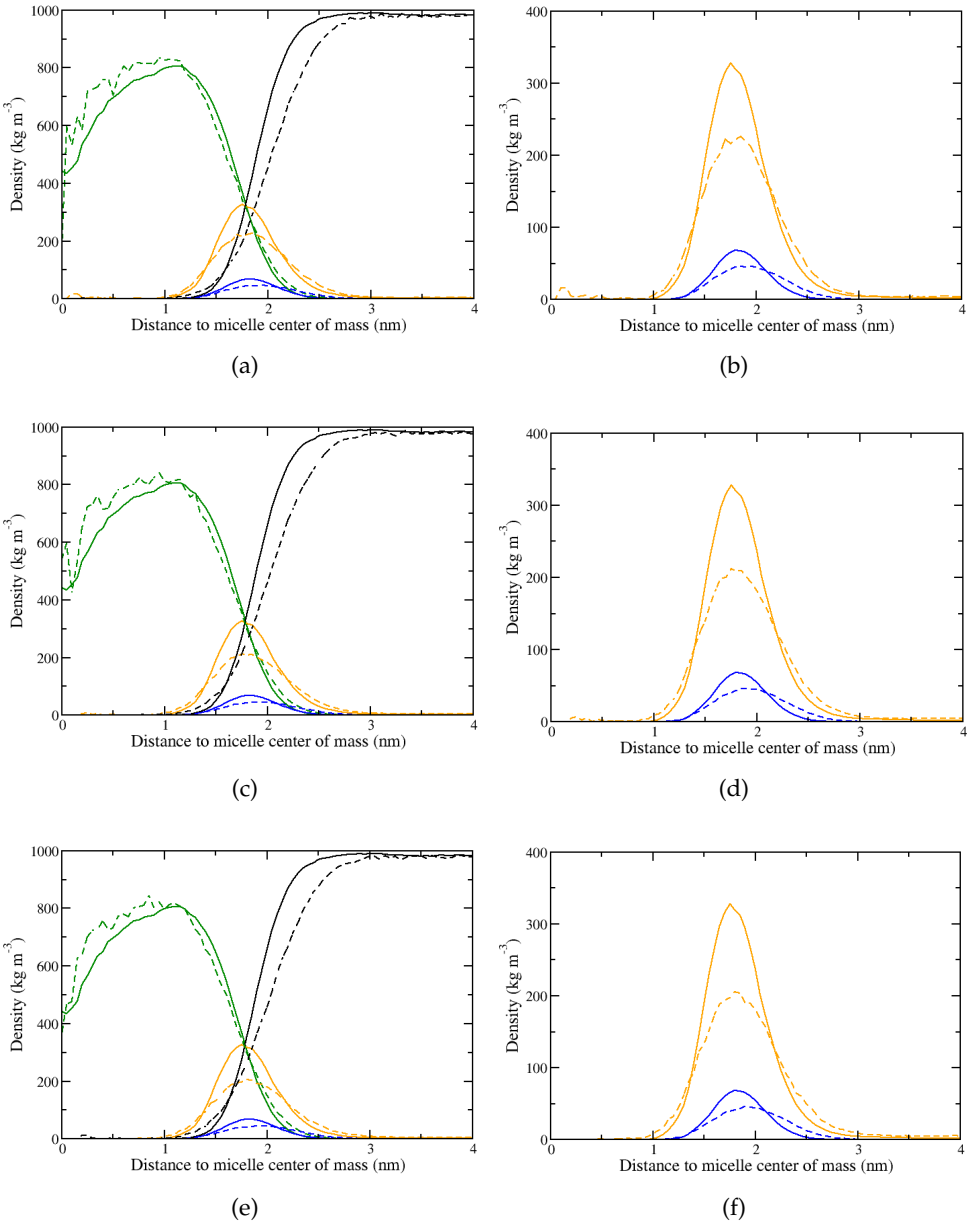

Figure 4.18: Comparison between atomistic (solid lines) and coarse-grained (dashed lines) average micelle density profiles obtained for the system containing DDA^+ surfactants and SI monomers. Different interaction levels are used for Q_{SI}-Q_d: (a)-(b) *supra attractive* (O), (c)-(d) *attractive* (I) and e-f *almost attractive* (II). Tails, dark green; charged heads, blue; anionic silica monomers, yellow and water, black.

Like in the previously discussed case, there are in total four new interactions to establish for this system:

- N_{SN}-N_{SN};
- N_{SN}-N_d;
- N_{SN}-C_2;
- N_{SN}-P_4.

Once again N_{SN}-N_{SN} and N_{SN}-P_4 interactions are taken from the work of Pérez-Sánchez et al. [7, 17] while N_{SN}-C_2 is assumed the same as N_{SN}-C_1 (also determined by Pérez-Sánchez et al. [7, 17]). Hence, the only unknown interaction is N_{SN}-N_d for which three possible values were considered: i) *supra attractive* (O), ii) *attractive* (I) or iii) *almost attractive* (II). Comparison between AA and CG density profiles obtained for the different interaction levels considered is shown in Figure 4.19. As noticed before, neutral micelles are more disordered than charged micelles. Addition of SN monomers to this system does not seem to improve order and only a few silica beads are found to interact with the surfactant heads (see Figure 4.20)-(a). In all profiles shown in Figure 4.19 the peak relative to SN monomers is significantly lower in CG than in AA. Interestingly, head peaks inside the micelle core are observed both at AA and at CG level, possibly suggesting that structural rearrangement is accelerated by the presence of SN monomers. The best agreement is found for the highest level of interaction (N_{SN}-N_d = O), which produced the narrowest distribution for both neutral heads and SN monomers, and was thus chosen for modelling this system.

DDA$^+$ WITH ANIONIC AND NEUTRAL SILICA MONOMERS At this point, it was decided to parametrise the system containing DDA$^+$ surfactants and an equal number of anionic and neutral silica monomers. Considering all the parameters so far established, there are only two unknown interactions for this system:

- Q_{SI}-N_{SN};
- N_{SN}-Q_d.

In Figures 4.21 and 4.22-(a) density profiles and a snapshot of the final configuration obtained are shown. Considering that for both silica monomers the self interaction (Q_{SI}-Q_{SI} and N_{SN}-N_{SN}) is set to *supra attractive*, the same value was

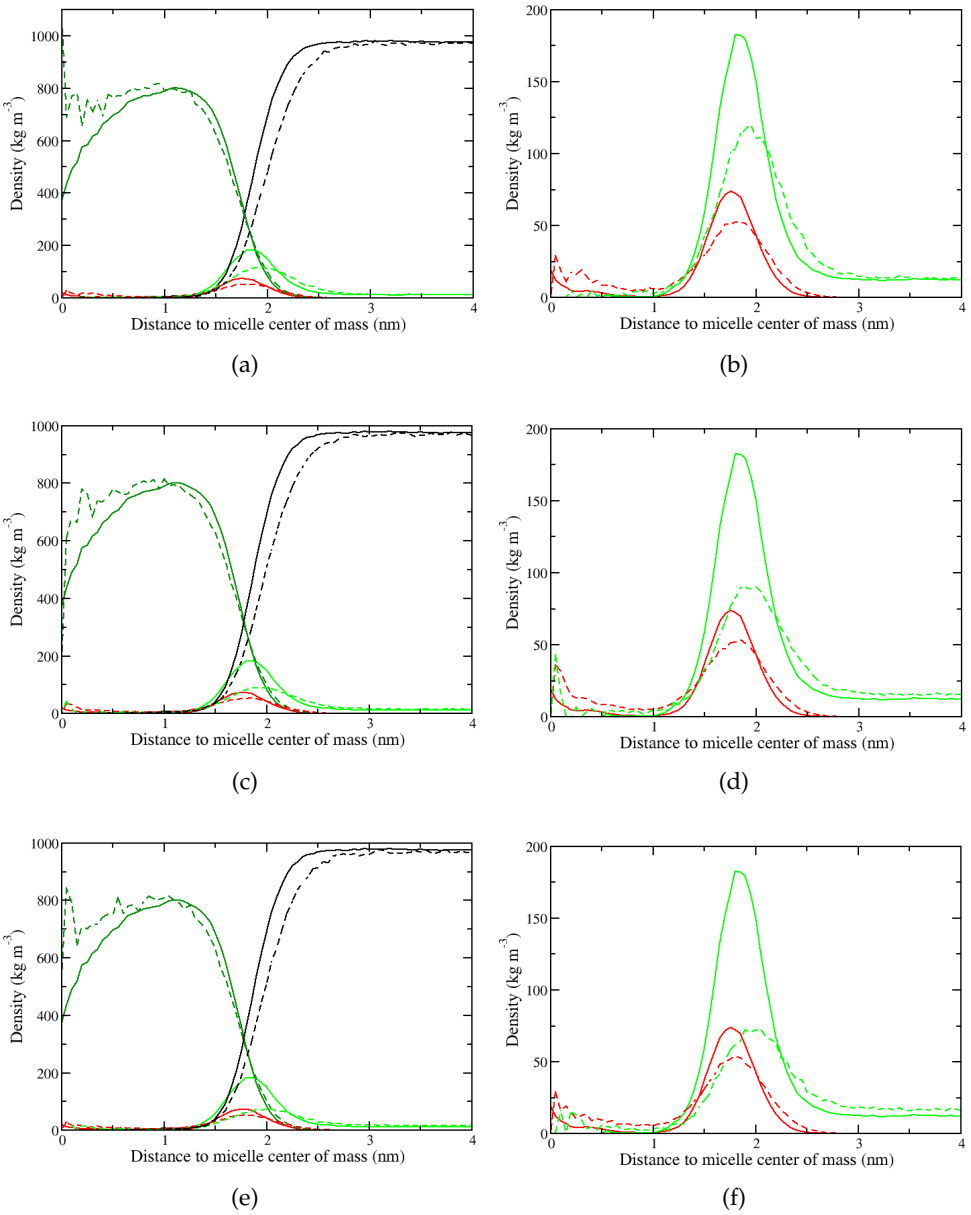

Figure 4.19: Comparison between atomistic (solid lines) and coarse-grained (dashed lines) average micelle density profiles obtained for the system containing DDA surfactants and SN monomers. Different interaction levels are used for N_{SN}-N_d: (a)-(b), *supra attractive* (O); (c)-(d), *attractive* (I) and (e)-(f), *almost attractive* (II). Tails, dark green; neutral heads, red; neutral silica monomers, green and water, black.

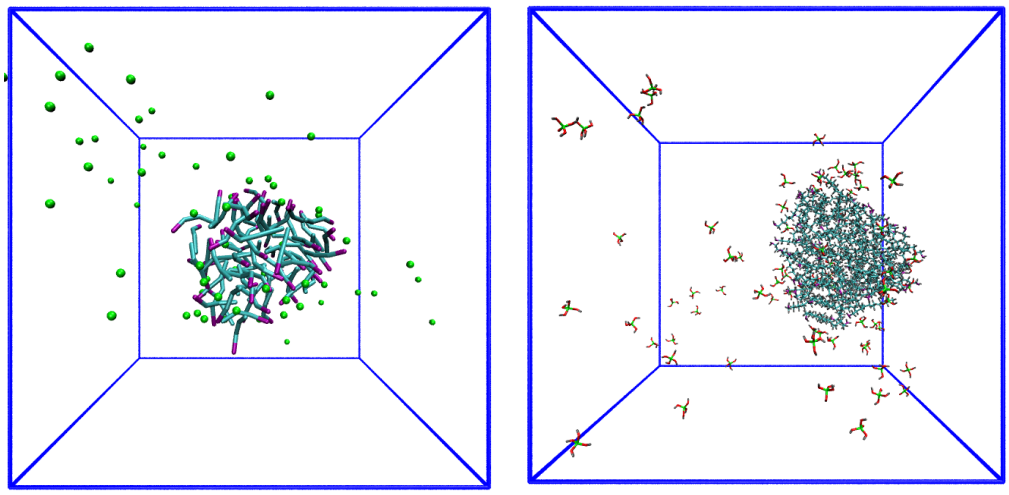

(a) (b)

Figure 4.20: Snapshot comparing the final configurations obtained with coarse-grained (a) and atomistic simulations (b) for the system with neutral silica monomers and DDA surfactants, using N_{SN}-N_d = O for the CG model. Colour code for the CG snapshot is the same as Figure 4.15 with SN in green. Colour code for AA snapshot is the same as Figure 4.5-(a)

also chosen for the monomer cross iteration Q_{SI}-N_{SN}. For the other interaction, two cases were considered: i) N_{SN}-Q_d = O (*supra attractive*) or ii) N_{SN}-Q_d = II (*almost attractive*). Again, the CG profiles do not match exactly the AA results, however some considerations can be made regarding these results. The position of the SI peak is matched quite well for both levels of interaction but the agreement with the SN profile becomes significantly worse for the lower interaction level tested. The SN distribution is already quite broad when N_{SN}-Q_d is *supra attractive*, suggesting that lower interaction strengths would not produce better agreement. Hence, N_{SN}-Q_d = O was chosen to model this system and no further tests (e.g. N_{SN}-Q_d = I) were performed.

DDA$^+$ WITH NEUTRAL SILICA MONOMERS AND CHLORIDE COUNTER-IONS

The next case considered is the system with charged surfactants and neutral silica monomers to which chloride counter-ions are added to neutralise charges. The only undefined interaction for this system is between SN monomers and counter-ions (N_{SN}-Q_a); however this was assumed the same as the interaction between Q_{SI} and Q_a, which Pérez-Sánchez et al. have found to be *almost attractive* [7]. Results

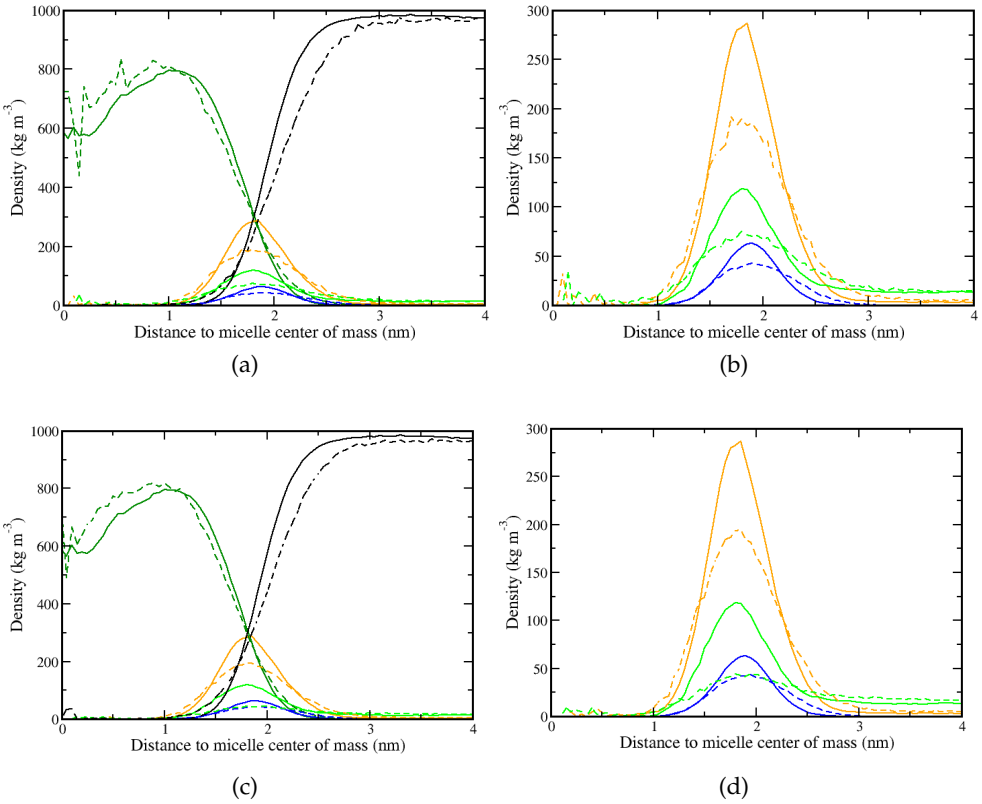

Figure 4.21: Comparison between atomistic (solid lines) and coarse-grained (dashed lines) average micelle density profiles obtained for the system containing DDA^+ surfactants and both SI and SN monomers. Different interaction levels are used for N_{SN}-Q_d: (a)-(b), *supra attractive* (O) and (c)-(d), *almost attractive* (II). Tails, dark green; charged heads, blue; anionic silica monomers, yellow; neutral silica monomers, green and water, black.

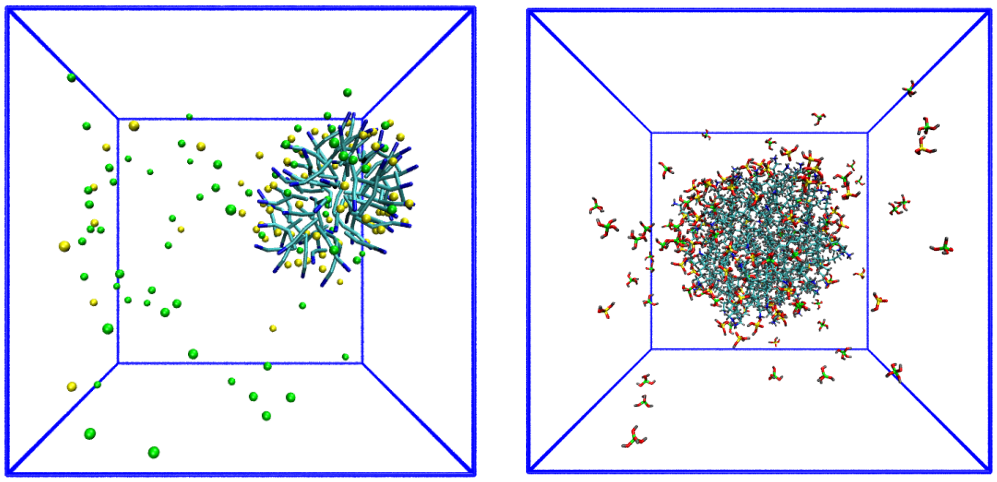

(a)

Figure 4.22: Snapshot comparing the final configurations obtained with coarse-grained (a) and atomistic (b) simulations for the system with DDA^+ surfactants and both anionic and neutral silica, using Q_{SI}-N_{SN} = O and N_{SN}-Q_d = O for the CG model. Colour code for the CG snapshot is the same as Figure 4.17. Colour code for the CG snapshot is the same as Figure 4.17 with SN monomer is green. Colour code for the AA snapshot is the same as Figure 4.8-(c).

for this system are shown in Figure 4.23 (density profile) and in Figure 4.24-(a) (final configuration), indicating, for the chosen set of parameters, agreement comparable with the previously discussed systems. No further tests were performed in this case since this interaction is of little importance for modelling HMS synthesis solutions (see later sections).

DDA WITH ANIONIC SILICA AND TMA COUNTER-IONS Two interactions are undefined for the system consisting of neutral surfactants with anionic silica and TMA counter-ions:

- Q_{SI}-N_d;
- Q_{SI}-Q_o.

With regard to the Q_{SI}-Q_o interaction, this was not parametrised and was assumed to be the same as for N_{SN}-Q_o which was already found by Pérez-Sánchez et al. to be *almost attractive* [7, 17]. For the remaining interaction, Q_{SI}-N_d, four possible cases were considered: i) *supra attractive*, ii) *attractive*, iii) *almost attractive* and iv)

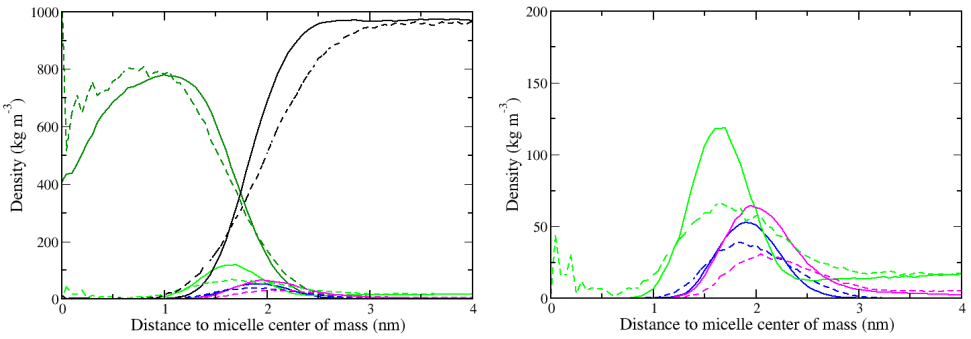

(a) (b)

Figure 4.23: Comparison between atomistic (solid lines) and coarse-grained (dashed lines) average micelle density profiles obtained for the system containing DDA^+ surfactants with SN monomers and chloride counter-ions, using N_{SN}-Q_a =II. Tails, dark green; heads, blue; chloride ions, pink; neutral silica monomers, green and waters black. Colour code for the AA snapshot is the same as in Figure 4.8-(c).

semi attractive. For all interaction levels tested, no significant differences were observed for any of the presented profiles with the exception of the SI profile, for which the best agreement was found when using the lowest interaction strength, as shown in Figure 4.25. Interactions levels lower than III (i.e. *semi attractive*) produced worse agreement for the SI distribution, which became progressively more spread out. For completeness, the final configuration obtained using the chosen set of parameters is shown in Figure 4.26.

DDA WITH ANIONIC AND NEUTRAL SILICA AND TMA COUNTER-IONS The last monomeric solution considered is identical to the previously discussed case but contains also neutral silica monomers. Two interactions are left to determine:

- N_{SN}-N_d;
- N_{SN}-Q_o.

However, the N_{SN}-Q_o was already determined by Pérez-Sánchez et al. [7] as being *almost attractive*, while for N_{SN}-N_d two values were considered: i) *supra attractive* and ii) *attractive*. Micelle density profiles (Figure 4.27) indicate that better agreement with AA is obtained when N_{SN}-N_d is *attractive*. The chosen set of parameters was then used to obtain the final configuration shown in Figure 4.28.

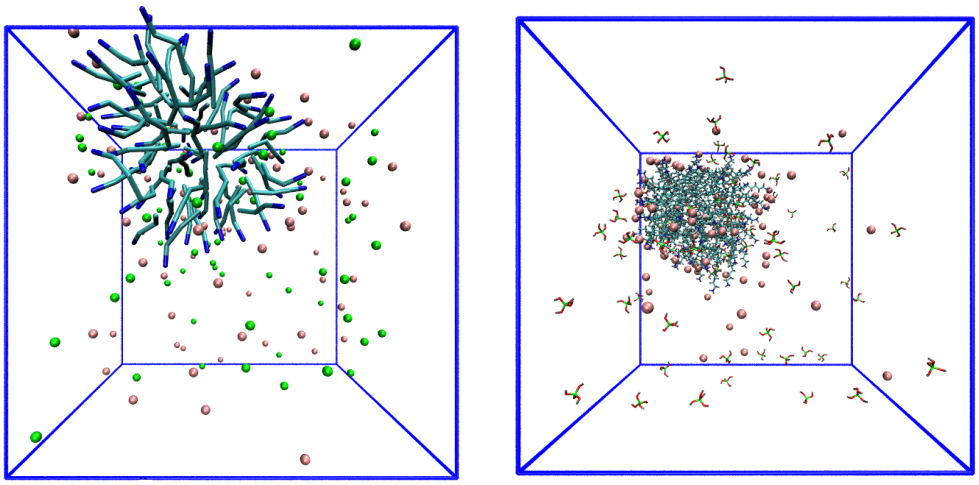

(a) (b)

Figure 4.24: Snapshot comparing the final configurations obtained with coarse-grained (a) and atomistic (b) simulations for the system with DDA^+ surfactants, neutral silica monomers and chloride counter-ions, using N_{SN}-Q_a = II for the CG model. Colour code for the CG snapshot is the same as in Figure 4.22 with chloride ions in pink. Colour code for the AA snapshot is the same as in Figure 4.5-(c)

Lastly, the systems containing charged surfactants and silica dimers was modelled. Three types of dimers were considered: with two charges (SISI), with one charge (SISN) and neutral (SNSN). It should be noted that interaction parameters have not been developed for the system containing dimers and neutral surfactants since, at the conditions of the synthesis, most surfactants (approximately 99 %) are expected to be in their protonated form (see section 4.2.4). In the following paragraphs, the development of interaction parameters for silica dimers is described.

DDA^+ WITH SISI DIMERS The first type of dimer considered is the one with two charges. The mapping scheme chosen is shown in Figure 4.10-(h). This comprises two Q_{SI}, each identical to the Q_{SI} bead type used for SI monomers, and bearing a negative charge. For comparison, the dimer consisting of two Q_{da} beads, which corresponds to the representation developed by Pérez-Sánchez et al. [7], was also tested. From the density profiles reproduced in Figure 4.29, the agreement with AA simulations improves with Q_{SI} beads. This result can be attributed to the different behaviour that doubly charged silica dimers have in the current system and in the system with CTAB surfactants modelled by Pérez-Sánchez et al. [7]. Because of the

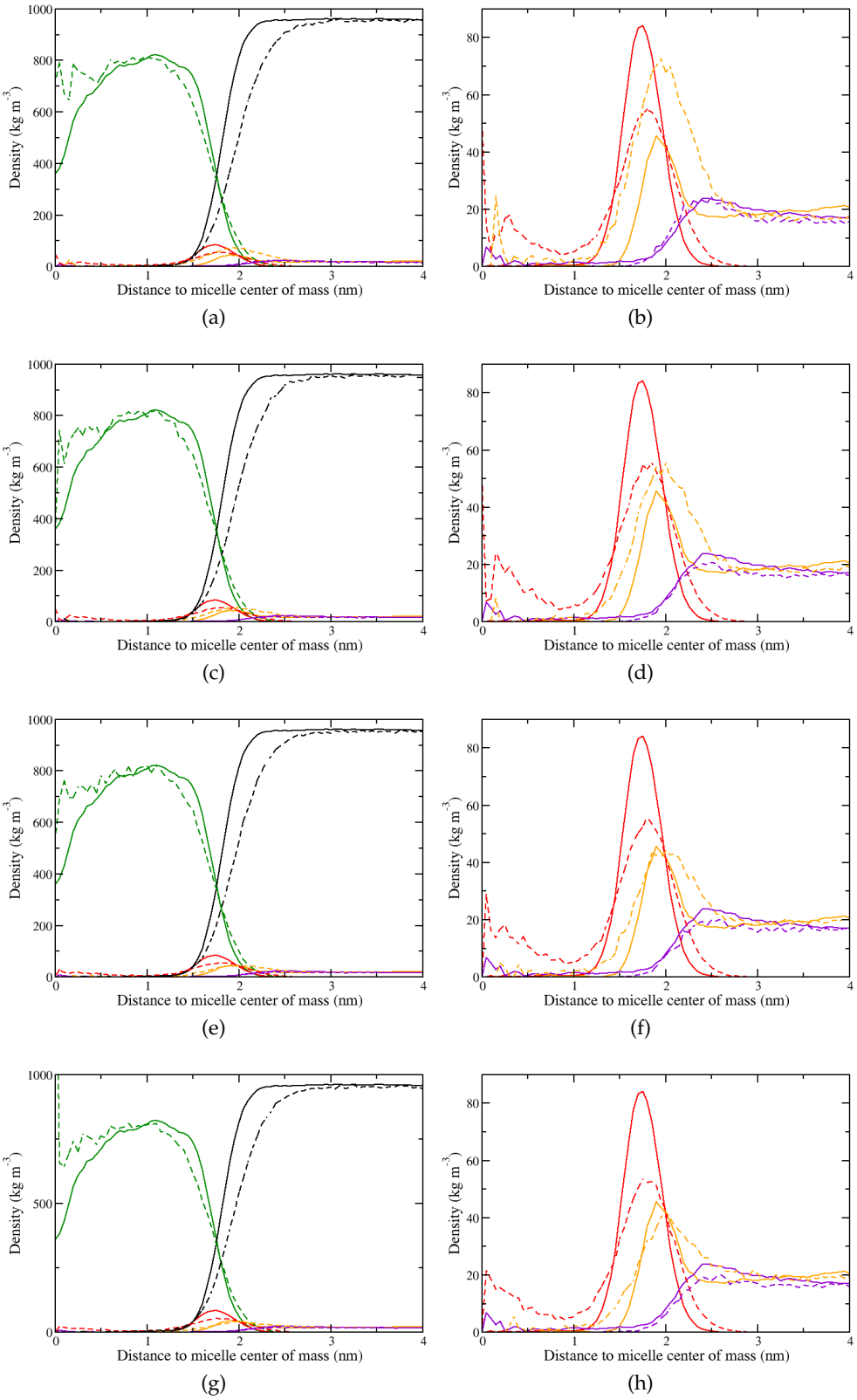

Figure 4.25: Comparison between atomistic (solid lines) and coarse-grained (dashed lines) average micelle density profiles obtained for the system containing DDA surfactants, SI monomers and TMA counter-ions. Different interaction levels are used for Q_{SI}-Nd: (a)-(b) *supra attractive* (O), (c)-(d) *attractive* (I), (e)-(f) *almost attractive* (II) and (g)-(h) *semi attractive* (III). Tails, dark green; neutral heads, red; anionic silica monomers, yellow; TMA counter-ions, purple and water, black.

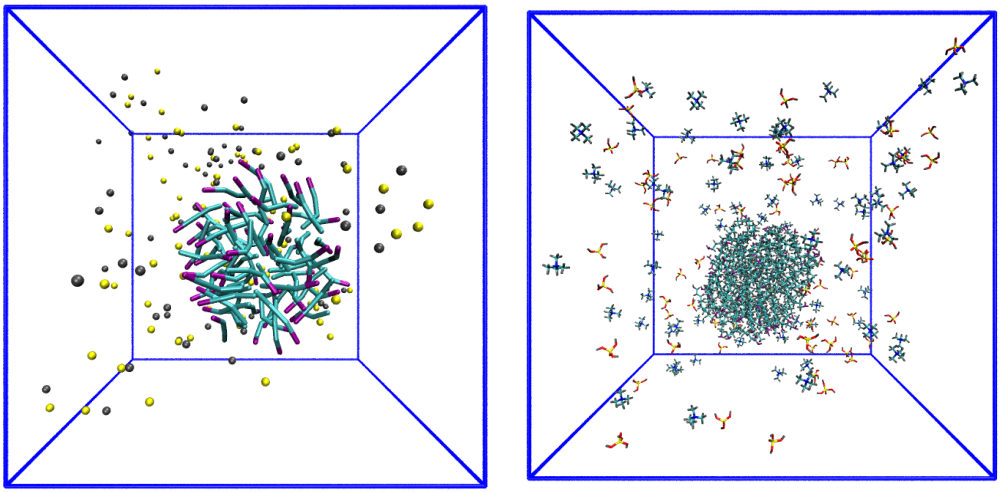

(a) (b)

Figure 4.26: Snapshot comparing the final configurations obtained with coarse-grained (a) and atomistic (b) simulations for the system with DDA surfactants, anionic silica monomers and TMA counter-ions, using Q_{SI}-N_d = III for the CG model. Colour code for the CG snapshot is the same as Figure 4.20 with SI monomers in yellow and TMA counter-ions in grey. Colour code for the AA snapshot is the same as Figure 4.7-(a)

.

small ammonium head group in DDA surfactant, both monomers and dimers are allowed to approach closely, as shown from the AA profiles (cf. Figure 4.7-(d) and Figure 4.9-(b)). On the contrary, when a surfactant with a larger head group, like CTAB, is used, SI monomers can still adsorb inside the micelle but SISI dimers become too large and, therefore, only adsorb on the outside of the micelle [7] [7]. In the MARTINI force field, the position where dimers (or monomers) adsorb on the micelle is essentially controlled by the Q_{SI} (or Q_{da})-C_2 interaction. When this is set to *super repulsive*, like for Q_{da}-C_2, dimers adsorb on the outside. Only by making the interaction with C_2 more favourable can silica dimers adsorb more closely to the surfactant head, like observed for DDA surfactants. For completeness, the final snapshot obtained when SISI are modelled with two Q_{SI} beads is provided in Figure 4.30-(a).

DDA$^+$ WITH SNSN DIMERS Satisfactory agreement was achieved by modelling the system containing neutral dimers with two N_{SN} beads (see Figure 4.10-(j)), identical to the bead type used for SN monomers. The micelle density profiles

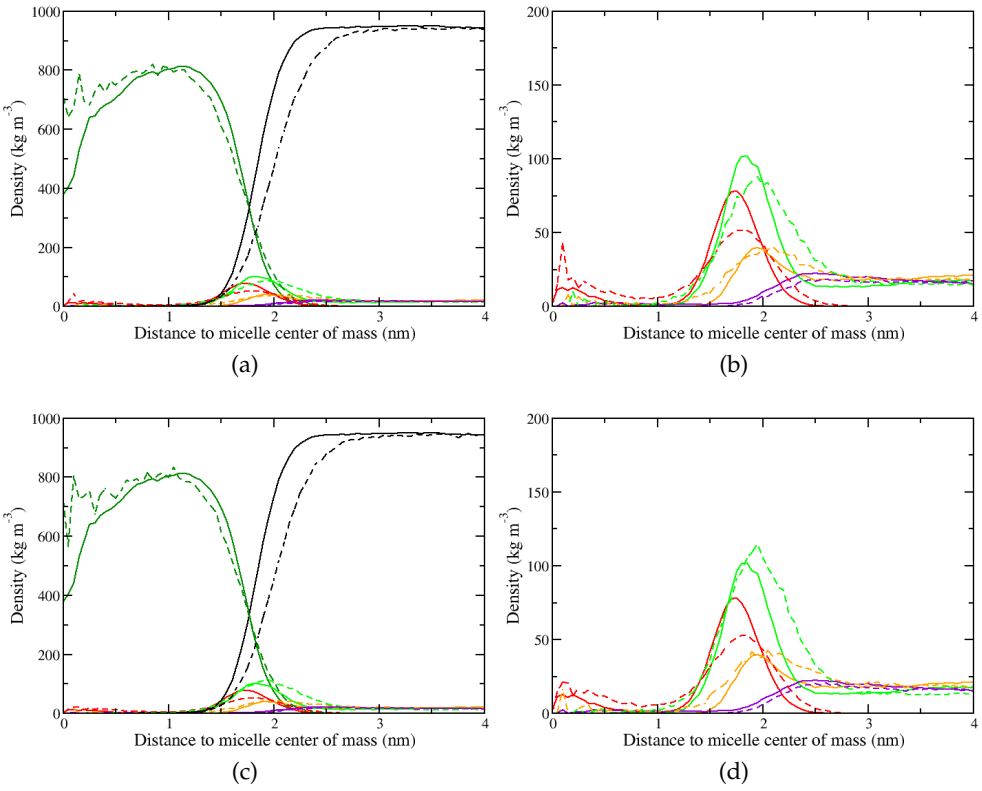

Figure 4.27: Comparison between atomistic (solid lines) and coarse-grained (dashed lines) average micelle density profiles obtained for the system containing DDA surfactants, both SN and SI monomers and TMA counter-ions. Different interaction levels are used for N_{SN}-N_d: (a)-(b) *supra attractive* (O), (c)-(d) *attractive* (I). Tails, dark green; neutral heads, red; anionic silica monomers, yellow; neutral silica monomers, green; TMA counter-ions, purple and water, black.

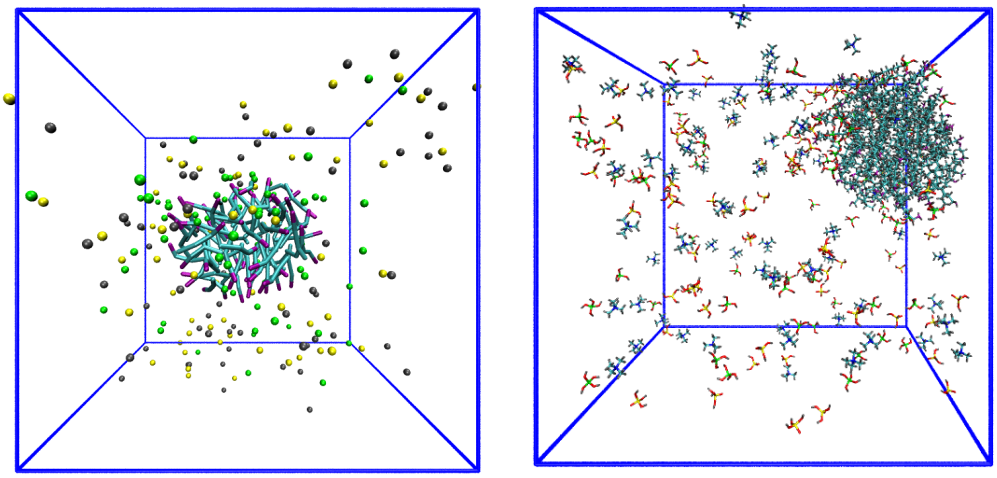

(a) (b)

Figure 4.28: Snapshot comparing the final configurations obtained with coarse-grained (a) and atomistic (b) simulations for the system with DDA surfactants, anionic silica monomers and TMA counter-ions, using Q_{SI}-N_d = III for the CG model. Colour code for the CG model is the same as in Figure 4.26 with SN monomer is green. Colour code for the AA model is the same as in Figure 4.8-(a)

obtained are shown in Figure 4.31 while the corresponding final configuration is displayed in Figure 4.32-(a). The position of the peaks is matched for both head and chloride profiles, while the shift in dimer profile is comparable to the results obtained for the systems containing neutral monomers. Hence, no further tests were performed for this case.

DDA$^+$ WITH SISN DIMERS Following the previous results, the system with singly charged dimers was modelled using one Q_{SI} bead and one N_{SN} bead (see Figure 4.10-(i)). Figure 4.33-(c) and (d) show the density profiles obtained, while the final snapshot is displayed in Figure 4.34-(a). In Figure 4.33-(a) and (b) the profiles obtained when Q_{SI} is replaced with a Q_{da} are shown. Like in the system with the doubly charged dimer, the agreement decreases and therefore Q_{da} beads were discarded.

4.2 CG SIMULATIONS OF HMS MATERIALS

In Table 4.4, interaction levels for all bead types used in this work are provided. Be-

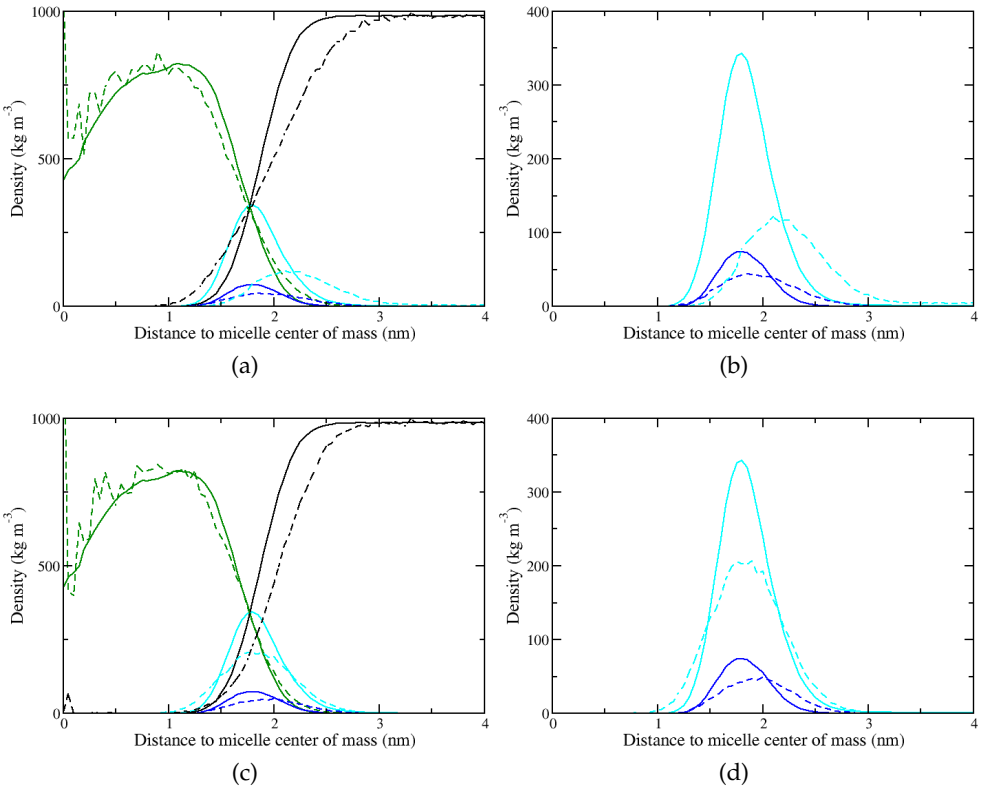

Figure 4.29: Comparison between atomistic (solid lines) and coarse-grained (dashed lines) average micelle density profiles obtained for the system containing DDA^+ surfactants and SISI dimers. Different bead types are used for the charged part of the dimer: (a)-(b), Q_{da} and (c)-(d), Q_{SI}. Tails, dark green; charged heads, blue; doubly charged dimers, cyan; and water, black.

Table 4.4: Matrix of interactions for CG beads used in this work.

Type	Q_d	Q_a	Q_o	Q_{SI}	P_4	N_d	N_{SN}	C_2
Q_d	O	O	II	II	O	III	O	IX
Q_a	O	I	II	II	O	I	II	IX
Q_o	II	II	IV	II	O	III	II	IX
Q_{SI}	II	II	II	O	II	III	O	IV
P_4	O	O	O	II	I	III	II	VII
N_d	III	I	III	III	III	III	O	VI
N_{SN}	O	II	II	O	II	O	O	IV
C_2	IX	IX	IX	IV	VII	VI	IV	IV

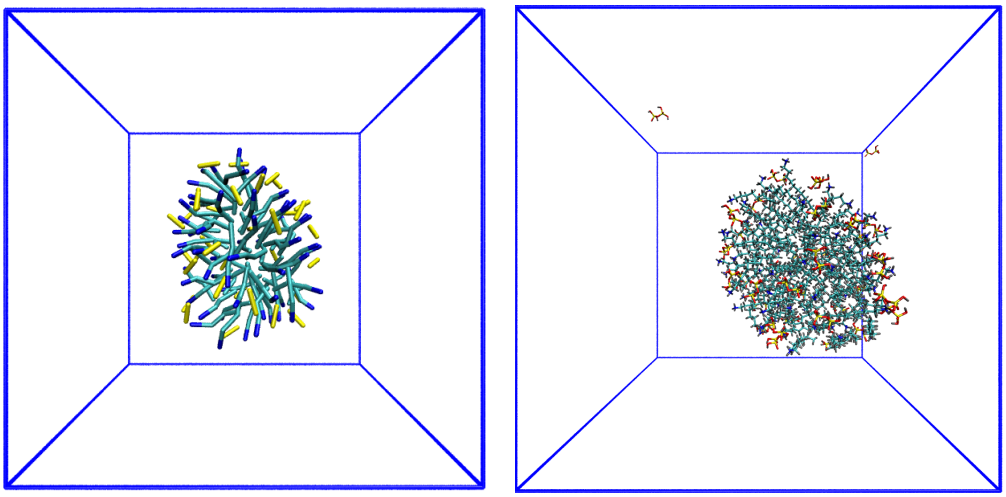

(a) (b)

Figure 4.30: Snapshot comparing the final configurations obtained with coarse-grained (a) and atomistic (b) simulations for the system with DDA^+ surfactants, silica dimers with two charges and chloride counter-ions, using Q_{SI} to model at CG level the charged beads of the dimer. Colour code for the CG system is the same as Figure 4.12 with SISI dimers in yellow. Colour code for the AA system is the same as in Figure 4.9-(a).

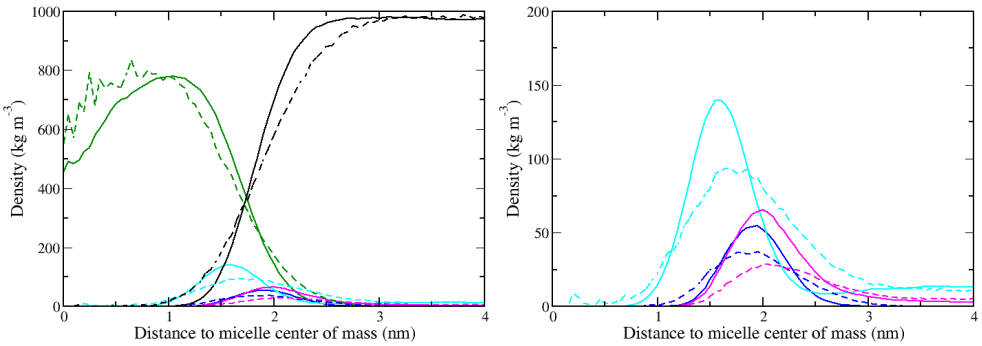

(a) (b)

Figure 4.31: Comparison between atomistic (solid lines) and coarse-grained (dashed lines) average micelle density profiles obtained for the system containing DDA^+ surfactants, SNSN dimers and chloride counter-ions, using two N_{SN} beads to model the dimer. Tails, dark green; charged heads, blue; doubly charged dimers, cyan; and water, black.

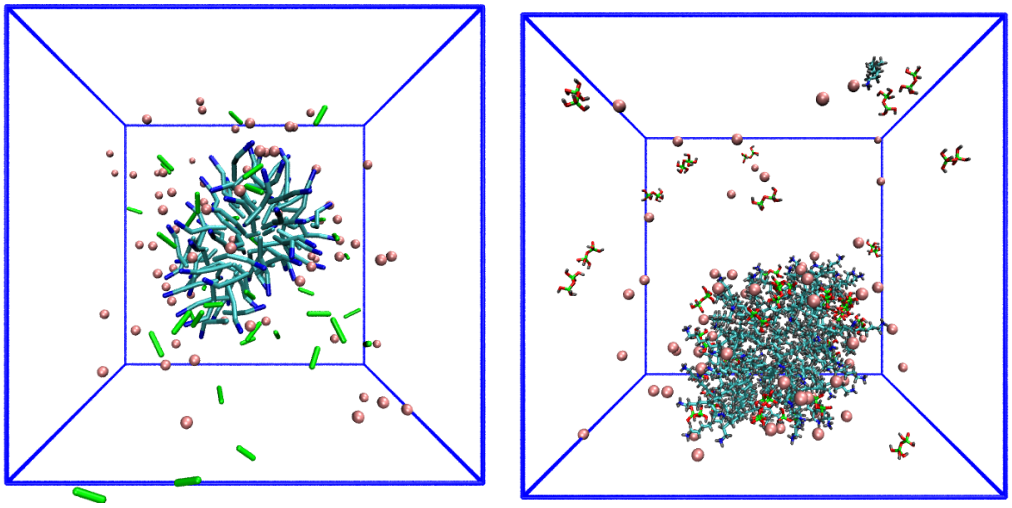

(a) (b)

Figure 4.32: Snapshot comparing the final configurations obtained with coarse-grained (a) and atomistic (b) simulations for the system with DDA^+ surfactants, neutral silica dimers and chloride counter-ions, using N_{SN} to model at the CG level the neutral beads of the dimer. Colour code for the CG snapshot is the same as Figure 4.30 with SNSN in green and chloride ions in pink. Colour code for the AA system is the same as in Figure 4.9-(e).

fore starting to investigate the behaviour of precursor solutions of HMS materials, the quality of the CG model for DDA surfactants was further assessed by reproducing available experimental data. For this purpose the system dodecylammonium chloride (DDACl) was considered since a few studies on aggregation properties (e.g. aggregation numbers, N_{agg}) of this system are available in the literature [143]. Furthermore, these properties can be calculated with MD simulations.

4.2.1 *The system dodecylammonium chloride-water*

As already discussed in section 4.1, depending on the pH, dodecylamine will be in charged or neutral form (see Figure 4.1). In the charged form, dodecylammonium surfactants are commonly associated with chloride counter-ions forming DDACl, which is obtained by adding gaseous HCl to the primary amine [144]. Several studies are available in the literature regarding the phase diagram of DDACl in water [145–147] as well as values of average micelle size and other aggregation properties [143]. Ternary phase diagrams are also available; for example Karlsson et al.

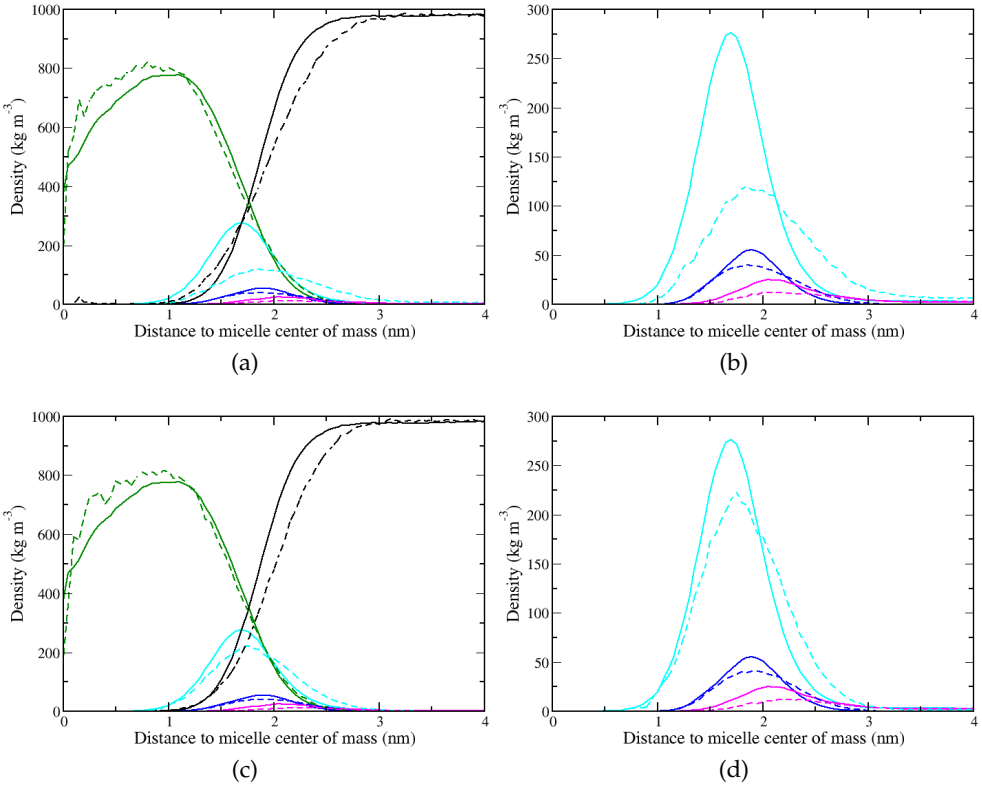

Figure 4.33: Comparison between atomistic (solid lines) and coarse-grained (dashed lines) average micelle density profiles obtained for the system containing DDA^+ surfactants, SISN dimers and chloride counter-ions. Different bead types are used for the charged part of the dimer: (a)-(b), Q_{da} and (c)-(d), Q_{SI}. Tails, dark green; charged heads, blue; doubly charged dimers, cyan; and water, black.

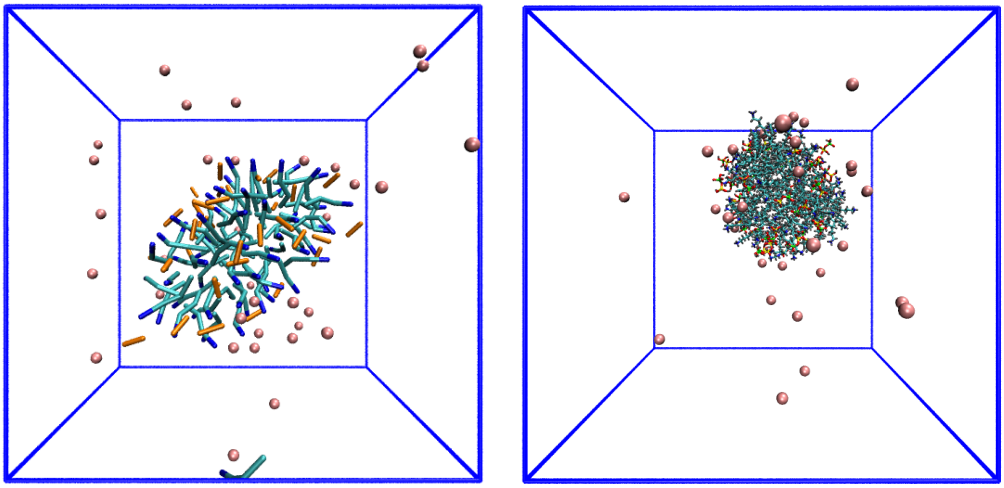

(a) (b)

Figure 4.34: Snapshot comparing the final configurations obtained with coarse-grained (a) and atomistic (b) simulations for the system with DDA^+ surfactants, silica dimers with one charge and chloride counter-ions, using Q_{SI} and Q_{SN} to model at the CG level the charged and neutral beads of the dimer. Colour code for the AA system is the same as in Figure 4.9-(c).

studied the phase diagrams of the system dodecylamine-acetic acid-water [148] while Hartmann et al. studied the systems dodecylamine-acrylic/methylacrylic acid- water [149]. However, these are in general more difficult to interpret and less information is available regarding system aggregation properties. Also from a computational point of view, in order to reproduce these phase diagrams with simulations a third component would need to be added to the system, increasing complexity and reducing computational expediency. Therefore, the more reasonable approach to assess CG model capability to reproduce experimental data, is by studying the system dodecylammonium chloride-water and testing if phases observed and micelle size values calculated experimentally can be reproduced with CG simulations.

Figure 4.35 shows the phase diagram of the system dodecylammonium chloride-water as determined by Broome et al. [145]. The first thing to notice is that at ambient temperature dodecylammonium chloride is soluble in water only in very small quantities. The solubility of DDACl as a function of pH at 25 °C was measured by Dai and Laskowski, showing a quite sharp decrease from 2×10^{-2} M at pH 7 to approximately 10^{-4} M at pH 10 [150]. These extremely low concentrations

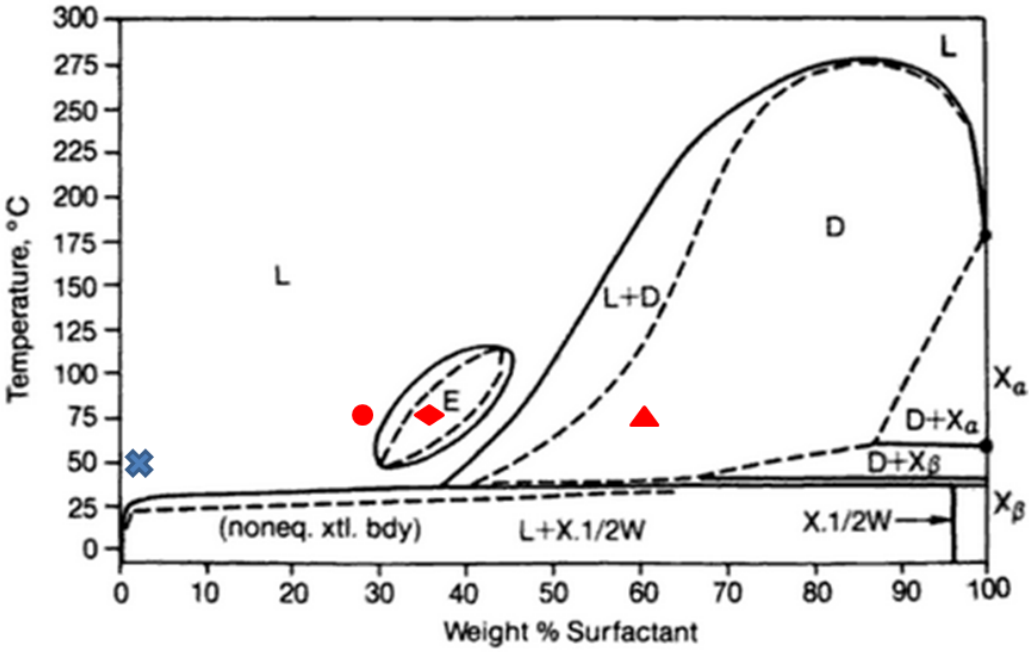

Figure 4.35: Phase diagram of the system dodecylammonium chloride-water from reference [145]. Phase symbols are: L, liquid; E, hexagonal liquid crystal; D, lamellar liquid crystal; X_α and X_β, dry crystal, X.nW, crystal hydrate having n water molecules. Dashed lines indicate limits of metastable regions. Symbols indicate simulation conditions: blue cross, simulations at 50 °C (i.e. 323 K) and 0.1 M concentration; red circle, simulation at 75 °C (i.e. 348 K) and 28 % surfactant weight; red diamond, simulation at 75 °C and 35 % surfactant weight and red triangle, simulation at 75 °C and 60 % surfactant weight; see Table 4.5 for more details.

are difficult to reproduce even with CG simulations. Above ambient temperature, however, solubility increases significantly and a liquid phase (L) is observed. This liquid phase is effectively an isotropic micellar solution and occupies a large part of the phase diagram. Furthermore, the system also exhibits two liquid crystalline phases: an hexagonal phase (E) and a lamellar phase (D). Interestingly, the hexagonal phase does not coexist with any other liquid crystal phase but is, instead, surrounded by the liquid phase. Also to notice is that no cubic phase has been reported for this system, contrary to other cationic surfactants systems, e.g. CTAB. The other regions in the diagram represent crystal hydrates and metastable crystal hydrates which will not be considered in this study.

Four points on the phase diagram were investigated with CG simulations, one in the micellar region (blue cross), one near the boundary between the micellar region and the hexagonal phase (red circle), and two in the liquid crystal regions (one hexagonal, red diamond and one lamellar, red triangle). Details of all the simulations performed can be found in Table 4.5.

Table 4.5: Coarse-grained MD simulations of the system dodecylammonium chloride-water.

System	DDA^+	Cl^-	water	T (K)	time (ns)	box (nm)
0.1 M preformed-small	210	210	28550	323	1200	15.3
0.1 M random-small	210	210	28550	323	1200	15.3
0.1 M preformed-large	2000	2000	274800	323	600	32.6
28 % random	4000	4000	25687	348	600	17.9
35 % random	4000	4000	16885	348	600	17.9
60 % random	4000	4000	2215	348	3600	13.8

Simulations of the micellar region were performed at 50 °C (i.e. 323 K) and at very low surfactant concentration (0.1 M). These conditions were chosen to compare simulation results with experimental values of micelle aggregation number estimated by Malliaris et al. [143]. To establish whether CG simulations reached equilibrium, two systems at the same concentration were considered: a small system, both starting from a single preformed micelle and from a random distribution of surfactants, and a large system (with approximately 10 times more surfactants) starting from a single preformed aggregate (see first three rows of Table 4.5 and point marked with a blue cross in Figure 4.35). The other points on the diagram were simulated for a slightly higher temperature (348 K) and using respectively

28, 35 and 60 surfactant weight % (see points marked with a red symbols in Figure 4.35). The higher temperature was chosen since it falls approximately in the middle of the hexagonal island. The exact number of surfactants and water molecules to use in each simulation was determined according to the following equation:

$$\text{surfactant weight\%} = \frac{N_{SURF} \times MW_{SURF}}{N_{SURF} \times MW_{SURF} + N_{WAT} \times MW_{WAT}} \tag{4.2}$$

where N_{SURF} and N_{WAT} are the number of surfactants and water molecules, respectively, while MW_{SURF} and MW_{WAT} are the corresponding molecular weights. Then the number of CG beads was derived using the standard MARTINI convention for water and ions (see section 3.3.2). Finally, all simulations were run using the same MD parameters used for CG model development (see section 4.1).

Figure 4.36 shows the final configurations obtained starting from a single preformed micelle (a) and from randomly dispersed surfactants (b) for the small system containing 210 DDA^+ and an equal number of chloride counter-ions in water to give a concentration of 0.1 M. Experimental data indicate that at 50 °C,

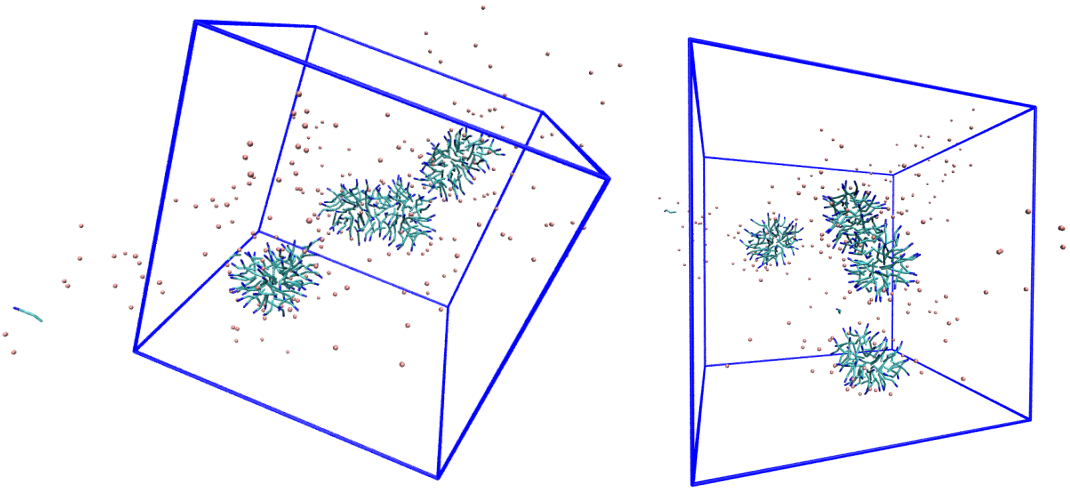

(a) (b)

Figure 4.36: Final configurations obtained for the system containing 210 DDACl in water at 0.1 M concentration starting from a single preformed micelle (a) and from a random distribution of surfactants (b). Water has been removed for clarity. Colour code is the same as in Figure 4.12.

the temperature at which the simulation was performed, micelles should contain approximately 68 surfactants on average [143]. For the considered systems (with 210 surfactants) this should lead to the formation of three aggregates, which is in

agreement with the results obtained. By using the cluster counting algorithm previously described, more detailed information about this system can be obtained. In Figure 4.37, number of clusters ((a) and (b)), average micelle size ((c) and (d)), average micelle radius ((e) and (f)) and micelle size distributions ((g) and (h)) obtained for these systems are compared. Both random and preformed systems converged to the same final equilibrium value of approximately 70 surfactants in a micelle (cf. Figure 4.37-(c) and (d)), in excellent agreement with experimental data. The number of clusters oscillates, for both systems, between 5 and 10, suggesting that individual monomers are also present in the system (Figure 4.37-(a) and (b)). This can also be seen by the first peak in the micelle size distribution ((Figure 4.37-(g) and (h)). Also, with regard to the micelle radius, the two systems converge to similar values, again suggesting that equilibrium was effectively reached. Lastly, the cluster size distribution obtained for the preformed system shows three peaks (Figure 4.37-(g)). Two aggregates have approximately the same size (between 50 and 65 molecules in the micelles) and a third one is larger (85-90 surfactants). This result also compares well with the experimental data giving an average cluster size of approximately 67 surfactants per aggregate. The lower values of micelle sizes obtained in the random simulations (Figure 4.37-(h)) can be attributed to the longer time spent by the system in configurations having smaller sizes due to the slow aggregation process.

Results obtained for the same concentration with a larger simulation box are shown in Figure 4.38. In this case approximately 30 aggregates are expected to form at 50 °C. This theoretical value is reproduced quite well with simulations, as can been seen by comparing Figure 4.38-(b), showing an average number of clusters of 65, and Figure 4.38-(d), which indicates that on average 35 surfactant molecules are present as monomers in the simulation box. Average micelle size and micelle size distribution for this system (Figure 4.38-(b) and (d)) also confirm that the CG surfactant model reproduces quite well the experimental data.

The next step was to test the applicability of the model at higher concentrations by trying to reproduce different points in the phase diagram at 75 °C (i.e. simulations at 348 K). The final configurations obtained for 28, 35 and 60 % surfactant weight are displayed in Figure 4.39. The first two points are located at the boundary between liquid and hexagonal phase (28 %) and inside the hexagonal island (35 %). The results obtained for both systems are very similar and show the formation of large disordered aggregates (Figure 4.39-(a) and (b)). The shape of these aggregates is elongated, similar to long twisted rods. This result implies that a sphere-to-rod

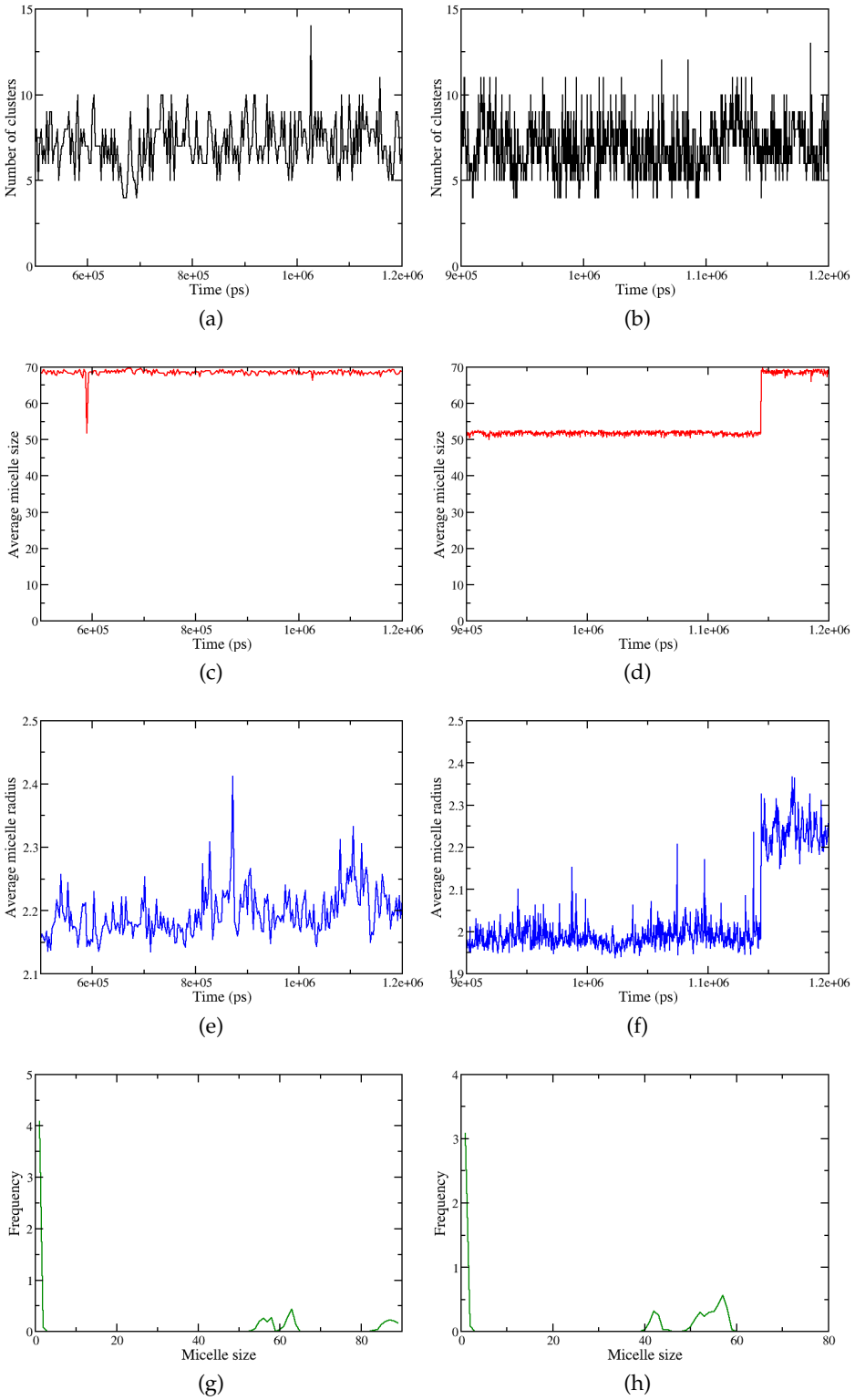

Figure 4.37: Comparison between average aggregation properties for the system containing 210 DDACl surfactants in water at concentration 0.1 M, starting from preformed (left panel) and random (right panel) initial configurations. (a) and (b), number of clusters; (c) and (d), average micelle size; (e) and (f), average micelle radius; (g) and (h), micelle size distribution. Results for the preformed system were averaged over the last 700 ns while for the random system averages were taken over the last 300 ns.

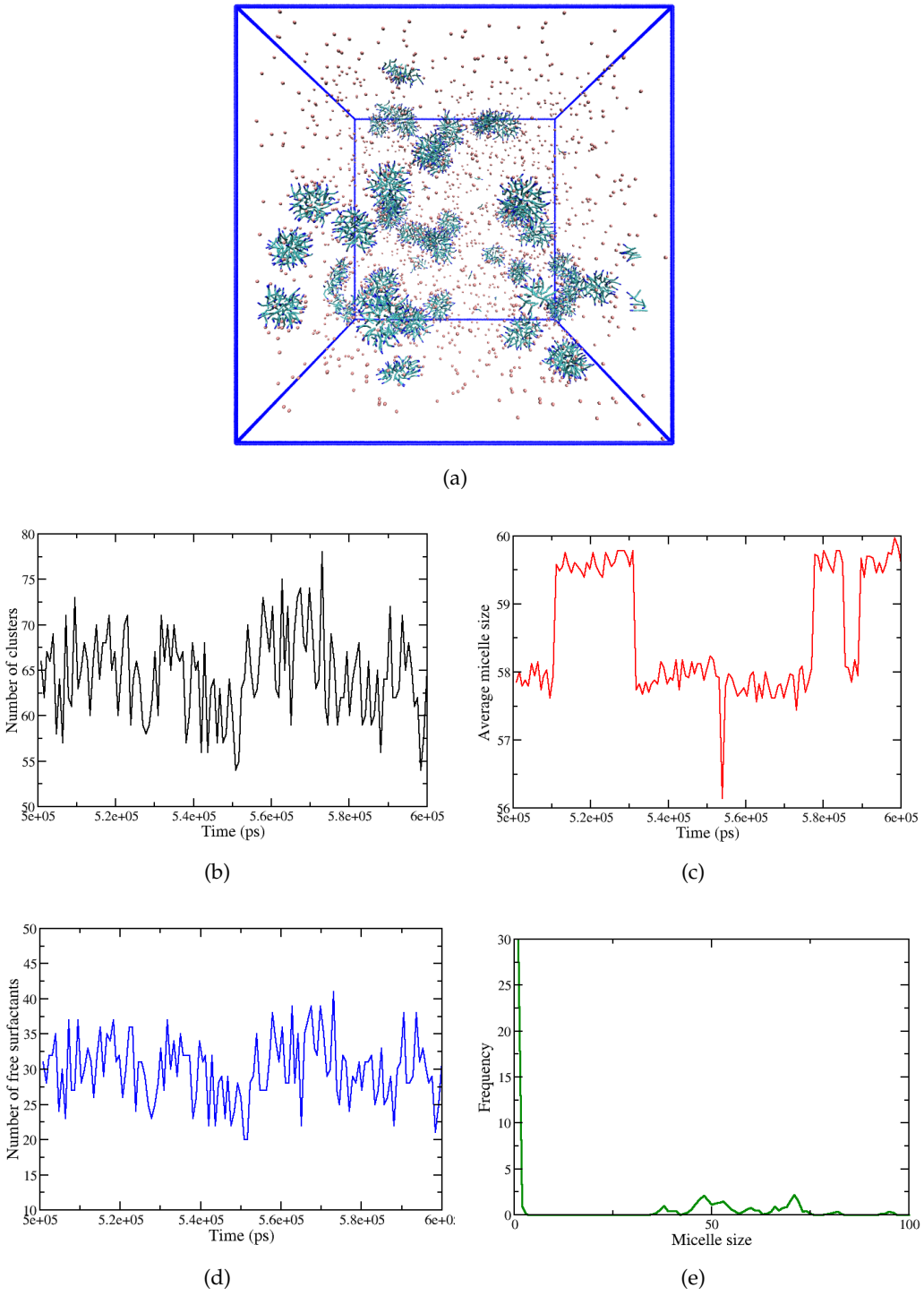

Figure 4.38: Final configuration obtained for the system system containing 2000 DDACl in water at 0.1 M concentration starting from a single preformed aggregate (a) and average aggregation properties for the same system. (b), number of clusters; (c), average micelle size; (d), number of free surfactants and (e), micelle size distribution. Averages were taken over the last 100 ns. Water has been removed for clarity. Colour code for the snapshot is the same as in Figure 4.12.

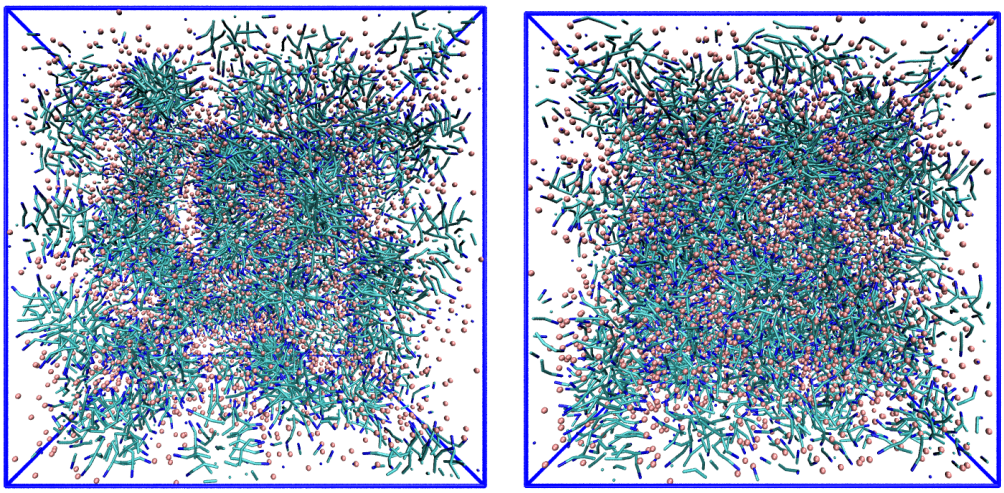

(a) (b)

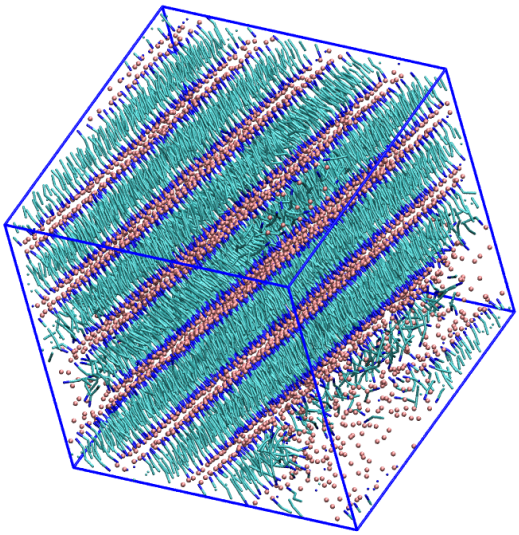

(c)

Figure 4.39: Final configurations obtained for the systems at 28, (a); 35, (b) and 60 %, (c) surfactant weight. Water has been removed for clarity. Colour code is the same as in Figure 4.12.

transition should take place between 0.1 M and 28 %. However, no experimental evidence supporting or disproving this prediction was found. Unfortunately, the hexagonal phase was not observed in the MD simulation at 35 %. In contrast, the simulation at 60 % surfactant weight shows the formation of a very ordered lamellar phase (Figure 4.39-(b)) in agreement with experimental data.

4.2.2 *The reference system*

In the following, CG simulations are used to simulate reference, monomeric and dimer systems at the experimental concentration used for the synthesis of HMS materials. All simulations were performed in the *NPT* ensemble fixing temperature at 323 K, pressure at 1 bar and following exactly the same simulation protocol described in section 4.1. Table 4.6 provides a list of all the simulations performed for this part of the study.

Table 4.6: Number of beads, simulation length and final box size for each coarse-grained MD simulation of HMS materials.

System	DDA^+	DDA	Cl^-	SI	SN	TMA^+	SISI	SISN	SNSN	water	time (ns)	box (nm)
DDA^+	1000		1000							61636	1200	20.1
DDA		1000								63136	600	20.1
DDA^+ + SI	1000			1000						63136	1200	20.2
DDA + SI		1000		1000		1000				63136	600	20.3
DDA + SN		1000			1000					63136	600	20.2
DDA^+ + SI + SN	1000		770	230	770					63136	2400	20.3
DDA^+ + 1to1 SISN + SNSN	1000		880					120	380	61816	3000	20.2
DDA^+ + 2to1 SISN + SNSN	1000		760					240	760	61996	1800	20.3
DDA^+ + 3to1 SISN + SNSN	1000		640					360	1400	62176	600	20.4
DDA^+ + 4to1 SISN + SNSN	1000		520					480	1520	62356	1200	20.4
DDA^+ + 4to1 SISI + SNSN	1000		520				240		1760	62356	600	20.5

As previously discussed (see section 2.1), one key aspect of templating synthesis is the interaction between organic and inorganic species. Therefore, to clearly assess the role played by surfactants and silicates, a preliminary study of the system containing only water and DDA was carried out. Experimentally, synthesis of HMS materials was conducted using a solution with 0.22 M concentration of surfactants [9]. In this section and in the following, the same concentration will be employed in all simulations.

For the reference system, two pH conditions were considered: below 8 (i.e. all surfactants are protonated) and above 12 (i.e. all surfactants are neutral). Figure 4.40 shows the final configurations obtained.

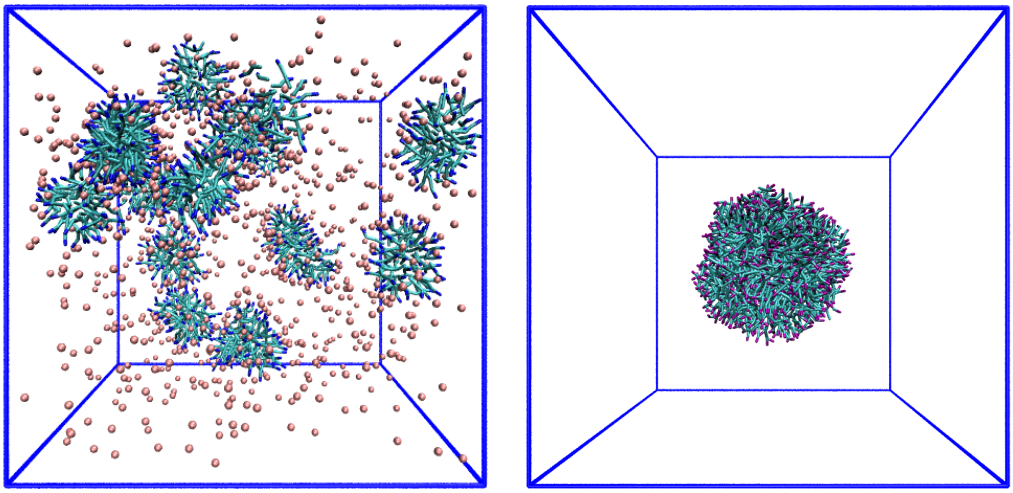

(a) (b)

Figure 4.40: Final configurations obtained for the reference systems at 0.22 M at different pH values: (a), charged surfactants at pH < 8 and (b), neutral surfactants at pH > 12. Water has been removed for clarity. Colour code is the same as in Figure 4.12 with neutral heads in purple.

The two systems produce significantly different results. When surfactants are charged, like discussed above, micellar aggregates are formed. The size of these aggregates has been determined using the cluster counter algorithm and is shown in Figure 4.41. The average micelle size obtained for this system is slightly higher than the values reported in the previous section from 0.1 M solution at 50 °C, both from experiments and simulations (approximately 80 instead of 67 surfactants per micelle). This is most likely due to the higher concentration of the system which tends to lead to micelle size increase [151]. Contrary to charged surfactants, neutral surfactants form a single disordered aggregate indicating that the system undergoes phase separation. This observation is in qualitative agreement with experimental evidence, which indicates that dodecylamine is essentially insoluble in water at these conditions [139].

4.2.3 *The monomeric solution*

In Figure 4.42 the final snapshots produced when anionic silica monomers (SI) are added to DDA^+ (low pH) and DDA (high pH) in a one-to-one ratio are shown. The first thing to notice is that the neutral system remains phase separated also

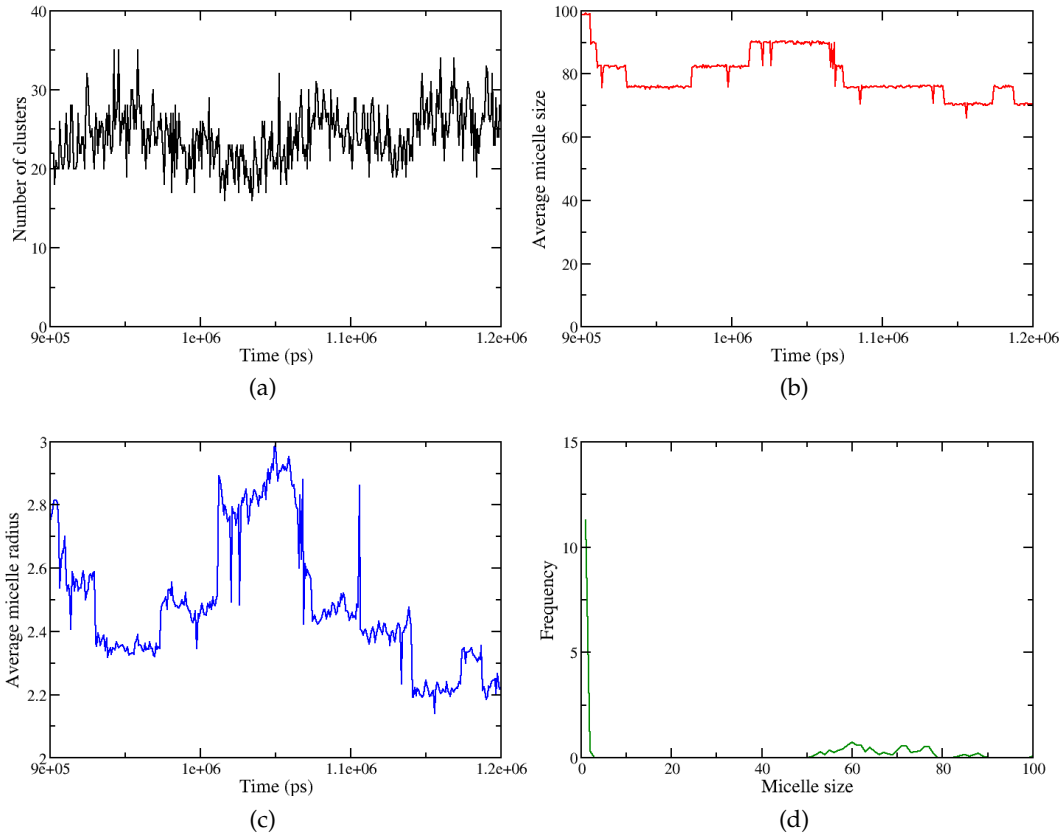

Figure 4.41: Average aggregation properties for the reference system containing charged surfactants: (a), number of clusters; (b), average micelle size; (c), average micelle radius and (d), micelle size distribution. Averages were taken over the last 300 ns.

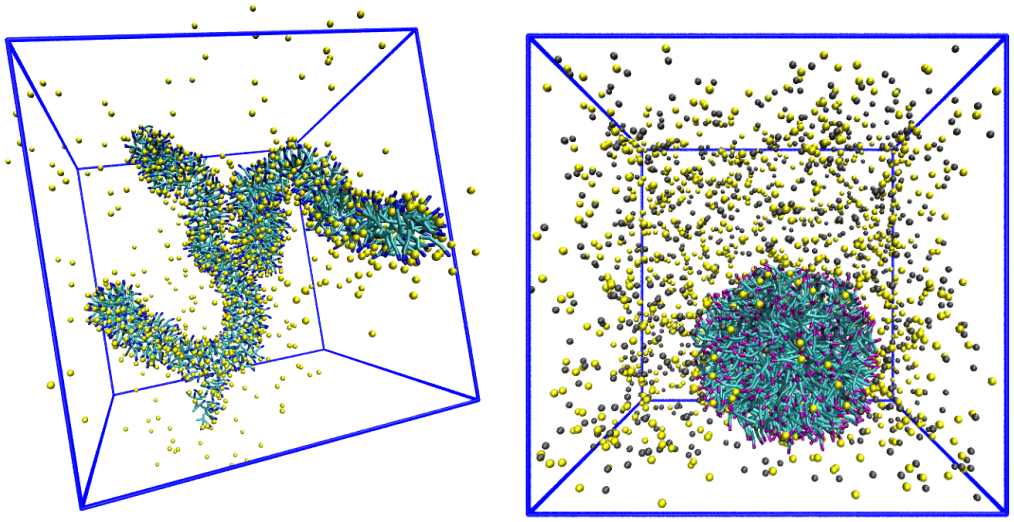

(a) (b)

Figure 4.42: Final configurations obtained for the monomeric solutions with SI monomers: (a), charged surfactants and (b), neutral surfactants. Water has been removed for clarity. Colour code is the same as in Figure 4.40 with SI in yellow and TMA in grey.

after addition of silica anions (Figure 4.42-(b)), with the latter remaining mostly in solution. On the other hand, in the system with charged surfactants and anionic silica monomers, micelle fusion and formation of two large branched rods is observed (Figure 4.42-(a)). The density profiles of single micelles discussed during the coarse-grained model development (Figure 4.18-(f)) revealed that SI monomers adsorb much closer to the charged surfactant heads than chloride counter-ions. By doing so, the repulsion between cationic surfactants is lowered and formation of larger aggregates with lower surface curvature is promoted. This mechanism has been proposed to explain sphere-to-rod transition in the precursor solution of MCM-41 materials [17], but can explain also the formation of branched rods observed in this system.

These results seem to suggest that charged surfactants are necessary in order to promote formation of ordered structures that can then act as templates for HMS materials. The distribution of species used, however, does not represent the actual conditions at which synthesis takes place. Unfortunately, the pH of the synthesis was not reported in the experimental study, however using the dissociation constants of DDA [152] and silicic acid [153], it was possible to estimate it to be approximately 8.9 through the utility CurTiPot [154]. At these conditions, most surfactants

are charged (99 %) while silica monomers are prevalently neutral (77 %). This more realistic distribution of species was tested considering a one-to-one silica to surfactant ratio. Results obtained at this estimated pH were then compared with simulations containing only neutral species (i.e. DDA surfactants and SN monomers) to represent the neutral templating route proposed by Tanev and Pinnavaia for the formation of these materials [9]. Final configurations obtained for these two systems (Figure 4.43) show, once again, phase separation for the system with neutral surfactants (b) and formation of branched rods for the system with charged surfactants and both anionic and neutral silica (a). This result suggests that small quantities of SI monomers are sufficient to promote micelle aggregation and formation of rods. Another possibility is, however, that the presence of both silicate species allows the transformation from small micelles to long branched rods. This second mechanism, involving both types of silica monomers, is supported by the results observed at AA level. AA simulations revealed that SN monomers tend to adsorb more closely to the surfactant heads when anionic monomers are also present (see Figure 4.8). It is then plausible to hypothesise that anionic species attract neutral ones on the micelle interface and, hence, both species participate in the screening of the positive surfactant charges, favouring formation of larger aggregates.

4.2.4 *The system with dimers*

So far, CG simulations have shown the formation of rod-like aggregates when silica monomers are added to the system containing charged surfactants. Pérez-Sánchez et al. have demonstrated that silica dimers are necessary in order to create hexagonal phases of CTAB surfactants for the synthesis of MCM-41. Their simulations show that these small oligomers can promote formation of hexagonal liquid crystals by bridging neighbouring rods [7]. This possibility was explored also in this work. Taking into account the first two dissociation constants for silica dimers [153], a pH of 8.4 was obtained for the precursor solution with dimers through the utility CurTiPot [154], as was done earlier for the monomeric solution. This corresponds to a solution containing approximately 99 % charged surfactants, 24 % of dimers with one charge and 76 % neutral dimers. This system was simulated considering an increasing silica-to-surfactant ratio (up to four-to-one) and neglecting neutral surfactants, as their concentration at this pH is very low (see Table 4.6). The results obtained are shown in Figure 4.44. For a silica-to-surfactant ratio higher

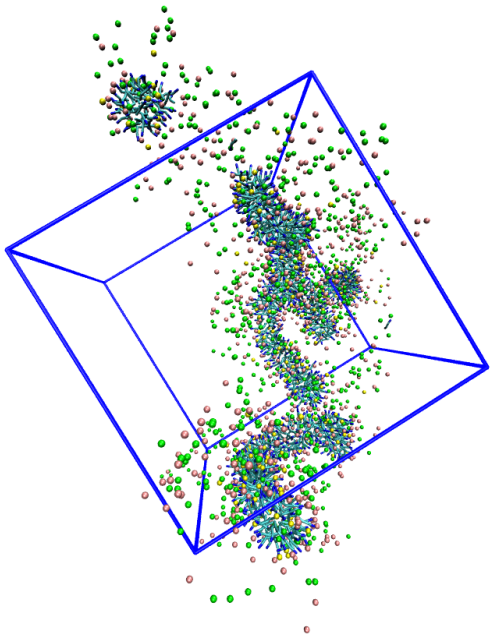

(a)

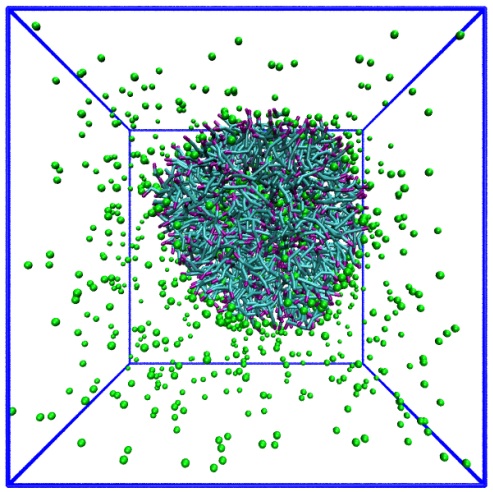

(b)

Figure 4.43: Final configurations obtained for the monomeric solutions with SI and SN monomers: (a), charged surfactants and (b), neutral surfactants. Water has been removed for clarity. Colour code is the same as in Figure 4.42 with SN in yellow and chloride in pink.

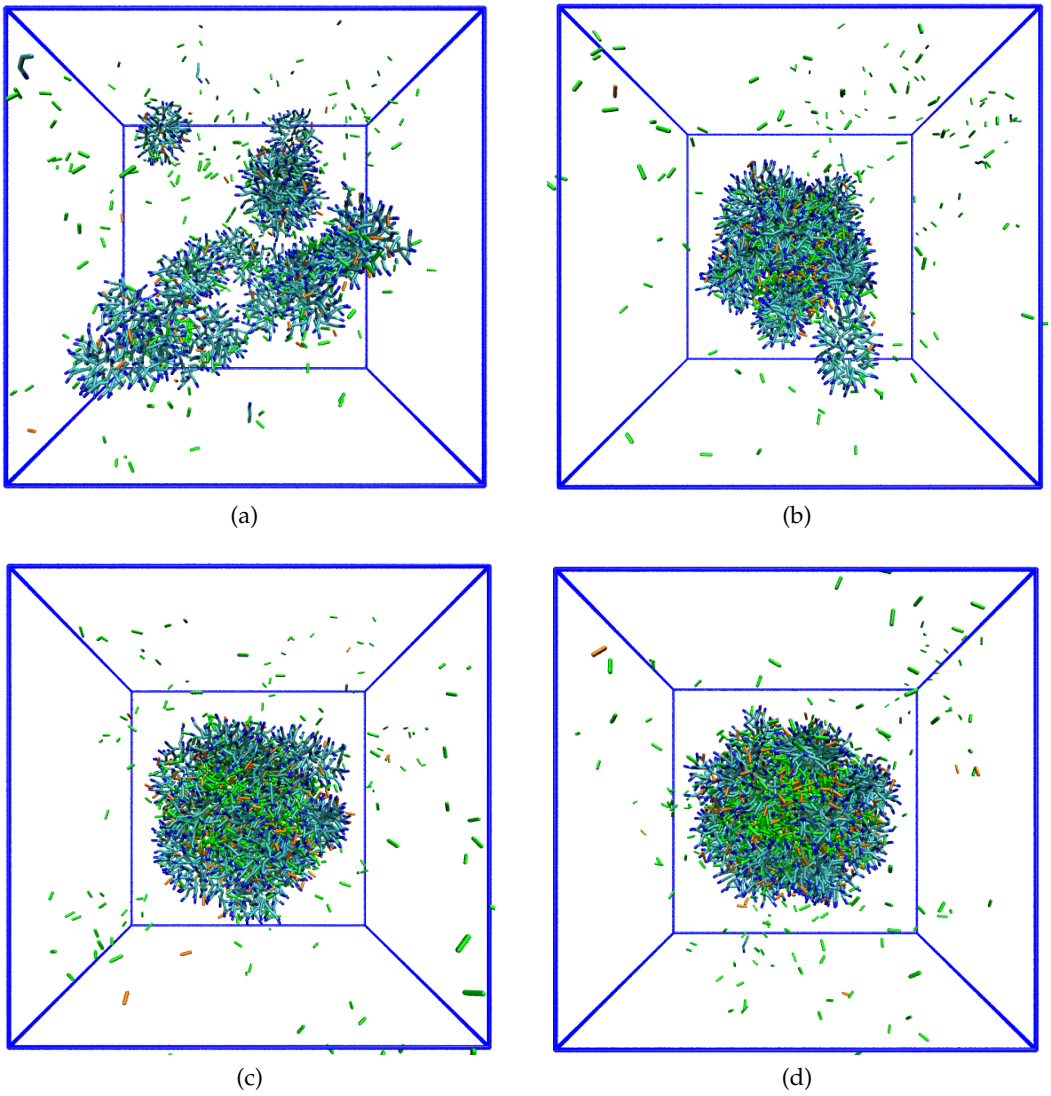

(a) (b)

(c) (d)

Figure 4.44: Final configurations obtained for the systems with SISN and SNSN using a increasing silica-to-surfactant ratio: a, one-to-one and b, two-to-one, c, three-to-one and d, four-to-one Water and chloride ions have been removed for clarity. Colour code is the same as in Figure 4.40 with SISI orange and SNSN green.

than one, a somewhat disordered packing of rod-like micelles is observed. Interestingly, the compactness of the aggregates formed seems to increase with the increasing number of silica dimers available. Both types of oligomers adsorb around the surfactant rods, promoting their assembly. However, the nature of the surfactant molecules favours formation of twisted rods, as can be seen in Figure 4.45, leading to much more disordered silica-surfactant mesophases in comparison to what was observed for MCM-41. This result is in agreement with the "worm-like" or "worm-

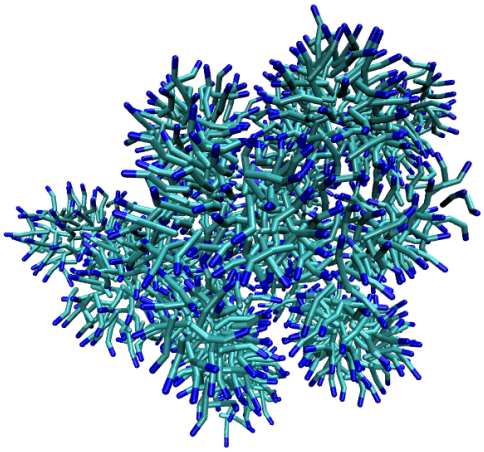

Figure 4.45: Final configurations showing only surfactants for the systems with SISN and SNSN and using a two-to-one ratio of silica to surfactants. Water has been removed for clarity. Colour code is the same as in Figure 4.40.

hole" aggregates described experimentally [126] and indicates that HMS materials are effectively much more disordered than MCM-41 analogues.

In Figure 4.46-(a) and (b) snapshots of the cross sections obtained for the systems in Figure 4.44-(d) and in Figure 4.43-(b), respectively, are provided. These cross section images reveal that, even though both systems produce disordered phase separation, the type of aggregates formed are quite different. The system containing dimers, on the left, shows rods packing and silicates adsorption around these organic structures. In contrast, in the neutral system, on the right, only few SN monomers are observed inside the surfactant aggregate, as confirmed also by looking at the density profile for this system displayed in Figure 4.46-(c). These results indicate substantially different behaviour of the silicates when they are in solution with charged or neutral surfactants. In one case, with DDA^+, dimers (but also monomers, as observed before) produce structural changes in the surfactant

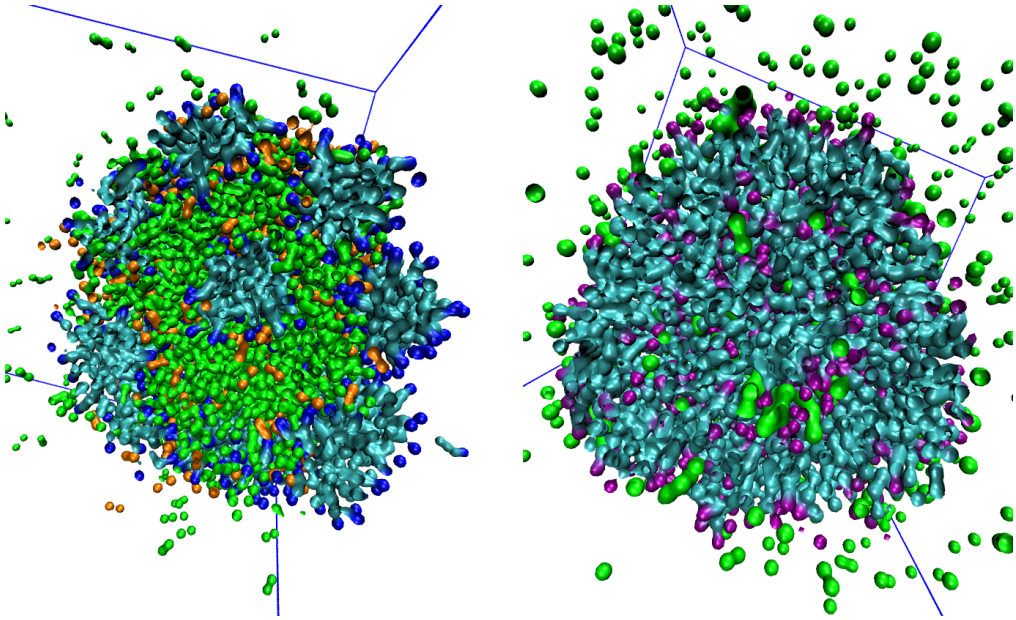

(a) (b)

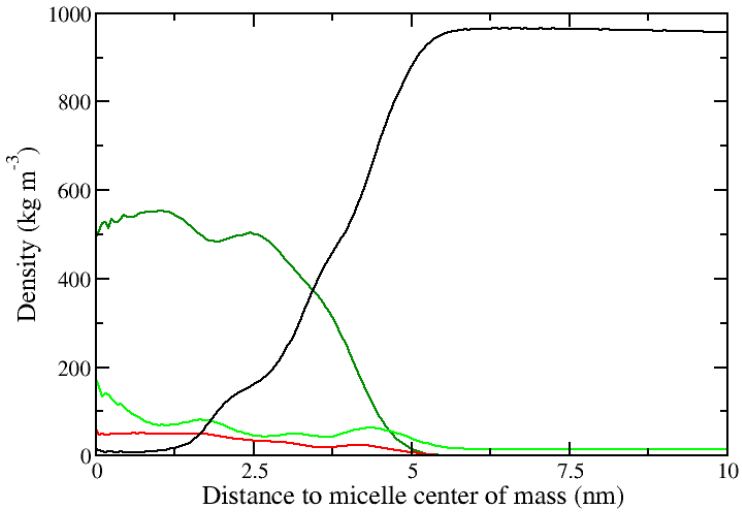

(c)

Figure 4.46: Snapshots showing the cross sections of the final configurations obtained for: (a), the systems with charged surfactants plus SISN and SNSN dimers, using a four-to-one ratio of silica to surfactants; (b), the system with neutral surfactants and SN monomers. Water has been removed for clarity. Colour code for snapshot-(a) is the same as in Figure 4.44. Colour code for snapshot-(b) is the same as in Figure 4.43-(b). (c), average aggregate density profile for the system in (b). Colour code for the density profile is the same as in Figure 4.19.

mesophase, whereas with DDA no significant alteration in the surfactant phase is observed.

To assess whether the presence of doubly charged silica dimers can produce more order structures, a further simulation containing these species was performed. The system simulated contains the same number of charges as the last discussed case (the system with SISI and SNSN dimers and a four-to-one silica to surfactant ratio), however these charges are condensed on half the number of SISI dimers (cf. last two rows of Table 4.6). The rationale for this choice is based on the fact that Pérez-Sánchez et al. have observed that these multiply charged species, which act as bridges, are necessary for the formation of hexagonal liquid crystals during PMS synthesis [7].

Results for these conditions are displayed in Figure 4.47. Due to the high concen-

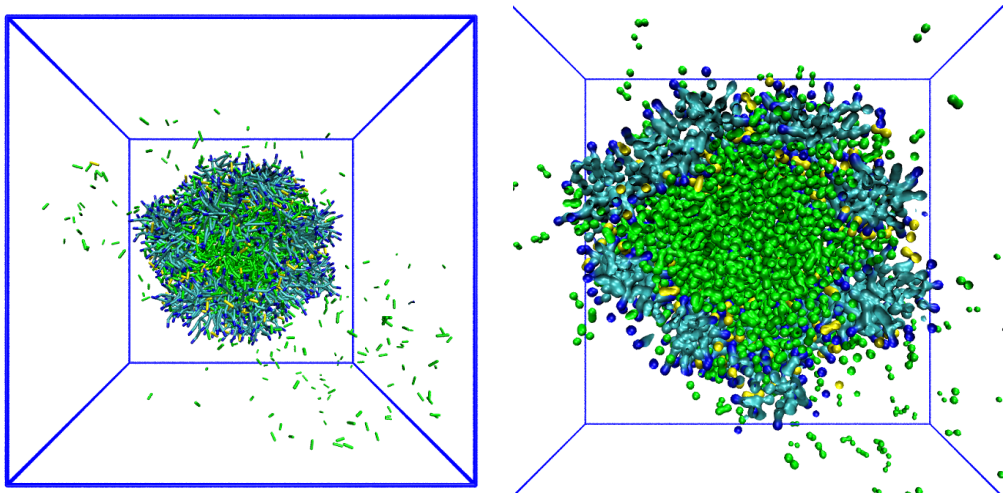

(a) (b)

Figure 4.47: Snapshots showing the final configuration (a) and the cross section (b) for the systems with charged surfactants plus SISI and SNSN dimers, using a four-to-one ratio of silica to surfactants. Water and chloride ions have been removed for clarity. Colour code is the same as in Figure 4.44 with SISI dimers in yellow.

tration of neutral dimers, the mesophase formed appears even more disordered that in the previous case. This result indicates that, if the ordering effect of SISI dimers applies also to the system with DDA surfactants, this low concentration is not enough to produce any significant order improvement. Another possibility is that the SNSN dimers, by clustering together, hinder the bridging character of SISI

dimers, hence producing more disordered packing and "worm-holes" aggregates. More detailed simulations are needed to fully clarify this effect.

4.3 CONCLUSIONS

In this chapter, a multi-scale approach for modelling the synthesis of HMS materials was presented. By performing atomistic (AA) simulations of preformed micelles of dodecylamine surfactants (DDA), at different pH conditions and with both silica monomers and dimers in solution, it was possible to develop, for the considered system, a coarse-grained (CG) model, based on the MARTINI force field [10]. The procedure adopted to derive CG parameters adjusts individual interactions between CG beads until reasonable agreement is obtained between AA and CG micelle density profiles of aggregates having the same size. Once parameters for all species were obtained, the CG model for charged surfactants (DDA^+) was validated by reproducing selected conditions on the dodecylammonium chloride-water phase diagram. Although the experimentally reported hexagonal phase was not observed, micellar and lamellar phases were reproduced using CG simulations. Furthermore, good agreement with experimental data [143] was obtained for the calculated average aggregation number at 50 °C in the micellar region.

Subsequently, CG simulations of HMS materials synthesis at different pH were performed. In the first step, the system containing only surfactants (the reference system) was investigated. Results for this system show that at high pH (> 12) neutral DDA surfactants phase separate producing disordered phases. On the contrary, charged DDA^+ at pH < 8 produce micellar aggregates in water and large branched rods when chloride counter-ions are replaced by anionic silica monomers (SI), to represent the monomeric solution. Interestingly, when silica monomers (both neutral, SN or anionic) were added to the system containing neutral surfactants, no significant changes were observed in the phase-separated aggregate formed at these conditions.

These results obtained indicate that charged surfactants are necessary in order to produce formation of ordered structures that can act as templates for HMS synthesis. Therefore, these conditions were studied in more detail by estimating the experimental pH of synthesis, both for the monomeric solution and for the solution with dimers (i.e. the latter representing a more advanced stage of the synthesis). Simulations of the monomeric solution at experimental pH (i.e. 77 % of the

monomers are neutral and 23 % charged) showed the formation of branched rods with both SN and SI monomers adsorbing around the surfactants aggregates. Finally, when dimers were added to the system, in the proportion obtained from pH calculation (i.e. 76 % neutral dimers and 24 % singly charged dimers), a somewhat disordered packing of rods is observed. These results are in agreement with the "worm-like" or "worm-hole" aggregates found experimentally, and indicate that HMS materials are significantly more disordered than MCM-41. Another implication of these results is that the neutral templating route proposed for the synthesis of HMS materials [9] does not seem to be possible to describe their formation, since simulations of neutral surfactants and neutral silicates lead to phase separation with only few inorganic species adsorbing around the disordered aggregates formed.

5

MODELLING THE SYNTHESIS OF MSU-V MATERIALS

As described in section 2.3.2, MSU-V materials can be regarded as one of the first examples of biomimetic templating synthesis [8, 37]. They exhibit hierarchical lamellar structures and are produced using diamine surfactants of different chain lengths (up to 22 carbons) as templates. Similarly to the HMS materials discussed in the previous chapter, also for MSU-V materials a neutral templating route (S^oI^o) has been proposed to describe their synthesis. It has, in fact, been suggested that weak hydrogen bond interactions, between uncharged layers of organic species and inorganic species adsorbing at the interface with water, direct their formation, although no clear evidence is given for the proposed mechanism. In the present chapter, atomistic (AA) molecular dynamics (MD) simulations of the precursor solutions of MSU-V materials are carried out to help elucidate the molecular interactions taking place during their synthesis. The methodology used is based on the work of Jorge et al. and Pérez-Sánchez et al., who have successfully applied AA and CG MD simulations to study the synthesis of MCM-41 type materials, providing more insight into their mechanism of formation [6, 16, 65].

5.1 ATOMISTIC SIMULATIONS OF MSU-V MATERIALS

To investigate the formation mechanism of bio-inspired silica materials, a solution of 1,12-diaminododecane (DADD) and a monomeric silica source at several pH values was considered. As already said, the experimental benchmark is the work of Tanev and Pinnavaia, which describes the synthesis of MSU-V materials with a relatively simple biomimetic approach [8, 37]. Their reacting mixture is composed of a solution of DADD in ethanol and water to which TEOS is added in the proportion 0.26 DADD : 13.1 ethanol: 50.8 water : 1 TEOS. For computational expediency, the system studied with MD simulations has been simplified: i) ethanol was neg-

Parts of this chapter have been published in: Centi, A. and Jorge, M. 'Molecular Simulation Study of the Early Stages of Formation of Bioinspired Mesoporous Silica Materials'. *Langmuir* 32.28 (2016), pp. 7228–7240. DOI: 10.1021/acs.langmuir.6b01731.

lected and replaced by water, since it is not expected to play an important role during the structure formation (this simplification was also done earlier to simulate the synthesis of HMS materials); ii) a lower silica to amine ratio was used (1 : 1 or 2 : 1 instead of approximately 4 : 1) to facilitate comparison between different solutions on a equal basis. This last point will be explained in more detail later.

5.1.1 *System preparation and computational details*

Three main types of simulations were performed:

- the reference solution, containing only DADD and water, discussed in section 5.1.2;
- the monomeric solution, which also included silica monomers to represent the early stage of formation of MSU-V materials, discussed in section 5.1.3;
- a system representing conditions close to experiment, discussed section 5.1.4.

Most simulations started from a random distribution of all species in the simulation box, but for several cases simulations starting from preformed surfactant layers were also performed. The idea was to establish whether or not the layer represents the real equilibrium structure for the system under evaluation. In molecular dynamics the equilibrium state is normally approached starting from random configurations, however some systems might be affected by very slow dynamics and reaching this equilibrium might be computationally very expensive. To overcome this problem one can think of also approaching equilibrium from the opposite side, e.g. starting the simulation from a highly ordered state and following its evolution. If the preformed states do not correspond to equilibrium structures, they should start collapsing quite rapidly and eventually become homogeneously dispersed in the system, however if they are stable aggregates they will only undergo small internal rearrangements.

Details about the entire set of simulations performed, including length, number of molecules and final box size, can be found in Table 5.1 and 5.2. The first letter of the simulation name refers to how the system was created: R indicates that all the molecules were randomly placed in the box at the start of the run and P designates a simulation in which preformed layers of surfactants were used as initial configuration. This letter is followed by a running number for each type of system analysed. Then the type of surfactant used is provided, with DADDn used for

Table 5.1: Simulation characteristics for section 5.1.2 and 5.1.3.

System	Length	n. of surf.	n. of water	n. of Br	n. of $Si(OH)_3O^-$	n. of TMA^+	final box size	concentration
	ns	molec.	molec	ions	molec	ions	nm	mol/L
R1-DADDn	11	75	3753	-	-	-	5.17	0.9
R2-DADDn	32	140	3130	-	-	-	5.20	1.65
R3-DADDn	22	193	2320	-	-	-	5.12	2.39
R4-DADDn	22	277	1452	-	-	-	5.17	3.33
P1-DADDn	20	278	1452	-	-	-	5.13	3.42
P2-DADDn	22	140	3256	-	-	-	5.24	1.62
R5-DADDs	20	142	3096	142	-	-	5.28	1.60
P3-DADDs	20	142	3128	142	-	-	5.28	1.60
R6-DADDd	20	140	3130	280	-	-	5.39	1.49
P4-DADDd	15	130	2798	260	-	-	5.22	1.52
P5-DADDd	20	100	3102	200	-	-	5.17	1.20
P6-DADDn-Si	26	140	1663	-	140	140	5.02	1.84
P7-DADDs-Si	30	142	2467	-	142	-	5.13	1.75
P8-DADDd-Si	20	130	1938	-	260	-	5.05	1.68

neutral diaminododecane molecules, DADDs for singly charged and DADDd for doubly charged. Finally "Si" is added for simulations containing silica monomers.

The reference system was investigated first, considering the effect of an increase in concentration of neutral polyamine molecules in water. It should be noted that the ratio of surfactants to water species used to represent each concentration has been determined so that, when the system reaches its equilibrium state, the final box size is kept constant at approximately 5.2 nm in each direction (see Table 5.1 for details about each simulation run). Next, the effect of a change in pH on this same system was investigated and, in order to establish a direct comparison with the previous set of simulations, only the concentration that produced a complete layer of neutral surfactants was used (simulation R2-DADDn). Once again, the number of water molecules was adjusted so that the final box size was approximately kept constant at equilibrium while the overall neutrality of the system was achieved by adding bromide counter-ions. The relative proportion of different surfactant species in the the system was determined considering specific pH conditions. Wang et al. found that nonionic DADD molecules are present at high pH (above 11), singly charged DADD at pH between 8 and 11 whereas doubly charged species are found at pH lower than 8 [155]. Ohtaki and Maeda determined the dissociation constants of several protonated diamines, among which 1-12-diaminododecane, using potentiometric methods [156]. These dissociation constants were used to obtain the titration curve for this system (see Figure 5.1-a) through the utility CurTiPot [154]. In agreement with the results of Wang et al., the titration curve indicates that the

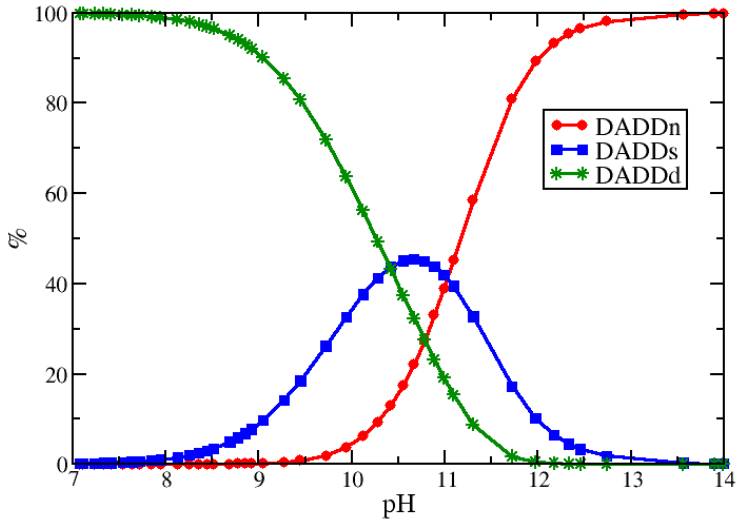

(a) Reference solution

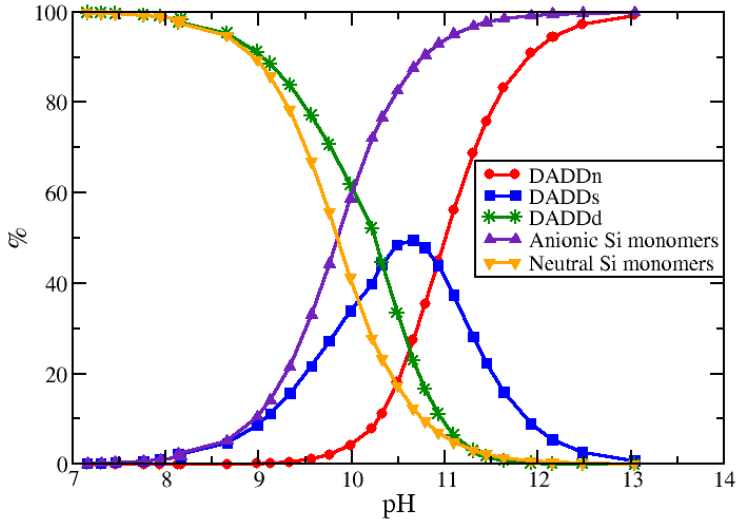

(b) Monomeric solution

Figure 5.1: Titration curves for the systems 1,12-diaminododecane-water, (a) and 1,12-diaminododecane-silicic acid-water, (b).

Table 5.2: Simulation details for experimental case, section 5.1.4.

		R7-EXP-reference	P9-EXP-reference		P10-EXP-monomeric
System	%	n. of molecules	n. of molecules	%	n. of molecules
DADDn	~27 %	38	38	~25 %	35
DADDs	~45 %	63	63	~51 %	71
DADDd	~27 %	39	39	~24 %	34
Br ions	-	141	141	-	-
TMA ions	-	-	-	-	112
water	-	2785	2784	-	1484
$Si(OH)_4$	-	-	-	~10 %	29
$Si(OH)_3O^-$	-	-	-	~90 %	251
time (ns)	-	100	20	-	91

fully charged and neutral species are dominant at the two extremes of the pH range, circum-neutral and high pH respectively, whereas in the range of intermediate pH all three species are present at the approximate ratio of 50 % for DADDs and 25 % for both DADDn and DADDd [155].

The preformed layer structures used as starting configurations in the stability tests were created with the procedure described here. First, a layer containing surfactant molecules was made using the software Packmol [131]; this allows to build initial configurations such as lamellar, vesicles or other ordered systems simply by placing molecules in the simulation box according to specific geometrical constraints. The size of the simulation box was chosen considering the equilibrium box size for the system obtained from corresponding "random" simulations. Then, the system containing only the preformed layer was relaxed and, subsequently, other species, such as counter-ions or silica, were added and the system solvated using a pre-equilibrated box of water as a source.

In the last part, the influence of the addition of anionic silica to preformed surfactant aggregates is studied for different pH conditions. The initial configurations were created with the procedure described above for the stability tests, with the only difference that $Si(OH)_3O^-$ monomers were added instead of bromide counter-

ions. It should be noted that when neutral surfactants are used, positive counter-ions need to be added to the system in order to balance the negative charge of the anionic silica species. Tetramethylammonium (TMA) ions are used for this purpose since they are not expected to play an important role during the aggregation process [16]. The titration curve in Figure 5.1-(b) was obtained in the same way as before but including the pKa for silicic acid [30], and shows that silica monomers are mostly in their neutral form at pH below 8 while at high pH they become predominantly anionic.

COMPUTATIONAL DETAILS All the simulations were performed using the package GROMACS 4.6 [88]. For all the concentrations and pH studied, production runs were performed in the *NPT* ensemble, by keeping the temperature constant at 298.15 K with the Nosé-Hoover thermostat [95] and the pressure fixed at 1 bar employing the Parrinello-Rahman barostat [97]. The equations of motions were integrated using the leap-frog algorithm [92] with a time step of 2 fs. The actual production simulations were preceded by an energy minimisation step as well as by two short equilibration simulations, first in the *NVT* and then in the *NPT* ensemble, the length of which depends on the time needed to equilibrate the system density. The simulation boxes were always cubic with periodic boundary conditions applied in x, y and z directions.

DADD surfactants are called "two-headed amphiphiles" or "bolaamphiphiles". This term is used to describe molecules consisting of two head groups separated by a long hydrocarbon chain [157]. To be more precise, a single DADD molecule contains, depending on the protonation state, 42 (DADDn, neutral surfactant), 43 (DADDs, singly charged surfactant) or 44 (DADDd, doubly charged surfactant) sites. A representation of the three surfactants used is provided in Figure 5.2: the amino group differentiates neutral surfactants from singly and doubly charged species. Atom labels are described in section 4.1 (cf. Figure 4.2). The OPLS (Optimized Potentials for Liquid Simulations) all-atom (AA) force field [80, 81] is used to describe surfactants and counter-ions, such as bromide and TMA. Water molecules were modelled using the SPC/E (Extended Simple Point Charge) potential [132] (see section 4.1 for more details). Parameters used for the neutral and anion silicic acid are taken from the work of Jorge et al. [6] (see Figure 4.3 and description there). Bond lengths were constrained by applying the LINCS algorithm [135], a cutoff of 1.2 nm was applied to short-range dispersion interactions and the same distance for the particle-mesh Ewald method (PME) [90, 136] to take into account

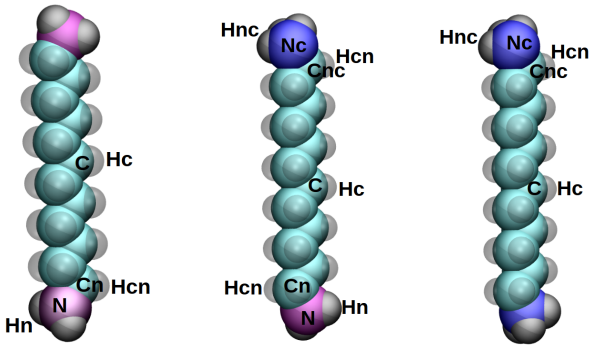

(a) DADDn (b) DADDs (c) DADDd

Figure 5.2: All-atom representations of DADD surfactants in different charge states. Neutral nitrogens, purple; charged nitrogens, blue; carbons, cyan and hydrogens, gray.

the long-range Coulomb electrostatics. Finally, a long-range dispersion correction term was added to both energy and pressure. Details of the entire set of parameters used can be found in Tables B.1 - B.4 of Appendix B.

One of the objectives of this work is to analyse the development of the surfactant aggregation process, with and without silica, in order to have a better insight of the role played by the latter. This means monitoring the evolution of the system over time and calculating characteristic properties such as the number of clusters and average cluster size as well as the distribution of surfactant aggregates. For this purpose, an adaptation of the Hoshen-Kopelman cluster-counting algorithm [138] was used to analyse sampled trajectories. Two DADD molecules were considered to belong to the same cluster if the distance between at least one of the three central atoms (one carbon C and two hydrogens Hc) was less than 0.65 nm. Different criteria (for example considering six central atoms instead of three) and values for the limiting distance between carbon/hydrogen atoms were tested by visually inspecting distinct time frames of the system. The final value chosen provides the correct cluster size distribution for all the types of surfactant molecules and is close to the position of the first minimum in the radial distribution function (RDF) between aliphatic hydrogen and carbon atoms (see Equation (4.1)).

For the simulations that produced layers, the interfacial tension was calculated in order to obtain an indication of the system tendency to evolve from layer-like structures into aggregates with higher interfacial areas, e.g. vesicles. This was done via the virial route [158, 159] by calculating the pressure tensor using the utility

g_energy in GROMACS [88], and averaging the values over the last 15 ns of the production run. It should be noted that each value must be divided by the number of surfaces, 2 in this case. Finally, all the images presented were produced using the software VMD [130].

5.1.2 *The reference solution*

Understanding the process of formation of bio-inspired mesoporous silica materials is the main objective of this work. However, to clearly assess the role played by both surfactants and silica species in the synthesis, it is first necessary to examine in detail the self-assembly process of the polyamine molecules in the absence of silicates and at different concentration and pH conditions, as it has not yet been addressed in the literature.

EFFECT OF CONCENTRATION Figure 5.3 shows the equilibrium configurations obtained in the reference solution for an increasing concentration of neutral surfactant molecules (see Table 5.1). Highly ordered lamellar aggregates are formed only for the two intermediate values of concentration, 1.65 and 2.39 mol/L (at the lower concentration, the aggregate formed appears to be a frustrated layer due to the finite size of the simulation box). Both layers appear to be completely dry and are composed, respectively, of 136 and 189 amine molecules. It is interesting to observe that when the number of surfactants is increased from 140 (R2-DADDn) to 193 (R3-DADDn), they tend to pack by maximising the number of molecules that can be accommodated in a single layer. In a cubic box this corresponds to a transition from a horizontal layer to a diagonal layer; in both cases, however, a small number of dispersed monomers in equilibrium are observed. When the number of surfactants is further increased to 277 (R4-DADDn), it would be expected that the reciprocal interactions between aggregates would become more important and the system would evolve towards more ordered configurations [21], however a less organised bi-continuous phase, made of three incomplete tilted layers intersecting each other, is formed. One possibility is that the size and the shape of the simulation box might not allow to observe the creation of a bilayer phase. This possibility can, however, be excluded by performing simulations with preformed bilayer structures containing the same number of surfactants and water molecules. For this purpose the system P1-DADDn was created by placing two identical lay-

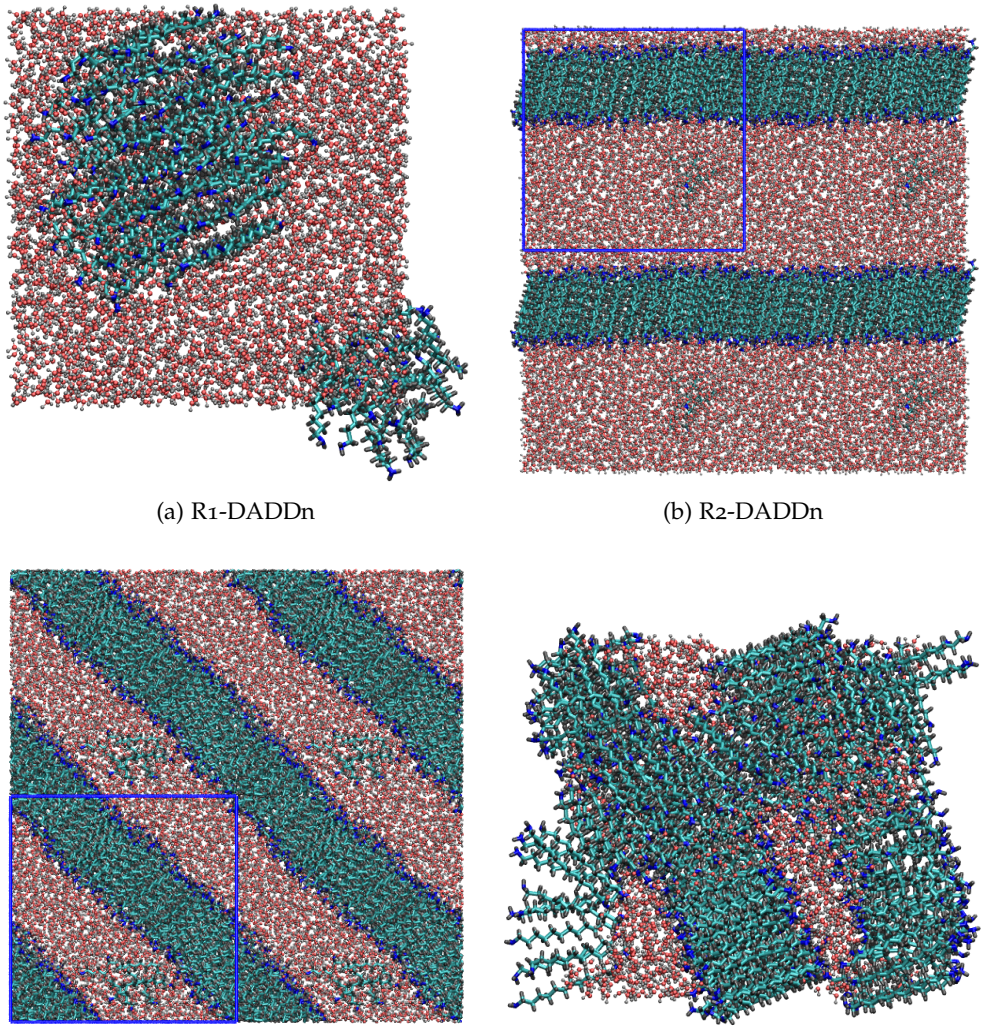

(a) R1-DADDn

(b) R2-DADDn

(c) R3-DADDn

(d) R4-DADDn

Figure 5.3: Snapshots of 2D cross-section of the simulation box at different concentrations. Nitrogens, blue; hydrogens, grey; carbons, cyan and oxygen, red. For clarity, periodic replicas have been added in (b) and (c) where the blue lines represent the boundaries of a single simulation box

.

ers, each containing 136 surfactants, separated by two water slabs containing 726 water molecules. The total number of water molecules is the same as that used in the simulation R4-DADDn (see Table 5.1) whereas the number of surfactants in the layer was chosen considering the results obtained for the system R2-DADDn, which produced a complete horizontal layer. Furthermore, to account for the remaining surfactants in R4-DADDn (277 in total) three DADDn molecules were added in each water slab. From Figure 5.4, where the final configuration obtained for the bilayer system P1-DADDn (a) and the corresponding density profile (b) are shown, it can be seen that these aggregates remain stable in water. Therefore,

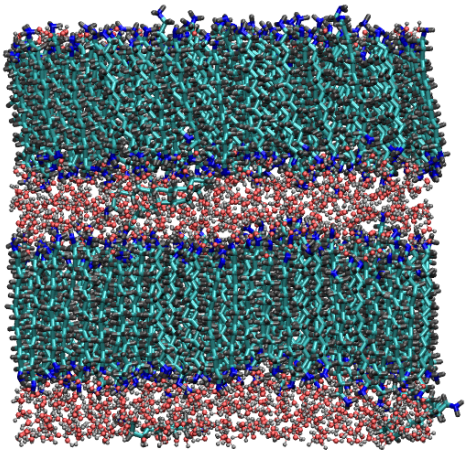

Figure 5.4: Snapshot of the final configuration obtained for the bilayer system. Colour code is the same as in Figure 5.3.

a more likely possibility is that the bicontinuous phase observed in R4-DADDn could just represent an intermediate structure and the process leading to the creation of an ordered arrangement occurs too slowly for our atomistic simulations.

In Figure 5.5 a comparison of the evolution of the number-average cluster size over time for the four systems represented in Figure 5.3 is shown. It should be noted that both equilibration steps (*NVT* and *NPT*) that preceded each MD production run are included in the cluster counting analysis; therefore the total length of the simulation is slightly different from what is reported in Table 5.1. For what concerns the lower concentration (R1-DADDn) the aggregation process occurs through three successive steps, each representing the fusion of two smaller clusters. In agreement with what has been just discussed, it can be noted that the initial aggregation process is substantially faster when the number of surfactants

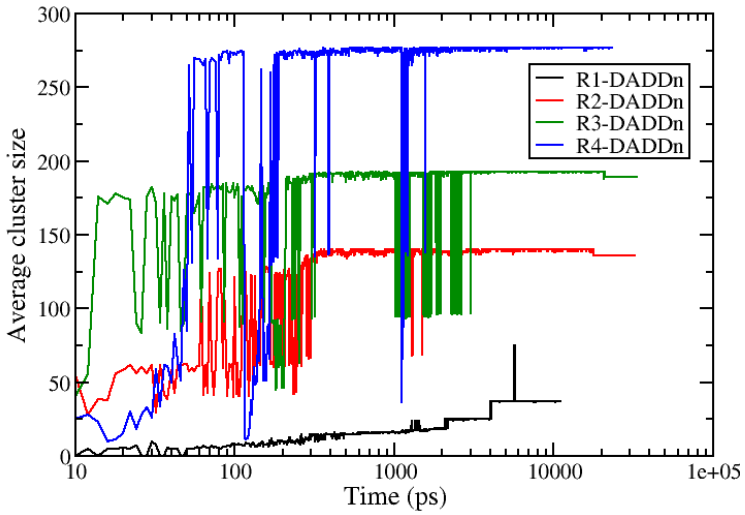

Figure 5.5: Evolution the average cluster size for simulations with different concentration of neutral surfactants, listed in Table 5.1. The total number of surfactants is respectively 75 (R1-DADDn), 140 (R2-DADDn), 193 (R3-DADDn), 277 (R4-DADDn).

is doubled (from R1-DADDn to R2-DADDn) and the system starts approaching the equilibrium value very quickly. This represents, in the case of R2-DADDn and R3-DADDn, the number of molecules that can be accommodated in a stable layer. Although increasing the concentration speeds-up the aggregation process, the system requires more time to reach a fully ordered state, like in the case of the bicontinuous system (R4-DADDn).

EFFECT OF PH Once the influence of the concentration on the aggregation process of DADD surfactants was understood, the effect of pH (i.e. the charged state of the surfactant molecules) on the structure and types of aggregates formed was studied. This is a very important aspect since the hydrophobic/hydrophilic character of surfactant molecules, and therefore their interactions with silicate species, will depend on their charged state. The focus is on the surfactant concentration that potentially leads to formation of single horizontal layers (approximately 1.6 mol/L, cf. Table 5.1).

Figure 5.6 shows the final configurations obtained, in the case of neutral surfactants, starting from a preformed layer (a) and from an initially random system (b). The two layers are practically identical as shown by looking at the density profiles across the box (Figure 5.6-(c)). The central part of the layer is occupied

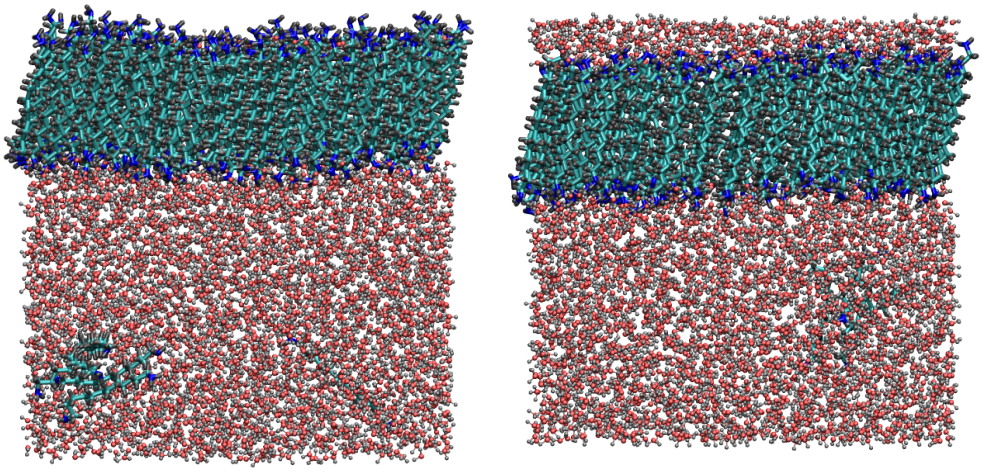

(a) P2-DADDn (b) R2-DADDn

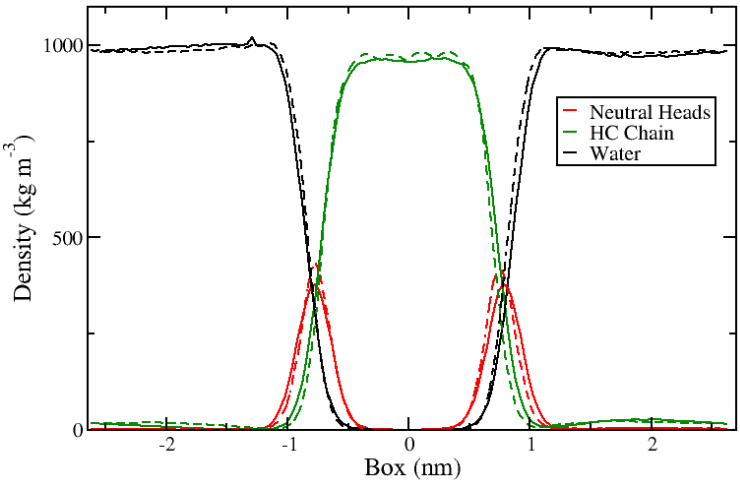

(c)

Figure 5.6: Snapshots of 2D cross-section of the simulation box for (a) P2-DADDn and (b) R2-DADDn and corresponding equilibrium density profiles across the box (c), starting from random initial configurations of surfactants (R2-DADDn, solid line) and from a preformed layer (P2-DADDn, dashed line). Colour code is the same as in Figure 5.3.

by the hydrocarbon chains, which in turn create, due to their strong hydrophobic character, a water depletion region. The neutral heads are localised at the interface with water where they establish favourable hydrophilic interactions. In Figure 5.7, a comparison between the number of clusters and number-average cluster size calculated for the two systems demonstrates that they both evolve towards the same final equilibrium values. It is worth noting that the number-average cluster size

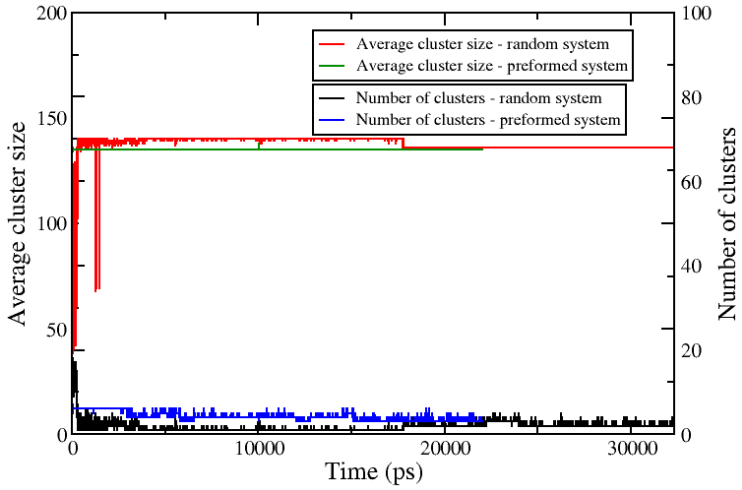

Figure 5.7: Comparison between simulation results starting from random initial configurations of surfactants (R2-DADDn) and from preformed layer (P2-DADDn).

computed for the preformed system is essentially constant, implying that the layer does not undergo any major rearrangement. This confirms that DADD neutral surfactants form stable layer structures in water.

Figure 5.8 displays the results of simulations with singly charged surfactants, comparing the final configurations obtained starting from preformed layers, (a) and (b), and from random configurations (c). Although the random system did not produce a complete layer, the formation of large ordered structures can be observed after approximately 5 ns (Figure 5.8-(c)). These separate blocks are likely to merge together and form a layer similar to the one we observed in the neutral system. Time limitations might not allow to obtain the equilibrium structures, but, once again, the use of simulations with preformed layers can help identifying possible stable states for this system. It was found that a layer of DADDs surfactants contains 141 molecules (5 more than a layer of neutral surfactants) in approximately the same box size (Figure 5.8-(a)).

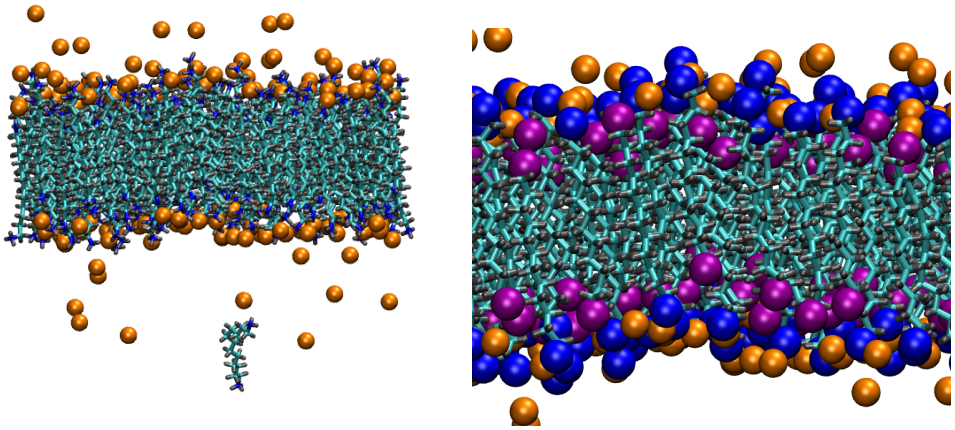

(a) P3-DADDs

(b) P3-DADDs

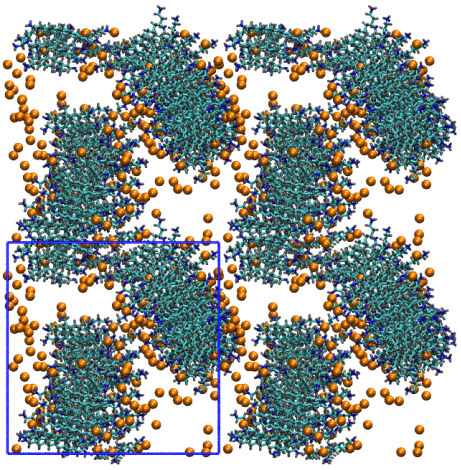

(c) R5-DADDs

Figure 5.8: Snapshots of 2D cross section of the simulation box for P3-DADDs, (a) starting from a preformed layer and (b) detail of the layer shown in (a); (c) snapshot of 2D cross section of simulation box obtained for R5-DADDs starting from a random initial configuration of surfactants. Colour code is the same as in Figure 5.6 with bromide orange, charged nitrogens blue and neutral nitrogens purple. Periodic replicas have been added in (c) where the blue lines represent the boundaries of a single simulation box. Water molecules are not shown for clarity.

More information about the singly charged system can also be extracted by looking at the evolution of the number of clusters and the number-average cluster size in Figure 5.9. The trajectory of the random simulation (R5-DADDs) was analysed

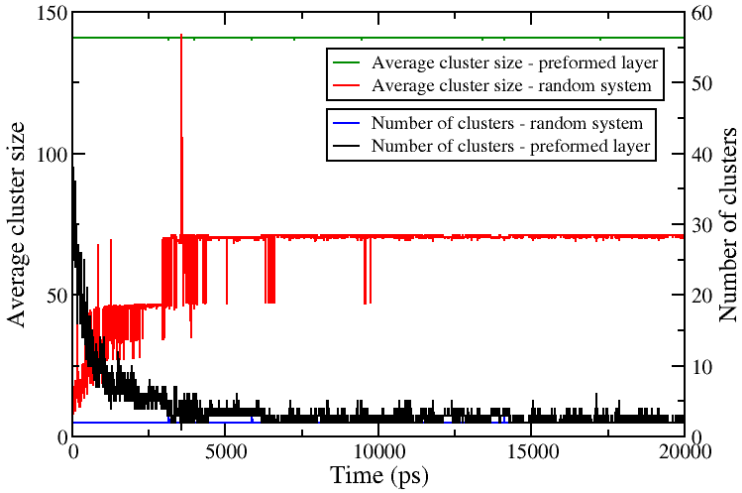

Figure 5.9: Comparison between simulation results obtained for the singly charged system for simulations starting from random (R5-DADDs) and from a preformed layer (P3-DADDs). Number of clusters: random, red and packmol, black. Number average cluster size: random, dark green and packmol, blue.

and compared to the one produced using the preformed layer for the same concentration of surfactants (P3-DADDs). The first trajectory seems to approach but does not really reach the final equilibrium value of 141 molecules packed in the layer. The aggregation process takes place by successive fusion steps similar to what was observed in the neutral system for the lowest concentration. The larger these aggregates are, the more stable they become and therefore the longer it takes for them to merge into bigger structures. This behaviour is also reflected in the evolution of the total number of clusters: it rapidly decreases at the very beginning of the simulation and then, after 5 ns approximately, essentially oscillates at very low numbers (mainly between 4 and 2) due to molecules that temporarily leave the two major aggregates. It is thus reasonable to expect to see a complete layer to form after a long simulation time, and this is supported by the fact that the preformed layer is highly stable in water during a long MD trajectory.

A detail of the final configuration obtained for P3-DADDs is provided in Figure 5.8-(b). Here a different color code has been used to distinguish between charged and neutral heads (blue and purple, respectively). The two types of heads

appear to be alternating in the lamellar structure, with the charged groups in close contact with the bromide ions while the neutral heads are located slightly below the interface with water. This arrangement produces the minimum repulsion interactions between the charged head groups and, at the same time, makes the layer more compact, so that more surfactant molecules can fit inside it. Another interesting feature is that the DADDs molecules inside the layer seem to have a more straight conformation in comparison to the neutral DADD molecules, which appear to be slightly tilted (Figure 5.6-(a) and (b)). This change in conformation could be related to the surface tension and will be discussed later.

Figure 5.10 compares neutral and singly charged layer density profiles. In both

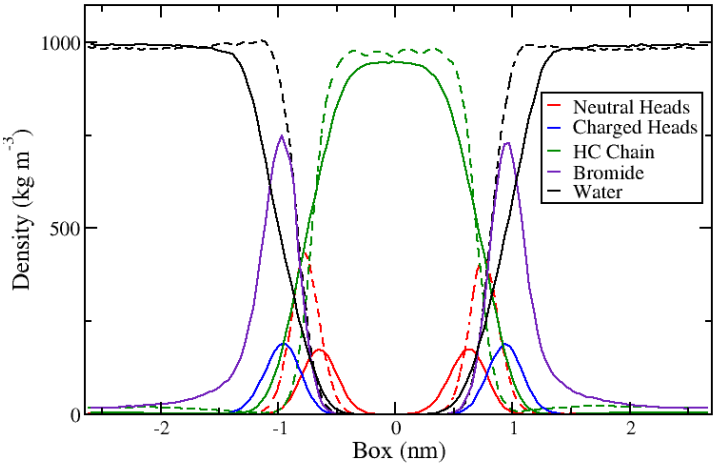

Figure 5.10: Comparison between density profiles across the box in the singly charged system (P3-DADDs, solid line) and in the neutral system (P2-DADDn, dashed line).

layers, the hydrocarbon chains are located in the central part producing a dry region. The shape of the singly charged profile is, however, slightly different compared to its counterpart in the neutral system: the peak appears to be narrower while the tails of the distribution extend further than in the neutral system. This is due to the alternating arrangement of surfactant heads in the layer, causing the neutral heads to slide towards the middle part of the layer while the charged ones prefer to stay at the interface. It is also worth noting that the peak corresponding to the head density distribution for the DADDn system is located at the mid-point between neutral and charged head profiles belonging to the DADDs system. The interface itself is in general more structured in the latter system because of the pres-

ence of bromide counter-ions. Bromide peaks essentially overlap with the charged head peaks, causing the water layer to move back (in comparison to the neutral system) while increasing the depletion region around the hydrocarbon chain.

In Figure 5.11 the RDFs between different regions are analysed to gain more insights into the structures resulting from DADDs surfactant aggregation. Both

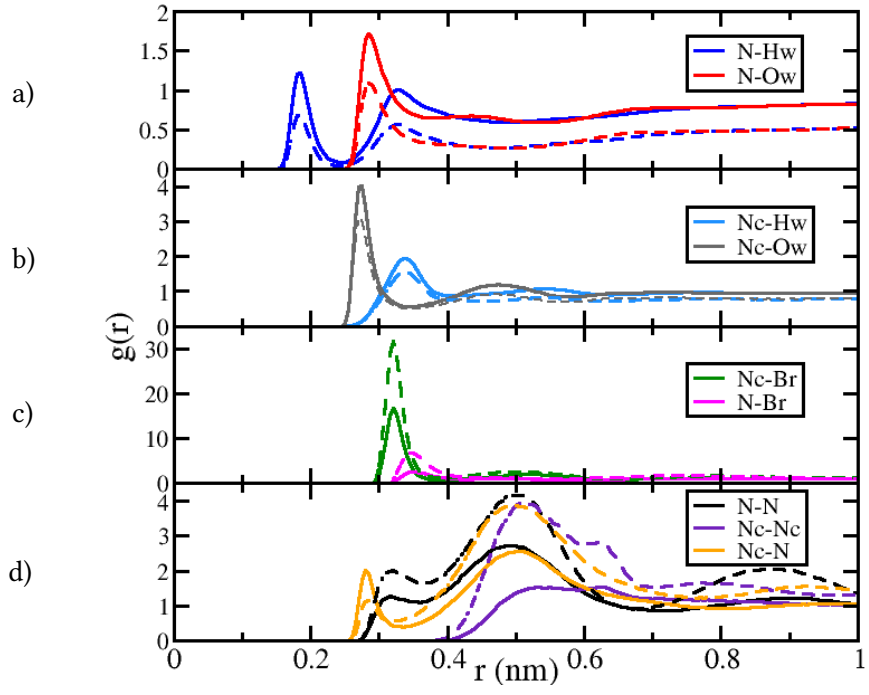

Figure 5.11: Radial distribution functions obtained in P3-DADDs (dashed lines) and R5-DADDs (solid lines): for (a), interactions between neutral heads and water; (b), interactions between charged heads and water; (c), interactions between heads and bromide and (d), interactions between neutral and charged heads.

charged and neutral heads (solid lines) exhibit stronger interactions with water in the incomplete layer and, as expected, the magnitude of these interactions is higher for positively charged nitrogens (see Figure 5.11-(a) and (b)). On the other hand, the increase of order and compactness in the complete layer favours the interactions between nitrogens and bromide ions as well as among head groups (see Figure 5.11-(c) and (d)). All the RDFs calculated between head groups show a main peak located approximately at 0.5 nm with a very similar magnitude of

interaction, confirming the regular alternated arrangement of surfactant molecules in the layer described by visual inspection of the final snapshots.

Figure 5.12 shows the equilibrium configuration obtained with a preformed layer of doubly charged surfactant molecules (P4-DADDd, (a)) and with random initial configurations (R6-DADDd, (b)). The final results appear to be very similar: the

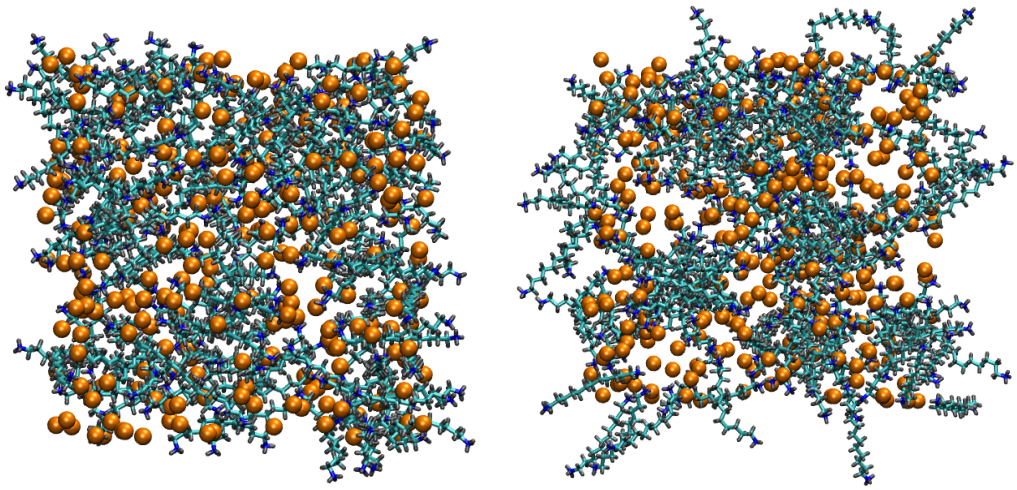

(a) P4-DADDd (b) R6-DADDd

Figure 5.12: Snapshot of 2D cross-section of the simulation box of P4-DADDd (a) and comparison with the 2D cross-section of the simulation box of R6-DADDd (b). The layer made with Packmol is quickly destroyed. Colour code is the same as in Figure 5.8. Water has been removed for clarity.

preformed layer starts breaking apart very quickly and it is practically entirely destroyed after the first 5 ns of simulation time, as shown in Figure 5.13-(a), while the random system only produced small aggregates. This is due to the stronger electrostatic repulsion between surfactant head groups in this system which tends to favour interactions with water. The high solubility of DADDd molecules results in a much lower value of the number-average cluster size and no evidence of formation of lamellar structures. Interestingly, the same behaviour was found also for a layer built with a lower concentration of surfactants (see results for simulation P5-DADDd) where a less strong repulsion between heads is expected.

The small aggregates formed are quite disordered and only loosely resemble spherical micelles commonly formed with single-head surfactants (see Reference [16] and section 4.1.1). It is also interesting to notice that all the simulations performed, with three different concentrations of doubly charged surfactants and

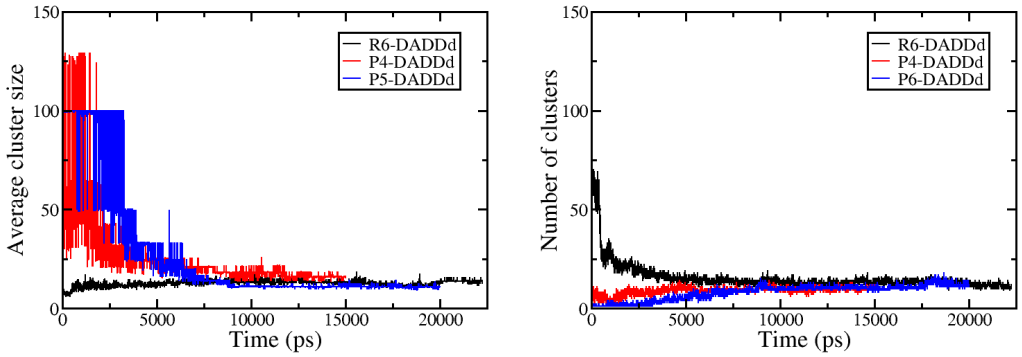

(a) (b)

Figure 5.13: Comparison between simulation results obtained for the reference solution with DADDd surfactants at different concentrations: number average cluster size, (a) and number of clusters, (b). R6-DADDd, black; P4-DADDd, red and P5-DADDd, blue.

starting either from random or from preformed layers, converge to a similar value of the number-average cluster size as displayed in Table 5.3.

Table 5.3: Number-average cluster size for R6-DADDd, P4-DADDd and P5-DADDd.

Name	Average cluster size
R6-DADDd	12.74
P4-DADDd	17.61
P5-DADDd	11.04

The RDFs in Figure 5.14 help explain why, in contrast to the neutral and singly charged systems, it was not possible to produce a stable layer of DADDd molecules. The interactions between charged heads and bromide ions are weaker in the doubly charged system in comparison to the DADDs system (see Figure 5.14-(c)). At the same time we note that the interaction of the charged group with water is comparable in the two systems. These observations suggest that the lack of order in the system lowers the peak of the head-bromide RDFs.

The head to head repulsion plays a crucial role determining equilibrium in these systems [157]. The aggregation of two-headed amphiphiles depends, in fact, on three contributions: the attraction between the hydrocarbon chains, the hydrophobic interactions of these chains with water at the interface and the repulsions between polar heads. The first two terms both favour the formation of large aggreg-

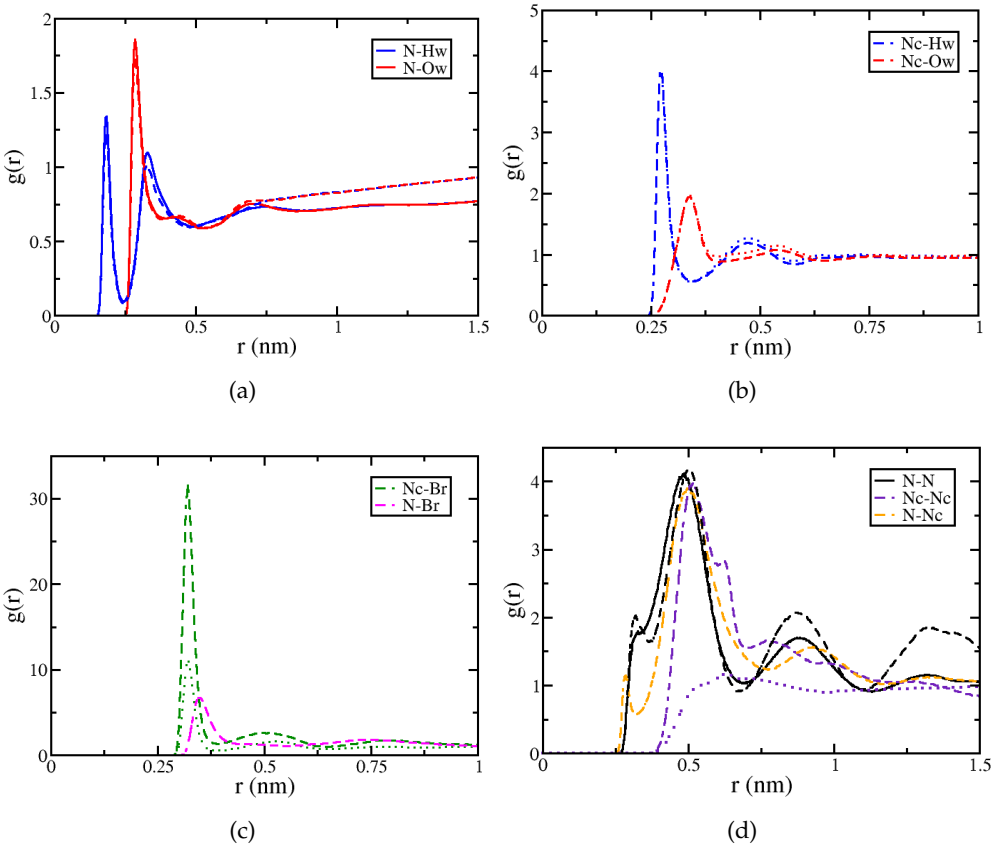

Figure 5.14: Comparison between radial distribution functions obtained for simulations starting from random configuration of surfactants R2-DADDn (solid lines), R5-DADDs (dashed lines) and R6-DADDd (dotted lines): for (a), interactions between neutral heads and water; (b), interactions between charged heads and water; (c), interactions between heads and bromide and (d), interactions between neutral and charged heads. See labels for details.

ates as a result of the dispersive attractions between hydrophobic groups and the tendency to minimise the interface with water respectively. On the other hand, the last contribution limits the size of these aggregates due to the repulsion between polar heads, which becomes higher with their increasing proximity. For neutral heads this term is small compared to the other two. In DADDs, it is minimised through the alternating arrangement observed in Figure 5.8-(b). In DADDd, however, it dominates the other two terms leading to layer breakup and formation of small disordered clusters. Figure 5.14-(d) confirms that for this system the interaction between charged heads is indeed strongly repulsive.

Further support to these observations is given by the energies of interactions calculated for the three preformed systems P2-DADDn (neutral), P3-DADDs (singly charged) and P4-DADDd (doubly charged), summarised in Table 5.4. Coulombic

Table 5.4: Energies of interactions in the reference systems P2-DADDn, P3-DADDs and P4-DADDd. Surfactant-Surfactant and Surfactant-Water energies are normalised by the number of surfactant molecules in each simulation, Surfactant-Bromide energies are normalised by the number of bromide counter-ions.

Surfactant-Surfactant						
	P2-DADDn		P3-DADDs		P4-DADDd	
Coulombic (kJ/mol)	10.26	0.05	52.76	0.16	78.44	0.69
LJ (kJ/mol)	-68.02	0.10	-62.93	1.93	-28.03	0.12
Total (kJ/mol)	-57.76	0.11	-10.16	1.94	50.41	0.70
Surfactant-Water						
	P2-DADDn		P3-DADDs		P4-DADDd	
Coulombic (kJ/mol)	-95.26	0.12	-132.98	0.99	-258.31	2.23
LJ (kJ/mol)	0.04	0.07	9.40	0.06	2.10	0.18
Total (kJ/mol)	-95.23	0.14	-123.58	0.99	-256.21	2.24
Surfactant-Bromide						
			P3-DADDs		P4-DADDd	
Coulombic (kJ/mol)	-	-	-192.73	1.13	-141.68	3.85
LJ (kJ/mol)	-	-	14.83	0.14	8.73	0.46
Total (kJ/mol)	-	-	-177.89	1.14	-132.96	3.87

and Lennard-Jones contributions to the total energy are compared in the three systems for three types of interactions: Surfactant-Surfactant, Surfactant-Water and

Surfactant-Bromide. It is worth noting that the values obtained using the utility *g_energy* have been normalised by the number of surfactant molecules or bromide ions in each system in order to perform a comparison on a equal basis. The first thing to notice is that the total Surfactant-Surfactant interaction energy is, as expected, attractive in the case of neutral and singly charged surfactants but repulsive in the case of doubly charged surfactants. In all three systems the coulombic contribution to the total energy is repulsive and its magnitude increases with the increasing charge of the surfactants, however, dispersion interactions more than compensate for this in P2-DADDn and P3-DADDs but not in P4-DADDd (see Table 5.4 for details). These results are consistent with the first two systems forming lamellar aggregates, whereas the third one only forms small clusters.

For simplicity, so far, in each simulation only a single type of surfactant has been considered. In reality, as will be further discussed in section 5.1.4, all three types of surfactant coexist at intermediate pH values (between 9 and 12), with DADDs being the most abundant species (approximately 50 %) as shown from the pH curves (see Figure 5.1). Although Tanev et al. do not report the pH of their synthesis solution [8], this has been estimated to be around 9.5 based on the starting composition of the mixture. As such, to more closely model the experimental scenario, it was chosen to run simulations at a pH of 10.6, which is slightly higher than experimental but more convenient from a modelling point of view, since DADDn and DADDd surfactants are in equal proportions so that they can balance each other. The reference system was studied starting from a random dispersion of surfactants (R7-EXP-reference) or from a preformed layer (P9-EXP-reference). The latter was built by packing DADDn, DADDs and DADDd molecules, according to the proportion reported in Table 5.2, in a layer geometry without any preferred distribution, so their lateral arrangements were as arbitrary as possible.

Figure 5.15 shows the final configurations obtained in these simulations. The first thing to notice is that, due to slow dynamics, the random system (Figure 5.15-(a)) did not produce a complete layer after 100 ns. However, as can be seen in Figure 5.15-(c), all three types of surfactants are incorporated in growing layer-like aggregates. These seem to be positioned without any specific preference inside the structures formed, as no domains where one type of surfactant remains separate from the others were observed. Furthermore, it appears like these aggregates might merge together to form a single layer at longer simulation times. This hypothesis was tested using the preformed layer simulation and the result is shown in Figure 5.15-(b). The preformed layer keeps its integrity, validating the hypothesis

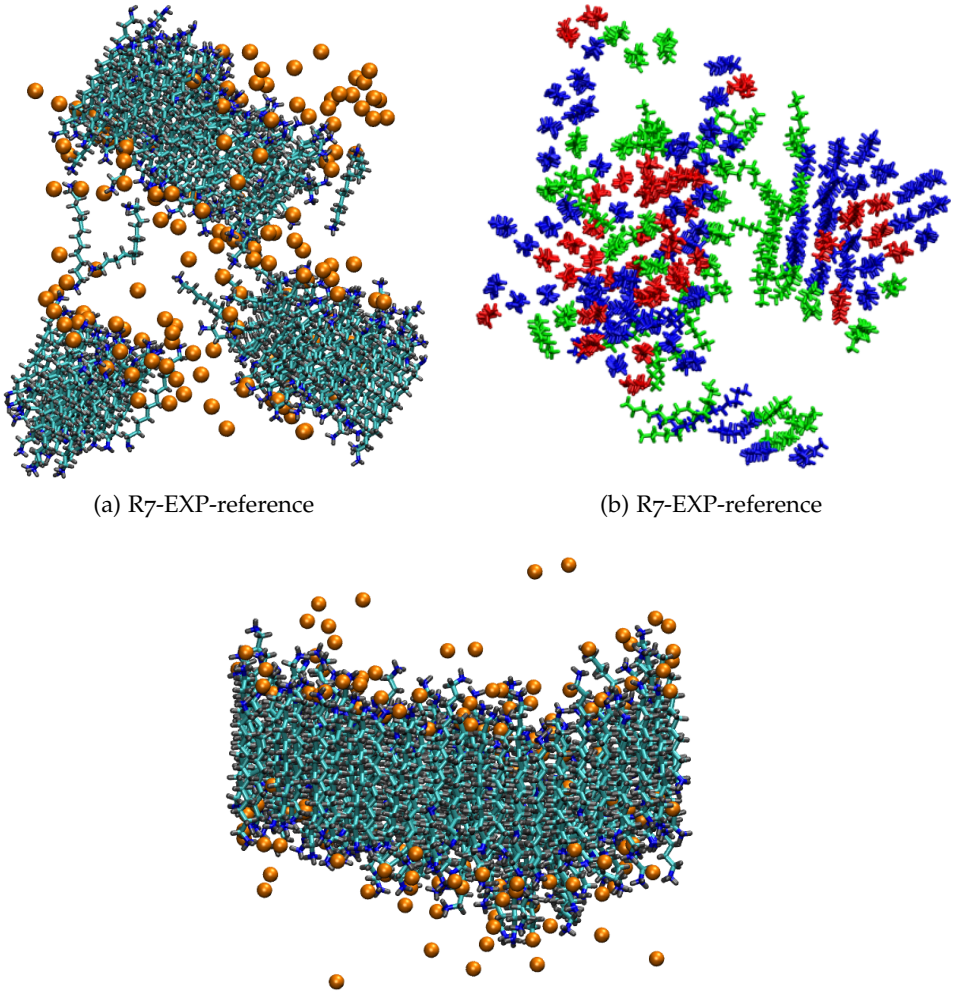

(a) R7-EXP-reference

(b) R7-EXP-reference

(c) P9-EXP-reference

Figure 5.15: Snapshots of 2D cross-section of the simulations corresponding to experimental conditions in the reference solution: (a), starting from random configurations of surfactants and (c), starting from a preformed layer with randomly arranged surfactants. Colour code is the same as in Figure 5.8. (b), top view of the layer-like aggregate in panel (a) to show that all types of surfactants are incorporated in the layer (DADDn, red; DADDs, blue and DADDd, green).

that the distinct aggregates observed before will eventually merge together. It is also interesting to notice that the interface is no longer flat but exhibits a quite pronounced undulation. The reasons for this wavy interface will be discussed in the next section.

5.1.3 *The monomeric solution*

In this section, the results obtained from the addition of anionic silica to preformed surfactant layers at different pH (Table 5.1) are discussed.

Figure 5.16 shows the final snapshots obtained for the three systems considered: high pH, (a) and (b), intermediate pH, (c) and (d) and low pH (e) and (f). The first thing to notice is that the addition of silica anions appears to keep the layers intact when neutral (a) or singly charged (c) surfactants are used, whereas for the system with doubly-charged surfactants (e) the presence of silica species does not enhance any structural organisation.

With regard to this last system, typical clusters produced in the reference system and in the monomeric solution are compared in Figure 5.17. Analysis of these aggregates, both by visual inspection and using the cluster-counting algorithm, reveals that they are very similar in size (from 7 up to 13 DADDd molecules in each cluster) and are surrounded by a comparable number of ions. By looking at the density profiles (Figure 5.17-(b) and (d)) measured from the cluster center of mass (COM), it can be noticed that they present very little order and only vaguely resemble micelle density profiles. In fact, the core of the clusters contains the hydrophobic chains of the molecules but also a few water molecules and ions, both in the reference system and in the monomeric solution. Moreover, the peak representing the heads of the surfactants is located at the interface with water but is quite broad due to the disordered nature of these aggregates.

Concerning the system containing neutral surfactants, when silica species are added the layer remains intact and the monomers are homogeneously dispersed in the bulk solution (Figure 5.16-(a)). In Figure 5.18 the density profiles of this system in the reference solution (solid line) and in the monomeric solution (dashed line) are compared. The lamellar layers of surfactants are practically identical in both systems, proving that no major structural changes have occurred. Looking at the area immediately around the layer, past the neutral heads, a region of approximately 0.5 nm in size where mostly water molecules are present can be observed in

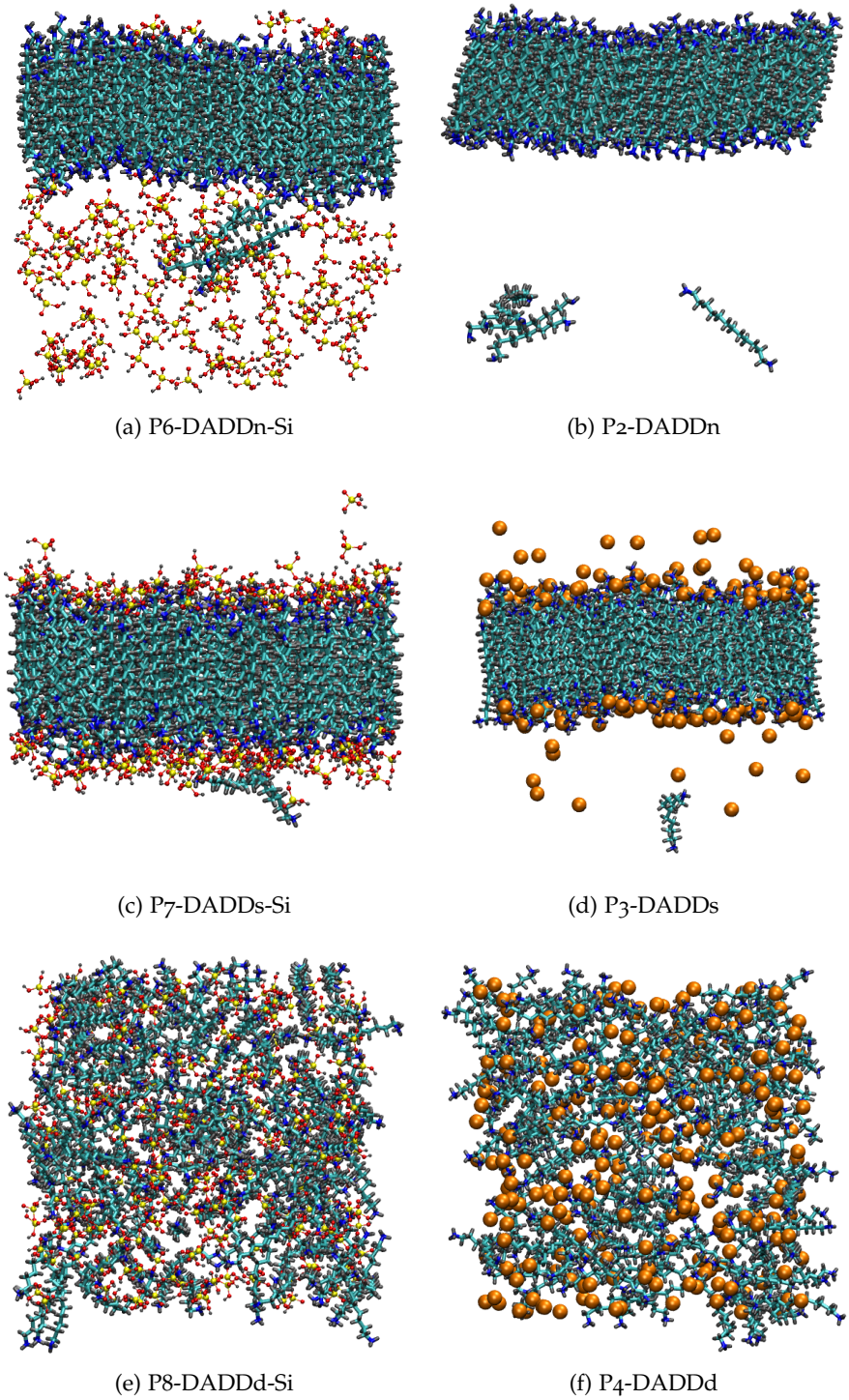

(a) P6-DADDn-Si

(b) P2-DADDn

(c) P7-DADDs-Si

(d) P3-DADDs

(e) P8-DADDd-Si

(f) P4-DADDd

Figure 5.16: Snapshots of the simulations for different monomeric solutions (left) in comparison with configurations obtained in the case of the reference system (right): (a), P6-DADDn-Si; (b), P2-DADDn; (c), P7-DADDs-Si; (d), P3-DADDs; (e), P8-DADDd-Si and (f), P4-DADDd. Colour code is the same as in Figure 5.8-(a) with silicon yellow. Panels (a), (b), (c) and (d) are shown in cross section of the x-z plane; panels (e) and (f) are shown in shown in cross section of the x-y plane. Water omitted for clarity.

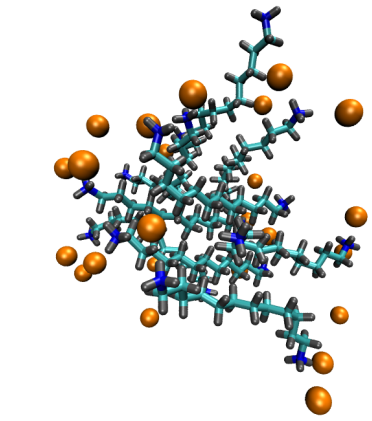

(a) P4-DADDd

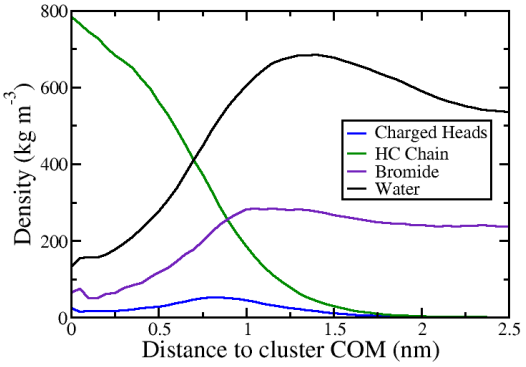

(b)

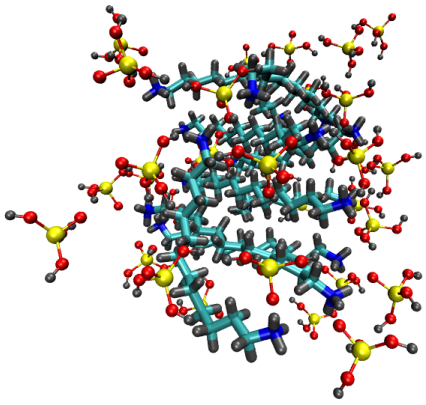

(c) P8-DADDs-Si

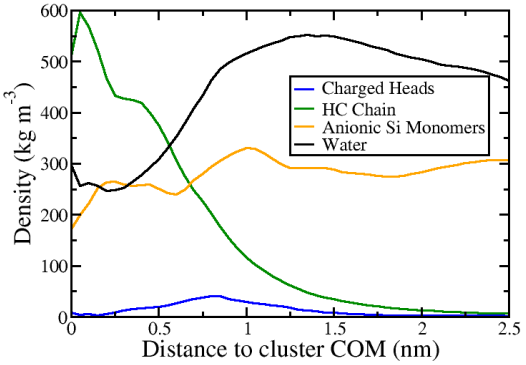

(d)

Figure 5.17: Snapshots of two clusters, both containing 9 surfactant molecules, obtained for P4-DADDd (a) and P8-DADDd-Si (c), and corresponding density profiles. Colour code is the same as in Figure 5.16. Water omitted for clarity.

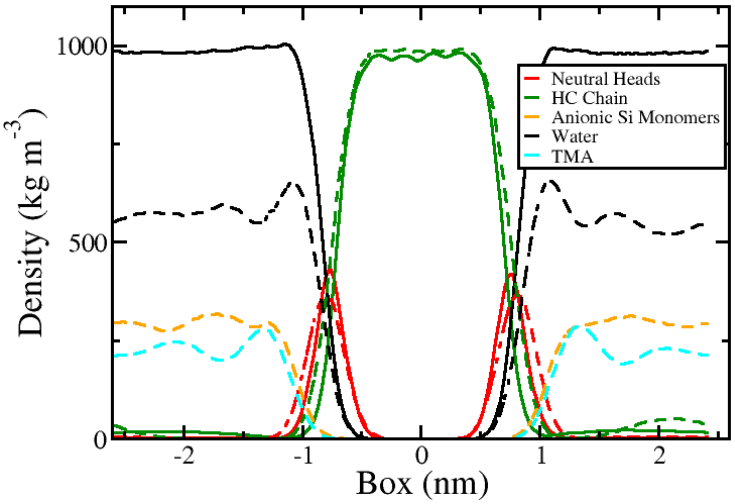

Figure 5.18: Comparison between density profiles across the box for the neutral system, reference solution P2-DADDn (solid line) and monomeric solution P6-DADDn-Si (dashed line).

the case of the monomeric solution, indicating the existence of a wet layer around the surfactants. Finally, TMA and silica monomers are found homogeneously dispersed in the bulk of the solution, reducing the overall density of water in comparison to the neutral system. These results suggest a stronger interaction between silica monomers and water rather than with the surfactants. This behaviour is confirmed by looking at the RDFs for the system in Figure 5.19. Clearly, the peak

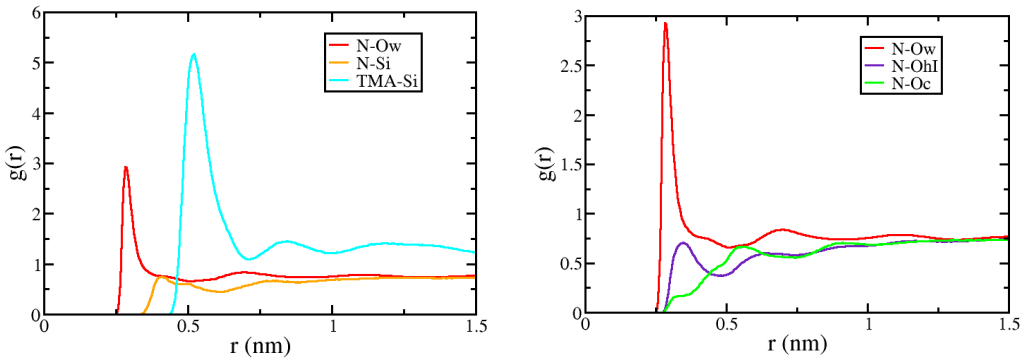

Figure 5.19: Radial distribution functions for the system P6-DADDn-Si; see labels for details.

representing the interactions between the TMA nitrogens and the silicon atoms is

the predominant one, located approximately at 0.55 nm, whereas the peak relative to the interactions between surfactant nitrogens and silica is very low in comparison (Figure 5.19-(a)). The reason for this has to be found in the comparatively strong electrostatic interaction between positively charged TMA molecules and anionic silica monomers. The second thing to notice is the location of the different peaks representing the interaction between surfactant nitrogens and oxygen atoms in water (Ow) and in silica (OhI is the oxygen belonging to the hydroxyl group and Oc is the charged oxygen), as shown in Figure 5.19-(b). The N-Ow peak is quite strong and occurs at a short distance, characteristic of hydrogen bond interactions. Conversely, there is practically no interaction between N and the charged oxygen of silica. The N-OhI peak is also very small (below 1) and probably caused by the few DADDn molecules dispersed in the bulk solution. These results provide additional evidence for the presence of the wet layer, and suggest that hydrogen bonding interactions between the surfactant amino group and silica monomers are at best quite weak and therefore not sufficient to promote silicates to adsorb and then condense around these lamellar templates (see Figure 5.16-(a)).

Finally, in the system containing singly charged surfactants, contrary to the previously discussed case, silica monomers strongly interact with the surfactant head groups, resulting in their adsorption at the interface (Figure 5.16-(c)). Looking at the density profiles across the box (Figure 5.20) it can be seen that the presence of silica dries the interface in comparison to the reference system. This result seems to be in qualitative agreement with the mechanism postulated experimentally for the formation of this class of materials [8]. However, given the charged nature of all the species in system, charge matching, rather than hydrogen bond interactions, appears to be responsible for the creation of the silica layer at the interface with DADDs surfactants.

To elucidate this point further, it is worth looking at the energies of interactions calculated for P6-DADDn-Si, P7-DADDs-Si, and P8-DADDd-Si in Table 5.5. Here, Coulombic and Lennard-Jones contributions are shown for Surfactant-Surfactant, Surfactant-Water, and Surfactant-Silica interactions, with the appropriate normalization (number of surfactant or silica molecules) to allow direct comparison on a equal basis. The Surfactant-Surfactant interaction energies have the same trend as in the reference system: dispersion interactions more than compensate for the repulsive Coulombic interactions only in the systems that produced stable layers (i.e. P6-DADDn-Si and P7-DADDs-Si). The Surfactant-Silica interactions also show an interesting trend. In the neutral system, this energy is only moderately

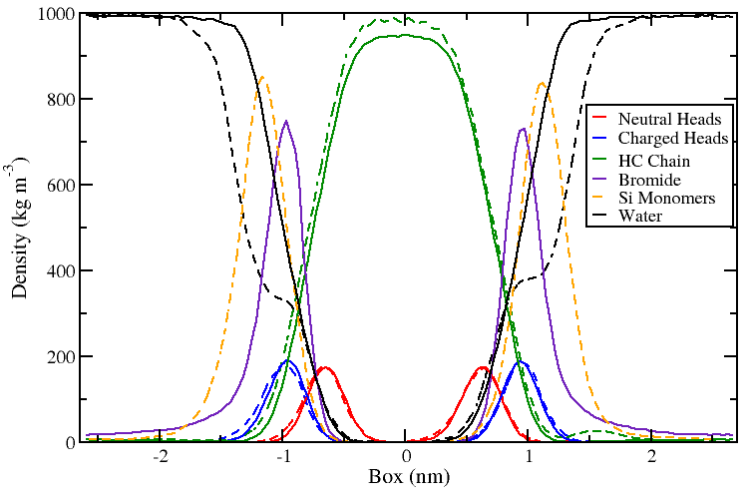

Figure 5.20: Comparison between density profiles across the box for the singly charged system in the reference system P3-DADDs (solid lines) and in the monomeric solution P7-DADDs-Si (dashed lines).

attractive because most of the silica monomers remain dispersed in the simulation box, favouring instead the interaction with water molecules. On the contrary, silica monomers strongly interact with surfactants in both singly and doubly charged systems (the Surfactant-Silica energy is -312.79 and -322.33 kJ/mol, respectively); however, in the first case, this interaction is with lamellar structures (surfactant-surfactant energy $= -3.48$ kJ/mol), and in the second case, it is with small clusters of surfactants (Surfactant-Surfactant energy $= 90.87$ kJ/mol). This further confirms the qualitative results discussed above.

5.1.4 *Simulations at pH close to the experiment*

The simulations discussed in the previous section strongly suggest that the mechanism postulated for the formation of MSU-V materials can only take place when singly charged surfactants and anionic silicates are available in the system to establish favourable electrostatic interactions while keeping the repulsion between charged heads to a minimum.

In this section, results from simulations performed at an intermediate pH of 10.6, slightly higher than the estimated experimental pH, are presented. It should be noticed that a $2:1$ ratio of silica monomers to surfactants (see Table 5.2 for details) is used, i.e. each surfactant head can theoretically interact on average with

Table 5.5: Energies of interactions in the monomeric systems P6-DADDn-Si, P7-DADDs-Si and P8-DADDdSi. Surfactant-Surfactant and Surfactant-Water energies are normalised by the number of surfactant molecules in each simulation, Surfactant-Silica energies are normalised by the number of silica monomers.

Surfactant-Surfactant						
	P6-DADDn		P7-DADDs		P8-DADDd	
Coulombic (kJ/mol)	8.79	0.06	64.45	0.94	120.40	0.42
LJ (kJ/mol)	-70.84	0.04	-67.93	0.1	-29.53	0.12
Total (kJ/mol)	-62.05	0.07	-3.48	0.94	90.87	0.43
Surfactant-Water						
	P6-DADDn		P7-DADDs		P8-DADDd	
Coulombic (kJ/mol)	-80.92	0.31	-67.43	1.27	-72.75	0.77
LJ (kJ/mol)	4.59	0.07	4.86	0.11	-4.63	0.42
Total (kJ/mol)	-76.32	0.32	-62.57	1.27	-77.39	0.88
Surfactant-Silica						
	P6-DADDn		P7-DADDs		P8-DADDd	
Coulombic (kJ/mol)	-7.56	0.08	-319.80	2.46	-318.86	0.85
LJ (kJ/mol)	-5.38	0.1	7.02	0.08	-3.48	0.25
Total (kJ/mol)	-12.93	0.13	-312.79	2.47	-322.33	0.88

one silicate. The reference system has already been presented in section 5.1.2, and will be used for comparison with the monomeric solution under the same set of conditions. Like in the reference system, a preformed layer containing all the three types of surfactants but with no particular lateral arrangement was used as initial configuration. All the simulations were performed using the same parameters as described in section 5.1.

Due to the size limitations of the simulations, only layers have been observed to form. However, multilamellar vesicles are expected to form in larger systems [8]. To analyse this possibility an interesting feature that was observed during the system analysis is described. It was noticed that the orientation of the DADD molecules in the layers and the degree of undulation of the layer changed with the presence of silica (e.g. compare Figure 5.16-(a) and (b)). These differences are believed to be related to the interfacial tension in the system. In Table 5.6 the values of the interfacial tension calculated for the simulations that produced a complete

layer are reported. The value of the interfacial tension assumes negative values

Table 5.6: Calculated interfacial tension.

Name	γ (mN m^{-1})	error (mN m^{-1})
R2-DADDn	36.89	3.45
P2-DADDn	40.53	0.19
P6-DADDn-Si	-35.66	1.85
P3-DADDs	31.56	1.5
P7-DADDs-Si	-23.40	3.4
P9-EXP-reference	-70.33	2.2
P10-EXP-monomeric	-82.77	4.65

in the systems containing silica species but also in the reference system when all three types of surfactants are present. This might appear as an unphysical result, however experimental [160] as well as computational [161, 162] studies suggest that a negative interfacial tension is an indication of an unstable surface. Therefore, the interfacial area will tend to increase, either by a change in the surface curvature or by mixing. The first possibility could be an indication that the system wants to evolve towards the formation of vesicles. The size and length of simulations discussed here does not allow to provide a conclusive answer to this question, and a more complete picture can only be achieved using coarse-grained (CG) molecular dynamics.

In can be seen from Figure 5.21-(a) that, similarly to what was observed for the reference system, the preformed layer keeps its integrity while producing a quite distinctive curvature. This observation seems to be in agreement with the surface tension calculations (Table 5.6), providing another indication that the system wants to evolve towards the creation of lamellar vesicles around which silicates precipitate.

Another thing to notice is that the layer presents a hole, as can be clearly seen in Figure 5.21-(c) where a top view of the layer is shown. Interestingly, anionic and neutral silica monomers were observed to spontaneously migrate into this hole (see Figure 5.21-(b)). Visual inspection of the simulation trajectory reveals that, in this region, 4 DADDd and 2 DADDs molecules are located in close proximity. This corresponds to 6 neighbouring positively charged heads on one side of the layer and 4 on the opposite side. Hence, this local excess of positive charges triggers the creation of the hole, making the cavity accessible to small water molecules (up

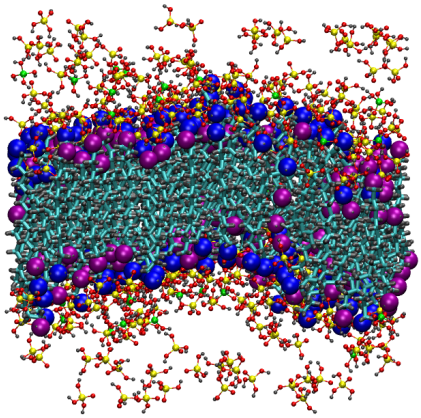

(a) P10-EXP-monomeric

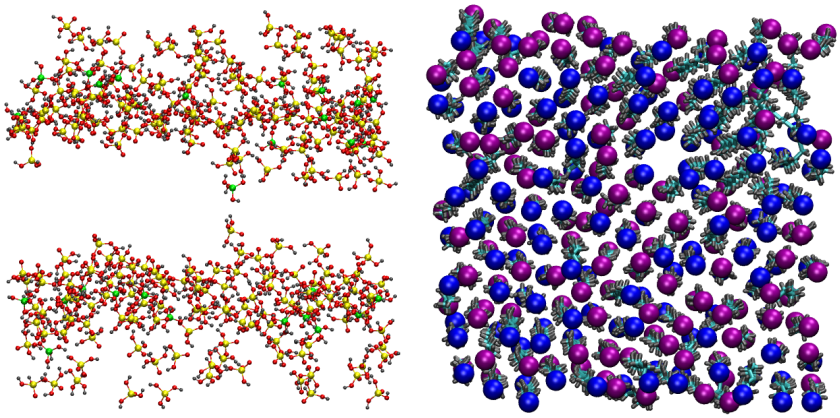

(b) (c)

Figure 5.21: Snapshots of the simulations corresponding to experimental conditions in the monomeric solution starting from a preformed layer with randomly arranged surfactants: (a), cross section of the y-z plane showing the layer with silica monomers adsorbed at the interface; (b), cross section of the y-z plane showing only the silica layers with silica monomers penetrating the hole in the surfactant layer and (c), top view (x-y plane) showing the location of the hole. Colour code is the same as in Figure 5.8 with silicon in anionic silica yellow and silicon in neutral silica green. Water omitted for clarity.

to two water molecules have been observed to temporarily occupy the hole) and to silica monomers, which penetrate the layer from both sides (i.e. from the upper part and from the lower part of the layer). The presence of local defects, like the one observed in this simulation, could help explain how the interconnecting pillars reported experimentally are created. Tanev and Pinnavaia suggest that silicates can penetrate the multilamellar surfactant vesicles, initiating silica growth also in the vertical direction, so that, eventually, two consecutive horizontal layers become connected [37]. Therefore, one can imagine that similar holes or defects will form across the lamellar plane with more silicates migrating inside them. These cavities will become progressively full of silica monomers that will eventually condense and remain trapped inside the template structure. Ultimately, silica polymerisation inside these cavities will generate the vertical pillars that connect the horizontal layers. It should be considered, however, that several defects of this type are probably needed to maintain the structural integrity of the multilamellar framework. Confirming this hypothesis is way beyond the limitations of the atomistic simulations performed in this work.

5.2 COARSE-GRAINED SIMULATIONS OF MSU-V MATERIALS

To probe the synthesis of MSU-V materials for longer times and length scales some preliminary CG simulations of this system have been performed. The CG model employed is essentially based on the parameters developed in the previous chapter to study the HMS system (see section 4.1.2), however some further testing and validation of the model was also done. Table 5.7 provides a list of all the simulations performed. The same convention used to label AA simulations is employed here to distinguish between simulations starting from random or preformed configuration as well as to indicate the type of system (neutral, singly or doubly charged) considered. It should be noted that 10 % of the water molecules have been replaced with MARTINI antifreeze particles (AF).

5.2.1 *Model details and validation*

Figure 5.22 shows the mapping scheme adopted for the three surfactants considered. Mapping schemes for all other species present are not shown here since they are the same as for the study of HMS synthesis (see Figure 4.10). Similarly

Table 5.7: Number of beads, simulation length and final box size for each coarse-grained MD simulation of MSU-V materials.

System	DADDn	DADDs	DADDd	Br^-	SI	SN	TMA^+	water	AF	time (ns)	box (nm)
R1-DADDn-CG	140							705	78	60	5.5
P1-DADDn-Si-CG	150				150	150		823	92	60	6
P2-DADDs-Si-CG		150			150			958	107	60	6.1
P3-DADDd-Si-CG			150		300			823	92	60	6
reference-CG	573	1169	550	2269				173509	19279	1000	30
monomeric-CG	573	1169	550		7899	878	5630	176572	19619	1050	30.5

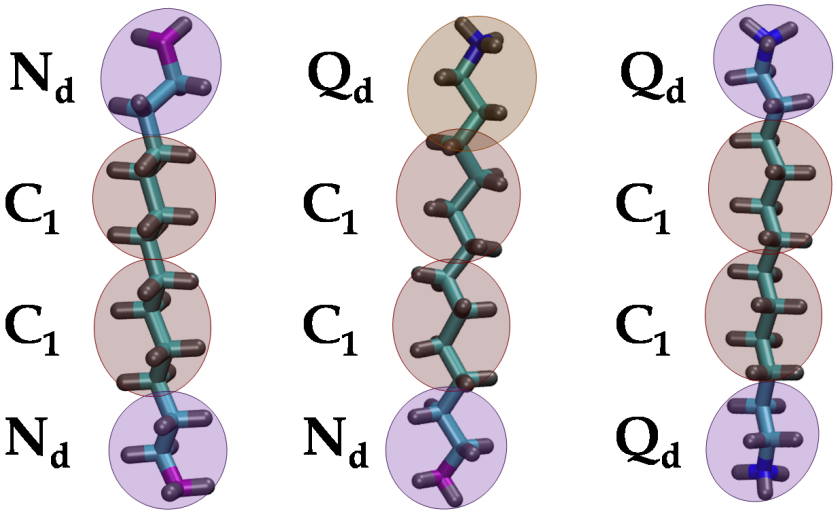

(a) (b) (c)

Figure 5.22: Schematic representation of the mapping scheme adopted for diamine surfactants. (a), DADDn; (b), DADDs and (c), DADDd.

to the model used for primary amines (DDA and DDA^+ in the previous chapter), neutral surfactant heads are represented with a N_d bead, while charged heads are represented with a Q_d bead. The only difference with the previous discussed system is that the carbon chain is modelled using C_1 beads instead of C_2 beads in order to more realistically represent the correct alkyl chain length. Furthermore, also in these double-headed surfactants, it was decided to increase the angle force constant (f) from 25 to 50 $kJ\,mol^{-1}$ to improve agreement with AA results. Figure 5.23 compares the final configurations obtained for the simulation labelled R1-DADDn-CG when using different values of the angle force constant. It should be noted that for this test, and for all the results described in this section, the same simulation protocol used for CG simulations of HMS materials was employed (see section 4.1). The only exceptions are the time step used to integrate the equation of motion, which was set to 30 fs instead of 40 fs, and the simulation temperature, fixed to 298 K like it was done at AA level.

The configuration produced using the lower force constant (a) is significantly more disordered than the one obtained with the higher force constant (b), which provides a better qualitative agreement with the AA result obtained for this system (c). Similar improvement was also observable for the system with singly charged surfactants. One interesting thing to notice is that, despite the equilibrium length of the simulation box being higher than the value measured for AA simulations of the analogous system (5.5 nm for R1-DADDn-CG and 5.2 nm for R2-DADDn at AA level), a smaller number of surfactants can be accommodated into the layer (136 for AA and 127 for CG). This is a consequence of the larger size of DADD surfactants at CG level which in turns prevents them to pack more efficiently.

With regard to interaction of the C_1 bead with silicates, this was already established by Pérez-Sánchez et al. to be *intermediate* (IV) [7]. However, when this *intermediate* level was used for simulating monomeric solutions of preformed surfactant layers (approximately equivalent, in terms of number of molecules, to the AA systems described in section 5.1.3), a significant distortion of the DADDn and DADDs layers was observed. These results suggest that for the current system a more repulsive level of interaction has to be adopted in order to obtain the correct physical behaviour, which was reproduced by reducing the interaction between C_1 and anionic silica monomers (Q_{SI}) to *super repulsive* (IX). Intermediate interaction values (between level V and level VII) produced a similar distortion of the layer due to Q_{SI} interacting too strongly with the hydrophobic part of the surfactants. As already pointed out in the previous chapter, the behaviour of Q_{SI} beads

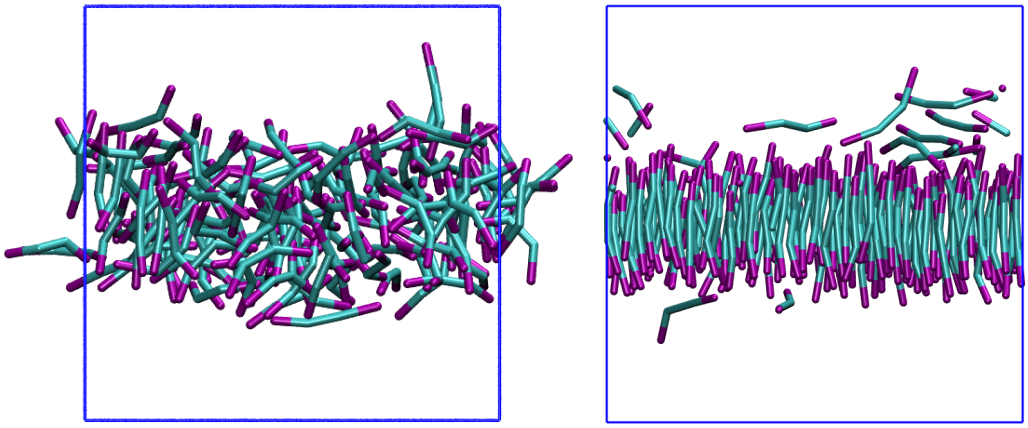

(a) (b)

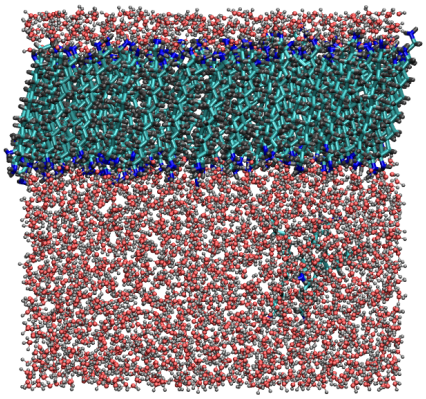

(c)

Figure 5.23: Snapshots showing the final configurations obtain for a CG simulation of the system R1-DADDn-CG. (a), using f = 25 kJ mol^{-1} and (b), using f = 50 kJ mol^{-1}. (c), atomistic results for the system R2-DADDn. Colour code for the CG snapshot is: neutral heads, purple and hydrocarbon chains, cyan. Colour code for the AA snapshot is the same as in Figure 5.3. Water has been removed for clarity from the CG simulations boxes.

is essentially determined by their interaction with hydrophobic groups (C_1 or C_2), hence only by making this interaction more or less favourable can one obtain the correct physical representation. This outcome seems to indicate a limitation of the MARTINI force field for systems where fine tuning of the interactions is crucial.

Finally, from the density profile shown in Figure 5.24 it can be noticed that the alternated arrangement of charged and neutral heads observed atomistically is also reproduced with CG simulations. A summary of the results is provided in Figure 5.25 where final configurations obtained for C_1-Q_{SI} = IV (left panels) are compared with the final configurations obtained for C_1-Q_{SI} = IX (middle panels) and for AA simulations (right panels). For completeness, the results obtained when simulating monomeric solutions with DADDd surfactants are also presented, however in this case no significant difference is observed between the two levels of interaction tested.

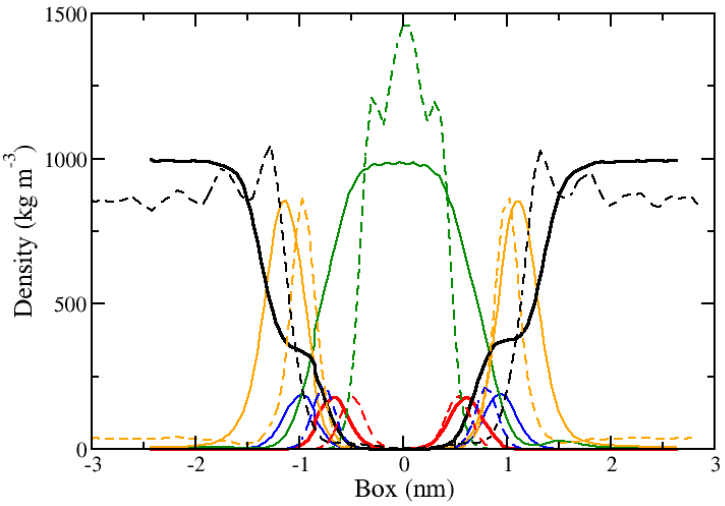

Figure 5.24: Comparison between atomistic (solid lines) and coarse-grained (dashed lines) density profiles obtained for the system P7-DADDs-Si and P2-DADDs-Si-CG, respectively. Colour code is the same as in Figure 5.20.

5.2.2 *CG simulations of reference and monomeric solution of MSU-V materials*

Table 5.8 contains the interaction levels for all bead types used to study the synthesis of MSU-V materials. It should be noted that for consistency the interaction

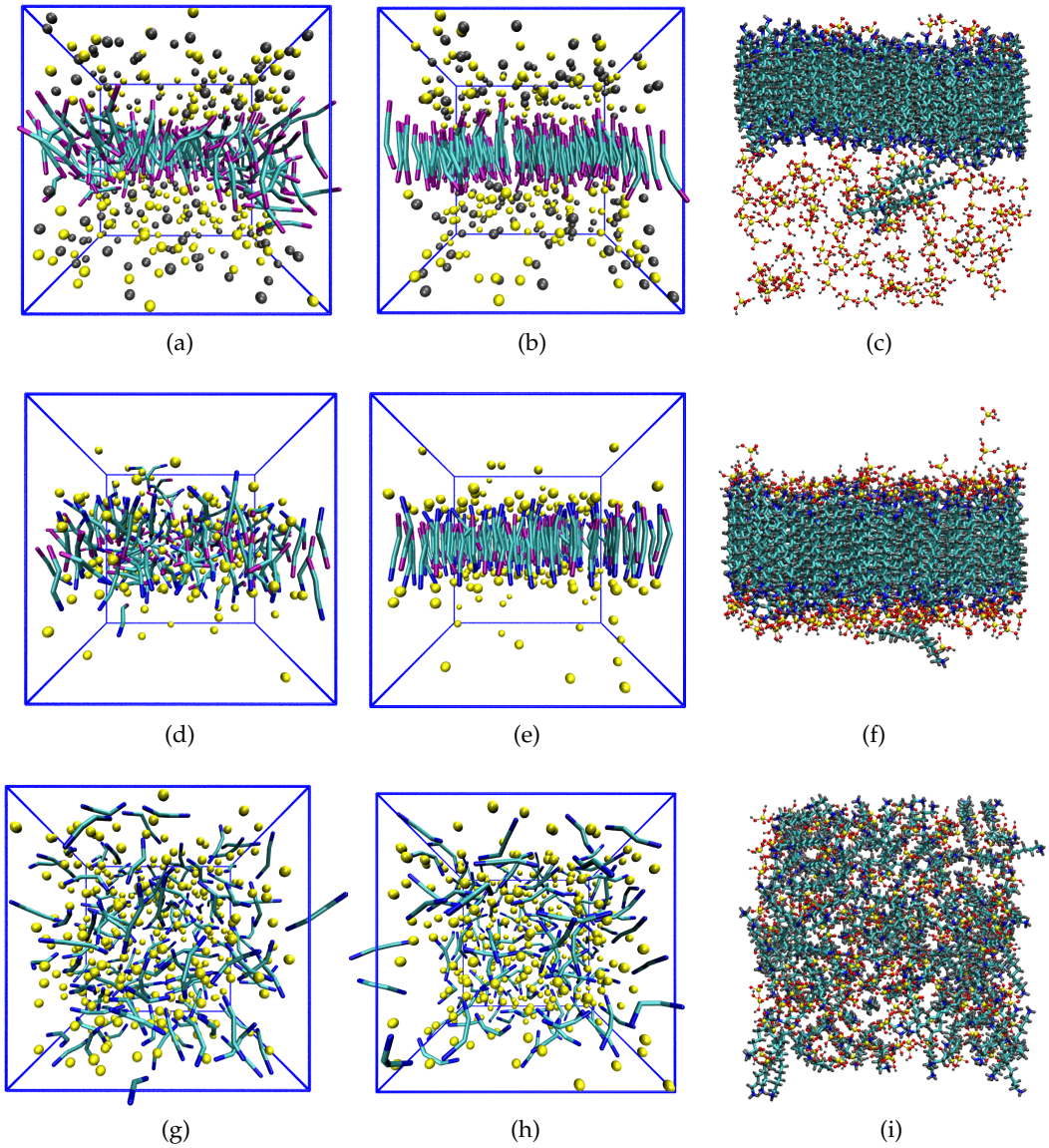

Figure 5.25: Snapshots showing the final configurations obtain for a CG simulation of the systems P1-DADDn-Si-CG ((a) and (b)), P2-DADDs-Si-CG ((d) and (e)) and P3-DADDd-Si-CG ((g) and (h)) and comparison with correspondent atomistic simulations ((c), (f) and (g)). Snapshots on the left panel have been produced using C_1-Q_{SI} = IV while for snapshots on the middle panels C_1-Q_{SI} = IX. Colour code for the CG snapshot is: neutral heads, purple; charged heads, blue; hydrocarbon chains, cyan; anionic silica monomers, yellow and TMA counterions, grey. Colour code for the AA snapshot is the same as in Figure 5.16. Water has been removed for clarity.

Table 5.8: Matrix of interactions for CG beads used in this work.

Type	Q_d	Q_a	Q_o	Q_{SI}	P_4	N_d	N_{SN}	C_1
Q_d	O	O	II	II	O	III	O	IX
Q_a	O	I	II	II	O	I	II	IX
Q_o	II	II	IV	II	O	III	II	IX
Q_{SI}	II	II	II	O	II	III	O	IX
P_4	O	O	O	II	I	III	II	VIII
N_d	III	I	III	III	III	III	O	VI
N_{SN}	O	II	II	O	II	O	O	IX
C_1	IX	IX	IX	IX	VIII	VI	IX	IV

between C_1 and neutral silica monomers (N_{SN}) has also been set to *super repulsive*. All other interaction levels are identical to those used in Chapter 4.

With all the CG parameters established, two large CG simulations, starting from initial random distributions of all species, were performed to represent the reference and monomeric solution at pH = 10.6 (see reference-CG and monomeric-CG in Table 5.7). For the monomeric solution, a silica to surfactant ratio of approximately four-to-one has been used. This value is close to the ratio reported experimentally [8, 37]. Production runs were performed in the *NPT* ensemble, following the same protocol discussed earlier, and produced the results displayed in Figure 5.26 and Figure 5.27. The reference system shows the formation of multiple layers of surfactants which, from visual inspection, appear to be essential dry. These surfactant layers are separated by chloride layers which neutralise the head charge. Earlier with AA simulations, it was observed that doubly charged surfactants can be incorporated in the layer (see Figure 5.15-(b)). At CG level, however, most of the doubly charged surfactants appear to be in the bulk, with only few of them present in the layer, as shown in Figure 5.26-(b) where different colours have been used to distinguish between surfactant types. One possible explanation for these results is that, due to their larger sizes, CG water beads cannot approach surfactant heads close enough to screen the repulsion interaction caused by neighbouring surfactants. To clarify this observation it is useful to look at the density profile shown in Figure 5.24. Even if this profile represents a different system (with only singly charged surfactants and with anionic silica monomers adsorbed on the layer), it can be observed that while atomistic water molecules partially penetrate

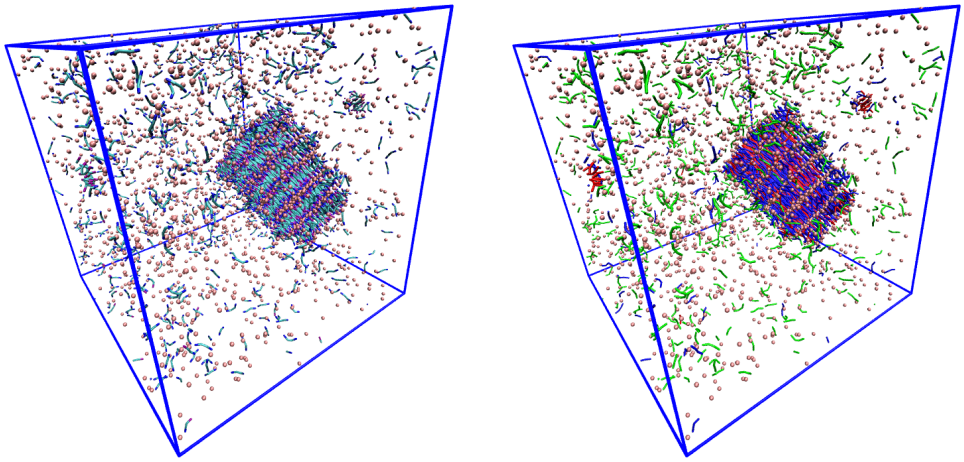

(a) (b)

Figure 5.26: Snapshots showing the final configurations obtain for a CG simulation of the systems reference-CG. Colour code for (a) is: neutral heads, purple; charged heads, blue; hydrocarbon chains, cyan and chloride counter-ions, pink. In (b) diffrent colours are used to distinguish between surfactant types: DADDn, red; DADDs, blue and DADDd green. Water omitted for clarity.

into the layer to solvate the charged surfactant heads (black and blue solid lines), CG water beads are mostly located beyond the peak corresponding to the charged heads (black and blue dashed lines), suggesting a steric limitation of the model.

Formation of multiple layers of surfactants was also observed for the monomeric solution. Neutral and anionic silica monomers adsorb around the layers like observed at AA level, however it was not possible to determine if they can also penetrate inside the layers due to difficulty in visualising such a large system. Also to notice is that addition of silica does not enhance incorporation of DADDd monomers in the layers, which remain prevalently dispersed in the simulation box.

Both the reference and the monomeric systems simulated here did not produce vesicles. Possibly the multilayer structures observed are precursors of the multilamellar vesicles described experimentally, however the size of these aggregates could exceed the current capabilities of CG simulations. It was not possible to find more information regarding the aggregation process through which such vesicles are formed. If this process occurs through fusion of vesicles of smaller sizes, then it could be possible to see initiation of this process with CG simulations. However, if a minimum concentration of surfactants is necessary to initiate aggregation, then

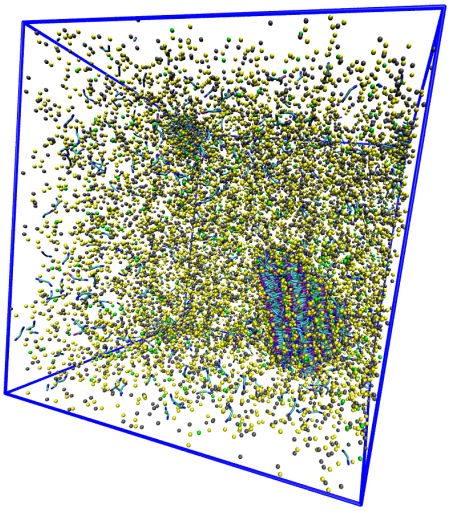

Figure 5.27: Snapshot showing the final configuration obtained for a CG simulation of the system monomeric-CG. Colour code is the same as in Figure 5.26 with anionic silica monomers in yellow, neutral silica monomers in green and TMA counter-ions in grey. Water omitted for clarity.

the number of species involved as well as the size and length of the simulation might be not easy to access even with CG simulations.

5.3 CONCLUSIONS

By performing detailed molecular dynamics simulations of 1,12-diaminododecane surfactants (DADD) in water (reference system) and in the presence of silicates (monomeric solution), the concentration and pH dependence of the aggregation process that leads to the formation of MSU-V materials was investigated. Dry lamellar structures were obtained in the system containing only neutral DADD surfactants (pH > 11) starting from random configurations as well as when preformed layers are used as inputs, indicating that these aggregates represent stable equilibrium states. When surfactants are singly charged (at pH between 8 and 11), the same type of structures are produced, as established using simulations starting from preformed layers. However, in this case surfactant molecules adopt an alternated arrangement inside the layer that can minimise the repulsion between charged heads. This strong electrostatic repulsion is, in fact, responsible for breakage of the

preformed layers at low pH when DADD surfactants are doubly charged, generating highly disordered aggregates consisting of small clusters rather than layers.

Notably, the addition of silica monomers to the doubly charged system does not enhance structural organisation nor does it change the average cluster size. Conversely, at high pH (> 11) the layer is kept intact but silicates remain homogeneously dispersed in the solution and no significant interaction occurs between silica and surfactant. At intermediate pH values (8-11), on the other hand, strong electrostatic interactions are established at the layer interface between anionic silicates and surfactant heads. This suggests that these simulations represent a state that more closely resembles the synthetic conditions leading to formation of MSU-V materials. Contrary to what was originally hypothesised [8], MD simulations show that charge-matching interactions rather than hydrogen bonds promote silica adsorption around the amine template.

Furthermore, simulations at a pH close to the experimental value show that silicate adsorption at the interface induces a considerable curvature in the layer comprising all three types of surfactants (neutral, singly and doubly charged). One possible explanation to this interesting behaviour is that these systems are in a "temporary frustrated state" and want to evolve towards the formation of aggregates with higher interfacial areas, i.e. vesicles, in agreement with the multilamellar aggregates described experimentally.

Furthermore, it is shown that a few silicates, together with water molecules, penetrated a hole spontaneously created inside the multi-surfactant layer. This observation represents a direct evidence of the intercalated pillaring mechanism proposed experimentally. The interpretation proposed in this work is that the presence of a local excess of charge triggers the formation of defects that become accessible to water and silica molecules; progressively these holes or defects are filled with silicates that will eventually condense inside the templating structure, leading to the formation of vertical pillars connected to the horizontal silica layers at the interface with water.

The system at pH close to experiments was also investigated with CG simulations. Both reference and monomeric solution showed the formation of multilayers of surfactants, prevalently containing the neutral and singly charged species, with counter-ions or silica monomers adsorbed at the interface. It was not possible to ascertain whether silica monomers can penetrate the CG layers, however most likely the insertion of these species will not be as favourable as at it was observed with AA simulations. This is due to the lack of excess charges produced by the DADDd

surfactants, which can promote formation of holes and provide access into the layer to the silicates. In future work more accurate CG models could be developed to clarify some of the questions raised herein.

6

AMINE TEMPLATE REMOVAL FROM BIO-INSPIRED SILICA NANOMATERIALS

So far the main focus of this work has been to describe the molecular interactions taking place during the templated synthesis of two classes of porous silicas, HMS (Chapter 4) and MSU-V materials (Chapter 5), with the purpose of understanding and, hence, gaining better control over the mechanism. As described in Chapter 2, once templated synthesis is achieved, further treatments are normally required before the material can actually be used. These treatments include template removal and, if necessary, surface functionalisation. The first is commonly obtained through calcination while functionalisation, which is done with the purpose of adding precise functionalities to the material, is achieved by grafting specific groups or molecules onto the silica surface. Typically, each of the steps necessary to produce functional porous silicas (synthesis, template removal and functionalisation) is accompanied by the use of expensive and sometimes hazardous chemicals or synthetic conditions, as well as by a certain degree of wastefulness. In the previous chapters it was discussed how the use of bio-inspired synthesis could possibly allow for the use of less intense (in terms of temperature, pressure and pH) and, therefore, greener synthetic conditions. However, costs and wastefulness in the purification step are still a significant issue, firstly because the template (the most expensive of the starting materials) is completely destroyed during calcination, and secondly because the process of calcination itself is highly energy expensive, due to the very high temperatures required. Several studies have investigated the possibility of using leaching as an alternative method for template removal [36, 163–166]. Contrary to calcination, leaching or solvent extraction has the advantage of allowing for template recycle, however these removal methods cannot be applied to new systems without further testing and development since they are usually template specific. Furthermore, the energy requirement of purific-

Parts of this chapter have been published in: Manning, J. R. H. et al. 'An eco-friendly, tunable and scalable method for producing porous functional nanomaterials designed using molecular interactions'. *ChemSusChem* (2017). DOI: 10.1002/cssc.201700027.

ation methods based on solvent extraction is also quite high since a considerable solvent reflux together with high temperatures are usually needed.

It is clear that if milder conditions are possible in the synthesis step by means of bio-inspired approaches (i.e. organic templates, ambient temperatures and approximately neutral pH), in the purification/functionalisation steps this is still far from being accomplished. In this chapter a new method to achieve purification is presented and the principles behind it investigated through a combination of experimental and computational techniques. The experimental part of this work was carried out by collaborators Joseph R. H. Manning, Thomas W. S. Yip and Siddharth V. Patwardhan but the main aspects are described in this chapter to enable comparison with the modelling results.

6.1 EXPERIMENTAL STUDY

The material used in this work (bio-inspired silica) as well as the purification and characterisation treatments performed experimentally are described in this section.

SYNTHETIC PROCEDURE Bio-inspired silica was synthesised using pentaethylenehexamine (PEHA) as structure directing agent, which was chosen for its high catalytic activity [56]. The synthetic procedure used to fabricate the material is as follows. At small scale (150 mL), solutions of sodium silicate pentahydrate (Fisher scientific, technical grade) and PEHA (Sigma Aldrich, technical grade) were added to deionised water yielding a final concentration of 30 mM for both Si and N. The mixture was subsequently neutralised using 1 M HCl and allowed to react at pH 7.0 ± 0.05 for 5 minutes. The particles were then isolated by centrifugation for 15 minutes at 8000 rpm, dried in an oven at 85 °C overnight and then washed with deionised water three times. In order to assess the scalability of the bio-inspired synthesis, and hence the viability of the process on an industrial level, the reaction was also performed at larger scale (1 and 5 L) using a Reactor-Ready TM system, either in batch or in continuous mode. The reactor stirrer was set to 500 rpm, while other parameters and procedures were as described above. Alternative additives used were diethylenetriamine (DETA) (Sigma Aldrich, 99 %) at a nitrogen concentration of 30 mM, and poly(ethyleneimine) and permethylated poly(etheleneimine) (Polysciences) at a concentration of 1 mg mL^{-1}.

POST-SYNTHETIC TREATMENTS Once synthesised, the suspension was treated with acid, by addition of further HCl, until it reached a desired pH between 7 and 2 (the isoelectric point of silica [30]) and left to stand for approximately 10 minutes before being isolated by centrifuge as described above. Water reflux was performed by suspending approximately 0.75 g of bio-inspired silica in 120 mL of deionised water and refluxing at 100 °C for 24 hours. The sample was then allowed to cool to ambient temperature before being filtered and washed with a further 120 mL of deionised water. The washed sample was then dried at 85 °C overnight prior to subsequent analyses.

The chemical and physical properties of silica were assessed by elemental analysis and nitrogen adsorption. Elemental (CHN) analysis was performed on a Perkin Elmer 2400 Series II CHNS Analyser to quantify the amount of template removed from the porous material after post-synthetic treatments, while nitrogen adsorption (Micromeritics ASAP 2420) was used to measure porosity. The latter was performed by first degassing the dried powders at 110 °C and 5 μm-Hg for 2 hours, then nitrogen was dosed onto the sample at 77 K and the volume adsorbed was measured as a function of pressure. This was then used to calculate the BET surface area [167], the BJH pore-size distribution [168], and the *t*-plot microporous surface area [169] of the samples.

The BET analysis [167] (from the initials of Brunauer, Emmett and Teller who first proposed this theory) is an extension of the Langmuir theory [170] to account for multilayer adsorption. It is commonly used to allow comparison between porous solids and it is based on the following assumptions:

1. at saturation pressure infinite layers can form on the adsorbent;
2. the heat of adsorption of the second and higher layers is equal to the heat of condensation;
3. there are no interactions between adsorbed layers;
4. all adsorption sites are identical.

The BET isotherm is expressed by the relation in Equation (6.1):

$$\frac{P}{V_a(P_0 - P)} = \frac{1}{V_m c} + \frac{c-1}{V_m c}\frac{P}{P_0}, \tag{6.1}$$

where P and P_0 are the equilibrium and saturation pressure of the adsorbate at the temperature of adsorption (77 K), V_a is the volume of gas adsorbed, V_m is the monolayer coverage and c a constant given by the relation:

$$c = \exp\left(\frac{E_1 - E_L}{RT}\right), \tag{6.2}$$

with E_1 being the heat of adsorption for the first layer and E_L being the heat of condensation for all the following layers [167]. By plotting the left-hand side of Equation (6.1) against P/P_0 a linear relation is obtained in the range $0.05 < P/P_0 < 0.3$ [171].

The BJH (Barrett, Joyner and Halenda) method to determine pore size distribution, on the other hand, is based on the classical Kelvin equation for pore filling and makes use of the following assumptions:

1. the pores of the materials are supposed to be cylindrical;
2. adsorption occurs through two mechanisms: a) physical adsorption around the pore walls and b) capillary condensation in the "inner capillary volume" [168].

It should be noted that this technique is limited to pores in the mesoporous and macroporous range (pore diameter > 2 nm).

6.1.1 *Bio-inspired silica synthesis and purification with acid treatment*

EFFECT OF THE ACID TREATMENT ON TEMPLATE REMOVAL As shown in Figure 6.1, upon acid treatment, the concentration of PEHA in silica decreased as the pH was lowered (black line). Treatment at pH $\geqslant$ 5 was found to have a small effect on additive content ($<$ 27 % additive removed), however after further treatment to pH 4, an additional 42 % of the additive was removed. Acidification to pH $\leqslant$ 3 lowered the additive content to below the limit of detection, indicating that all of the additive was removed. Overall, the change in additive concentration was most pronounced between pH 4-5 as it can be observed from the blue line in Figure 6.1.

EFFECT OF THE ACID TREATMENT ON MICROPOROSITY Previous work has shown that purification by calcination introduces microporosity to silica [56], there-

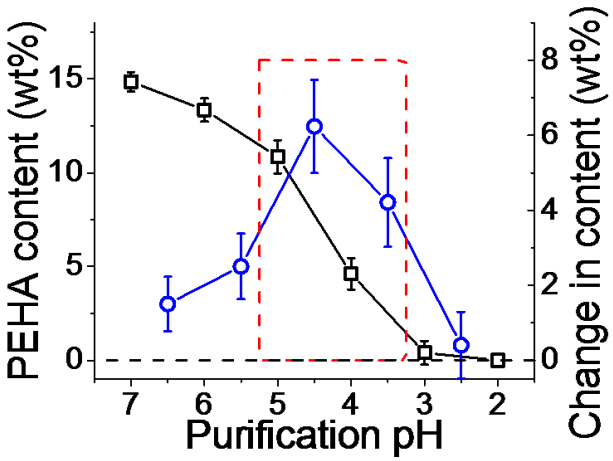

Figure 6.1: PEHA content in bio-inspired silica obtained from elemental analysis (black line) and calculated derivatives (blue line) as a function of pH during acid treatment. Error bars are one standard deviation from the mean value over three samples.

fore in this work the porosity of the samples was measured at each pH to examine the effect that acid treatment has on material properties. Similar to treatment with calcination, the surface area of bio-inspired silica increased as the additive was removed (see Figure 6.2) from approximately $\leqslant 30\ m^2\,g^{-1}$ at treatment pH $\geqslant 5$ to $\approx 300\ m^2\,g^{-1}$ at treatment pH $\leqslant 4$. Although the change in porosity occurs less gradually than the changes in PEHA content (cf. Figures 6.1 and 6.2), it should be noted that, also for the porosity, the majority of the change occurs between pH 5 and 4. A further thing to consider it that, despite marked changes in porosity, SEM analysis of the samples shows that the morphology remained largely unchanged (Figure 6.3).

By using a *t*-plot method, the total non-microporous surface area was found to be $< 15\ m^2\,g^{-1}$ (see Figure 6.2), indicating that all of the pores generated upon acid treatment were in the microporous region (< 2 nm). Given the size of the PEHA molecules used (reported as 1.8 nm [172]), it is tempting to assume that the width of each pore created corresponds to the size of an individual PEHA molecule removed. In order to further support this notion, the amount of PEHA removed was converted into the corresponding volume freed, and compared to the volume of micropores created (Figure 6.4). General good agreement between the measured pore volume of the samples and the estimated volume of additive lost is observed with the sole exception of pH 5, where the measured pore volume is lower than

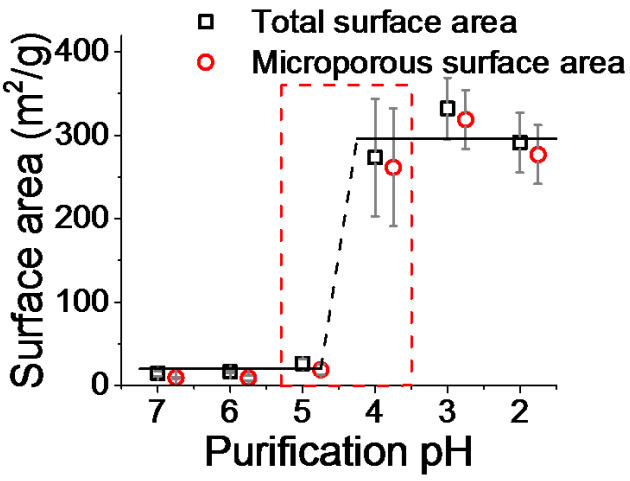

Figure 6.2: Total and microporous surface area as measured by *t*-plot (microporous data offset for clarity), with overlay lines at 30 $m^2\,g^{-1}$ and 300 $m^2\,g^{-1}$.

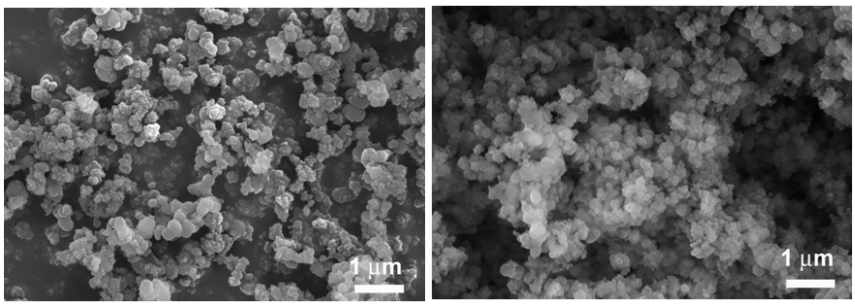

(a) (b)

Figure 6.3: Scanning electron micrographs of DETA silica before (a) and after (b) acid treatment, showing no observable change in morphology.

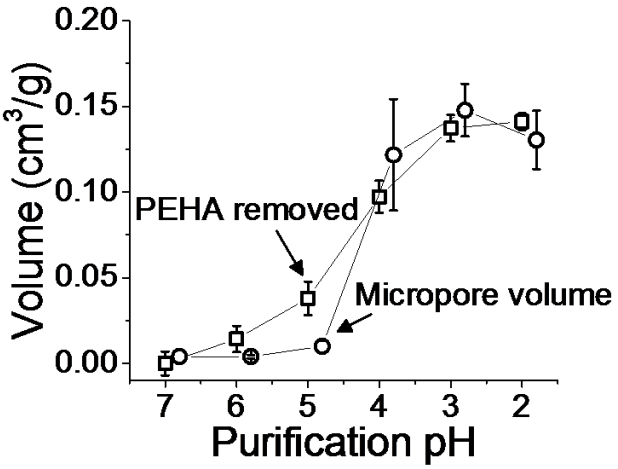

Figure 6.4: Calculated additive volume removed (squares) and measured micropore volume created from additive removal (circles) against acidification pH.

the amount of amine removed. This result may suggest that the initial additive was removed from the external surface of the material, as has been reported previously [173]. This will be further explored in section 6.2.3.

The ability of the acid treatment to control the removal of amine additives opens the possibility of tuning silica properties based on their chemical composition and porosity. Although the relationship between the treatment pH and the additive removal (Figure 6.1) was found to be non-linear, if the amount of additive removed is plotted against the amount of acid used, rather than against the acidification pH, a linear relationship can be obtained (see Figure 6.5). Repeating the synthesis with the homologous additive DETA showed that such linear relationship between amount of additive removed and amount of acid used found for PEHA is common to the alternative bio-inspired additive. The difference in values observed for the two additives can be attributed to different sizes, chemistry and architectures of the template molecules, known factors affecting the protonation behaviour of amines [172]. These results strongly suggest that it is possible to predictively design bio-inspired silica of desired composition, which would lead to the possibility of optimising the materials properties towards specific applications.

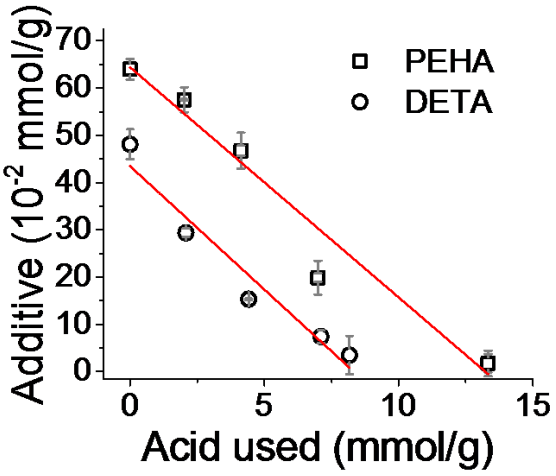

Figure 6.5: Residual additive content versus acid amount used for treatment. Lines represent linear fits with the equations $[\text{PEHA}] = 0.644 - 0.0487\,[\text{H}^+]$ ($R2 = 0.96$) and $[\text{DETA}] = 0.435 - 0.0522\,[\text{H}^+]$ ($R2 = 0.93$); all concentrations are mmol g^{-1} of silica treated.

6.1.2 *Comparison with other established purification methods*

The effectiveness of acid treatment as a purification method was compared against other established methods such as high temperature solvent extraction and calcination [166, 174] for template removal. In particular, the untreated (U) samples were subject to boiling water reflux (WR), calcination (C), or acid treatment followed by calcination (A+C), and then compared to the samples that only underwent acid treatment (A). Calcination was carried out in a tube furnace where approximately 0.5 g of sample were heated to 500 °C and held under flowing nitrogen for 8 hours. Silica was then cooled to ambient temperature and collected for further analysis.

By looking at Figure 6.6-(a), it is clear that additive removal using water reflux was not effective. This observation suggests that as-synthesised amine-silica composites were highly stable and, most important, that in order to achieve additive removal simple washing with water is not sufficient but the driving force of low pH must be present. Calcination increased the surface area of silica similarly to the acid treatment, however the pore size analysis showed that larger pores were generated in the samples treated with calcination compared to those that were subjected to acid treated or even to the acid-treated-then-calcined silica (see Figure 6.6-(b)). Such degradation of the pore structure, which was only observed in the calcin-

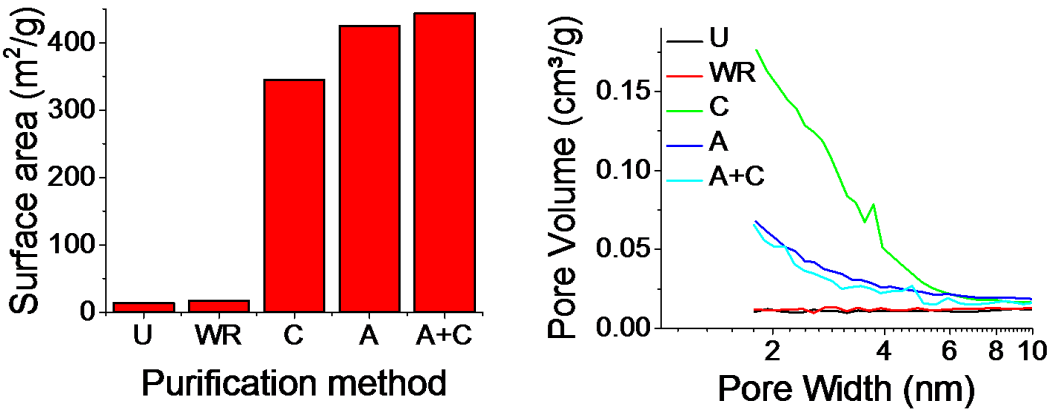

(a) (b)

Figure 6.6: Effect of treatment method on (a), total surface area and (b), pore size: U, untreated; WR, water reflux; C, calcinated; A, acid treatment and A+C, acid treatment then calcinated. It should be noted that the BJH method is limited to pores in the mesoporous and macroporous range (pore diameter > 2).

ated but not in acid treated or acid-treated-then-calcined silica, seems to suggest that the cause of the pore structure degradation has to be found in the thermal decomposition of PEHA during calcination, an issue which has been reported for calcination of other templated materials [164]. Therefore it can be concluded that acid treatment can avoid the degradation of delicate structures during purification due to the mild nature of this method compared to conventional techniques. The need for a pH driving force for the mild removal of additive rather than just solvothermal conditions indicates a dynamic change in the additive-silica interactions. Understanding these interactions and how they depend on pH would allow for generalisation of acid treatment to systems other than bio-inspired silica, leading to milder purification for a variety of templated materials.

6.2 COMPUTATIONAL STUDY

As discussed in the previous sections, the region between pH 4 and 5 (Figures 6.1 and 6.2) is of particular importance as most of the additive removal takes place in this pH range. In this section, atomistic molecular dynamics simulations are used to investigate the mechanism underlying the template removal observed experimentally with the objective of understanding the key features of this process. The

procedure adopted is based on the work of Emami et al. [175] and consists in the calculation of the energies of interaction between amines and an amorphous silica surface, representative of the bio-inspired material produced experimentally, at the different pH conditions of interest. These energies can then be related to the experimental results to infer, in a first instance, how the affinity of the additive for the substrate changes when the pH is lowered. Furthermore, by computing separately electrostatic and dispersion components of the energy, more information can be inferred with regards to the nature of the silica-template interactions. The chosen approach is relatively simple and fast, however cannot account for kinetics or possible confinement effects that in reality may affect the migration of the template molecules away from the silica pore network.

In the following sections, details about the force field parameters (section 6.2.1), the choice of the appropriate surface/amine population to represent each pH condition (section 6.2.2), and the simulation parameters used will be discussed.

6.2.1 *Model details and validation*

PEHA template molecules were modelled using the OPLS all-atom force field [80, 81] (see parameters in Tables C.1- C.4 and Figure C.1 in Appendix C) combined with the SPC/E model for water [132]. Parameters for silica surfaces (see Tables 6.1-6.3) were taken from the INTERFACE force field [176], which has been used to successfully study adsorption of amine-containing peptides onto silica surfaces [175–177], but were adapted in order to be used with the software GROMACS 4.6 [178]. The INTERFACE potential [176] was developed to be used in combination with several generic force fields such as AMBER, CHARMM, CVFF, PCFF, COMPASS, however, some adjustments are necessary to use it in the OPLS framework, due to the different conventions adopted in the OPLS and in CHARMM force fields for dealing with the 1-4 interactions (CHARMM takes 100 % of the 1-4 interactions whereas OPLS only takes half of them, more details can be found in Appendix C). To account for this difference, additional terms for non-bonded interactions have been added in the silica surface parameters (see Table 6.4). The atom names for all silica interactions follow the nomenclature used in Figure 6.7: labels HOY and OC24 are used to represent respectively hydrogen and oxygen atoms in silanol groups, SC5 and OC25 for silicon and oxygen atoms belonging to a siloxide group and SC4 and OC23 are silicon and oxygen atoms in the bulk.

Table 6.1: Lennard-Jones parameters, point charges and atomic masses for silica surfaces adapted from [175] to be used in GROMACS 4.6 software in the OPLS framework.

Site	Mass (a.u.)	q (a.u.)	σ (nm)	ε (kJ mol^{-1})
SC4	28.0860	1.1	0.369724	0.389112
SC5	28.0860	0.725	0.369724	0.389112
OC23	15.9994	-0.55	0.30914	0.225936
OC24	15.9994	-0.675	0.30914	0.510448
OC25	15.9994	-0.9	0.30914	0.510448
HOY	1.0080	0.4	0.09667	0.06276
NA+	22.98977	1	0.282415	0.393296

Table 6.2: Bond lengths and harmonic force constants.

Bond	b_o(nm)	k_b (kJ mol^{-1} nm^{-2})
SC4-OC23	0.165	238488
SC4-OC24	0.165	238488
SC5-OC23	0.165	238488
SC5-OC24	0.165	238488
SC5-OC25	0.165	238488
OC24-HOY	0.14710	414216

Table 6.3: Bond angles and harmonic force constants.

Angle	θ_o(deg)	k_θ (kJ mol^{-1} rad^{-2})
SC4-OC23-SC4	149.0	836.8
SC4-OC24-HOY	115.0	418.4
SC5-OC23-SC4	149.0	836.8
SC5-OC24-HOY	115.0	418.4
OC23-SC4-OC23	109.5	836.8
OC23-SC4-OC24	109.5	836.8
OC23-SC5-OC23	109.5	836.8
OC23-SC5-OC24	109.5	836.8
OC23-SC5-OC25	109.5	836.8
OC24-SC4-OC24	109.5	836.8
OC25-SC5-OC24	109.5	836.8
SC5-OC24-HOY	115.0	418.4

Table 6.4: Non-bonded parameters.

Interaction	C^6 (nm)	C^{12} (kJ mol^{-1})
SC4-SC4	0.369724	0.389112
SC4-SC5	0.369724	0.389112
SC4-OC23	0.338078	0.296504
SC4-OC24	0.338078	0.44567
SC4-OC25	0.338078	0.44567
SC4-HOY	0.189053	0.156271
SC5-SC5	0.369724	0.389112
SC5-OC23	0.338078	0.296504
SC5-OC24	0.338078	0.44567
SC5-OC25	0.338078	0.44567
SC5-HOY	0.189053	0.156271
OC23-OC23	0.309140	0.225936
OC23-OC24	0.309140	0.339601
OC23-OC25	0.309140	0.339601
OC23-HOY	0.172872	0.119079
OC24-OC24	0.309140	0.510448
OC24-OC25	0.309140	0.510448
OC24-HOY	0.172872	0.178985
OC25-OC25	0.309140	0.510448
OC25-HOY	0.172872	0.178985
HOY-HOY	0.096670	0.06276

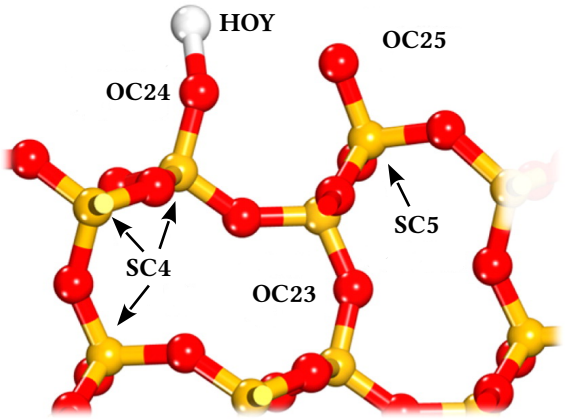

Figure 6.7: Schematic representation of the silica model showing the different atom types: hydrogen, white; silicon, yellow and oxygen, red. Figure adapted from Emami [175].

CALCULATION OF THE HEAT OF IMMERSION To make sure that the approach based on OPLS with the appropriate corrections is equivalent to the CHARMM approach originally used to develop the INTERFACE force field parameters [176], the heat of immersion of a pyrogenic silica surface with 0 % ionization (see Figure 6.8) was calculated and this value compared with the value reported by Emami et al. [175]. Pyrogenic silica surface was chosen to match the original force field validation protocol. This is a crystalline Q^3 surface (i.e. each surface Si atom is connected to three bridging oxygens and one hydroxyl group), however all force field parameters are exactly the same as those used to describe amorphous silica. In addition to this, in all simulations of this work water molecules are represented with SPC/E model [132], whereas in the work of Emami et al. [175] silica-water interfacial properties were tested for SPC, TIP3P and PCFF water models. Hence, the calculation of the heat of immersion with the adapted OPLS parameters and SPC/E water will provide not just an indication of the transferability of the INTERFACE force field in the OPLS framework, but also of its performance in combination with a different water model. For this purpose, four different systems were considered: i) CHARMM framework with SPC water, ii) CHARMM framework with SPC/E water, iii) OPLS framework with non-bonded interactions and SPC water and iv) OPLS framework with non-bonded interactions and SPC/E water. Apart

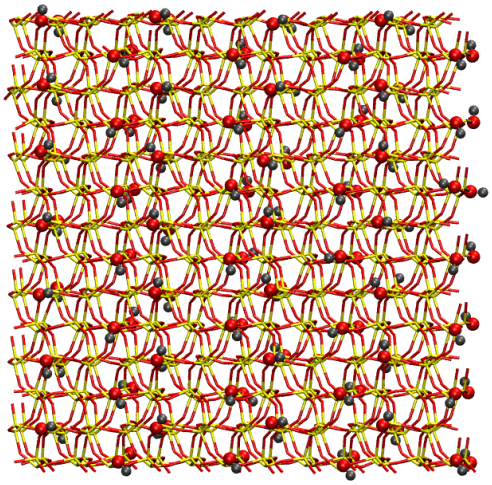

Figure 6.8: Top view of pyrogenic Q^3 surface used to validate the combination of INTERFACE and OPLS force fields used in this work. Silicons, yellow; oxygens, red and hydrogens, gray. The location of silanol groups has been highlighted representing OC24 and HOY atoms with small beads.

from adding a term to account for the additional 50 % of non-bonded interactions in the OPLS framework, the only other difference is the length of the Si-O bond, which increases from 0.165 nm to 0.168 nm in the case of the CHARMM framework (also to account for the different scaling of 1-4 interactions in the two force fields). Parameters used for water and silica surface in the CHARMM environment can be found in Tables C.5- C.10 of Appendix C. Parameters for silica in the OPLS environment are listed in Tables 6.1- 6.4.

The heat of immersion is defined as:

$$\Delta H_{imm} = \frac{E_{surface-in-water} - E_{surface-in-vacuum} - E_{water}}{2A}, \tag{6.3}$$

where the total energy of the surface immersed in water is $E_{surface\text{-}in\text{-}water}$, the energy of the surface in vacuum is $E_{surface\text{-}in\text{-}vacuum}$ and the energy of a box containing 1600 water molecules is E_{water}. This energy is normalised by the total surface area ($2A$) so that units are $mJ\,m^{-2}$. A schematic representation of the computational procedure [175] adopted can be seen in Figure 6.9. This requires that, for each of the systems studied, three molecular simulations corresponding to the three energy terms in Equation (6.3) are performed, with the sole exception of the vacuum term which is independent of the model used for water. The system representing the

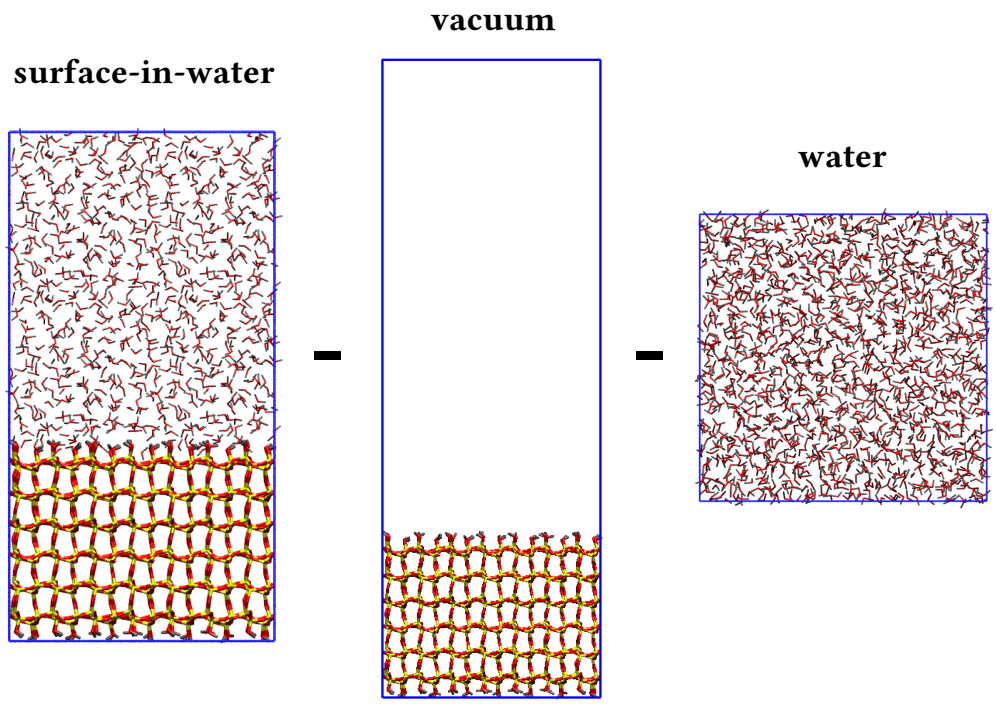

Figure 6.9: Schematic representation of the computational procedure used to calculate the heat of immersion. The energy of the vacuum and water system is subtracted from the system surface-in-water (Equation (6.3)). It must be noted that the real box used for the vacuum simulations is significantly taller (30 nm) than the one shown here (10 nm). Colour code is the same as in Figure 6.8.

surface immersed in water was created by adding 1600 water molecules to a simulation box containing the surface. This was followed by energy minimisation and equilibration in the *NPT* ensemble with semi-isotropic pressure coupling at 273 K before data were collected at 300 K in the *NVT* ensemble for 6 ns using a time step of 1 fs. The exact same steps of equilibration were followed also for the system containing only 1600 water molecules, whereas the system in vacuum was created by deleting all the water molecules from the surface-in-water system while extending the box height to 30 nm. In this last case no *NPT* equilibration is required. A cut-off of 1.2 nm was applied to short-range dispersion interactions, and the same distance was used for the particle-mesh Ewald method (PME) [90, 136] to take into account the long-range Coulomb electrostatics. Finally, a long-range dispersion correction term was added to both energy and pressure. For all simulations, total energy was calculated averaging over the last 4 ns providing the results shown in Table 6.5. It can be seen that, with the exception of the system in the CHARMM

Table 6.5: Comparison between heat of immersion of pyrogenic silica surface in water from simulations and experiments.

Publication	ΔH (model used) ($mJ\,m^2$)
This work	157 ± 1 (CHARMM-SPC), 199 ± 1 (CHARMM-SPC/E), 157 ± 1 (OPLS-SPC), 167 ± 2 (OPLS-SPC/E)
Emami et al. [175]	167 ± 2 (SPC), 160 ± 2 (TIP3P), 157 ± 2 (PCFF)
Taylor and Hockey [179]	160 ± 5 (EXP)

framework using the SPC/E water model, very good agreement with both experimental [179] and previous simulation results [175] was obtained, confirming that using the OPLS framework with the additional non-bonded interaction term and the SPC/E model for water can be considered a valid approximation to represent interactions with silica surfaces, including amorphous surfaces that are the main interest of this work.

6.2.2 *System preparation*

PH DEPENDENCE OF THE SURFACE CHARGE The choice of the appropriate surface model to represent each experimental pH condition is a crucial part of this study since from this choice will depend the number of siloxide groups (i.e. SC5 and OC25 atoms in the surface topology) available for interactions with the amine

additive. It is known that the degree of ionisation of silanol groups depends on several properties, among which pH, ionic strength, particle size, porosity and synthetic method [30]. However, due to the large number of variables that influence surface ionisation, the values available in literature are sometimes contrasting or difficult to compare even for the same pH. In order to get a reasonable estimate of the surface charge at the three pH values of interest (i.e. 3, 5 and 6.5) three studies that, by means of potentiometric methods, calculate the surface density of charge of different colloidal silica particles as a function of pH were considered [180–182].

The surface charge data collected from references [180–182] are reproduced in Figure 6.10. From the surface charge value it is possible to obtain the number

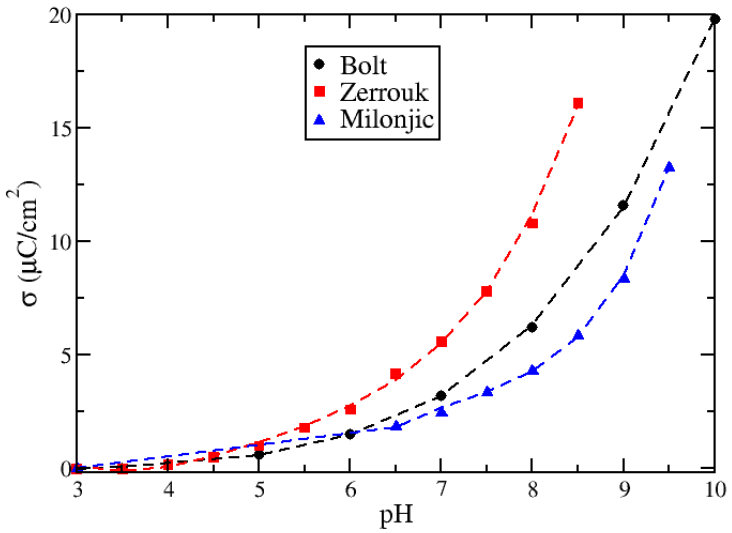

Figure 6.10: Surface density of charge as a function of pH from potentiometric calculations. Data from Bolt have been taken from reference [180] and correspond to a silica sol consisting of spherical particles with an average diameter of 15 nm and specific surface area, determined by nitrogen adsorption measurements, of 180 $m^2\,g^1$. Data from Zerrouk have been taken from reference [181] and correspond to a silica sol consisting of particles with an average diameter of 30 nm and specific surface area, calculated from the surface/volume ratio, of 90 $m^2\,g^1$. Data from Milonjic have been taken from reference [182] and correspond to to a silica sol consisting of particles with an average diameter of 9.0 nm and specific surface area, determined from titration with sodium hydroxide, of 300 $m^2\,g^1$.

of SIO^- groups, their average separation and the percentage of ionisation (see Tables 6.6- 6.8). It must be noted that the values marked with an asterisk have been interpolated using a power function (see Appendix C.5 for more details) and

Table 6.6: Surface density of charge as a function of pH at electrolyte concentration 0.1 N NaCl, σ in μC cm^{-2} [180].

pH	Surface charge density σ (μC cm^{-2})	Siloxide ion density (SIO^-/nm^2)	SIO^- ions in the simulation box	Average SIO^- separation distance (nm)	%
3.5	0	0	0	0	0
4 *	0.19	0.01	0.42	9.3	0.25
4.5 *	0.35	0.02	0.77	6.9	0.45
5	0.6	0.04	1.32	5.3	0.77
5.5*	0.96	0.06	2.11	4.2	1.23
6	1.50	0.09	3.29	3.3	1.91
6.5*	2.23	0.13	4.9	2.7	2.85
7	3.2	0.19	7.03	2.3	4.09
7.5*	4.59	0.28	10.07	1.9	5.86
8	6.2	0.37	13.62	1.6	7.91
8.5*	8.62	0.52	18.93	1.4	11.00
9	11.6	0.7	25.47	1.2	14.81
9.5*	15.09	0.91	33.14	1.1	19.27
10	19.8	1.19	43.48	0.9	25.28

* data interpolated (see Appendix C for more details); 10 μC cm^{-2} = 0.6 SIO^-/nm^2.

Table 6.7: Surface density of charge as a function of pH at electrolyte concentration 0.1 M NaCl ionic, σ in μC cm^{-2} [181].

pH	Surface charge density σ (μC cm^{-2})	Siloxide ion density (SIO^-/nm^2)	SIO^- ions in the simulation box	Average SIO^- separation distance (nm)	%
3.5	0	0	0	0	0
4	0.18	0.01	0.2 1.0	9.6	0.23
4.5	0.5	0.03	0.55	5.8	0.64
5	1	0.06	1.10	4.1	1.28
5.5	1.8	0.11	1.98	3	2.3
6	2.60	0.156	2.85	2.5	3.32
6.5	4.20	0.252	4.61	2.0	5.36
7	5.60	0.336	6.15	1.7	7.15
7.5	7.80	0.468	8.56	1.5	9.96
8	10.80	0.648	11.86	1.2	13.79
8.5	16.10	0.966	17.68	1.0	20.55

10 μC cm^{-2} = 0.6 SIO^-/nm^2.

Table 6.8: Surface density of charge as a function of pH at electrolyte concentration 0.1 mol/dm^3 NaCl ionic, σ in μC cm^{-2} [182].

pH	Surface charge density σ (μC cm^{-2})	Siloxide ion density (SIO^-/nm^2)	SIO^- ions in the simulation box	Average SIO^- separation distance (nm)	%
3	0	0	0	0	
3.5*	0.08	0.005	0.17	14.7	0.1
4*	0.15	0.01	0.33	10.5	0.19
4.5*	0.27	0.02	0.6	7.8	0.35
5*	0.46	0.03	1.01	6	0.59
5.5*	0.74	0.04	1.62	4.7	0.94
6*	1.14	0.07	2.50	3.8	1.46
6.5	1.86	0.11	4.08	3	2.37
7	2.48	0.15	5.45	2.6	3.17
7.5	3.38	0.20	7.42	2.2	4.31
8	4.31	0.26	9.46	2	5.50
8.5	5.86	0.35	12.87	1.7	7.48
9	8.34	0.50	18.31	1.4	10.65
9.5	13.27	0.80	29.14	1.1	16.94

* data interpolated (see Appendix C for more details); 10 μC cm^{-2} = 0.6 SIO^-/nm^2.

that the number of SIO^- groups and percentage of ionisation have been calculated considering a surface area of 18.3 nm^2 and a density of silanol groups of 4.7 per nm^2. These correspond to the average properties of the atomistic surface models used in a single simulation box.

From Tables 6.6- 6.8 and from Figure 6.10 it can be seen that the surface charge increases for increasing pH values, however, especially at higher pHs, a great variability of values can be observed. For the purpose of this work, the type of surface analysed in the paper by Milonjic [182] is the one that most resembles the material produced experimentally (similar ionic strength and size of the silica particles). Therefore the data shown in Table 6.8 are the ones considered when setting up the simulations that will be presented in the following sections. It follows that the amorphous silica surface used is completely neutral at pH 3, whereas at pH 5 and 6.5 the ionisation is approximately 0.6 % and 2.4 % respectively. Surface structures and parameters used to represent pH 3 are already available in the INTERFACE package [176] while the surfaces at pH 5 and pH 6.5 were created by removing respectively one or four randomly chosen hydrogen atoms from the neutral surface and adding an equal number of sodium ions into the system. In the topology file, parameters for oxygen and silicon atoms were also replaced with the corres-

ponding parameters for siloxide groups (atoms SC5 and OC25). Snapshots of the surface models used can be seen in Figure 6.11.

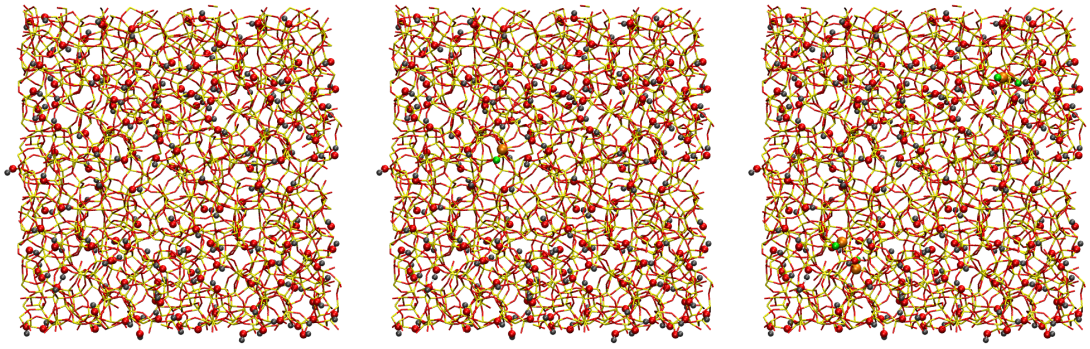

(a) pH = 3, 0 % (b) pH = 5, 0.6 % (c) pH = 6.5, 2.4 %

Figure 6.11: Top view of amorphous silica surfaces at different pH used in the corresponding simulations. (a), surface with 0 % ionisation representing pH 3; (b), surface with 0.6 % ionisation representing pH 5 and (c), surface with 2.4 % ionisation representing pH 6.5. For all surfaces the density of silanol groups is 4.7 per nm^2. Colour code is the same as in Figure 6.8. The position of siloxide groups has been highlighted using small beads for the atom types SC5, green and OC25, orange.

TEMPLATE IONISATION WITH PH Like the silica material, also the amine template changes ionisation state depending on the pH, i.e. PEHA molecules become progressively neutral as the pH is increased. In Figure 6.12 a representation of all the amine species used in this study is provided, where the blue colour has been used to indicate a charged nitrogen (N^+) while the purple is used for a nitrogen with no charge (N). The degree of protonation of the amines as a function of pH and their relative amount was determined using the SPARC online calculator [183] (see Table 6.9 for more details). It must be noted that species that are only present at very low concentrations ($\leqslant 0.01$) are not reported in the table since they were not considered in this study.

SIMULATION DETAILS Table 6.10 contains all the simulations that were performed to estimate the interaction energies of amine molecules with silica surfaces

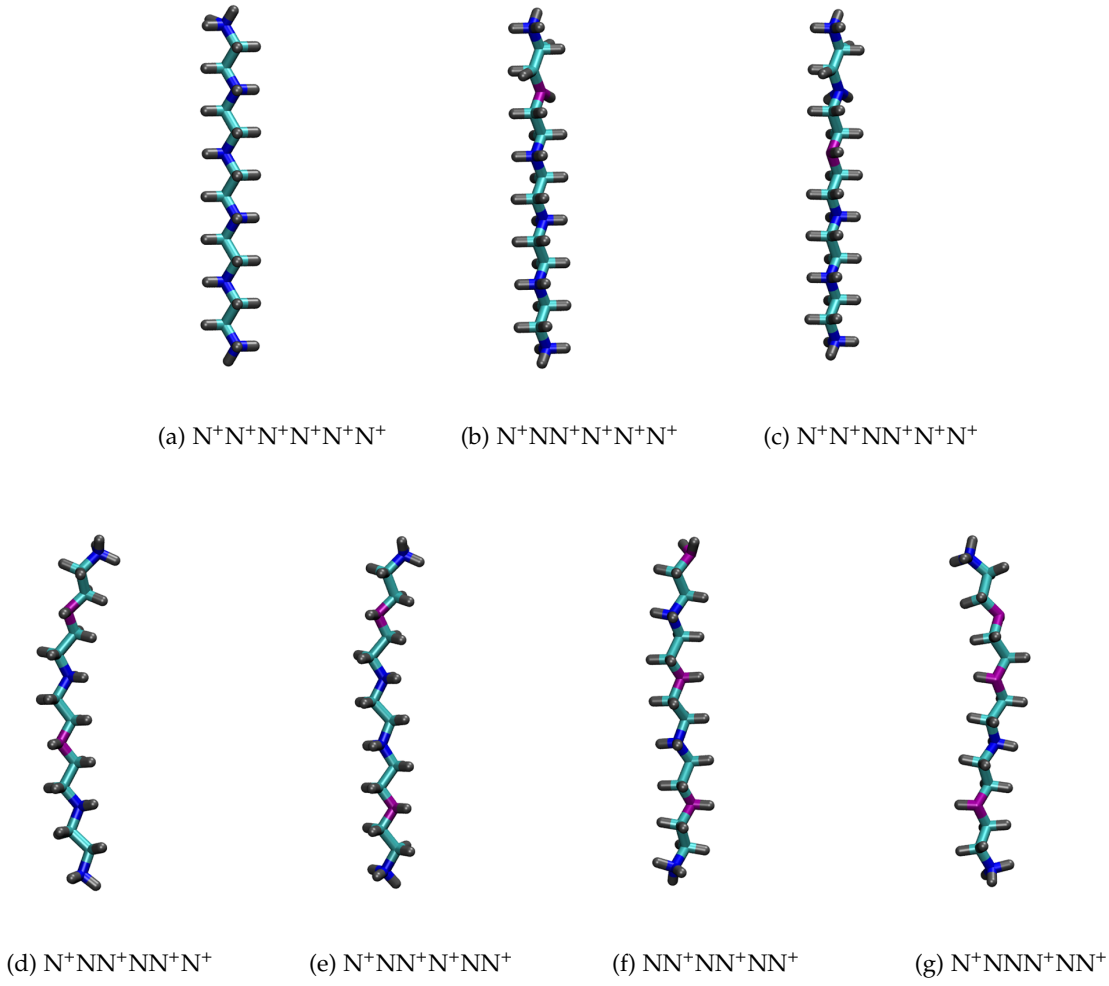

(a) $N^+N^+N^+N^+N^+N^+$ (b) $N^+NN^+N^+N^+N^+$ (c) $N^+N^+NN^+N^+N^+$

(d) $N^+NN^+NN^+N^+$ (e) $N^+NN^+N^+NN^+$ (f) $NN^+NN^+NN^+$ (g) $N^+NNN^+NN^+$

Figure 6.12: Schematic representation of the different ionisation states of PEHA molecule considered in this study (see Table 6.9). Charged nitrogens, blue; neutral nitrogens, purple; hydrogens, gray and carbons, cyan.

Table 6.9: Relative population of amines between pH 3 and 7. Ionisation data obtained from SPARC online calculator [183], N, neutral and N^+, ionised.

pH	$N^+N^+N^+N^+N^+N^+$	$N^+NN^+N^+N^+N^+$	$N^+N^+NN^+N^+N^+$	$N^+NN^+NN^+N^+$	$N^+NN^+N^+NN^+$	$NN^+NN^+NN^+$	$N^+NNN^+NN^+$
3	0.51	0.13	0.37	0.01	0.01	0	0
3.2	0.39	0.16	0.45	0.03	0.1	0	0
3.4	0.28	0.19	0.51	0.05	0.02	0	0
3.6	0.19	0.2	0.55	0.08	0.03	0	0
3.8	0.12	0.2	0.55	0.08	0.03	0	0
4	0.07	0.19	0.52	0.2	0.08	0	0
4.2	0.04	0.16	0.45	0.28	0.12	0	0
4.4	0.02	0.14	0.38	0.37	0.15	0	0
4.6	0.01	0.11	0.29	0.45	0.19	0	0
4.8	0	0.08	0.21	0.52	0.22	0	0.01
5	0	0.05	0.15	0.58	0.24	0	0.01
5.2	0	0.04	0.1	0.62	0.26	0	0.02
5.4	0	0.02	0.07	0.64	0.27	0.01	0.03
5.6	0	0.02	0.04	0.65	0.27	0.01	0.05
5.8	0	0.01	0.03	0.64	0.26	0.02	0.07
6	0	0.01	0.02	0.61	0.25	0.03	0.11
6.2	0	0	0.01	0.57	0.24	0.04	0.16
6.4	0	0	0.01	0.51	0.21	0.06	0.23
6.6	0	0	0	0.44	0.18	0.08	0.31
6.8	0	0	0	0.35	0.15	0.11	0.4
7	0	0	0	0.27	0.11	0.13	0.48

at different pH (3, 5 and 6.5). A typical input system was prepared by placing a

Table 6.10: List of all simulations performed to study silica-amines interactions. SC, small system with amine close to the surface; SA, small system with amine away from the surface; LC, large system with amine close to the surface and LA, large system with amine away from the surface.

pH	$N^+N^+N^+N^+N^+N^+$	$N^+NN^+N^+N^+N^+$	$N^+N^+NN^+N^+N^+$	$N^+NN^+NN^+N^+$	$N^+NN^+N^+NN^+$	$NN^+NN^+NN^+$	$N^+NNN^+NN^+$
3	SC, SA	LC	LC	SC, SA, LC, LA	SC, SA, LC, LA		
5	SC	SC	LC, LA	LC, LA	LC, LA		
6.5				SC, LC	LC	LC	LC

pre-equilibrated slab of water containing a single amine molecule (i.e. simulating the infinite dilution limit) above a slab of amorphous silica with a thickness of approximately 2.5 nm and a cross-sectional area of 18.3 nm^2. Periodic boundary conditions were applied in all directions and, after energy minimisation, production simulations were run in the canonical (*NVT*) ensemble at 298 K using the same parameters adopted for the validation of the model (see section 6.2.1). To confirm equilibrium had been reached, in some cases, two different starting configurations were tested until simulated energies were independent of the starting positions: one in which the amine was placed in the centre of the water slab (referred with letter A - away) and another in which the amine was placed as close to the surface

as possible (referred with letter C - close), following an energy optimization in vacuum. Similarly, to discount the possibility of finite-size effects on the simulated energies, box lengths of 7 nm (referred with letter S - small) and 14 nm (referred with letter L - large) perpendicular to the surface were both tested (cf. Table 6.10). In Figure 6.13 an example of the four different types of simulations is shown for the case of $N^+NN^+N^+NN^+$ at pH 3.

6.2.3 *Molecular-level mechanism of template removal based on pH control*

The results obtained with MD simulations suggest that there are two key interactions controlling the removal of amine additives from silica: ionic attractions between oppositely charged species and solvation of additive in surrounding bulk water. However, the balance between these two types of interactions varies with pH, leading to interesting effects. For example, at pH 5-7 the silica surface is negatively charged and the amine additive positively charged, leading to strong charge-charge interactions between the additive and the surface siloxide groups (SiO^-), and consequently resulting in very little-to-no removal of the additive (see Figure 6.14-(b) and (c)). Under these conditions, the average separation between surface siloxide anions (< 2.6 nm) is significantly larger than the length of the additive (≈ 1.8 nm, cf. Table 6.8). It was observed that each additive molecule can interact with at the most a single siloxide group when adsorbed (Figure 6.15), meaning that the interaction energies of individual adsorbed molecules over this pH range were similar (around -250 kJ mol^{-1}). Conversely, at pH < 4, while additives remain positively charged, the silica surface becomes predominantly uncharged (see Table 6.8). In this case the additive appears to be fully solvated away from the surface (see Figure 6.14-a) since solvation is more energetically favourable than surface-additive interactions under these conditions. It was found that the amine-silica interaction energy was effectively zero, which explains the complete removal of PEHA at low pH.

To further probe this balance between ionic interactions and additive solvation, the methylated analogues of pentaethylenehexamine (m-PEHA, see Figure 6.16-(a)), i.e. making their charge permanent but increasing their hydrophobicity, was investigated. The results from simulation of the methylated additive indicate that solvent extraction becomes ineffective even at pH 3 (Figure 6.16-(b)) due to reduced solvation of the additive and to the formation of sufficient non-ionic interactions

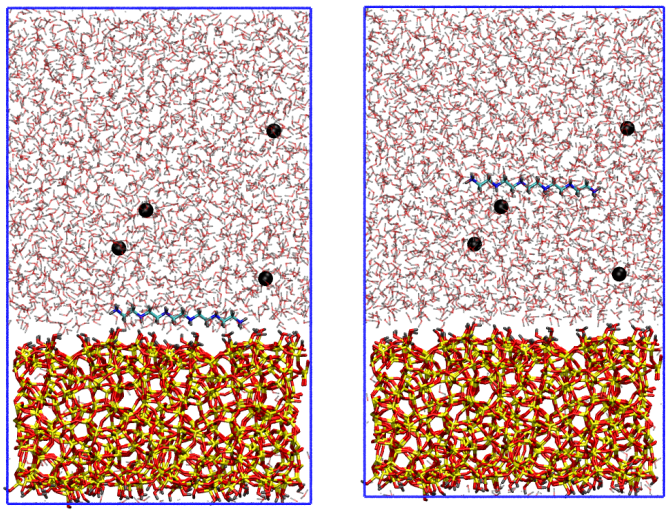

(a) (b)

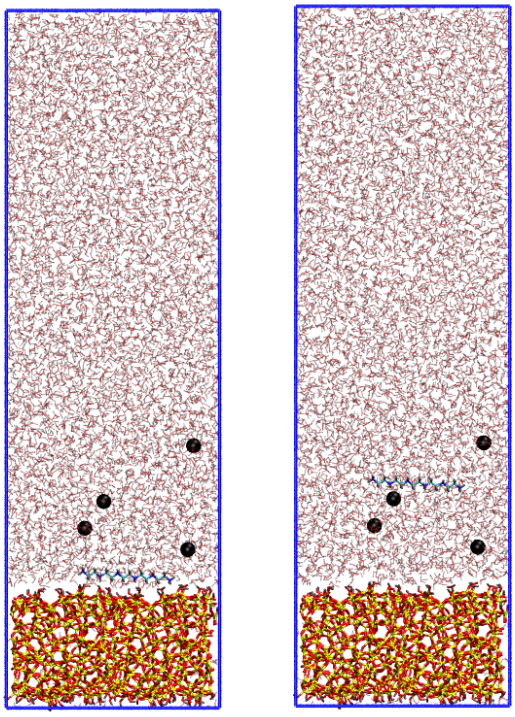

(c) (d)

Figure 6.13: Snapshots showing the initial configurations used for the simulations of $N^+NN^+N^+NN^+$ at pH 3: (a), small box with PEHA close to the surface; (b), small box with PEHA away from the surface; (c), large box with PEHA close to the surface and (d), large box with PEHA away from the surface. Colour code is the same as in Figure 6.8 with chloride counter-ions shown as black spheres.

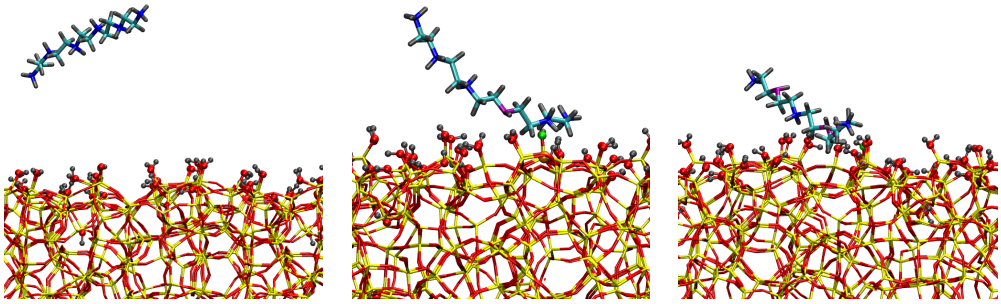

(a) pH = 3 (b) pH = 5 (c) pH = 6.5

Figure 6.14: Snapshots showing the interaction of PEHA molecules with silica surface at different pH. (a), $N^+N^+N^+N^+N^+N^+$; (b), $N^+N^+NN^+N^+N^+$ and (c), $N^+NNN^+NN^+$. Colour code is the same as in Figure 6.11.

with the silica surface (calculated interaction strength of ca. −135 kJ mol^{-1} for the m-PEHA compared to ca. 0 kJ mol^{-1} for PEHA). Indeed, a 25 % reduction in the removal efficiency for methylated additives was observed experimentally when compared to the non-methylated counterparts (shown in Figure 6.17). Similarly, for traditional mesoporous silicas, it has been reported that solvent extraction cannot fully remove methylated templates such as cetyltrimethylammonium bromide (CTAB), while the nonmethylated counterparts e.g. dodecylamine (DDA) can be completely removed [9, 184]. In fact, the removal of CTAB is 25 % less effective than removal of DDA [9], which closely matches the results discussed here and strongly supports the proposed mechanism. Another outcome of this work is that the general agreement observed between simulated and experimental results indicates that MD simulations can be a useful predictive tool for assaying non-destructive template removal techniques for porous materials. This point will be further explored in the next section by assessing the suitability of alternative solvents for purification of silica materials from m-PEHA additives.

Using the simulated interaction strengths, a relationship between the pH and average surface interaction strength per additive molecule can be inferred (Equation (6.4)), where [≡ SiO^-] and [Additive] represent the number of siloxide ions and additive molecules per area of silica surface, respectively.

$$\langle E_{int} \rangle = \frac{[\equiv SiO^-]}{[\text{Additive}]} E_{\text{Additive-}SiO^-}, \tag{6.4}$$

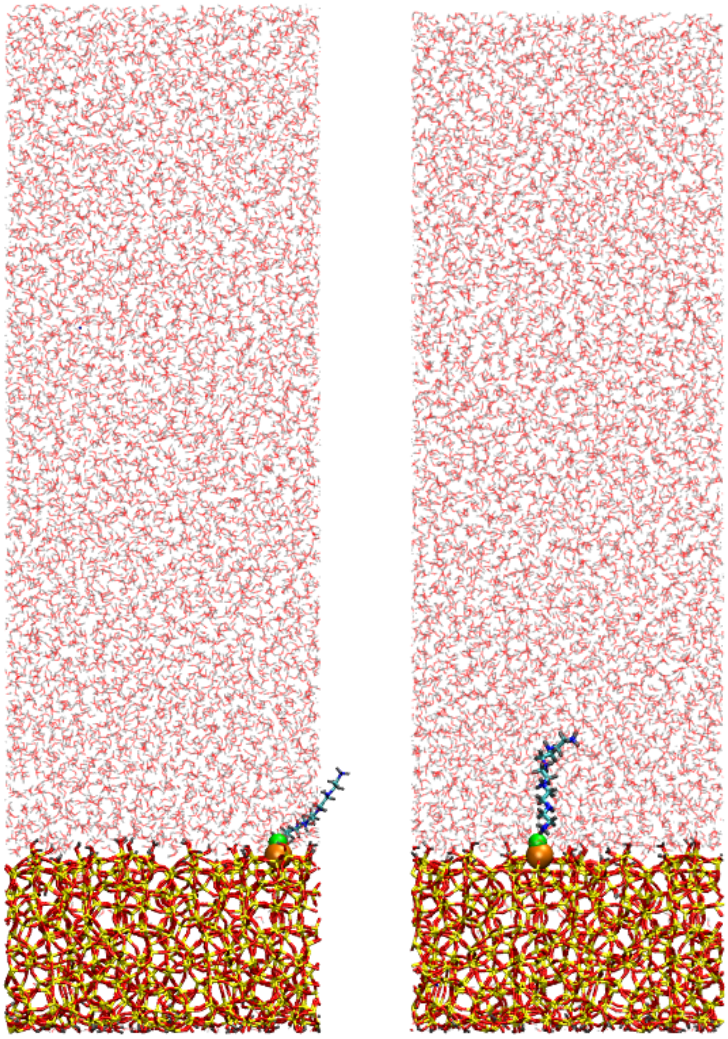

(a) (b)

Figure 6.15: Snapshots showing the final configurations obtained for the simulations of $N^+NN^+N^+NN^+$ at pH 5 when starting with amine away from the surface (a) and close to the surface (b). Colour code is the same as in Figure 6.11.

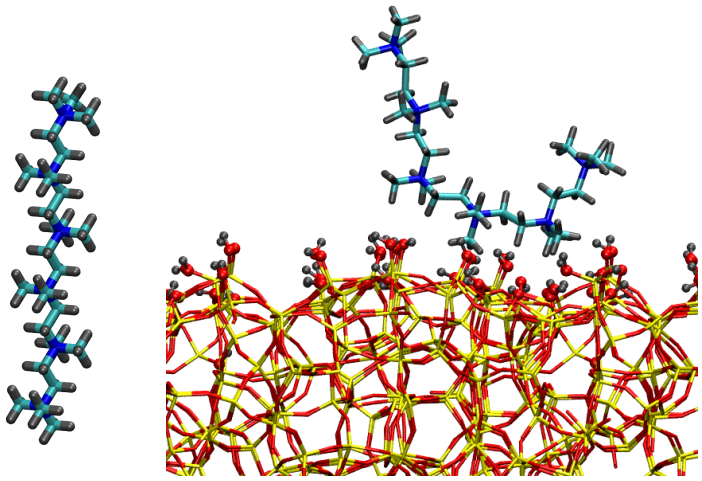

(a) (b)

Figure 6.16: Schematic representation of m-PEHA molecule (a) and snapshot showing its interaction with silica surface at pH 3 (b). Colour code is the same as in Figure 6.11.

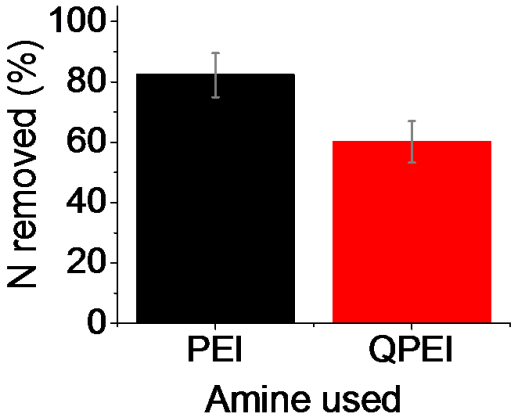

Figure 6.17: Comparison of additive removal effectiveness between poly(ethyleneimine) (referred here as PEI) and methyl-substituted poly(ethyleneimine) (referred here as QPEI), showing 25 % decrease in effectiveness when using QPEI.

As noted above, under the pH range considered here (pH 3-7), each PEHA molecule can only interact with a single siloxide group and PEHA will always be protonated (partially or fully), hence Equation (6.4) uses [Additive] for simplicity rather than the concentration of protonated amines. As [$\equiv SiO^-$] is a function of pH, the relationship predicted using this equation shows an exponential decrease in interaction strength with reducing pH (Figure 6.18), eventually becoming lower than the energy of thermal fluctuations (i.e. , RT, where R is the ideal gas constant) at around pH 4.2. This suggests that above pH 4.2, most additives are still able to

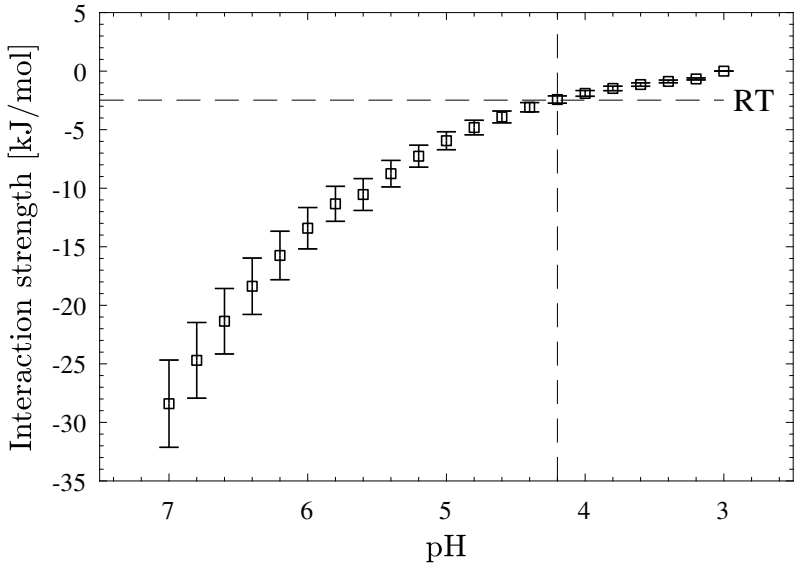

Figure 6.18: Simulated PEHA-siloxide ion interaction strengths, normalised against availability of precursor ions.

(on average) remain attached to the surface, whereas below pH 4.2, thermal fluctuations are sufficient to cause a widespread release of additive molecules. This agrees with experimental findings that show that both the majority of additive removal and a step change in porosity take place between pH 5 and 4 (dotted box in Figure 6.1 and Figure 6.2).

The simulation results from Figure 6.18 also imply that all additive should be removed between pH 4-5, however, the experimental results (Figure 6.1) clearly show that a complete removal only occurs at pH < 4. Further, the simulation does not explain the discrepancy seen between the amount of the additive removed and the resultant silica pore volume created at pH 5 (Figure 6.4). In order to explain these, the confinement of additives within the silica pore system must be considered. In

the simulations, the additives interact with a flat silica surface, while bio-inspired silica particles are made up of a network of primary particles (5-10 nm) fused together to form larger secondary particles (> 100 nm), creating an interstitial pore network wherein the majority of additive molecules are likely to be encapsulated (shown in the scheme in Figure 6.19-(a)) [185]. Due to confinement effects between multiple silica surfaces, the silica-additive interactions are expected to be stronger than predicted in the simplified MD simulations of a bare surface [186]. When the pH was lowered slightly, where the interactions were reduced but did not disappear (i.e. pH 5), it is likely that only surface-bound additives were initially removed due to their lower interaction strengths compared to the entrapped additives (Figure 6.19-(b)). Further treatment to lower pH removes the interaction entirely such that even entrapped additives can be released from the pore structure (Figure 6.19-(c)), leaving behind the pure silica network.

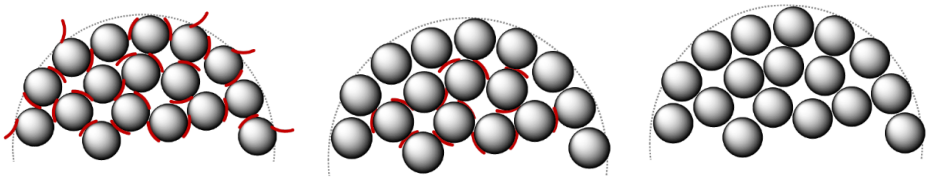

(a) pH = 7 (b) pH = 5 (c) pH = 2

Figure 6.19: Schematic representation of the pore networks in bio-inspired silica and location of the additive at different stages of the acid treatment: (a), untreated silica with PEHA molecules (red lines) adsorbed both to the particle surface and inside the network of smaller primary particles (grey circles); (b), after partial treatment to pH 5 the surface-adsorbed PEHA molecules are released due to loss of available siloxide ions whereas internally held PEHA molecules still have significant interactions due to confinement effects and (c), all PEHA molecules are released after treatment at pH 2.

6.3 SCREENING OF ALTERNATIVE SOLVENTS FOR TEMPLATE REMOVAL WITH MD SIMULATIONS

As discussed in the previous section, experimental and simulation results show that acid treatment becomes ineffective for removal of m-PEHA additives. It was

also found that the effectiveness of removal depended on a balance between surface adsorption and solvation. Here, using the same simulation protocol, the suitability of alternative solvents for purification of bio-inspired silica is investigated. A schematic representation of the solvents considered for this study is provided in Figure 6.20. These are hexane, dichloromethane (DCM), acetone, dimethyl sulfoxide (DMSO) and ethanol.

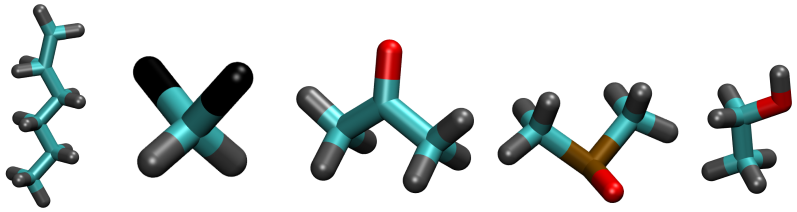

(a) (b) (c) (d) (e)

Figure 6.20: Schematic representation of the alternative solvents investigated, a) hexane, b) DCM, c) acetone, d) DMSO, e) ethanol. Carbon - cyan, hydrogen - gray, chloride - black, oxygen - red, sulphur - brown.

Depending on their polarity, solvents are divided into nonpolar and polar solvents. Polar solvents possess large dielectric constants and dipole moments as a result of the presence of bonds between atoms with different electronegativities. Furthermore, polar solvents that possess hydrogens in O-H or N-H groups are called protic. Protic solvents can donate protons and form hydrogen bonds, contrary to aprotic solvents. A classification of the solvents investigated and relative properties is provided in Table 6.11.

Table 6.11: Properties and classification of the different solvents screened with MD simulations for template removal.

Classification	Solvent	Density (g/L)	Dielectric constant	Dipole (D) moment	Boiling point (°C)	Freezing point (°C)
Nonpolar Solvents	Hexane	654.8	1.8	0.00	68.5 to 69.1	-96 to -94
"Borderline" Polar Aprotic Solvents	DCM	1326.6	9.1	1.60	39.6	-96.7
Polar Aprotic Solvents	Acetone	784.5	21	2.88	56.05	-94.7
	DMSO	1100.4	47	3.96	189	19
Polar Protic Solvents	Ethanol	789	25	1.69	78.37	-114
	Water	1000	80	1.85	100	0

SIMULATION DETAILS The initial configurations were prepared, like described above, by placing a single m-PEHA molecule on a slab representing a silica surface

at pH = 3 (cross-sectional area of 18.3 nm² and thickness of approximately 2.5 nm). The remaining volume (the simulation box measures 14 nm in the z-direction) was filled with a pre-equilibrated box of the specific solvent and periodic boundary conditions were applied in all directions. The system was then energy minimised and production runs in the canonical ensemble were performed using the same parameters adopted before (see section 6.2.1). All cases were studied first at 25°C (298 K) but additional simulations at higher temperatures were also performed for the acetone and DMSO systems.

SIMULATIONS OF TEMPLATE REMOVAL USING ALTERNATIVE SOLVENTS AT AMBIENT TEMPERATURE Table 6.12 summarises the energies of interactions obtained with different solvents for simulations of one m-PEHA molecule interacting with an amorphous silica surface at pH = 3 (the surface is uncharged).

Table 6.12: Calculated energies of interactions at T = 25°C for the system m-PEHA-silica surface at pH = 3 with different solvents.

Energy (kJ mol^{-1})		Hexane	DCM	Acetone	DMSO	Ethanol	Water
surface-amine	Coul	-356.00	-124.51	-63.83	-55.58	-86.22	-104.09
	LJ	149.24	-56.04	-35.36	-29.31	-56.08	-43.58
	Tot	-206.76	-180.55	-99.19	-84.88	-142.29	-147.6
amine-solvent	Coul	349.80	-63.85	-657.92	-724.85	-293.41	-534.27
	LJ	-138.94	-144.55	-227.43	-298.33	-153.36	-121.00
	Tot	210.86	-208.40	-885.43	-1023.17	-446.77	-655.27
surface-solvent	Coul	-6448.63	-373.35	-2180.73	-3273.44	-4439.15	-7156.96
	LJ	6189.15	-1653.04	-1583.16	-2147.45	-1254.65	-216.68
	Tot	-259.48	-2026.59	-3763.89	-5420.59	-5693.80	-7373.64

For hexane and DCM the total surface-amine interaction energy is higher than the value obtained with pure water, suggesting that nonpolar and mildly polar solvents do not favour template removal at low pH. Moreover, when ethanol is used the total energy of interaction between silica and m-PEHA is very close to the value obtained with water indicating that other polar protic solvents are also ineffective in removing amine template molecules. On the other hand, the total silica-amine energy is lowered when polar aprotic solvents are used while the amine-solvent energy is increased indicating that solubilisation is more favourable in this case. The decrease observed in the total silica-amine energy is not sufficient

to achieve the release of m-PEHA at ambient temperature but suggests that complete release could be achieved at higher temperatures. This hypothesis is further explored in the next section.

SIMULATIONS OF TEMPLATE REMOVAL WITH DMSO AT HIGH TEMPERATURES

Table 6.13 shows the values obtained for the energy between m-PEHA and amorphous silica surface at different temperatures when DMSO is used as solvent.

Table 6.13: Calculated energies of interactions at different temperatures for the system m-PEHA-silica surface at pH = 3 when DMSO is used as solvent for extraction. Calculated error in parenthesis.

Energy (kJ mol^{-1})		T=25°C	T=30°C	T=35°C	T=40°C
surface-amine	Coul	-55.58 (4)	-152.98 (1.2)	0.49 (0.41)	0.00 (0.00)
	LJ	-29.31 (1.2)	-78.65 (0.41)	-2.00 (0.4)	0.00 (0.00)
	Tot	-84.88 (1.2	-231.64 (1.3)	-1.50 (0.6)	-0.00 (0.00)
amine-solvent	Coul	-724.85 (33.0)	-507.59 (45.0)	-678.88 (40.0)	-823.34 (18.0)
	LJ	-298.33 (2.6)	-230.11 (4.3)	-321.68 (3.3)	-342.06 (2.0)
	Tot	-1023.17 (33.1)	-737.70 (45.2)	-1000.56 (40.1)	-1165.40 (18.1)
surface-solvent	Coul	-3273.44 (9.9)	-3219.11 (19.0)	-3280.49 (5.0)	-3272.05 (2.3)
	LJ	-2095.77 (2.1)	-2158.58 (3.4)	-2165.43 (4.9)	-1890.25 (3.1)
	Tot	-5420.89 (11.4)	-5314.88 (19.1)	-5439.07 (6.0)	-5437.48 (5.4)

MD simulations predict that by simply increasing the temperature to 35°C the energy is reduced by more than 95 % and when the temperature is as high as 40°C the interaction is effectively zero. These results are not supported by any experimental evidence at the moment but could be used by experimentalists as a guide for testing of alternative solvents for template extraction.

6.4 CONCLUSIONS

In this work a simple, mild method of controlling organic additive content in bio-inspired silica through post-synthetic acid treatment was demonstrated. By modifying the pH of silica suspensions a range of silica-organic composites with modified porosity, chemical activity and organic content were synthesised. Using atomistic MD simulations the mechanism underlying the template removal was investigated at molecular level. This revealed that acid treatment was found to work by changing silica-additive surface interactions, depending on changes in silica spe-

ciation and additive solvation. The bio-inspired silica material was purified due to a weakening and eventual loss of charge-charge interactions between additive and surface, allowing for full or partial purification with high reproducibility. It was also shown that methylated PEHA additives are only partially removed when extraction is performed with pure water at ambient temperature, however results of molecular simulations suggest that by replacing water with other solvents, such as acetone or DMSO, enhancement of template removal can be achieved at ambient temperature and complete removal is achieved already at 35 °C. Therefore, acid-treated bio-inspired silicas, which reduce environmental wastefulness, have the potential to replace traditional silicas in a wide range of established and new applications. Furthermore, the agreement between experiments and simulation results indicate that molecular simulations can be used as an inexpensive, simple and fast tool for screening of alternative solvents to use for the purification of silica materials.

7

CONCLUSIONS AND FUTURE WORK

A computational study on the processes occurring during the formation of bio-inspired silica materials was presented in this thesis. In the first part, the focus was on understanding the mechanisms underlying the synthesis of this class of mesoporous silicas, while in the second part simulations were used to complement experiments in elucidating the nature of the interactions occurring during template removal by means of solvent extraction methods. Obtaining a more comprehensive understanding of the different stages of the process through which these materials are created could allow to exploit the advantages of bio-inspired synthesis even further, and open the way to potential new applications of this synthetic strategy. Furthermore, by investigating the synthesis using a multi-scale approach, it was possible to maintain the realism of atomistic (AA) models also at a mesoscale level, while significantly reducing the computational costs and allowing access to longer times and length scales.

With regard to the first part of the work, the formation of two examples of bio-inspired materials, MSU-V and HMS materials, was investigated through a combination of atomistic and coarse-grained simulations. The initial steps of this study involved the development of coarse-grained (CG) models, based on the MARTINI force field [10], to describe the interactions between organic and inorganic species participating in the synthesis of HMS materials. Here, dodecylamines (DDA) are considered as the template to direct structure formation. These are amphiphilic molecules whose speciation changes with pH and, in particular, charged species dominate at low pH while at high pH DDA is mostly neutral. The other species considered are silica monomers as well as dimers at different charge states. Hence, the CG models were developed following the same procedure adopted by Pérez-Sánchez et al. to study the synthesis of periodic mesoporous silicas [7]. This consisted in adjusting the CG parameters until reasonable agreement between AA and CG density profiles of preformed aggregates was obtained. Even though the main function of the AA simulations is to act as benchmarks for CG development, they provided some interesting insight. For example, in agreement with experimental evidence that indicates that neutral DDA surfactants are essentially insoluble in

water [139], micelle disruption was observed when these contained only neutral amines. Another interesting result is that, in the system with charged surfactants (DDA^+), adsorption of neutral silica monomers on the micelle surface appears to be favoured when anionic monomers were also present. Overall, good agreement was obtained with the parameters previously determined by Pérez-Sánchez et al. [7], with the sole exception of the parameters used to model doubly charged silica dimers (SISI). In fact, these dimers adsorb on the surfactant head in the present system, whereas SISI adsorb on the outside of the surfactant head in the CTAB system considered by Pérez-Sánchez et al. [7]. This behaviour can be ascribed to the different head size of CTAB and DDA surfactants (larger for CTAB than for DDA), which allows penetration of the dimer into the micelle in the latter but not in the former. Therefore, to obtain the correct physical behaviour, a new parametrisation was adopted to describe the interaction between dimers and the hydrophobic part of the surfactants. This outcome seems to indicate a certain limitation of the MARTINI model [10], since the position where silica dimers can adsorb on the micelle is essentially controlled by the strength of this interaction.

Once all parameters were established, the model for DDA^+ was further validated against experimental data (aggregation numbers and observed phases), thereby showing good reproducibility with the chosen CG surfactant model. In the next step, simulations of HMS at different pH and at experimental concentration were performed. CG simulations containing only surfactants (reference systems) revealed that neutral surfactants undergo phase separation, due to their limited solubility in water, whereas charged surfactants form micellar aggregates. Interestingly, phase separation of neutral surfactants is also observed when silicates are added to the system, while in the charged surfactant system micelles are converted into large branched rods. This result indicates that, contrary to the hypothesised mechanism based on interactions between neutral species [9], charged species are necessary to promote rod formation. Hence, the synthesis of HMS materials was further studied including the effect of more highly condensed species, showing that dimers produce disordered packing of rods in agreement with the "worm-like" or "worm-hole" structures reported experimentally [126], hence reinforcing the hypothesis that charge matching interactions generate HMS materials.

The second type of bio-inspired material considered, MSU-V, was initially studied using atomistic simulations. Like HMS materials, MSU-V materials also make use of amphiphilic surfactants as templates, however diamines are used in this case [37]. As in the previous system, to account for the effect of pH, three different sur-

factant types were considered: neutral (DADDn), singly charged (DADDs) and doubly charged (DADDd) 1,12-diaminododecane (DADD). Simulations at high ($>$ 11) and intermediate (8-11) pH, where the majority of surfactants is either neutral or singly charged, showed formation of dry layers of surfactants for both systems. However, when silicates are added, strong adsorption of silica monomers on the layer only occurred in the system with DADDs, while the monomers remained homogeneously dispersed in the solution with DADDn. Conversely, when doubly charged surfactants dominate (pH $<$ 8), formation of disordered clusters is observed, also after the addition of silica. Furthermore, simulations containing all three types of surfactants (i.e. conditions close to the calculated pH of synthesis), produced curved layers and spontaneous formation of a hole, inside which a few silica monomers, together with water molecules, migrated. It is hypothesised that, due to excess of charges, similar holes or defects could be created across template layers allowing more silicates to penetrate and eventually condense inside. This result, therefore, represents a direct evidence for the pillaring mechanism postulated experimentally [37]. However, similar to HMS materials, the proposed neutral templating route does not seem to be feasible. Preliminary CG simulations of MSU-V materials showed the formation of multiple layers of surfactants, alternated by layers of silica monomers. Unfortunately, it was not possible to observe formation of the multi lamellar vesicles described experimentally, possibly due to the limited size of the simulations.

In the last part of the thesis, simulations were used to complement experiments in elucidating the mechanism of template removal from bioinspired silica. The purification method used is based on solvent extraction by addition of acid, so that pH values between 2 and 7 are reached. By using a simplified approach, based on the calculation of energies of interactions between amines (i.e. the template) and an amorphous silica surface (i.e. representing the bio-inspired material) [175], it was possible to demonstrate that removal of the template is caused by the loss of charge-charge interactions between amines and surface. Particularly, it was found that below pH $=$ 4.2 thermal fluctuations are enough to cause the widespread release of the template, which is observed experimentally between pH 5 and 4. Experimental and computational results indicate that this mild and "greener" method is a valid alternative for template removal from bio-inspired silica materials. Furthermore, this result suggests that molecular dynamics simulations could be used in the future as a tool for choosing the most appropriate solvent and conditions in purification/elution processes.

FUTURE WORK Although it was possible to shed some light on the molecular processes taking place during the synthesis of bio-inspired silica, further understanding of this topic could be achieved by overcoming some of the limitations encountered.

For example, at the CG level, the silicate models could be further validated and optimised by means of partition free energy calculations, with a similar approach used to parametrise the original MARTINI force field [10]. In fact, although experimentally partition free energies cannot be measured for these species, they can be obtained using AA simulations. Hence, CG models for silicates could be developed not only by matching structural characteristics but also by reproducing thermodynamic properties. This should provide a more correct physical behaviour and possibly improve transferability between different systems.

With regard to the transferability issues, it was shown that, for the considered systems, they mostly arise for interactions between hydrophobic groups and silicates. In this work only interaction levels already present in the MARTINI force field have been considered, however new levels of interactions might be necessary in order to improve agreement and transferability between systems. The proposed free energy method could help finding these new parameters.

One of the simplifications made in the simulations of both HMS and MSU-V is that ethanol does not influence the synthesis since, independently of its presence in the reacting mixture, ethanol is always produced after hydrolysis of the silica precursor. This assumption is most likely true for MSU-V materials, however it might be less applicable for HMS materials, where surfactant solubility is an issue. Hence, in the future simulations the effect of ethanol addition could be considered.

Larger simulations could be performed to investigate whether higher long range order can be observed in the HMS system and vesicle formation in the MSU-V system. Also, simulations at higher temperature could be performed to further probe the surfactant phase diagram and assess whether the DDA surfactant model can produce a hexagonal phase.

The multi-scale methodology for studying material synthesis introduced in this thesis could be extended to other families of ordered solids such as SBA-15, organosilicas or MOFs by developing appropriate atomistic or coarse-grained models that describe the precursors solutions for these systems.

Generally, it is desirable to have accurate experimental studies to validate model predictions. With regard to HMS and MSU-V materials, continuous measurement of pH as the synthesis progress could allow to obtain more detailed information

about the system speciation, enabling more accurate simulations of the early stages of synthesis. Similarly, detailed experimental evidence of the sphere-to-rod transition would provide essential insight into the aggregation of DDA surfactants and would further serve as a benchmark for the here presented modelling and simulation tools.

Regarding the last topic, a more realistic simulation set-up could be used to account for confinement effects in the calculation of the energies of interactions between templates and surface. This methodology could also be extended to assess and optimise other applications that require removal or elution of molecules from supports or substrates when the driving force for these processes is pH shifting.

Finally, both modelling approaches introduced in this thesis could be used to assist experimental studies in designing not only bio-inspired materials but also other classes of materials (where appropriate models are available); thereby, helping to identify the most favourable and cost-effective synthetic conditions, by providing indications regarding the most appropriate type of surfactant, pH or temperature to use.

APPENDIX A

A.1 FORCE FIELD PARAMETERS FOR ATOMISTIC SIMULATIONS OF HMS MATERIALS

Tables A.1- A.4 contain all force field parameters used to run the atomistic simulations discussed in Chapter 4. Parameters used to model amine surfactants, chloride and TMA ions were taken from the OPLS all-atom force field [80, 81]. Water molecules were modelled using the SPC/E potential [132] and parameters for silica monomers and dimers were taken from the work of Jorge et al. [6].

Table A.1: Lennard-Jones parameters, point charges and atomic masses.

Site	Mass (a.u)	q (a.u.)	σ (nm)	ε (kJ mol^{-1})
Ow	15.9994	-0.8476	0.31656	0.65019
Hw	1.0080	0.4238	0.0	0.0
N	14.0067	-0.900	0.330	0.711280
Nc	14.0067	-0.300	0.3250	0.711280
Nt	14.0067	0.000	0.3250	0.711280
Cn	12.0110	0.060	0.350	0.276144
Cnc	12.0110	0.190	0.350	0.276144
C	12.0110	-0.120	0.350	0.2761444
C3	12.011	-0.18	0.350	0.2761444
Ct	12.0110	0.130	0.350	0.2761444
Hc	1.0080	0.060	0.250	0.125520
Hn	1.0080	0.360	0.0	0.0
Hnc	1.0080	0.330	0.0	0.0
Hcn	1.0080	0.060	0.250	0.06276
SiN	28.0855	1.3292	0.4435	0.39748
Br	79.9040	-1.0	0.462376	0.376560
SiI	28.0855	1.0801	0.4435	0.39748
OhN	15.9994	-0.7641	0.34618	0.665674
OhI	15.9994	-0.7481	0.34618	0.665674
HoN	1.0080	0.4318	0.23541	0.413379
HoI	1.0080	0.3684	0.23541	0.413379
Oc	15.9994	-0.9410	0.34618	0.665674
ONN	15.9994	-0.6646	0.34506	0.67864
OII	15.9994	-0.7594	0.34506	0.67864
OIN	15.9994	-0.7120	0.34506	0.67864

Table A.2: Bond lengths.

Bond	Lenght (nm)
Ow-Hw	0.100
N-Hn	0.101
N-Cn	0.1448
Nc-Hcn	0.101
Nc-Cnc	0.1471
Nt-Ct	0.1471
Cn-Hcn	0.109
Cn-C	0.1529
Cnc-Hc	0.109
Cnc-C	0.1529
C-Hc	0.109
C-C	0.1529
C3-C	0.1529
C3-Hc	0.1529
Ct-Hc	0.109
SiN-OhN	1652
SiI-OhI	0.1695
SiI-Oc	0.1581
SiN-ONN	0.1651
SiN-OIN	0.1651
SiI-OII	0.169
SiI-OIN	0.169
OhN-HoN	0.0968
OhI-HoI	0.0968

Table A.3: Bond angles and harmonic force constants.

Angle	θ_o (deg)	k_θ (kJ mol^{-1} rad^{-2})
Hw-Ow-Hw	109.47	—
Hn-N-Hn	106.4	364.845
Hn-N-Cn	109.5	292.880
Hnc-Nc-Hnc	109.5	292.880
Hnc-Nc-Cnc	109.5	292.880
N-Cn-C	109.47	470.281
N-Cn-Hcn	109.5	292.880
Nc-Cnc-C	111.2	669.44
Nc-Cnc-Hcn	109.5	292.800
Nt-Ct-Hc	109.5	292.880
Hcn-Cn-Hcn	107.8	276.144
Hcn-Cn-C	110.7	313.800
Hcn-Cnc-Hcn	107.8	276.144
Hcn-Cnc-C	110.7	313.800
Cn-C-C	112.7	488.273
Cn-C-Hc	110.7	313.800
Cnc-C-C	112.7	488.273
Cnc-C-Hc	110.7	313.800
Ct-Nt-Ct	113.0	418.400
Hc-C-C	110.7	313.800
C3-C-Hc	110.7	313.800
C-C3-HC	110.7	313.800
Hc-C-Hc	107.8	276.144
Hc-C3-Hc	107.8	276.144
Hc-Ct-Hc	107.8	276.144
C-C-C	112.7	488.273
SiN-OhN-HoN	118.0442	109.29
SiI-OhI-HoI	118.0442	109.29
OhN-SiN-OhN	116.2621	255.64
OhI-SiI-OhI	116.2621	255.64
OhI-SiI-Oc	166.2621	255.64
SiN-ONN-SiN	174.2152	19.52
SiN-OIN-SiI	174.2152	19.52
SiI-OII-SiI	174.2152	19.52
OhN-SiN-ONN	111.0860	7343.28
OhN-SiN-OIN	111.0860	7343.28
OhI-SiI-OIN	111.0860	7343.28
OhI-SiI-OII	111.0860	7343.28
Oc-SiI-ONI	111.0860	7343.28
Oc-SiI-OII	111.0860	7343.28

Table A.4: Dihedral torsion parameters.

Dihedral	C_0 (kJ mol^{-1})	C_1 (kJ mol^{-1})	C_2 (kJ mol^{-1})	C_3 (kJ mol^{-1})	C_4 (kJ mol^{-1})	C_5 (kJ mol^{-1})
Hn-N-Cn-Hcn	0.83680	2.51040	0.0	-3.34720	0.0	0.0
Hn-N-Cn-C	-1.26775	3.02085	1.74473	-3.49782	0.0	0.0
Hnc-Nc-Cnc-Hcn	0.54601	1.63803	0.0	-2.18405	0.0	0.0
Hnc-Nc-Cnc-C	-1.26775	3.02085	1.74473	-3.49782	0.0	0.0
N-Cn-C-Hc	-4.09614	5.08775	2.96645	-3.95806	0.0	0.0
N-Cn-C-C	3.33465	-1.5526	2.82001	-4.60240	0.0	0.0
Nc-Cnc-C-C	5.77183	-2.67148	0.95814	-4.05848	0.0	0.0
Nc-Cnc-C-Hc	0.8033	2.4099	0.0	-3.21331	0.0	0.0
Hcn-Cn-C-Hc	0.62760	1.88280	0.0	-2.51040	0.0	0.0
Hcn-Cn-C-C	0.62760	1.88280	0.0	-2.51040	0.0	0.0
Hcn-Cnc-C-Hc	0.62760	1.88280	0.0	-2.51040	0.0	0.0
Hc-C-C-Hc	0.62760	1.88280	0.0	-2.51040	0.0	0.0
Hc-C-C3-Hc	0.62760	1.88280	0.0	-2.51040	0.0	0.0
Hcn-Cnc-C-C	0.62760	1.88280	0.0	-2.51040	0.0	0.0
Hc-Ct-Nt-Ct	0.63179	1.89535	0.0	-2.52714	0.0	0.0
Cn-C-C-C	2.92880	-1.46440	0.20920	-1.67360	0.0	0.0
Cnc-C-C-C	2.92880	-1.46440	0.20920	-1.67360	0.0	0.0
C-C-C-C	2.92880	-1.46440	0.20920	-1.67360	0.0	0.0
OhN-SiN-OhN-HoN	14.8473	9.1554	-3.6233	2.0686	0.0	0.0
OhI-SiI-OhI-HoI	14.8473	9.1554	-3.6233	2.0686	0.0	0.0
Oc-SiI-OhI-HoI	14.8473	9.1554	-3.6233	2.0686	0.0	0.0
ONN-SiN-OhN-HoN	15.2038	23.8622	-2.5673	-9.8910	0.0	0.0
OIN-SiN-OhN-HoN	15.2038	23.8622	-2.5673	-9.8910	0.0	0.0
OII-SiI-OhI-HoI	15.2038	23.8622	-2.5673	-9.8910	0.0	0.0
OIN-SiI-OhI-HoI	15.2038	23.8622	-2.5673	-9.8910	0.0	0.0
OhN-SiN-ONN-SiN	-3.3698	-4.0041	-0.6343	0.0	0.0	0.0
OhN-SiN-OIN-SiI	-3.3698	-4.0041	-0.6343	0.0	0.0	0.0
OhI-SiI-OII-SiI	-3.3698	-4.0041	-0.6343	0.0	0.0	0.0
OhI-SiI-OIN-SiN	-3.3698	-4.0041	-0.6343	0.0	0.0	0.0
Oc-SiI-OII-SiI	-3.3698	-4.0041	-0.6343	0.0	0.0	0.0
Oc-SiI-OIN-SiN	-3.3698	-4.0041	-0.6343	0.0	0.0	0.0

APPENDIX B

B.1 FORCE FIELD PARAMETERS FOR ATOMISTIC SIMULATIONS OF MSU-V MATERIALS

Tables B.1- B.4 contain all force field parameters used to run atomistic simulations in Chapter 5. Parameters used to model damine surfactants, bromide and TMA ions were taken from the OPLS all-atom force field [80, 81]. Water molecules were modelled using the SPC/E potential [132] and parameters for both neutral and anionic silica monomers were taken from the work of Jorge et al. [6].

Table B.1: Lennard-Jones parameters, point charges and atomic masses.

Site	Mass (a.u.)	q (a.u.)	σ (nm)	ε (kJ mol^{-1})
Ow	15.9994	-0.8476	0.31656	0.65019
Hw	1.0080	0.4238	0.0	0.0
N	14.0067	-0.900	0.330	0.711280
Nc	14.0067	-0.300	0.3250	0.711280
Nt	14.0067	0.000	0.3250	0.711280
Cn	12.0110	0.060	0.350	0.276144
Cnc	12.0110	0.190	0.350	0.276144
C	12.0110	-0.120	0.350	0.2761444
Ct	12.0110	0.130	0.350	0.2761444
Hc	1.0080	0.060	0.250	0.125520
Hn	1.0080	0.360	0.0	0.0
Hnc	1.0080	0.330	0.0	0.0
Hcn	1.0080	0.060	0.250	0.06276
Br	79.9040	-1.0	0.462376	0.376560
SiI	28.0855	1.0801	0.4435	0.39748
OhI	15.9994	-0.7481	0.34618	0.665674
HoI	1.0080	0.3684	0.23541	0.413379
Oc	15.9994	-0.9410	0.34618	0.665674

Table B.2: Bond lengths.

Bond	Lenght (nm)
Ow-Hw	0.100
N-Hn	0.101
N-Cn	0.1448
Nc-Hcn	0.101
Nc-Cnc	0.1471
Nt-Ct	0.1471
Cn-Hcn	0.109
Cn-C	0.1529
Cnc-Hc	0.109
Cnc-C	0.1529
C-Hc	0.109
C-C	0.1529
Ct-Hc	0.109
SiI-OhI	0.169
SiI-Oc	0.158
OhI-HoI	0.097

Table B.3: Bond angles and harmonic force constants.

Angle	θ_o (deg)	k_θ (kJ mol^{-1} rad^{-2})
Hw-Ow-Hw	109.47	—
Hn-N-Hn	106.4	364.845
Hn-N-Cn	109.5	292.880
Hnc-Nc-Hnc	109.5	292.880
Hnc-Nc-Cnc	109.5	292.880
N-Cn-C	109.47	470.281
N-Cn-Hcn	109.5	292.880
Nc-Cnc-C	111.2	669.44
Nc-Cnc-Hcn	109.5	292.800
Nt-Ct-Hc	109.5	292.880
Hcn-Cn-Hcn	107.8	276.144
Hcn-Cn-C	110.7	313.800
Hcn-Cnc-Hcn	107.8	276.144
Hcn-Cnc-C	110.7	313.800
Cn-C-C	112.7	488.273
Cn-C-Hc	110.7	313.800
Cnc-C-C	112.7	488.273
Cnc-C-Hc	110.7	313.800
Ct-Nt-Ct	113.0	418.400
Hc-C-C	110.7	313.800
Hc-C-Hc	107.8	276.144
Hc-Ct-Hc	107.8	276.144
C-C-C	112.7	488.273
SiI-OhI-HoI	109.8	103.46
OhI-SiI-OhI	104.9	232.96
OhI-SiI-Oc	114.2	232.96

Table B.4: Dihedral torsion parameters.

Dihedral	C_0 (kJ mol^{-1})	C_1 (kJ mol^{-1})	C_2 (kJ mol^{-1})	C_3 (kJ mol^{-1})	C_4 (kJ mol^{-1})	C_5 (kJ mol^{-1})
Hn-N-Cn-Hcn	0.83680	2.51040	0.0	-3.34720	0.0	0.0
Hn-N-Cn-C	-1.26775	3.02085	1.74473	-3.49782	0.0	0.0
Hnc-Nc-Cnc-Hcn	0.54601	1.63803	0.0	-2.18405	0.0	0.0
Hnc-Nc-Cnc-C	-1.26775	3.02085	1.74473	-3.49782	0.0	0.0
N-Cn-C-Hc	-4.09614	5.08775	2.96645	-3.95806	0.0	0.0
N-Cn-C-C	3.33465	-1.5526	2.82001	-4.60240	0.0	0.0
Nc-Cnc-C-C	5.77183	-2.67148	0.95814	-4.05848	0.0	0.0
Nc-Cnc-C-Hc	0.8033	2.4099	0.0	-3.21331	0.0	0.0
Hcn-Cn-C-Hc	0.62760	1.88280	0.0	-2.51040	0.0	0.0
Hcn-Cn-C-C	0.62760	1.88280	0.0	-2.51040	0.0	0.0
Hcn-Cnc-C-Hc	0.62760	1.88280	0.0	-2.51040	0.0	0.0
Hcn-Cnc-C-C	0.62760	1.88280	0.0	-2.51040	0.0	0.0
Hc-Ct-Nt-Ct	0.63179	1.89535	0.0	-2.52714	0.0	0.0
Cn-C-C-C	2.92880	-1.46440	0.20920	-1.67360	0.0	0.0
Cnc-C-C-C	2.92880	-1.46440	0.20920	-1.67360	0.0	0.0
C-C-C-C	2.92880	-1.46440	0.20920	-1.67360	0.0	0.0
OhI-SiI-OhI-HoI	14.8473	9.1554	-3.6233	2.0686	0.0	0.0
Oc-SiI-OhI-HoI	14.8473	9.1554	-3.6233	2.0686	0.0	0.0

APPENDIX C

C.1 FORCE FIELD PARAMETERS FOR AMINES TEMPLATES

Tables C.1- C.4 contain parameters used to model all amines species used in Chapter 6. Atom names for amines are according to the representations displayed in Figure C.1. Parameters for amines are taken from the OPLS all-atom force field [80, 81].

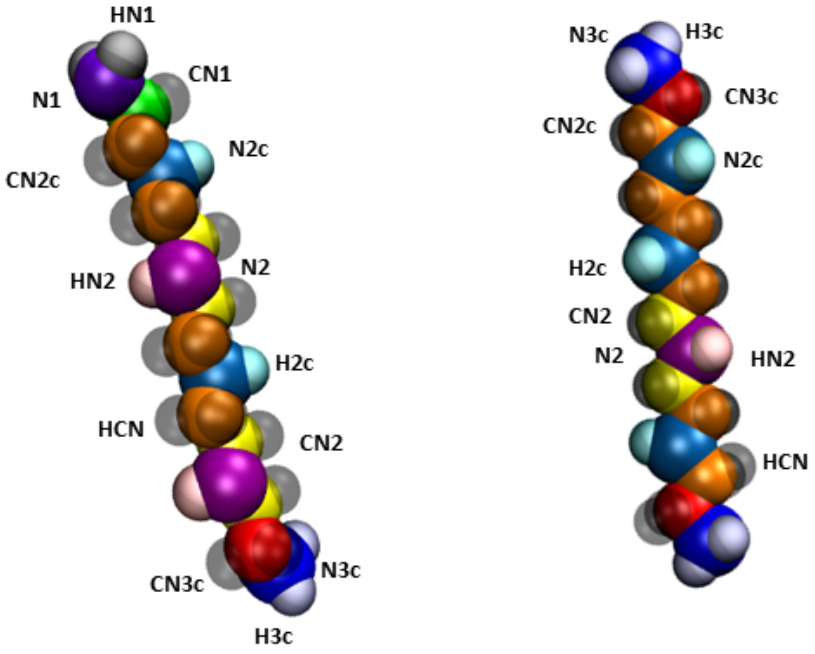

(a) (b)

Figure C.1: Schematic representation of two amine topologies covering all different atom types: N1, violet; N2, purple; N3c, blue; N2c, light blue; HN1, gray; HN2, pink; H3c, ice blue; H2c, cyan; HCN, black; CN1, green; CN2, yellow; CN2c, orange and CN3, red.

Table C.1: Lennard-Jones parameters, point charges and atomic masses for all amine atom types.

Site	Mass (a.u.)	q (a.u.)	σ (nm)	ε (kJ mol^{-1})
N1	14.0067	-0.9	0.33	0.71128
N2	14.0067	-0.9	0.33	0.71128
CN1	12.011	0.06	0.35	0.276144
CN2	12.011	0.06	0.35	0.276144
HN1	1.008	0.36	0	0
HN2	1.008	0.38	0	0
HN1	1.008	0.06	0.25	0.06576
N3c	14.0067	-0.3	0.325	0.71128
H3c	1.008	0.33	0	0
CN3c	12.011	0.19	0.35	0.276144
N2c	14.0067	-0.2	0.325	0.71128
H2c	1.008	0.31	0	0
CN2c	12.011	0.17	0.35	0.276144

Table C.2: Bond lengths and harmonic force constants for amines.

Bond	b_o(nm)	k_b (kJ mol^{-1} nm^{-2})
N1-HN1	0.101	363171.2
N2-HN2	0.101	363171.2
N3c-H3c	0.101	363171.2
N2c-H2c	0.101	363171.2
N1-CN1	0.1448	319657
N2-CN2	0.1448	319657
N3c-CN3c	0.1471	307105.6
N2c-CN2c	0.1471	307105.6
CN2-CN2	0.1529	224262.4
CN2-CN3c	0.1529	224262.4
CN1-CN2c	0.1529	224262.4
CN2-CN2c	0.1529	224262.4
CN2c-CN3c	0.1529	224262.4
CN2c-CN2c	0.1529	224262.4
CN1-HCN	0.109	284512
CN2-HCN	0.109	284512
CN3c-HCN	0.109	284512
CN2c-HCN	0.109	284512

Table C.3: Bond angles and harmonic force constants for amines.

Angle	θ_o (deg)	k_θ (kJ mol^{-1} rad^{-2})
HN1-N1-HN1	106.4	364.845
CN1-N1-HN1	109.5	292.88
CN2-N2-HN2	109.5	292.88
HCN-CN1-N1	109.5	292.88
HCN-CN2-N2	109.5	292.88
H3c-N3c-H3c	109.5	292.88
H2c-N2c-H2c	109.5	292.88
CN3c-N3c-H3c	109.5	292.88
CN2c-N2c-H2c	109.5	292.88
HCN-CN3c-N3c	109.5	292.88
HCN-CN2c-N2c	109.5	292.88
CN2-CN2-N2	109.47	470.281
N1-CN1-CN2c	109.47	470.281
N2-CN2-CN2c	109.47	470.281
N2-CN2-CN3c	109.47	470.281
HCN-CN1-HCN	107.80	276.144
HCN-CN2-HCN	107.80	276.144
HCN-CN3c-HCN	107.80	276.144
HCN-CN2c-HCN	107.80	276.144
CN2-CN2-HCN	110.70	313.8
CN2c-CN3c-HCN	110.70	313.8
CN2c-CN1-HCN	110.70	313.8
CN3c-CN2c-HCN	110.70	313.8
CN3c-CN2-HCN	110.70	313.8
CN2-CN3c-HCN	110.70	313.8
CN1-CN2c-HCN	110.70	313.8
CN2c-CN2c-HCN	110.70	313.8
CN2-CN3c-N3c	111.20	669.44
CN1-CN2c-N2c	111.20	669.44
CN2-CN2c-N2c	111.20	669.44
CN3c-CN2c-N2c	111.20	669.44
CN2c-CN3c-N3c	111.20	669.44
CN2c-CN2c-N2c	111.20	669.44
CN2-CN3c-N3c	111.20	669.44
CN2c-N2c-CN2c	113.00	418.4
CN2-N2-CN2	107.20	433.462

Table C.4: Dihedral torsion parameters for amines.

Dihedral	C_0 (kJ mol^{-1})	C_1 ((kJ mol^{-1})	C_2 (kJ mol^{-1})	C_3 (kJ mol^{-1})	C_4 (kJ mol^{-1})	C_5 (kJ mol^{-1})
H3c-N3c-CN3c-HCN	0.54601	1.63803	0	-2.18405	0	0
H2c-N2c-CN2c-HCN	0.54601	1.63803	0	-2.18405	0	0
H3c-N3c-CN3c-CN2c	-1.26775	3.02085	0 1.74473	-3.49782	0	0
H2c-N2c-CN2c-CN3c	-1.26775	3.02085	0 1.74473	-3.49782	0	0
H2c-N2c-CN2c-CN2c	-1.26775	3.02085	0 1.74473	-3.49782	0	0
HN2-N2-CN2-CN3c	-1.26775	3.02085	0 1.74473	-3.49782	0	0
HN2-N2-CN2-CN2c	-1.26775	3.02085	0 1.74473	-3.49782	0	0
H2c-N2c-CN2c-CN2	-1.26775	3.02085	0 1.74473	-3.49782	0	0
HN1-N1-CN1-CN2c	-1.26775	3.02085	0 1.74473	-3.49782	0	0
H2c-N2c-CN2c-CN1	-1.26775	3.02085	0 1.74473	-3.49782	0	0
N3c-CN3c-CN2c-N2c	19.59994	-21.3907	4.05011	2.25936	0	0
N2c-CN2c-CN2c-N2c	19.59994	-21.3907	4.05011	2.25936	0	0
N3c-CN3c-CN2-N2	19.59994	-21.3907	4.05011	2.25936	0	0
N2-CN2-CN2c-N2c	19.59994	-21.3907	4.05011	2.25936	0	0
N1-CN1-CN2c-N2c	19.59994	-21.3907	4.05011	2.25936	0	0
N2-CN2-CN2-N2	19.59994	-21.3907	4.05011	2.25936	0	0
N3c-CN3c-CN2c-HCN	0.80333	2.40999	0	-3.21331	0	0
N2c-CN2c-CN2c-HCN	0.80333	2.40999	0	-3.21331	0	0
N3c-CN3c-CN2-HCN	0.80333	2.40999	0	-3.21331	0	0
HCN-CN3c-CN2c-HCN	0.62760	1.88280	0	-2.5104	0	0
HCN-CN2c-CN2c-HCN	0.62760	1.88280	0	-2.5104	0	0
HCN-CN3c-CN2-HCN	0.62760	1.88280	0	-2.5104	0	0
HCN-CN1-CN2c-HCN	0.62760	1.88280	0	-2.5104	0	0
HCN-CN2-CN2-HCN	0.62760	1.88280	0	-2.5104	0	0
HCN-CN3c-CN2c-N2c	0.97069	2.91206	0	-3.88275	0	0
HCN-CN2-CN2c-N2c	0.97069	2.91206	0	-3.88275	0	0
HCN-CN1-CN2c-N2c	0.97069	2.91206	0	-3.88275	0	0
CN3c-CN2c-N2c-CN2c	3.04176	-1.35144	-0.51881	2.20915	0	0
CN2c-N2c-CN2c-CN2c	3.04176	-1.35144	-0.51881	2.20915	0	0
CN1-CN2c-N2c-CN2c	3.04176	-1.35144	-0.51881	2.20915	0	0
HCN-CN2c-N2c-CN2c	0.63179	1.89535	0	2.52714	0	0
HCN-CN3c-CN2-N2	4.09614	5.08775	2.96645	-3.95806	0	0
HCN-CN2c-CN1-N1	4.09614	5.08775	2.96645	-3.95806	0	0
CN3c-CN2-N2-CN2	1.78866	3.49154	0.53555	-5.81576	0	0
CN2c-CN2-N2-CN2	1.78866	3.49154	0.53555	-5.81576	0	0
HCN-CN2-N2-HN2	0.83680	2.51040	0	-3.34720	0	0
HCN-CN2-N2-CN2	1.17152	3.51456	0	-4.68608	0	0

C.2 FORCE FIELD PARAMETERS FOR WATER MODELS SPC AND SPC/E IN CHARMM AND OPLS FRAMEWORKS

Tables C.5- C.7 contain parameters for water according to the SPC and SPC/E [132] models.

Table C.5: Lennard-Jones parameters, point charges and atomic masses for water models SPC and SPC/E [132] .

Site	Mass (a.u.)	q (a.u.)	σ (nm)	ε (kJ mol^{-1})
		SPC		
OW	15.99940	-0.82	3.16557e-01	6.50194e-01
HW	1.00800	0.41	0	0
		SPC/E		
OW	15.99940	-0.8476	3.16557e-01	6.50194e-01
HW	1.00800	0.4238	0	0

Table C.6: Bond lengths.

Bond	b_0(nm)	k_b (kJ mol^{-1} nm^{-2})
OW-HW	0.1	345000

Table C.7: Bond angle and harmonic force constant.

Angle	θ_0(deg)	k_θ (kJ mol^{-1} rad^{-2})
HW-OW-HW	109.47	383

C.3 COMBINATION RULES FOR CALCULATION OF NON-BONDED PARAMETERS

Combination rules used for the calculation of the non-bonded parameters listed in Table 6.4:

$$C_{ij}^{6} = (C_{ii}^{6}\, C_{jj}^{6})^{\frac{1}{2}}, \tag{C.1}$$

$$C_{ij}^{12} = (C_{ii}^{12}\, C_{jj}^{12})^{\frac{1}{2}}, \tag{C.2}$$

where $C^{6} = \sigma$ and $C^{12} = \epsilon$.

C.4 FORCE FIELD PARAMETERS FOR SILICA SURFACES IN THE CHARMM FRAMEWORK

Tables C.8- C.10 contain parameters for silica surfaces in the CHARMM framework.

Table C.8: Lennard-Jones parameters, point charges and atomic masses for silica surfaces adapted from [175] to be used in GROMACS 4.6 software in the CHARMM framework.

Site	Mass (a.u.)	q (a.u.)	σ (nm)	ε (kJ mol^{-1})
SC4	28.0860	1.1	0.369724	0.389112
OC23	15.9994	-0.55	0.30914	0.225936
OC24	15.9994	-0.675	0.30914	0.510448
HOY	1.0080	0.4	0.09667	0.06276

Table C.9: Bond lengths and harmonic force constants.

Bond	b_o(nm)	k_b (kJ mol^{-1} nm^{-2})
SC4-OC23	0.168	238488
SC4-OC24	0.168	238488
OC24-HOY	0.0945	414216

It must be noted that the equation used to express the potential energy in the the paper by Emami et al. [175] (Equation C.5) differs from the one used in GROMACS 4.6 [178] (Equation C.3).

Table C.10: Bond angles and harmonic force constants.

Angle	θ_o(deg)	k_θ (kJ mol^{-1} rad^{-2})
SC4-OC23-SC4	149.0	836.8
SC4-OC24-HOY	115.0	418.4
OC23-SC4-OC23	109.5	836.8
OC23-SC4-OC24	109.5	836.8
OC24-SC4-OC24	109.5	836.8

GROMACS

$$V_{ij} = 4\varepsilon_{ij}\left[\left(\frac{\sigma_{ij}}{r_{ij}}\right)^{12} - \left(\frac{\sigma_{ij}}{r_{ij}}\right)^{6}\right], \tag{C.3}$$

WORK BY EMAMI ET AL.[175]

$$V_{ij} = \varepsilon_{ij}\left[\left(\frac{\sigma_{ij}}{r_{ij}}\right)^{12} - 2\left(\frac{\sigma_{ij}}{r_{ij}}\right)^{6}\right], \tag{C.4}$$

Therefore σ_{EMAMI} was converted into $\sigma_{GROMACS}$ using the following equation:

$$\sigma_{i,GROMACS} = 2^{-1/6}\sigma_{i,EMAMI}, \tag{C.5}$$

C.5 TREND LINES FOR SURFACE CHARGE CALCULATION

Equations used to interpolate surface charge data displayed in Tables 6.6-6.7.

BOLT

$$f(x) = 0.00018x^{5.038} \tag{C.6}$$

$$R^2 = 0.99987 \tag{C.7}$$

ZERROUK

$$f(x) = 0.00010^{5.629} \tag{C.8}$$

$$R^2 = 0.98893 \tag{C.9}$$

MILONJIC

$$f(x) = 0.00015x^{4.986} \tag{C.10}$$

$$R^2 = 0.97976 \tag{C.11}$$

BIBLIOGRAPHY

[1] Centi, A. and Jorge, M. 'Molecular Simulation Study of the Early Stages of Formation of Bioinspired Mesoporous Silica Materials'. *Langmuir* 32.28 (2016), pp. 7228–7240. DOI: 10.1021/acs.langmuir.6b01731.

[2] Manning, J. R. H., Yip, T., Centi, A., Jorge, M. and Patwardhan, S. V. 'An eco-friendly, tunable and scalable method for producing porous functional nanomaterials designed using molecular interactions'. *ChemSusChem* (2017). DOI: 10.1002/cssc.201700027.

[3] Beck, J. S., Vartuli, J. C., Kennedy, G. J., Kresge, C. T., Roth, W. J. and Schramm, S. E. 'Molecular or Supramolecular Templating: Defining the Role of Surfactant Chemistry in the Formation of Microporous and Mesoporous Molecular Sieves'. *Chemistry of Materials* 6.10 (1994), pp. 1816–1821. DOI: 10.1021/cm00046a040.

[4] ALOthman, Z. A. 'A Review: Fundamental Aspects of Silicate Mesoporous Materials'. *Materials* 5.12 (2012), pp. 2874–2902. DOI: 10.3390/ma5122874.

[5] Gröger, C., Lutz, K. and Brunner, E. 'Biomolecular self-assembly and its relevance in silica biomineralization'. *Cell Biochemistry Biophysics* 50.1 (2008), pp. 23–39. DOI: 10.1007/s12013-007-9003-2.

[6] Jorge, M., Gomes, J. R. B., Cordeiro, M. N. D. S. and Seaton, N. A. 'Molecular Dynamics Simulation of the Early Stages of the Synthesis of Periodic Mesoporous Silica'. *The Journal of Physical Chemistry B* 113.3 (2009), pp. 708–718. DOI: 10.1021/jp806686w.

[7] Pérez-Sánchez, G., Chien, S.-C., Gomes, J. R. B., Cordeiro, M. N. D. S., Auerbach, S. M., Monson, P. A. and Jorge, M. 'Multiscale Model for the Templated Synthesis of Mesoporous Silica: The Essential Role of Silica Oligomers'. *Chemistry of Materials* (2016). DOI: 10.1021/acs.chemmater.6b00348.

[8] Tanev, P. T., Liang, Y. and Pinnavaia, T. J. 'Assembly of Mesoporous Lamellar Silicas with Hierarchical Particle Architectures'. *Journal of the American Chemical Society* 119.37 (1997), pp. 8616–8624. DOI: 10.1021/ja970228v.

[9] Tanev, P. T. and Pinnavaia, T. J. 'Mesoporous Silica Molecular Sieves Prepared by Ionic and Neutral Surfactant Templating: A Comparison of Physical Properties'. *Chemistry of Materials* 8.8 (1996), pp. 2068–2079. DOI: 10.1021/cm950549a.

[10] Marrink, S. J., Risselada, H. J., Yefimov, S., Tieleman, D. P. and de Vries, A. H. 'The MARTINI Force Field: Coarse Grained Model for Biomolecular Simulations'. *The Journal of Physical Chemistry B* 111.27 (2007), pp. 7812–7824. DOI: 10.1021/jp071097f.

[11] Yanagisawa, T., Shimizu, T., Kuroda, K. and Kato, C. 'The Preparation of Alkyltriinethylaininonium-Kaneinite Complexes and Their Conversion to Microporous Materials'. *Bulletin of the Chemical Society of Japan* 63.4 (1990), pp. 988–992. DOI: 10.1246/bcsj.63.988.

[12] Beck, J. S., Vartuli, J. C., Roth, W. J., Leonowicz, M. E., Kresge, C. T., Schmitt, K. D., Chu, C. T. W., Olson, D. H. and Sheppard, E. W. 'A new family of mesoporous molecular sieves prepared with liquid crystal templates'. *The Journal of the American Chemical Society* 114.27 (1992), pp. 10834–10843. DOI: 10.1021/ja00053a020.

[13] Bhattacharya, A. and Mahanti, D. S. 'Self-assembly of ionic surfactants and formation of mesostructures'. *Journal of Physics: Condensed Matter* 13.7 (2001), p. 1413. DOI: 10.1088/0953-8984/13/7/306.

[14] Siperstein, F. R. and Gubbins, K. E. 'Phase Separation and Liquid Crystal Self-Assembly in Surfactant-Inorganic-Solvent Systems'. *Langmuir* 19.6 (2003), pp. 2049–2057. DOI: 10.1021/la026410d.

[15] Patti, A., Mackie, A. D. and Siperstein, F. R. 'Monte Carlo Simulation of Self-Assembled Ordered Hybrid Materials'. *Langmuir* 23.12 (2007), pp. 6771–6780. DOI: 10.1021/la063296g.

[16] Jorge, M. 'Molecular Dynamics Simulation of Self-Assembly of n-Decyltrimethylammonium Bromide Micelles'. *Langmuir* 24.11 (2008), pp. 5714–5725. DOI: 10.1021/la800291p.

[17] Pérez-Sánchez, G., Gomes, J. R. B. and Jorge, M. 'Modeling Self-Assembly of Silica/Surfactant Mesostructures in the Templated Synthesis of Nanoporous Solids'. *Langmuir* 29.7 (2013), pp. 2387–2396. DOI: 10.1021/la3046274.

[18] Liu, Y., Goebl, J. and Yin, Y. 'Templated synthesis of nanostructured materials'. *Chemical Society Reviews* 42.7 (2013), pp. 2610–2653. DOI: 10.1039/C2CS35369E.

[19] Tanford, C. 'The hydrophobic effect and the organization of living matter'. *Science* 200.4345 (1978), pp. 1012–1018. DOI: 10.1126/science.653353.

[20] Gecol, H. 'The Basic Theory'. In: *Chemistry and Technology of Surfactants*. Ed. by R. J. Farn. DOI: 10.1002/9780470988596.ch2. Blackwell Publishing Ltd, 2006, pp. 24–45.

[21] Israelachvili, J. N. *Intermolecular and Surface Forces: Revised Third Edition*. Academic Press, 2011.

[22] Nagarajan, R. and Ruckenstein, E. 'Theory of surfactant self-assembly: a predictive molecular thermodynamic approach'. *Langmuir* 7.12 (1991), pp. 2934–2969. DOI: 10.1021/la00060a012.

[23] US Geological Survey, Water Science School. *Surface Tension and Water*. URL: https://water.usgs.gov/edu/surface-tension.html (visited on 12/03/2017).

[24] Marrink, S. J., Tieleman, D. P. and Mark, A. E. 'Molecular Dynamics Simulation of the Kinetics of Spontaneous Micelle Formation'. *The Journal of Physical Chemistry B* 104.51 (2000), pp. 12165–12173. DOI: 10.1021/jp001898h.

[25] Tanford, C. *The hydrophobic effect: formation of micelles and biological membranes*. Wiley Interscience publication. Wiley, 1973.

[26] Israelachvili, J. N., Mitchell, D. J. and Ninham, B. W. 'Theory of self-assembly of hydrocarbon amphiphiles into micelles and bilayers'. *Journal of Chemical Socirty, Faraday Transaction 2* 72 (0 1976), pp. 1525–1568. DOI: 10.1039/F29767201525.

[27] Nagarajan, R. and Ruckenstein, E. 'Aggregation of amphiphiles as micelles or vesicles in aqueous media'. *Journal of Colloid and Interface Science* 71.3 (1979), pp. 580–604. DOI: http://dx.doi.org/10.1016/0021-9797(79)90331-X.

[28] Nagarajan, R. 'Molecular Packing Parameter and Surfactant Self-Assembly: The Neglected Role of the Surfactant Tail'. *Langmuir* 18.1 (2002), pp. 31–38. DOI: 10.1021/la010831y.

[29] Brinker, C. J. and Scherer, G. W. 'Introduction'. In: *Sol-Gel Science*. Ed. by C. J. Brinker and G. W. Scherer. San Diego: Academic Press, 1990, pp. xvi–18. DOI: http://dx.doi.org/10.1016/B978-0-08-057103-4.50006-4.

[30] Iler, R. K. *The Chemistry of Silica: Solubility, Polymerization, Colloid and Surface Properties and Biochemistry of Silica*. John Wiley & Sons, 1979.

[31] Carman, P. C. 'Constitution of colloidal silica'. *Transactions of the Faraday Society* 36 (0 1940), pp. 964–973. DOI: 10.1039/TF9403600964.

[32] Brinker, C. J. and Scherer, G. W. '{CHAPTER} 3 - Hydrolysis and Condensation II: Silicates'. In: *Sol-Gel Science*. Ed. by C. J. Brinker and G. W. Scherer. San Diego: Academic Press, 1990, pp. 96–233. DOI: http://doi.org/10.1016/B978-0-08-057103-4.50008-8.

[33] Hendricks, W. M., Bell, A. T. and Radke, C. J. 'Effects of organic and alkali metal cations on the distribution of silicate anions in aqueous solutions'. *The Journal of Physical Chemistry* 95.23 (1991), pp. 9513–9518. DOI: 10.1021/j100176a087.

[34] Hoffmann, F., Cornelius, M., Morell, J. and Fröba, M. 'Silica-Based Mesoporous Organic-Inorganic Hybrid Materials'. *Angewandte Chemie International Edition* 45.20 (2006), pp. 3216–3251. DOI: 10.1002/anie.200503075.

[35] Zhao, D., Feng, J., Huo, Q., Melosh, N., Fredrickson, G. H., Chmelka, B. F. and Stucky, G. D. 'Triblock Copolymer Syntheses of Mesoporous Silica with Periodic 50 to 300 Angstrom Pores'. *Science* 279.5350 (1998), pp. 548–552. DOI: 10.1126/science.279.5350.548.

[36] Tanev, P. T. and Pinnavaia, T. J. 'A Neutral Templating Route to Mesoporous Molecular Sieves'. *Science* 267.5199 (1995), pp. 865–867. DOI: 10.1126/science.267.5199.865.

[37] Tanev, P. T. and Pinnavaia, T. J. 'Biomimetic Templating of Porous Lamellar Silicas by Vesicular Surfactant Assemblies'. *Science* 271.5253 (1996), pp. 1267–1269. DOI: 10.1126/science.271.5253.1267.

[38] Tanev, P. T. and Pinnavaia, T. J. 'Biomimetic assembly of porous lamellar silica molecular sieves with a vesicular particle architecture'. *Supramolecular Science* 5.3–4 (1998), pp. 399–404. DOI: 10.1016/S0968-5677(98)00039-X.

[39] Chen, C.-Y., Burkett, S. L., Li, H.-X. and Davis, M. E. 'Studies on mesoporous materials II. Synthesis mechanism of MCM-41'. *Microporous Materials* 2.1 (1993), pp. 27–34. DOI: 10.1016/0927-6513(93)80059-4.

[40] Monnier, A., Schüth, F., Huo, Q., Kumar, D., Margolese, D., Maxwell, R. S., Stucky, G. D., Krishnamurty, M., Petroff, P., Firouzi, A., Janicke, M. and Chmelka, B. F. 'Cooperative formation of inorganic-organic interfaces in the synthesis of silicate mesostructures'. *Science* 261.5126 (1993), pp. 1299–1303. DOI: 10.1126/science.261.5126.1299.

[41] Steel, A., W. Carr, S. and W. Anderson, M. '14 N NMR study of surfactant mesophases in the synthesis of mesoporous silicates'. *Journal of the Chemical Society, Chemical Communications* 0.13 (1994), pp. 1571–1572. DOI: 10.1039/C39940001571.

[42] Firouzi, A., Kumar, D., Bull, L., Besier, T., Sieger, P., Huo, Q., Walker, S., Zasadzinski, J., Glinka, C., Nicol, J., Margolese, D., Stucky, G. and Chmelka, B. 'Cooperative organization of inorganic-surfactant and biomimetic assemblies'. *Science* 267.5201 (1995), pp. 1138–1143. DOI: 10.1126/science.7855591.

[43] Soler-Illia, G. J. d. A. A., Sanchez, C., Lebeau, B. and Patarin, J. 'Chemical Strategies To Design Textured Materials: from Microporous and Mesoporous Oxides to Nanonetworks and Hierarchical Structures'. *Chemical Reviews* 102.11 (2002). PMID: 12428985, pp. 4093–4138. DOI: 10.1021/cr0200062.

[44] Huo, Q., Margolese, D. I., Ciesla, U., Demuth, D. G., Feng, P., Gier, T. E., Sieger, P., Firouzi, A. and Chmelka, B. F. a. 'Organization of Organic Molecules with Inorganic Molecular Species into Nanocomposite Biphase Arrays'. *Chemistry of Materials* 6.8 (1994), pp. 1176–1191. DOI: 10.1021/cm00044a016.

[45] Bagshaw, S. A., Prouzet, E. and Pinnavaia, T. J. 'Templating of Mesoporous Molecular Sieves by Nonionic Polyethylene Oxide Surfactants'. *Science* 269.5228 (1995), pp. 1242–1244. DOI: 10.1126/science.269.5228.1242.

[46] Auerbach, S. M., Fan, W. and Monson, P. A. 'Modelling the assembly of nanoporous silica materials'. *International Reviews in Physical Chemistry* 34.1 (2015), pp. 35–70. DOI: 10.1080/0144235X.2014.988038.

[47] Tréguer, P., Nelson, D. M., Van Bennekom, A. J., DeMaster, D. J., Leynaert, A. and Quéguiner, B. 'The Silica Balance in the World Ocean: A Reestimate'. *Science* 268.5209 (1995), pp. 375–379. DOI: 10.1126/science.268.5209.375.

[48] Sun, Q., Vrieling, E. G., van Santen, R. A. and Sommerdijk, N. A. J. M. 'Bioinspired synthesis of mesoporous silicas'. *Current Opinion in Solid State and Materials Science* 8.2 (2004), pp. 111–120. DOI: 10.1016/j.cossms.2004.01.005.

[49] Patwardhan, S. V. 'Biomimetic and bioinspired silica: recent developments and applications'. *Chemical Communications* 47.27 (2011), pp. 7567–7582. DOI: 10.1039/C0CC05648K.

[50] Kröger, N., Lorenz, S., Brunner, E. and Sumper, M. 'Self-Assembly of Highly Phosphorylated Silaffins and Their Function in Biosilica Morphogenesis'. *Science* 298.5593 (2002), pp. 584–586. DOI: 10.1126/science.1076221.

[51] Sumper, M. 'A Phase Separation Model for the Nanopatterning of Diatom Biosilica'. *Science* 295.5564 (2002), pp. 2430–2433. DOI: 10.1126/science.1070026.

[52] Wenzl, S., Deutzmann, R., Hett, R., Hochmuth, E. and Sumper, M. 'Quaternary Ammonium Groups in Silica-Associated Proteins'. *Angewandte Chemie International Edition* 43.44 (2004), pp. 5933–5936. DOI: 10.1002/anie.200461236.

[53] Sumper, M., Lorenz, S. and Brunner, E. 'Biomimetic Control of Size in the Polyamine-Directed Formation of Silica Nanospheres'. *Angewandte Chemie International Edition* 42.42 (2003), pp. 5192–5195. DOI: 10.1002/anie.200352212.

[54] Mizutani, T., Nagase, H., Fujiwara, N. and Ogoshi, H. 'Silicic Acid Polymerization Catalyzed by Amines and Polyamines'. *Bulletin of the Chemical Society of Japan* 71.8 (1998), pp. 2017–2022. DOI: 10.1246/bcsj.71.2017.

[55] Vrieling, E. G., Sun, Q., Beelen, T. P. M., Hazelaar, S., Gieskes, W. W. C., van Santen, R. A. and Sommerdijk, N. A. J. M. 'Controlled silica synthesis inspired by diatom silicon biomineralization'. *Journal of Nanoscience and Nanotechnology* 5.1 (2005), pp. 68–78.

[56] Belton, D. J., Patwardhan, S. V., Annenkov, V. V., Danilovtseva, E. N. and Perry, C. C. 'From biosilicification to tailored materials: Optimizing hydrophobic domains and resistance to protonation of polyamines'. *PNAS* 105.16 (2008), pp. 5963–5968. DOI: 10.1073/pnas.0710809105.

[57] Patarin, J., Lebeau, B. and Zana, R. 'Recent advances in the formation mechanisms of organized mesoporous materials'. *Current Opinion in Colloid & Interface Science* 7.1-2 (2002), pp. 107–115. DOI: http://doi.org/10.1016/S1359-0294(02)00012-2.

[58] Zhang, J., Luz, Z. and Goldfarb, D. 'EPR Studies of the Formation Mechanism of the Mesoporous Materials MCM-41 and MCM-50'. *The Journal of Physical Chemistry B* 101.36 (1997), pp. 7087–7094. DOI: 10.1021/jp9709621.

[59] Galarneau, A., Renzo, F. D., Fajula, F., Mollo, L., Fubini, B. and Ottaviani, M. 'Kinetics of Formation of Micelle-Templated Silica Mesophases Monitored by Electron Paramagnetic Resonance'. *Journal of Colloid and Interface Science* 201.2 (1998), pp. 105–117. DOI: http://dx.doi.org/10.1006/jcis.1998.5413.

[60] Frasch, J., Lebeau, B., Soulard, M., Patarin, J. and Zana, R. 'In Situ Investigations on Cetyltrimethylammonium Surfactant/Silicate Systems, Precursors of Organized Mesoporous MCM-41-Type Siliceous Materials'. *Langmuir* 16.23 (2000), pp. 9049–9057. DOI: 10.1021/la000295u.

[61] Boissière, C., Larbot, A., Bourgaux, C., Prouzet, E. and Bunton, C. A. 'A Study of the Assembly Mechanism of the Mesoporous MSU-X Silica Two-Step Synthesis'. *Chemistry of Materials* 13.10 (2001), pp. 3580–3586. DOI: 10.1021/cm011031b.

[62] Larson, R. G., Scriven, L. E. and Davis, H. T. 'Monte Carlo simulation of model amphiphile-oil-water systems'. *The Journal of Chemical Physics* 83.5 (1985), pp. 2411–2420. DOI: 10.1063/1.449286.

[63] Jin, L., Auerbach, S. M. and Monson, P. A. 'Simulating the Formation of Surfactant-Templated Mesoporous Silica Materials: A Model with Both Surfactant Self-Assembly and Silica Polymerization'. *Langmuir* 29.2 (2013), pp. 766–780. DOI: 10.1021/la304475j.

[64] Firouzi, A., Atef, F., Oertli, A. G., Stucky, G. D. and Chmelka, B. F. 'Alkaline Lyotropic Silicate-Surfactant Liquid Crystals'. *Journal of the American Chemical Society* 119.15 (1997), pp. 3596–3610. DOI: 10.1021/ja963007i.

[65] Jorge, M., Gomes, J. R. B., Cordeiro, M. N. D. S. and Seaton, N. A. 'Molecular Simulation of Silica/Surfactant Self-Assembly in the Synthesis of Periodic Mesoporous Silicas'. *Journal of the American Chemical Society* 129.50 (2007), pp. 15414–15415. DOI: 10.1021/ja075070l.

[66] Marrink, S. J., de Vries, A. H. and Mark, A. E. 'Coarse Grained Model for Semiquantitative Lipid Simulations'. *The Journal of Physical Chemistry B* 108.2 (2004), pp. 750–760. DOI: 10.1021/jp036508g.

[67] Ingólfsson, H. I., Lopez, C. A., Uusitalo, J. J., de Jong, D. H., Gopal, S. M., Periole, X. and Marrink, S. J. 'The power of coarse graining in biomolecular simulations'. *Wiley Interdisciplinary Reviews. Computational Molecular Science* 4.3 (2014), pp. 225–248. DOI: 10.1002/wcms.1169.

[68] Sugita, Y. and Okamoto, Y. 'Replica-exchange molecular dynamics method for protein folding'. *Chemical Physics Letters* 314.1–2 (1999), pp. 141–151. DOI: http://dx.doi.org/10.1016/S0009-2614(99)01123-9.

[69] Marrink, S. J., Tieleman, D. P. and Mark, A. E. 'Molecular Dynamics Simulation of the Kinetics of Spontaneous Micelle Formation'. *The Journal of Physical Chemistry B* 104.51 (2000), pp. 12165–12173. DOI: 10.1021/jp001898h.

[70] Friemann, R., Larsson, D. S. D., Wang, Y. and van der Spoel, D. 'Molecular Dynamics Simulations of a Membrane Protein-Micelle Complex in Vacuo'. *Journal of the American Chemical Society* 131.46 (2009). PMID: 19877613, pp. 16606–16607. DOI: 10.1021/ja902962y.

[71] Garrido, N. M., Jorge, M., Queimada, A. J., Macedo, E. A. and Economou, I. G. 'Using molecular simulation to predict solute solvation and partition coefficients in solvents of different polarity'. *Physical Chemistry Chemical Physics* 13 (20 2011), pp. 9155–9164. DOI: 10.1039/C1CP20110G.

[72] Rahman, A. 'Correlations in the Motion of Atoms in Liquid Argon'. *Physical Review* 136.2 (1964), A405–A411. DOI: 10.1103/PhysRev.136.A405.

[73] Frenkel, D. and Smit, B. *Understanding Molecular Simulation : from algorithms to applications*. 2nd. Vol. 1. Computational Science Series. San Diego: Academic Press, 2001. 600 pp.

[74] Vlugt, T. J., van der Eerden, J. P., Dijkstra, M., Smit, B. and Frenkel, D. *Introduction to Molecular Simulation and Statistical Thermodynamics*. Delft, 2008.

[75] *RCSB Protein Data Bank*. URL: www.rcsb.org/pdb (visited on 24/11/2016).

[76] Schaftenaar, G. and Noordik, J. H. 'Molden: a pre- and post-processing program for molecular and electronic structures'. *Journal of Computer-Aided Molecular Design* 14.2 (2000), pp. 123–134. DOI: 10.1023/A:1008193805436.

[77] Hanwell, M. D., Curtis, D. E., Lonie, D. C., Vandermeersch, T., Zurek, E. and Hutchison, G. R. 'Avogadro: an advanced semantic chemical editor, visualization, and analysis platform'. *Journal of Cheminformatics* 4.1 (2012), p. 17. DOI: 10.1186/1758-2946-4-17.

[78] Allen, M. P. and Tildesley, D. J. *Computer Simulation of Liquids*. Oxford, New York: Oxford University Press, 1989. 408 pp.

[79] Wick, C. D., Stubbs, J. M., Rai, N. and Siepmann, J. I. 'Transferable potentials for phase equilibria. 7. Primary, secondary, and tertiary amines, nitroalkanes and nitrobenzene, nitriles, amides, pyridine, and pyrimidine'. *The Journal of Physical Chemistry. B* 109.40 (2005), pp. 18974–18982. DOI: 10.1021/jp0504827.

[80] Jorgensen, W. L., Maxwell, D. S. and Tirado-Rives, J. 'Development and Testing of the OPLS All-Atom Force Field on Conformational Energetics and Properties of Organic Liquids'. *Journal of the American Chemical Society* 118.45 (1996), pp. 11225–11236. DOI: 10.1021/ja9621760.

[81] Wang, J., Wolf, R. M., Caldwell, J. W., Kollman, P. A. and Case, D. A. 'Development and testing of a general amber force field'. *Journal of Computational Chemistry* 25.9 (2004), pp. 1157–1174. DOI: 10.1002/jcc.20035.

[82] Leach, A. *Molecular Modelling: Principles and Applications*. 2nd ed. Prentice Hall, 2001.

[83] Hess, B., Bekker, H., Berendsen, H. J. C. and Fraaije, J. G. E. M. 'LINCS: A linear constraint solver for molecular simulations'. *Journal of Computational Chemistry* 18.12 (1997), pp. 1463–1472. DOI: 10.1002/(SICI)1096-987X(199709)18:12<1463::AID-JCC4>3.0.CO;2-H.

[84] Ryckaert, J.-P., Ciccotti, G. and Berendsen, H. J. C. 'Numerical integration of the cartesian equations of motion of a system with constraints: molecular dynamics of n-alkanes'. *Journal of Computational Physics* 23.3 (1977), pp. 327–341. DOI: 10.1016/0021-9991(77)90098-5.

[85] Miyamoto, S. and Kollman, P. A. 'Settle: An analytical version of the SHAKE and RATTLE algorithm for rigid water models'. *Journal of Computational Chemistry* 13.8 (1992), pp. 952–962. DOI: 10.1002/jcc.540130805.

[86] Schlick, T. *Molecular Modeling and Simulation: An Interdisciplinary Guide*. Vol. 21. Interdisciplinary Applied Mathematics. New York, NY: Springer New York, 2010.

[87] Shirts, M. R., Mobley, D. L., Chodera, J. D. and Pande, V. S. 'Accurate and efficient corrections for missing dispersion interactions in molecular simulations'. *The Journal of Physical Chemistry B* 111.45 (2007), pp. 13052–13063. DOI: 10.1021/jp0735987.

[88] van der Spoel, D., Lindahl, E., Hess, B. and the GROMACS development team. *GROMACS User Manual version 4.6.3*. 2013. URL: ftp.gromacs.org/pub/manual/manual-4.6.3.pdf (visited on 24/02/2017).

[89] Ewald, P. P. 'Die Berechnung optischer und elektrostatischer Gitterpotentiale'. *Annalen der Physik* 369.3 (1921), pp. 253–287. DOI: 10.1002/andp.19213690304.

[90] Darden, T., York, D. and Pedersen, L. 'Particle mesh Ewald: An N log(N) method for Ewald sums in large systems'. *The Journal of Chemical Physics* 98.12 (1993), pp. 10089–10092. DOI: 10.1063/1.464397.

[91] Essmann, U., Perera, L., Berkowitz, M. L., Darden, T., Lee, H. and Pedersen, L. G. 'A smooth particle mesh Ewald method'. *The Journal of Chemical Physics* 103.19 (1995), pp. 8577–8593. DOI: 10.1063/1.470117.

[92] Hockney, R., Goel, S. and Eastwood, J. 'Quiet high-resolution computer models of a plasma'. *Journal of Computational Physics* 14.2 (1974), pp. 148–158. DOI: 10.1016/0021-9991(74)90010-2.

[93] Verlet, L. 'Computer "Experiments" on Classical Fluids. I. Thermodynamical Properties of Lennard-Jones Molecules'. *Physical Review* 159.1 (1967), pp. 98–103. DOI: 10.1103/PhysRev.159.98.

[94] Berendsen, H. J. C., Postma, J. P. M., van Gunsteren, W. F., DiNola, A. and Haak, J. R. 'Molecular dynamics with coupling to an external bath'. *The Journal of Chemical Physics* 81.8 (1984), pp. 3684–3690. DOI: 10.1063/1.448118.

[95] Nosé, S. 'A molecular dynamics method for simulations in the canonical ensemble'. *Molecular Physics* 52.2 (1984), pp. 255–268. DOI: 10.1080/00268978400101201.

[96] Hoover, W. G. 'Canonical dynamics: Equilibrium phase-space distributions'. *Physical Review A* 31.3 (1985), pp. 1695–1697. DOI: 10.1103/PhysRevA.31.1695.

[97] Parrinello, M. and Rahman, A. 'Polymorphic transitions in single crystals: A new molecular dynamics method'. *Journal of Applied Physics* 52.12 (1981), pp. 7182–7190. DOI: 10.1063/1.328693.

[98] Born, M. and Oppenheimer, R. 'Zur Quantentheorie der Molekeln'. *Annalen der Physik* 389.20 (1927), pp. 457–484. DOI: 10.1002/andp.19273892002.

[99] Dada, J. O. and Mendes, P. 'Multi-scale modelling and simulation in systems biology'. *Integrative Biology* 3.2 (2011), pp. 86–96. DOI: 10.1039/C0IB00075B.

[100] Perfahl, H., Byrne, H. M., Chen, T., Estrella, V., Alarcón, T., Lapin, A., Gatenby, R. A., Gillies, R. J., Lloyd, M. C., Maini, P. K., Reuss, M. and Owen, M. R. 'Multiscale Modelling of Vascular Tumour Growth in 3D: The Roles of Domain Size and Boundary Conditions'. *PLOS ONE* 6.4 (2011), e14790. DOI: 10.1371/journal.pone.0014790.

[101] Clancy, C. E., An, G., Cannon, W. R., Liu, Y., May, E. E., Ortoleva, P., Popel, A. S., Sluka, J. P., Su, J., Vicini, P., Zhou, X. and Eckmann, D. M. 'Multiscale Modeling in the Clinic: Drug Design and Development'. *Annals of Biomedical Engineering* 44.9 (2016), pp. 2591–2610. DOI: 10.1007/s10439-016-1563-0.

[102] Chen, S., Wang, M. and Xia, Z. 'Multiscale Fluid Mechanics and Modeling'. *Procedia IUTAM*. Mechanics for the World: Proceedings of the 23rd International Congress of Theoretical and Applied Mechanics, ICTAM2012 10 (2014), pp. 100–114. DOI: 10.1016/j.piutam.2014.01.012.

[103] Perdikaris, P., Grinberg, L. and Karniadakis, G. E. 'Multiscale modeling and simulation of brain blood flow'. *Physics of Fluids* 28.2 (2016), p. 021304. DOI: 10.1063/1.4941315.

[104] Suter, J., Groen, D., Kabalan, L. and Coveney, P. V. 'Distributed Multiscale Simulations of Clay-Polymer Nanocomposites'. *MRS Online Proceedings Library Archive* 1470 (2012). DOI: 10.1557/opl.2012.1009.

[105] Petukhov, K., Alam, M., Rupp, H., Strömsdörfer, S., Müller, P., Scheurer, A., Saalfrank, R., Kortus, J., Postnikov, A., Ruben, M., Thompson, L. and Lehn, J.-M. 'STM spectroscopy of magnetic molecules'. *Coordination Chemistry Reviews* 253.19–20 (2009), pp. 2387–2398. DOI: 10.1016/j.ccr.2009.01.024.

[106] zset-software. *Zébulon: Non-linear finite element solver*. URL: http://www.zset-software.com/products/zebulon/ (visited on 17/12/2016).

[107] Saunders, M. G. and Voth, G. A. 'Coarse-Graining Methods for Computational Biology'. *Annual Review of Biophysics* 42.1 (2013), pp. 73–93. DOI: 10.1146/annurev-biophys-083012-130348.

[108] Bahar, I. and Jernigan, R. 'Inter-residue potentials in globular proteins and the dominance of highly specific hydrophilic interactions at close separation 1'. *Journal of Molecular Biology* 266.1 (1997), pp. 19–214. DOI: http://dx.doi.org/10.1006/jmbi.1996.0758.

[109] Arkhipov, A., Freddolino, P. L., Imada, K., Namba, K. and Schulten, K. 'Coarse-Grained Molecular Dynamics Simulations of a Rotating Bacterial Flagellum'. *Biophysical Journal* 91.12 (2006), pp. 4589–4597. DOI: 10.1529/biophysj.106.093443.

[110] Deserno, M. 'Mesoscopic Membrane Physics: Concepts, Simulations, and Selected Applications'. *Macromolecular Rapid Communications* 30.9-10 (2009), pp. 752–771. DOI: 10.1002/marc.200900090.

[111] Shen, J.-W., Li, C., van der Vegt, N. F. and Peter, C. 'Transferability of Coarse Grained Potentials: Implicit Solvent Models for Hydrated Ions'. *Journal of Chemical Theory and Computation* 7.6 (2011). PMID: 26596452, pp. 1916–1927. DOI: 10.1021/ct2001396.

[112] Hadley, K. R. and McCabe, C. 'Coarse-Grained Molecular Models of Water: A Review'. *Molecular Simulation* 38.8-9 (2012), pp. 671–681. DOI: 10.1080/08927022.2012.671942.

[113] van Hoof, B., Markvoort, A. J., van Santen, R. A. and Hilbers, P. A. J. 'The CUMULUS coarse graining method: transferable potentials for water and solutes'. *The Journal of Physical Chemistry B* 115.33 (2011), pp. 10001–10012. DOI: 10.1021/jp201975m.

[114] Hadley, K. R. and McCabe, C. 'On the Investigation of Coarse-Grained Models for Water: Balancing Computational Efficiency and the Retention of Structural Properties'. *The Journal of Physical Chemistry B* 114.13 (2010), pp. 4590–4599. DOI: 10.1021/jp911894a.

[115] Yesylevskyy, S. O., Schäfer, L. V., Sengupta, D. and Marrink, S. J. 'Polarizable Water Model for the Coarse-Grained MARTINI Force Field'. *PLOS Computational Biology* 6.6 (2010), e1000810. DOI: 10.1371/journal.pcbi.1000810.

[116] Wu, Z., Cui, Q. and Yethiraj, A. 'A New Coarse-Grained Model for Water: The Importance of Electrostatic Interactions'. *The Journal of Physical Chemistry B* 114.32 (2010), pp. 10524–10529. DOI: 10.1021/jp1019763.

[117] Orsi, M. and Essex, J. W. 'The ELBA force field for coarse-grain modeling of lipid membranes'. *PLOS ONE* 6.12 (2011), e28637. DOI: 10.1371/journal.pone.0028637.

[118] Brini, E., Algaer, E. A., Ganguly, P., Li, C., Rodríguez-Ropero, F. and van der Vegt, N. F. A. 'Systematic coarse-graining methods for soft matter simulations - a review'. *Soft Matter* 9.7 (2013), pp. 2108–2119. DOI: 10.1039/C2SM27201F.

[119] Mirzoev, A. and Lyubartsev, A. P. 'MagiC: Software Package for Multiscale Modeling'. *Journal of Chemical Theory and Computation* 9.3 (2013), pp. 1512–1520. DOI: 10.1021/ct301019v.

[120] Reith, D., Pütz, M. and Müller-Plathe, F. 'Deriving effective mesoscale potentials from atomistic simulations'. *Journal of Computational Chemistry* 24.13 (2003), pp. 1624–1636. DOI: 10.1002/jcc.10307.

[121] Lyubartsev, A. P. and Laaksonen, A. 'Calculation of effective interaction potentials from radial distribution functions: A reverse Monte Carlo approach'. *Physical Review. E, Statistical Physics, Plasmas, Fluids, and Related Interdisciplinary Topics* 52.4 (1995), pp. 3730–3737. DOI: 10.1103/PhysRevE.52.3730.

[122] Henderson, R. L. 'A uniqueness theorem for fluid pair correlation functions'. *Physics Letters A* 49.3 (1974), pp. 197–198. DOI: 10.1016/0375-9601(74)90847-0.

[123] Ercolessi, F. and Adams, J. B. 'Interatomic Potentials from First-Principles Calculations: The Force-Matching Method'. *EPL (Europhysics Letters)* 26.8 (1994), p. 583. DOI: 10.1209/0295-5075/26/8/005.

[124] Izvekov, S. and Voth, G. A. 'A multiscale coarse-graining method for biomolecular systems'. *The Journal of Physical Chemistry B* 109.7 (2005), pp. 2469–2473. DOI: 10.1021/jp044629q.

[125] Marrink, S. J. and Tieleman, D. P. 'Perspective on the Martini model'. *Chemical Society Reviews* 42.16 (2013), pp. 6801–6822. DOI: 10.1039/c3cs60093a.

[126] Zhang, W., Pauly, T. R. and Pinnavaia, T. J. 'Tailoring the Framework and Textural Mesopores of HMS Molecular Sieves through an Electrically Neutral (S^0I^0) Assembly Pathway'. *Chemistry of Materials* 9.11 (1997), pp. 2491–2498. DOI: 10.1021/cm970354y.

[127] Cassiers, K., Van Der Voort, P., Linssen, T., Vansant, E. F., Lebedev, O. and Van Landuyt, J. 'A Counterion-Catalyzed (S^0H^+)(X^-I^+) Pathway toward Heat- and Steam-Stable Mesostructured Silica Assembled from Amines in Acidic Conditions'. *The Journal of Physical Chemistry B* 107.16 (2003), pp. 3690–3696. DOI: 10.1021/jp026696v.

[128] Caldararu, H., Caragheorgheopol, A., Savonea, F., Macquarrie, D. J. and Gilbert, B. C. 'A Spin Probe Study of Mesoporous Silica Formation via a Neutral Templating Route'. *The Journal of Physical Chemistry B* 107.25 (2003), pp. 6032–6038. DOI: 10.1021/jp021004o.

[129] Galarneau, A., Sartori, F., Cangiotti, M., Mineva, T., Renzo, F. D. and Ottaviani, M. F. 'Sponge Mesoporous Silica Formation Using Disordered Phospholipid Bilayers as Template'. *The Journal of Physical Chemistry B* 114.6 (2010). PMID: 20104922, pp. 2140–2152. DOI: 10.1021/jp908828q.

[130] Humphrey, W., Dalke, A. and Schulten, K. 'VMD: visual molecular dynamics'. *Journal of Molecular Graphic* 14.1 (1996), pp. 33–38, 27–28.

[131] Martínez, L., Andrade, R., Birgin, E. G. and Martínez, J. M. 'PACKMOL: a package for building initial configurations for molecular dynamics simulations'. *Journal of Computational Chemistry* 30.13 (2009), pp. 2157–2164. DOI: 10.1002/jcc.21224.

[132] Berendsen, H. J. C., Grigera, J. R. and Straatsma, T. P. 'The missing term in effective pair potentials'. *The Journal of Physical Chemistry* 91.24 (1987), pp. 6269–6271. DOI: 10.1021/j100308a038.

[133] Swain, M. 'chemicalize.org'. *Journal of Chemical Information and Modeling* 52.2 (2012), pp. 613–615. DOI: 10.1021/ci300046g.

[134] Caleman, C., van Maaren, P. J., Hong, M., Hub, J. S., Costa, L. T. and van der Spoel, D. 'Force Field Benchmark of Organic Liquids: Density, Enthalpy of Vaporization, Heat Capacities, Surface Tension, Isothermal Compressibility, Volumetric Expansion Coefficient, and Dielectric Constant'. *Journal of Chemical Theory and Compution* 8.1 (2012), pp. 61–74. DOI: 10.1021/ct200731v.

[135] Hess, B., Bekker, H., Berendsen, H. J. C. and Fraaije, J. G. E. M. 'LINCS: A linear constraint solver for molecular simulations'. *Journal of Computional Chemistry* 18.12 (1997), pp. 1463–1472. DOI: 10.1002/(SICI)1096-987X(199709)18:12<1463::AID-JCC4>3.0.CO;2-H.

[136] Darden, T., Perera, L., Li, L. and Pedersen, L. 'New tricks for modelers from the crystallography toolkit: the particle mesh Ewald algorithm and its use in nucleic acid simulations'. *Structure* 7.3 (1999), R55–R60. DOI: 10.1016/S0969-2126(99)80033-1.

[137] Bussi, G., Donadio, D. and Parrinello, M. 'Canonical sampling through velocity rescaling'. *The Journal of Chemical Physics* 126.1 (2007), p. 014101. DOI: 10.1063/1.2408420.

[138] Hoshen, J. and Kopelman, R. 'Percolation and cluster distribution. I. Cluster multiple labeling technique and critical concentration algorithm'. *Physical Review B* 14.8 (1976), pp. 3438–3445. DOI: 10.1103/PhysRevB.14.3438.

[139] CAMEO Chemicals. *DODECANAMINE | CAMEO Chemicals | NOAA*. URL: https://cameochemicals.noaa.gov/chemical/21833 (visited on 13/03/2017).

[140] Bhat, M. and Gaikar, V. G. 'Characterization of Interaction between Butyl Benzene Sulfonates and Cetyl Trimethylammonium Bromide in Mixed Aggregate Systems'. *Langmuir* 15.14 (1999), pp. 4740–4751. DOI: 10.1021/la981439w.

[141] Mata, J., Varade, D. and Bahadur, P. 'Aggregation behavior of quaternary salt based cationic surfactants'. *Thermochimica Acta* 428.1–2 (2005), pp. 147–155. DOI: http://dx.doi.org/10.1016/j.tca.2004.11.009.

[142] Jeffrey, G. *An Introduction to Hydrogen Bonding*. Topics in Physical Chemistry - Oxford University Press. Oxford University Press, 1997.

[143] Malliaris, A., Le Moigne, J., Sturm, J. and Zana, R. 'Temperature dependence of the micelle aggregation number and rate of intramicellar excimer formation in aqueous surfactant solutions'. *The Journal of Physical Chemistry* 89.12 (1985), pp. 2709–2713. DOI: 10.1021/j100258a054.

[144] de Oliveira Wanderley Neto, A., Ferreira Moura, E., Scatena Júnior, H., de Castro Dantas, T. N., Dantas Neto, A. A. and Gurgel, A. 'Preparation and application of self-assembled systems containing dodecylammonium bromide and chloride as corrosion inhibitors of carbon-steel'. *Colloids and Surfaces A: Physicochemical and Engineering Aspects* 398 (2012), pp. 76–83. DOI: http://dx.doi.org/10.1016/j.colsurfa.2012.02.014.

[145] Broome, F. K., Hoerr, C. W. and Harwood, H. J. 'The Binary Systems of Water with Dodecylammonium Chloride and Its N-Methyl Derivatives1'. *Journal of the American Chemical Society* 73.7 (1951), pp. 3350–3352. DOI: 10.1021/ja01151a104.

[146] Rizzatti, M. R. and Gault, J. D. 'Phase diagrams of the decylammonium chloride/ammonium chloride/water system in the nematic micellar region'. *Journal of Colloid and Interface Science* 110.1 (1986), pp. 258–262. DOI: 10.1016/0021-9797(86)90375-9.

[147] Rubingh, D. *Cationic Surfactants: Physical Chemistry*. Surfactant Science. Taylor & Francis, 1990.

[148] Karlsson, S., Friman, R., Björkqvist, M., Lindström, B. and Backlund, S. 'Phase Behavior and Characterization of the System Acetic Acid-Dodecylamine-Water'. *Langmuir* 17.12 (2001), pp. 3573–3578. DOI: 10.1021/la001594m.

[149] Hartmann, P. C., Dieudonné, P. and Sanderson, R. D. 'Self-assembly and influence of the organic counterion in the ternary systems dodecylamine/acrylic acid/water and dodecylamine/methacrylic acid/water'. *Journal of Colloid and Interface Science* 284.1 (2005), pp. 289–297. DOI: 10.1016/j.jcis.2004.10.009.

[150] Dai, Q. and Laskowski, J. S. 'The Krafft point of dodecylammonium chloride: pH effect'. *Langmuir* 7.7 (1991), pp. 1361–1364. DOI: 10.1021/la00055a012.

[151] Attwood, D., Collett, J. and Tait, C. 'The micellar properties of the poly(oxyethylene) - poly(oxypropylene) copolymer Pluronic F127 in water and electrolyte solution'. *International Journal of Pharmaceutics* 26.1 (1985), pp. 25–33. DOI: 10.1016/0378-5173(85)90197-8.

[152] Perrin, D. D. *Dissociation constants of organic bases in aqueous solution: supplement 1972*. Butterworths, 1972.

[153] Šefčík, J. and McCormick, A. V. 'Thermochemistry of aqueous silicate solution precursors to ceramics'. *AIChE Journal* 43.S11 (1997), pp. 2773–2784. DOI: 10.1002/aic.690431324.

[154] Gutz, I. G. R. *CurTiPot. pH and Acid Base Titration Curves: Analysis and Simulation freeware, version 4.2*.

[155] Wang, F., Shi, Z., Gong, F., Jiu, J. and Motonari, A. 'Morphology Control of Anatase TiO2 by Surfactant-assisted Hydrothermal Method'. *Chinese Journal of Chemical Engineering* 15.5 (2007), pp. 754–759. DOI: 10.1016/S1004-9541(07)60158-X.

[156] Ohtaki, H. and Maeda, M. 'Ionic Equilibria in Mixed Solvents. VIII. Solvent Effects on the Dissociation of Diprotic Acids in Aqueous Methanol Mixtures'. *Bulletin of the Chemical Society of Japan* 46.7 (1973), pp. 2052–2056. DOI: 10.1246/bcsj.46.2052.

[157] Nagarajan, R. 'Self-Assembly of Bola Amphiphiles'. *Chemical Engineering Communications* 55.1-6 (1987), pp. 251–273. DOI: 10.1080/00986448708911931.

[158] Kirkwood, J. G. and Buff, F. P. 'The Statistical Mechanical Theory of Surface Tension'. *The Journal of Chemical Physics* 17.3 (1949), pp. 338–343. DOI: 10.1063/1.1747248.

[159] Irving, J. H. and Kirkwood, J. G. 'The Statistical Mechanical Theory of Transport Processes. IV. The Equations of Hydrodynamics'. *The Journal of Chemical Physics* 18.6 (1950), pp. 817–829. DOI: 10.1063/1.1747782.

[160] Prince, L. M. 'A theory of aqueous emulsions I. Negative interfacial tension at the oil/water interface'. *Journal of Colloid and Interface Science* 23.2 (1967), pp. 165–173. DOI: 10.1016/0021-9797(67)90099-9.

[161] Chakraborty, P. and Zachariah, M. R. '"Effective" Negative Surface Tension: A Property of Coated Nanoaerosols Relevant to the Atmosphere'. *The Journal of Physical Chemistry A* 111.25 (2007), pp. 5459–5464. DOI: 10.1021/jp070226p.

[162] Baoukina, S., Monticelli, L., Amrein, M. and Tieleman, D. P. 'The Molecular Mechanism of Monolayer-Bilayer Transformations of Lung Surfactant from Molecular Dynamics Simulations'. *Biophysical Journal* 93.11 (2007), pp. 3775–3782. DOI: 10.1529/biophysj.107.113399.

[163] Gu, D., Zhang, F., Shi, Y., Zhang, F., Wu, Z., Deng, Y., Zhang, L., Tu, B. and Zhao, D. 'A "teardown" method to create large mesotunnels on the pore walls of ordered mesoporous silica'. *Journal of Colloid and Interface Science* 328.2 (2008), pp. 338–343. DOI: 10.1016/j.jcis.2008.09.043.

[164] Huang, Z., Miao, H., Li, J.-h., Wei, J.-l., Kawi, S. and Lai, M. W. 'Modifier-enhanced supercritical CO2 extraction of organic template from aluminosilicate MCM-41 materials: Effect of matrix Al/Si ratios and different modifiers'. *Separation and Purification Technology* 118 (2013), pp. 170–178. DOI: 10.1016/j.seppur.2013.06.048.

[165] Jabariyan, S. and Zanjanchi, M. A. 'A simple and fast sonication procedure to remove surfactant templates from mesoporous MCM-41'. *Ultrasonics Sonochemistry* 19.5 (2012), pp. 1087–1093. DOI: 10.1016/j.ultsonch.2012.01.012.

[166] Gérardin, C., Reboul, J., Bonne, M. and Lebeau, B. 'Ecodesign of ordered mesoporous silica materials'. *Chemical Society Reviews* 42.9 (2013), pp. 4217–4255. DOI: 10.1039/C3CS35451B.

[167] Brunauer, S., Emmett, P.H. and Teller, E. 'Adsorption of Gases in Multimolecular Layers'. *Journal of the American Chemical Society* 60.2 (1938), pp. 309–319. DOI: 10.1021/ja01269a023.

[168] Barrett, E.P., Joyner, L.G. and Halenda, P.P. 'The Determination of Pore Volume and Area Distributions in Porous Substances. I. Computations from Nitrogen Isotherms'. *Journal of the American Chemical Society* 73.1 (1951), pp. 373–380. DOI: 10.1021/ja01145a126.

[169] de Boer, J.H., Lippens, B.C., Linsen, B.G., Broekhoff, J.C.P., van den Heuvel, A. and Osinga, T.J. 'Thet-curve of multimolecular N2-adsorption'. *Journal of Colloid and Interface Science* 21.4 (1966), pp. 405–414. DOI: 10.1016/0095-8522(66)90006-7.

[170] Langmuir, I. 'The Adsorption of Gases on Plane Surfaces of Glass, Mica and Platinum.' *Journal of the American Chemical Society* 40.9 (1918), pp. 1361–1403. DOI: 10.1021/ja02242a004.

[171] Walton, K.S. and Snurr, R.Q. 'Applicability of the BET Method for Determining Surface Areas of Microporous Metal-Organic Frameworks'. *Journal of the American Chemical Society* 129.27 (2007). PMID: 17580944, pp. 8552–8556. DOI: 10.1021/ja071174k.

[172] Belton, D.J., Patwardhan, S.V. and Perry, C.C. 'Spermine, spermidine and their analogues generate tailored silicas'. *Journal of Materials Chemistry* 15.43 (2005), pp. 4629–4638. DOI: 10.1039/B509683A.

[173] Steven, C.R., Busby, G.A., Mather, C., Tariq, B., Briuglia, M.L., Lamprou, D.A., Urquhart, A.J., Grant, M.H. and Patwardhan, S.V. 'Bioinspired silica as drug delivery systems and their biocompatibility'. *Journal of Material Chemistry B* 2.31 (2014), pp. 5028–5042. DOI: 10.1039/C4TB00510D.

[174] Lehman, S.E. and Larsen, S.C. 'Zeolite and mesoporous silica nanomaterials: greener syntheses, environmental applications and biological toxicity'. *Environmental Science: Nano* 1.3 (2014), pp. 200–213. DOI: 10.1039/C4EN00031E.

[175] Emami, F.S., Puddu, V., Berry, R.J., Varshney, V., Patwardhan, S.V., Perry, C.C. and Heinz, H. 'Force Field and a Surface Model Database for Silica to Simulate Interfacial Properties in Atomic Resolution'. *Chemistry of Materials* 26.8 (2014), pp. 2647–2658. DOI: 10.1021/cm500365c.

[176] Heinz, H., Lin, T.-J., Kishore Mishra, R. and Emami, F.S. 'Thermodynamically Consistent Force Fields for the Assembly of Inorganic, Organic, and Biological Nanostructures: The INTERFACE Force Field'. *Langmuir* 29.6 (2013), pp. 1754–1765. DOI: 10.1021/la3038846.

[177] Emami, F. S., Puddu, V., Berry, R. J., Varshney, V., Patwardhan, S. V., Perry, C. C. and Heinz, H. 'Prediction of Specific Biomolecule Adsorption on Silica Surfaces as a Function of pH and Particle Size'. *Chemistry of Materials* 26.19 (2014), pp. 5725–5734. DOI: 10.1021/cm5026987.

[178] Hess, B., Kutzner, C., van der Spoel, D. and Lindahl, E. 'GROMACS 4: Algorithms for Highly Efficient, Load-Balanced, and Scalable Molecular Simulation'. *Journal of Chemical Theory and Computation* 4.3 (2008), pp. 435–447. DOI: 10.1021/ct700301q.

[179] Taylor, J. A. G. and Hockey, J. A. 'Heats of Immersion in Water of Characterized Silicas of Varying Specific Surface Area'. *The Journal of Physical Chemistry* 70.7 (1966), pp. 2169–2172. DOI: 10.1021/j100879a016.

[180] Bolt, G. H. 'Determination of the Charge Density of Silica Sols'. *The Journal of Physical Chemistry* 61.9 (1957), pp. 1166–1169. DOI: 10.1021/j150555a007.

[181] Zerrouk, R., Foissy, A., Mercier, R., Chevallier, Y. and Morawski, J.-C. 'Study of Ca2+-induced silica coagulation by small angle scattering'. *Journal of Colloid and Interface Science* 139.1 (1990), pp. 20–29. DOI: http://dx.doi.org/10.1016/0021-9797(90)90441-P.

[182] Milonjic, S. K. 'Determination of surface ionization and complexation constants at colloidal silica/electrolyte interface'. *Colloids and Surfaces* 23.4 (1987), pp. 301–312. DOI: 10.1016/0166-6622(87)80273-1.

[183] Hilal, S. H., Karickhoff, S. W. and Carreira, L. A. 'A Rigorous Test for SPARC's Chemical Reactivity Models: Estimation of More Than 4300 Ionization pKas'. *Quantitative Structure-Activity Relationships* 14.4 (1995), pp. 348–355. DOI: 10.1002/qsar.19950140405.

[184] Cassiers, K., Van Der Voort, P. and Vansant, E. F. 'Synthesis of stable and directly usable hexagonal mesoporous silica by efficient amine extraction in acidified water'. *Chemical Commununications* 24 (2000), pp. 2489–2490. DOI: 10.1039/B0072970.

[185] Belton, D., Patwardhan, S. V. and Perry, C. C. 'Putrescine homologues control silica morphogenesis by electrostatic interactions and the hydrophobic effect'. *Chemical Communications* 27 (2005), pp. 3475–3477. DOI: 10.1039/B504310G.

[186] Wu, D. and Navrotsky, A. 'Small molecule - Silica interactions in porous silica structures'. *Geochimica et Cosmochimica Acta* 109 (2013), pp. 38–50. DOI: 10.1016/j.gca.2013.01.038.